*energies*

Special Issue Reprint

# The Study of Emerging Electrical Machine Technologies and Their Applications

Edited by
Rong-Jie Wang and Maarten J. Kamper

MDPI

# The Study of Emerging Electrical Machine Technologies and Their Applications

# The Study of Emerging Electrical Machine Technologies and Their Applications

Editors

**Rong-Jie Wang**
**Maarten J. Kamper**

MDPI • Basel • Beijing • Wuhan • Barcelona • Belgrade • Manchester • Tokyo • Cluj • Tianjin

**MDPI**

*Editors*
Rong-Jie Wang
Stellenbosch University
South Africa

Maarten J. Kamper
Stellenbosch University
South Africa

This is a reprint of articles from the Special Issue published online in the open access journal *Energies* (ISSN 1996-1073) (available at: https://www.mdpi.com/journal/energies/special_issues/cool_electrical_machines).

For citation purposes, cite each article independently as indicated on the article page online and as indicated below:

LastName, A.A.; LastName, B.B.; LastName, C.C. Article Title. *Journal Name* **Year**, *Volume Number*, Page Range.

Cover image courtesy of Rong-Jie Wang and Pushman Tlali

# Contents

# About the Editors

**Rong-Jie Wang**

Rong-Jie Wang (Senior Member, IEEE) received his M.Sc. (Eng.) degree from the University of Cape Town in June 1998 and his Ph.D. (Eng.) degree from Stellenbosch University, both of South Africa, in April 2003. He is currently a Professor with the Department of Electrical and Electronic Engineering, Stellenbosch University. His research interests include novel topologies of permanent magnet machines, computer-aided design, and optimization of electrical machines, cooling design and analysis, and renewable energy systems. He is a rated researcher by the South African National Research Foundation and a registered Professional Engineer in South Africa.

**Maarten J. Kamper**

Maarten J. Kamper (Senior Member, IEEE) received the M.Sc. (Eng.) and Ph.D. (Eng.) degrees from Stellenbosch University, South Africa, in 1987 and 1996, respectively. Since 1989, he has been with the Academic Staff of the Department of Electrical and Electronic Engineering, Stellenbosch University, where he is currently a Distinguished Professor of electrical machines and drives. His research interests include computer-aided design and control of reluctance, permanent magnet, and induction machine drives. Prof. Kamper is supported by the South African National Research Foundation, and is also a Registered Professional Engineer in South Africa.

# Preface to "The Study of Emerging Electrical Machine Technologies and Their Applications"

In recent years, the field of electrical machine technologies has experienced significant growth, primarily driven by the introduction of new materials, innovative machine topologies, and drive technologies, as well as expanding application areas, coupled with stricter energy efficiency regulations. This upsurge in the field has prompted researchers and engineers to investigate novel and emerging electrical machine technologies.

The main purpose of this Special Issue is to provide a platform for researchers to showcase their latest research work on electrical machines. The focus of this issue is on pioneering electrical machine technologies that have the potential to emerge as the next generation of electrical machines. In addition, the papers in this issue also explore various application areas, including electric transportation and renewable energy power generation.

This Special Issue compiles a total of 12 papers. Some of them concentrate on novel machine technologies, such as flux-intensifying memory machines, Vernier machines, flux-reversal machines, wound rotor machines, line start motors, and doubly fed machines. The remaining papers delve into a range of topics, encompassing the design and optimization of electrical machines, drive-cycle-based design strategies for traction motor design, the utilization of response surface methodology for the optimal design of brushless DC motors, and harmonic reduction strategies for non-overlap wound rotor machines, as well as the design and sensorless control of dual three-phase PM machines.

The contributors to this Special Issue are active researchers in electrical machines and drives. Their contributions offer new knowledge and insight into the latest developments in this fast-moving field. We hope that this book will serve as a useful resource for researchers, engineers, and students who are interested in emerging electrical machine technologies.

**Rong-Jie Wang and Maarten J. Kamper**
*Editors*

*Article*

# Performance Evaluation of Harmonic Reduced Non-Overlap Winding Wound Rotor Synchronous Machine

**Karen S. Garner \*, Maarten J. Kamper and Andrew T. Loubser \***

Department of Electrical and Electronic Engineering, Stellenbosch University, Stellenbosch 7600, South Africa; kamper@sun.ac.za

\* Correspondence: garnerks@sun.ac.za (K.S.G.); atloubser@sun.ac.za (A.T.L.)

**Abstract:** The analysis and performance evaluation of a harmonic reduction strategy of a non-overlap winding wound rotor synchronous machine is conducted in this paper. The harmonic reduction strategy utilizes phase-shifts between coil currents to reduce sub- and higher-order harmonics. The design is performed on a 3 MW wound rotor synchronous machine with a 16/18 pole/slot combination. The application results in a lowered torque ripple and an increased efficiency of the designed machine. The manufacturing and testing of a 3 kW prototype to ascertain the effectiveness of the design is also presented. The practical measurements correlate successfully with the theoretical results.

**Keywords:** harmonic reduction; non-overlap; phase-shifting; star-delta; synchronous machine; wound rotor

## 1. Introduction

The drive to reduce costs and improve efficiency of electric machines in power generation applications, amongst others, is an ongoing study. Much focus has been applied to the renewable energy sphere to provide sustainable energy solutions to growing global power demands. Wind generation registered a growth of 10% from 2018 to 2019, according to the Renewables Global Status Report for 2019 [1]. Permanent magnet synchronous machines (PMSMs) have been the preferred solution for wind generation systems, partly because of the reduced size of the generator, but methods to improve other synchronous machines are in demand to avoid the use of rare-earth materials and reduce the cost of generation. This study focuses on a wound rotor synchronous machine (WRSM), attractive for, amongst other reasons, the ability to vary flux and thus its reactive power when directly connected to the electrical grid. A non-overlap winding structure is used for the WRSM to improve torque density of the machine and to lower manufacturing costs associated with winding complexity [2]. It is well-known, however, that non-overlap windings contain sub- and higher-order harmonics in the magneto-motive force (MMF) distribution [2]. Numerous strategies have been applied to non-overlap windings to eliminate or reduce sub-harmonic MMF content. The study in [3] theorizes that because of the difference in harmonic content between a single-layer and a double-layer winding, applying a multi-layer winding could potentially reduce sub-harmonics further. A four-layer winding was applied to the stator of a 10/12 pole/slot combination machine and an 8/9 pole/slot combination machine. Despite the obvious added cost and complexity of a four-layer winding, it was also concluded that the strategy reduced all the MMF harmonics, including the working harmonic. For example, the winding factor of the fourth harmonic of the 8/9 pole/slot machine decreased from 0.945 to 0.888 with the first version of the design and to 0.931 with the second version of the design.

The use of concentrated coils to improve the MMF waveform was first explored with distributed windings in [4]. The designed winding uses a combination of two turn numbers such that all slots have two coil sides with a ratio of N1/N2 turns. However, the improvement of the MMF waveform was not significant compared to the increased

winding complexity and manufacturing costs. Some studies show an improvement in the working harmonic of the prototypes in question [5–7]. Unfortunately, the method does not reduce higher-order harmonics and is limited to certain pole/slot combinations. Stator shifting is another technique that has been investigated to reduce sub- and higher-order harmonics and was applied to a 14/12 pole/slot machine where the number of stator slots is then doubled [8]. The winding is divided into two separate windings that are shifted mechanically by an angle and the coil pitch is modified from 1 slot to 2 slots. As such, the windings then overlap. This structure shows a decrease in the sub-harmonics, but the winding structure is no longer a non-overlap concentrated winding, and the benefits of the original winding are lost. The same concept of stator shifting is applied in [9], but without changing the structure to an overlap winding. The base winding is a single layer non-overlap winding of a 14/24 pole/slot combination machine. A second winding is applied with the same distribution of coils, but mechanically shifted from the base winding and the two windings are then connected in series. The study shows an elimination of the first harmonic and a vast reduction of the fifth harmonic in comparison to a 10/12 pole/slot combination, but higher-order harmonics are still present in the MMF spectrum. The pitch factor is also reduced which leads to a reduced winding factor. To overcome this reduction, the number of turns is increased which leads to increased copper losses. This has also only been implemented on the pole/slot combinations stated and no general rule is available for the method.

The intent of this research is to apply a harmonic reduction strategy to a non-overlap winding as in [10]. The method augments the concept of stator shifting. The work in [10] successfully applies the strategy to a 10/12 pole/slot machine, but does not provide a general approach for the harmonic reduction strategy for other pole/slot combinations. Previous research has shown that a mechanical displacement between the winding coils in a phase set alone is not sufficient to markedly decrease the sub-harmonics without reducing the distribution factor of the main harmonic. An electrical phase displacement between the winding coil currents of a phase set is necessary as well. Classical MMF harmonic analysis assumes that no phase shift exists between the currents of the coils in a phase set. Hence, applying a phase shift requires the development of a new winding factor or, more specifically, a new distribution factor as developed in [11].

This study applies the wye-delta coil-current phase-displacement technique to a large 3 MW 16/18 (or else 8/9) pole/slot combination WRSM presented for a medium-speed geared solution with a setup as proposed in [12]. This paper develops harmonic winding factors and considers the harmonic torques in a detailed analysis of the theoretical performance of the 3 MW machine. A finite element analysis model is built and simulated in the commercial tool ANSYS Maxwell. A 3 kW prototype with the proposed phase-shifted winding is manufactured and experimentally analysed for the first time to assist with the validation process.

## 2. Theoretical Harmonic Analysis

Classical harmonic analysis of a non-overlap winding assumes that all the coils in a phase set are in phase or, in other words, in series. Introducing an electrical phase-shift between the coils of a phase set requires a new approach to the analysis of the coil set.

### 2.1. Proposed 16/18 Phase-Shifted Non-Overlap Winding

A cross-section of the proposed 16/18 non-overlap winding is displayed in Figure 1. The 16/18 winding has two winding sections, $W_s$. The number of coils, $u$, per phase set is described by

$$u = \frac{Q}{mW_s},\tag{1}$$

where $Q$ is the number of stator slots/coils, $m$ is the number of phases and $W_s$ is the number of winding sections. This yields $u = 3$ for the 16/18 non-overlap winding.
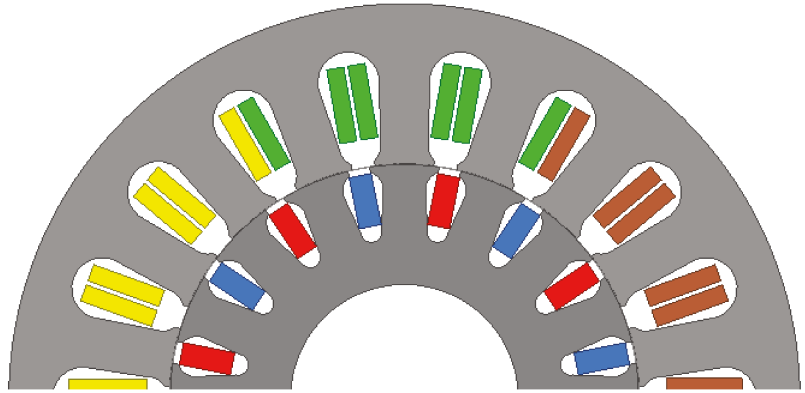
**Figure 1.** Cross-section of the 16/18 WRSM.

The conventional 16/18 non-overlap winding has all three coils of a phase group in series, as depicted in Figure 2a. The harmonic analysis of [11] explains that to achieve a distribution factor of unity for the working harmonic, $v = 4$, while also greatly diminishing the sub- and higher-order harmonics, the phase-shift required between the coils of the phase set is $-20°$. To negate the need for an additional current supply to achieve the phase-shift between the coils, the phase-shift is implemented by configuring the layout and connection of the coils. The closest phase-shift that can be achieved by manipulating the layout of the coils in the phase set is $-30°$, which results in a distribution factor of the working harmonic of 0.9899 while still decreasing the effect of the sub- and higher-order harmonics. The $-30°$ shift is created by instituting a physical wye-delta connection between the coils of each phase set, as seen in Figure 2b.



(a)



(b)
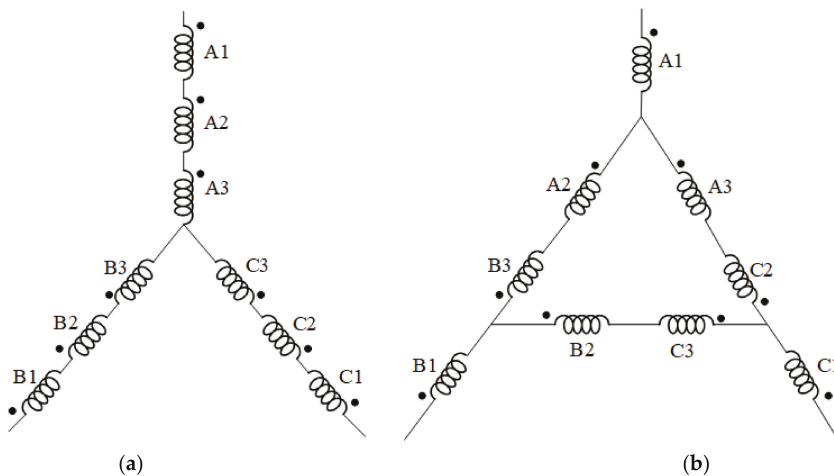
**Figure 2.** (**a**) Coil layout of a 16/18 conventional non-overlap winding; (**b**) Coil layout of the 16/18 phase-shifted non-overlap winding.

*2.2. Harmonic MMF and Distribution Factor*

In [11], a harmonic MMF function, $F_{sv}$, and a harmonic distribution factor, $K_v$, for the phase-shifted winding of Figure 2b above are described by

$$F_{sv} = \frac{3Nk_{pv}}{a\pi|v|}K_vI\sin(\omega t - v\theta - \beta) \tag{2}$$

and

$$K_v = \frac{\sqrt{(1 - \cos b - \cos c)^2 + (\sin c - \sin b)^2}}{u} \tag{3}$$

where

$$b = \alpha_2 - v\theta_s, \tag{4}$$

$$c = \alpha_3 - v\theta_s \tag{5}$$

and

$$\beta = \tan^{-1}\left(\frac{\sin c - \sin b}{1 - \cos b - \cos c}\right). \tag{6}$$

In Equations (1)–(4) the harmonic number is represented by $v$, $N$ is the number of turns of each coil, $k_{pv}$ is the pitch factor, $a$ is the number of parallel paths in the winding, $I$ is the peak amplitude of the phase current with rated $q$-axis current, and $\theta_s$ the electrical slot pitch angle given by

$$\theta_s = \frac{2\pi}{S}, \tag{7}$$

where $S$ is the number of stator slots per machine section.

The angles $\alpha_2$ and $\alpha_3$ in Equations (4) and (5) are the required phase shifts of the second and third coil currents respectively and their total effect is represented by $\beta$. With $\alpha_2 = \alpha_3 = 0$ the coil currents are in phase as in the Y-connection of Figure 2a. With $\alpha_2 = \alpha_3 = -30°$ the coil currents are out of phase as in the Y-Δ connection of Figure 2b. It is shown in Table 1 that the distribution factors of the working and fifth harmonics are increased, but those of the other harmonics are notably reduced.

*2.3. Flux Density and Torque Harmonic Analysis*

It is necessary to investigate the effect of the phase-shift in terms of the harmonics of the air gap flux density as well as the torque harmonics. The air gap flux density harmonics are first determined due to the stator MMF and then in reference to the rotor MMF. The air gap flux density generated is determined from the stator MMF by

$$b_{sv} = \frac{\mu_0 F_{sv}}{gk_c} \tag{8}$$

Substituting Equation (2) into Equation (8),

$$b_{sv} = \frac{\mu_0}{gk_c}\frac{3Nk_{pv}}{a\pi|v|}K_vI\sin(\omega t - v\theta - \beta) \tag{9}$$

$$b_{rv} = \frac{\mu_0}{gk_c}\frac{3Nk_{pv}}{a\pi|v|}K_vI\sin(\omega_{rv}t - v\theta - \beta) \tag{10}$$

where the angle $\theta$ now refers to the rotor and the angular frequency $\omega_{rv}$ is given by

$$\omega_{rv} = \left(1 - \frac{2v}{p}\right)\omega. \tag{11}$$

It is noted from these equations that the changing winding factor will influence the air gap flux density harmonics. The only difference between Equations (9) and (10) is the angular frequency of the flux density and thus the amplitudes are the same. The effect of

the phase-shift can be seen in Figure 3 where the flux density of the working harmonic and the fifth harmonic is increased, while the sub- and higher-order harmonics are reduced. This is expected from the results of the winding factor presented in [11]. The percentage difference in the flux density between the conventional non-overlap and phase shifted winding is detailed in Table 1.
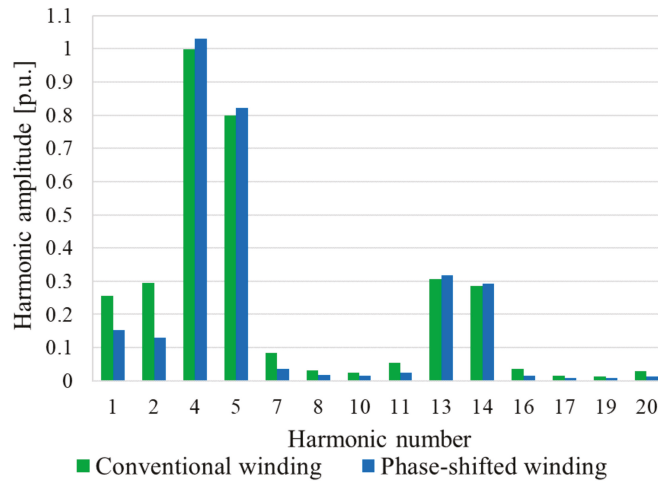


**Figure 3.** Per unit air gap flux density harmonics due to the stator MMF.

In a similar way as Equation (9) the air gap flux density harmonics created by the rotor field winding MMF are described by

$$b_{sv} = \frac{2\mu_0 p k_{prv}}{v\pi g k_c} K_{rv} I \cos\left(\frac{2v\omega t}{M_s p} - v\theta - \beta\right),$$ (12)

where $k_{prv}$ and $K_{rv}$ are the pitch factor and distribution factor of the rotor field winding respectively. These rotor winding factors are unchanged with the application of the phase shift in the stator winding and thus the flux density harmonics will remain the same. The rotor pitch factor is responsible for the presence of only harmonic multiples of the working harmonic.

**Table 1.** Air gap flux density harmonics of the 16/18 pole/slot conventional and phase-shifted non-overlap windings [11].

| Harmonic Number | Air Gap Flux Density Harmonics in per Unit | | |
| --- | --- | --- | --- |
| | Conventional 16/18 Winding | Phase-Shifted 16/18 Winding | % Difference |
| $v = 1$ | 0.2580 | 0.1532 | −10.48 |
| $v = -2$ | 0.2971 | 0.1300 | −16.71 |
| $v = 4$ | 1 | 1.0313 | +3.13 |
| $v = -5$ | 0.7968 | 0.8218 | +2.49 |
| $v = 7$ | 0.08262 | 0.0362 | −4.65 |

The amplitude of the back-EMF induced voltage in the stator winding due to the rotor field can now be calculated as

$$E_{sv} = -\frac{16u\omega N l d_g B_{sv}}{vpM_s} K_v k_{psv},$$ (13)

Energies **2021**, 14, 7501

with

$$B_{sv} = \frac{2\mu_0 p k_{prv}}{v \pi g k_c} K_{rv} I. \tag{14}$$

Figure 4 shows the difference in the induced phase voltage between the two windings. Again, for the working harmonic the phase-shifted winding shows an increase (3.13%) over the conventional winding. This is expected because the induced phase voltage is directly proportional to the winding factor. The percentage of total harmonic distortion (THD) for the theoretical induced voltage is 2.15%.
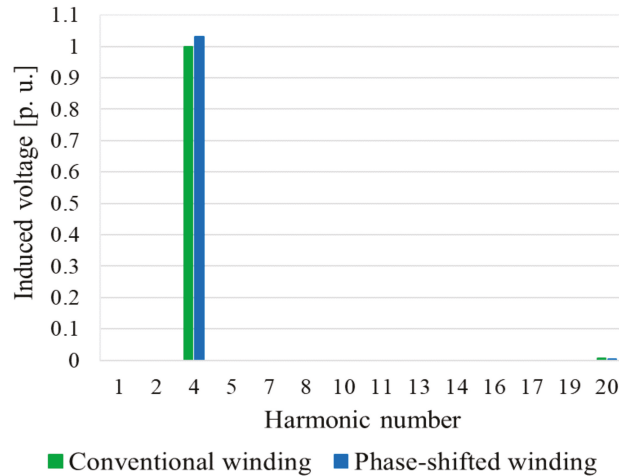


**Figure 4.** Induced phase voltage in the stator winding in per unit.

The instantaneous torque developed by the machine is described from the power developed by

$$T_s = \frac{p M_s}{2\omega} \sum_v [i_{abc}]^T \left[ e_{abc(v)} \right], \tag{15}$$

where $i_{abc}$ and $e_{abc(v)}$ are the phase currents and the induced voltages of the machine. With the phase current considered in phase with the induced voltage and thus only $q$-axis current available, this expression is further simplified as

$$T_s = \frac{3 p M_s}{2\omega} I E_{s(p/2)} + \sum_j I \left( E_{s(j+1)p/2} + E_{s(j-1)p/2} \right) \cos(j\omega t),$$
$$j = 6, 12, 18, .. \tag{16}$$

The first term of Equation (16) is the average torque produced, while the second term refers to the oscillation or ripple of the developed torque. The theoretical torque profile of both winding structures is displayed in Figure 5. Only $j = 6$ is considered in the figure for illustrative purposes. The average torque of the phase-shifted winding shows an improvement of 3.13% as seen with the induced voltage. Figure 6 also shows that the torque ripple is suppressed by 11%, indicating the reduction of the sub- and higher-order harmonic content.

6
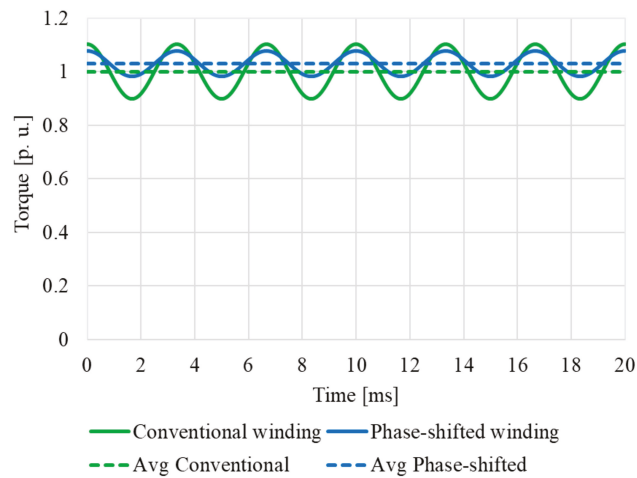
**Figure 5.** Comparison of the developed torque of the conventional and phase-shifted non-overlap windings.
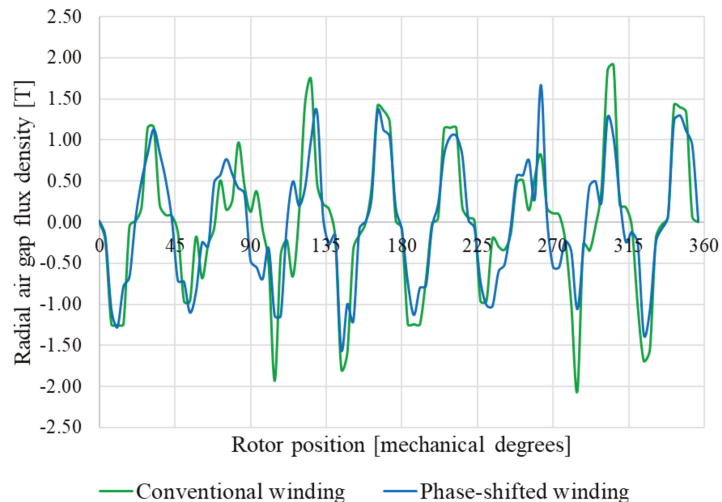


**Figure 6.** Simulated air gap flux density of the conventional and phase-shifted 16/18 non-overlap windings.

## 3. Simulated Performance Results

The specifications of the 3 MW generator used for the first investigation are stated in Table 2. The finite element analysis (FEA) simulated performance evaluation is conducted with rated q-axis current. The simulated air gap flux density of both winding structures is depicted in Figure 6. The air gap flux density of the phase-shifted winding is seen to be more consistent and prone to fewer fluctuations in amplitude because of the harmonic reduction. Further to this, Figure 7 displays the fourth harmonic component of both windings and confirms the dampening of the fluctuation.

**Table 2.** Specifications of the 3 MW 16/18 WRSM.

| Specifications | Value |
|---|---|
| Rated terminal power (MW) | 3 |
| Rated torque (kNm) | 76 |
| Rated speed (r/min) | 375 |
| Rated frequency (Hz) | 50 |
| Rated line voltage (V) | 580 |
| Rated phase current (A) | 3000 |
| Rated field current (A) | 200 |
| Stator outer diameter (mm) | 1600 |
| Rotor outer diameter (mm) | 981 |
| Rotor inner diameter (mm) | 460 |
| Stack length (mm) | 1500 |
| Air gap length (mm) | 3 |
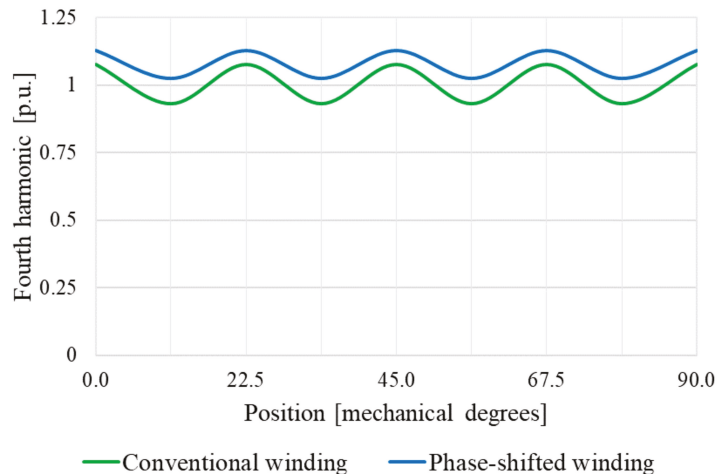


**Figure 7.** Variation of the per unit fourth harmonic air gap flux density with rotor position of the conventional and phase-shifted 16/18 non-overlap winding machines.

Figure 8 shows the theoretical torque curves of the conventional and the phase-shifted 16/18 machines with a rated torque of 76 kNm. The average torque of the conventional winding is 75.36 kNm with a torque ripple of approximately 15.32%. The average torque of the phase-shifted winding is increased to 77.58 kNm and torque ripple is reduced to 9.53%. Further performance characteristics of the two machines are presented in Table 3. As is shown, the power output and efficiency of the machine are improved. The input current is the same for both cases, but the terminal voltage differs. The improved winding factor leads to an increased induced voltage. Although the total machines losses are reduced as a result of the overall reduction of sub-harmonics, the rotor core losses are increased after the implementation of the phase-shifting technique. This can be accredited to the improvement of, amongst others, the 5th harmonic's distribution factor.
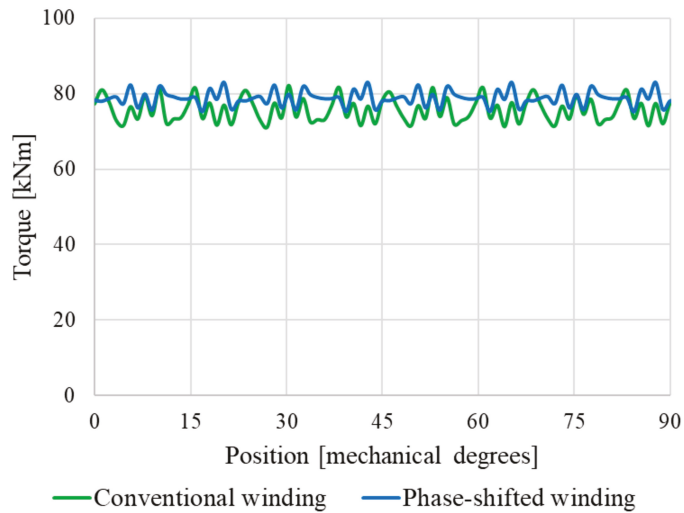
**Figure 8.** Torque curves of the conventional and phase-shifted 3 MW 16/18 winding machines.

**Table 3.** Performance of the conventional and phase-shifted winding machines.

| Performance Parameter ↓ | Conventional Winding | Phase-Shifted Winding | Percentage Difference |
|---|---|---|---|
| Terminal power (MW) | 2.96 | 3.05 | +3% |
| Shaft torque (kNm) | 77.14 | 79.45 | +3% |
| Torque ripple (%) | 15.32 | 9.53 | −5.79% |
| Rotor core loss (kW) | 8.76 | 8.84 | +0.91% |
| Stator core loss (kW) | 25.58 | 23.19 | −9.3% |
| Copper loss (kW) | 43.08 | 43.08 | −0% |
| Efficiency (%) | 97.40 | 97.57 | +0.17% |

## 4. Measured Performance Results

A prototype of the design is required for the testing phase. Due to the impracticality of building a 3 MW prototype, the prototype of [13] was selected. The model was optimized using single line optimization to maximize the output torque. The model is not an exact scaled-down replica of the 3 MW prototype but serves to prove the concept of the harmonic reduction technique employed. The cross-section is displayed in Figure 9 and the specifications of the prototype are detailed in Table 4. The coil connections of the stator winding are completed on a terminal box. Figure 10 shows the test setup of the prototype for direct grid connection.

### 4.1. Machine Parameters from Tests

To confirm the characteristics of the prototype, the standard open-circuit and short-circuit tests are performed. Figure 11 displays the theoretical and experimental results of the open-circuit test of the 16/18 WRSM with phase-shifted non-overlap winding. The results of the short-circuit test are presented in Figure 12.

The equivalent circuit parameters of the 3 kW prototype are given in Table 5 and the measured machine losses are listed in Table 6. The windage and friction losses are determined with zero field current at the rated speed of 375 r/min. The core losses are determined by measuring the rotational losses at rated field current and rated speed and subtracting the measured windage and friction losses. The copper losses given are that of the stator winding at rated current.
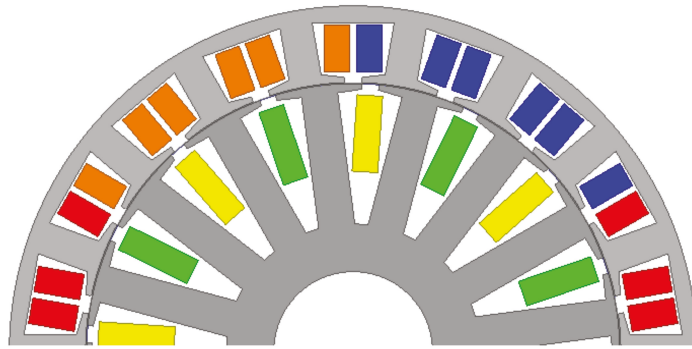
**Figure 9.** Cross-section of the 3 kW 16/18 pole/slot WRSM prototype.

**Table 4.** Specifications of the 3 kW 16/18 WRSM prototype.

| Specifications | Numerical Value |
|---|---|
| Rated terminal power (kW) | 3 |
| Rated torque (Nm) | 76.5 |
| Rated speed (r/min) | 375 |
| Rated frequency (Hz) | 50 |
| Rated line voltage (V) | 350 |
| Rated phase current (A) | 4.86 |
| Rated field current (A) | 5.00 |
| Number of rotor poles | 16 |
| Number of stator slots | 18 |
| Stator outer diameter (mm) | 260 |
| Rotor outer diameter (mm) | 203.6 |
| Rotor inner diameter (mm) | 60 |
| Stack length (mm) | 125 |
| Air gap thickness (mm) | 0.45 |
| Number turns per coil Y connected | 67 |
| Number turns per coil Δ connected | 116 |
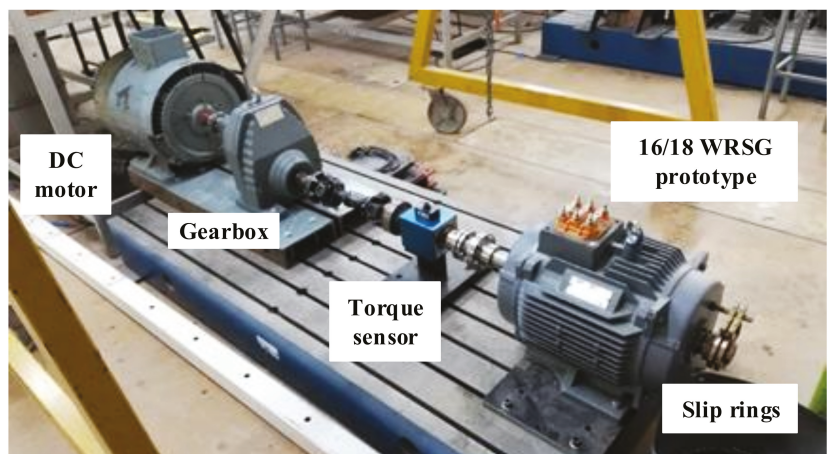


**Figure 10.** Testing station of the 3 kW 16/18 pole/slot WRSM prototype.
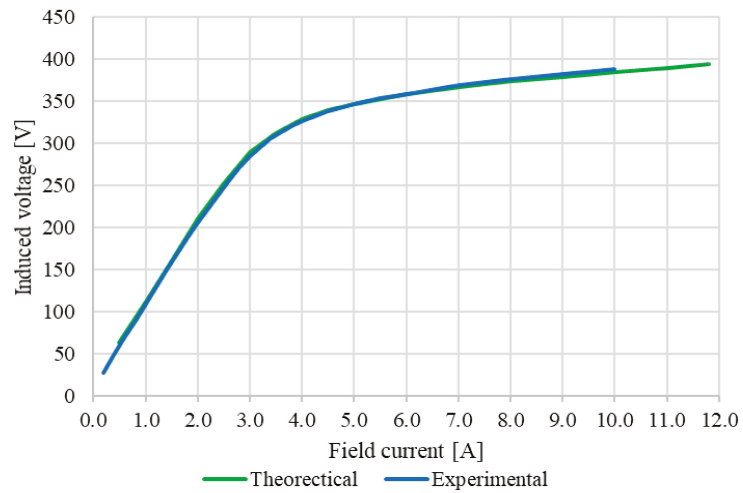
**Figure 11.** Open-circuit line-to-line induced voltage versus field current of the non-overlap winding and phase-shift winding prototypes.
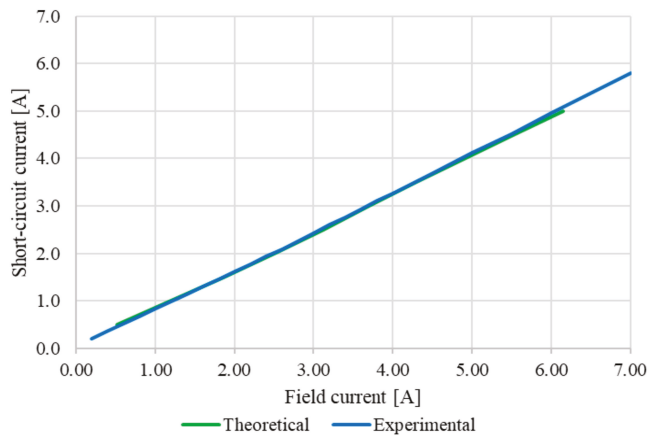


**Figure 12.** Predicted and experimental short-circuit current of the non-overlap winding and phase-shift winding prototypes.

**Table 5.** Measured equivalent circuit parameters of the phase-shifted winding prototype.

| Parameter | Measured Value |
|---|---|
| Phase resistance, $R_s$ | 4.7 Ω (0.11 per unit) |
| Field resistance, $R_f$ | 8.1 Ω |
| Synchronous reactance, $X_s$ | 42.1 Ω (1.0 per unit) |

**Table 6.** Measured machine losses of the phase-shifted winding prototype.

| Windage and Friction Losses [W] | Core Losses [W] | Copper Losses [W] |
|---|---|---|
| 19.6 | 62.8 | 94.5 |

### 4.2. Grid-Connected Tests

For the load performance tests the prototype is synchronised with the 50 Hz grid supply at the rated field current of 5 A. The mechanical input power is then increased by means of the DC motor in Figure 10, while also increasing the rotor field current to maintain unity power factor and grid synchronization. Figure 13 displays the measured power factor and field current versus generated electrical power. The phase-shifted winding machine is able to perform favourably and is able to maintain unity power factor until approximately 2.5 kW at a maximum field current of 10 A. Figure 14 displays the results of the efficiency and field current versus generated power of the machine. The results show the expected improved efficiency from the theoretical analysis. Figure 15 shows the predicted and experimental full-load torque curves of the prototype with the phase-shifted winding. The measured torque ripple is 8.2% and the results differ by 1.5%, which is an acceptable deviation. The measured full-load torque of the phase-shifted winding machine confirms the predicted improvements of the phase-shift application in terms of lowered torque ripple.

### 4.3. THD of Wye and Delta Phase Currents

It is necessary to determine to what extent circulating currents are present in the delta configuration of the phase-shifted non-overlap winding. With the machine open-circuited and at rated speed, the field current is varied and the current in a branch of the delta configuration is measured. The results are shown in Figure 16. As the field current increases, so too does the zero-sequence circulate current in the delta winding, though the circulating current remains relatively small (5.14% of the rated stator current at rated field current). A sample of the circulating current at rated field current at open circuit is displayed in Figure 17 and clearly illustrates the expected 150 Hz third harmonic characteristic.
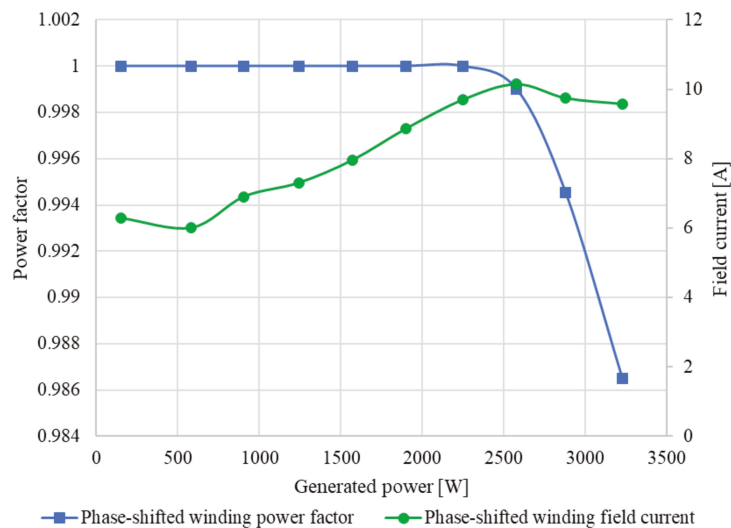


**Figure 13.** Power factor and field current versus generated power of the grid-connected phase-shift winding prototype.

The phase currents in the wye and the delta branches are shown in Figure 18 at a load phase current of 3.5 A and at unity power factor. The effect of the circulating current is clear on the delta phase current, which explains the presence of more harmonics when compared to the phase current in the wye branch. Further, the phase current waveforms in the different branches at a load phase current of 5 A and a power factor of $pF = 0.987$ are displayed in Figure 19. The total harmonic distortions (THD) of the wye and delta branch

currents for each of the three conditions are given in Table 7. This shows that the total harmonic distortion of the grid wye phase current is substantially below the 8% limit as required by some utility grid codes. In addition, the THD of the delta current reduces with load below the 8% and slightly higher than the THD of the grid wye current. For reference, the total harmonic distortion of the supply voltage during testing was 3%.
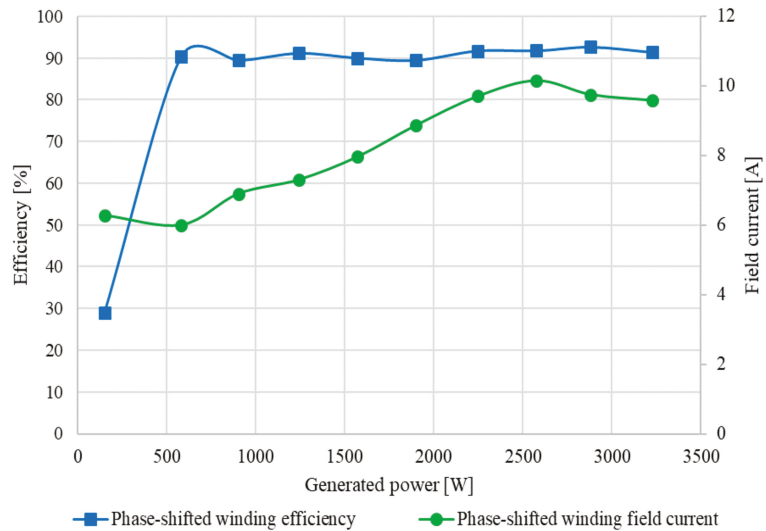


**Figure 14.** Efficiency and field current versus generated power of the grid-connected phase-shift winding prototype.
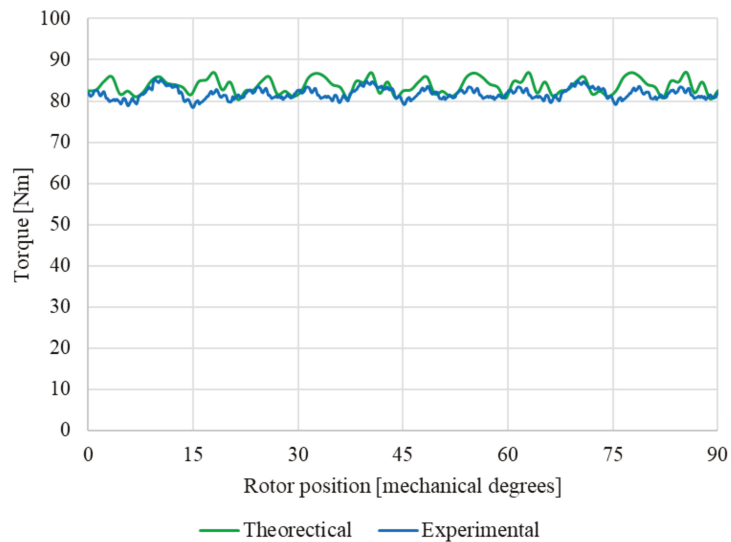


**Figure 15.** FEA-predicted and experimental torque versus rotor position of the 3 kW 16/18 WRSM prototype with phase-shifted non-overlap winding at 375 r/min and full-load.
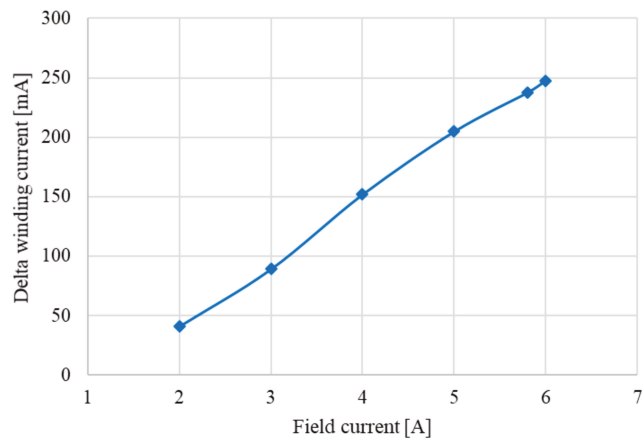
**Figure 16.** RMS delta winding current versus field current of the 3 kW 16/18 WRSG prototype with phase-shifted non-overlap winding at open-circuit.
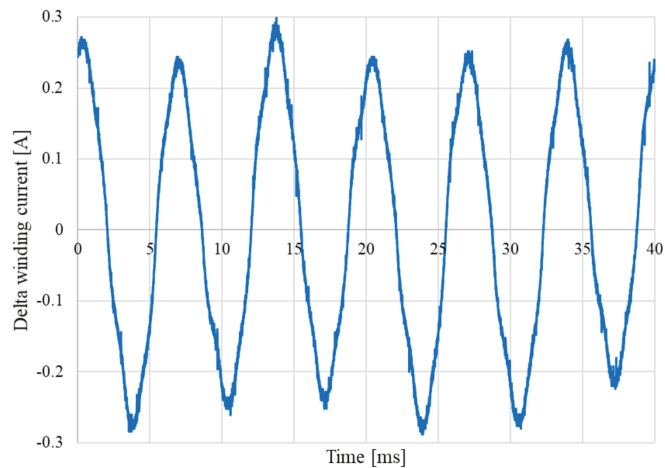


**Figure 17.** Delta winding circulating current at rated field current of the 3 kW 16/18 WRSG prototype with phase-shifted non-overlap winding at open-circuit.

**Table 7.** Total harmonic distortion of the wye and delta branch currents of the phase-shifted winding prototype with varying load conditions.

| | Load Condition | | Wye Branch Current THD [%] | Delta Branch Current THD [%] |
|---|---|---|---|---|
| $I_s = 0$ A | $I_f = 5$ A | – | 0 | 8.9 |
| $I_s = 3.5$ A | $I_f = 10$ A | $pF = 1$ | 5.6 | 7.2 |
| $I_s = 5$ A | $I_f = 9.6$ A | $pF = 0.987$ | 4.5 | 6.1 |
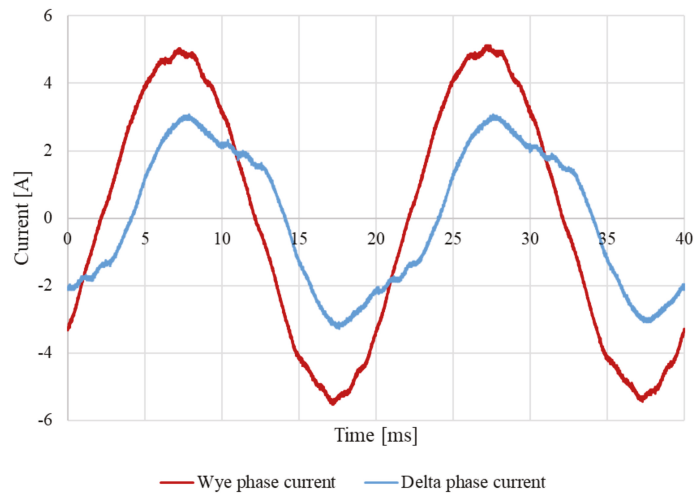
**Figure 18.** Grid-connected wye and delta phase currents at 3.5 A phase current and 10 A field current of the 3 kW 16/18 WRSG prototype with phase-shifted non-overlap winding at *pF* = 1.
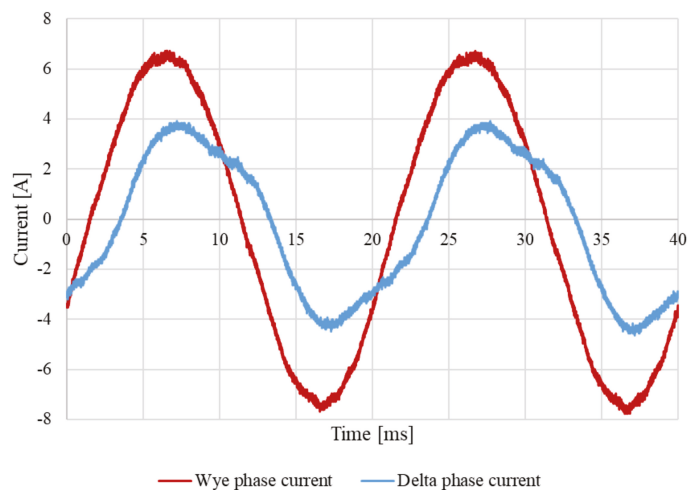


**Figure 19.** Grid-connected wye and delta phase currents at 5 A phase current and 9.6 A field current of the 3 kW 16/18 WRSG prototype with phase-shifted non-overlap winding at *pF* = 0.987.

## 5. Conclusions

In this paper the effect of the reduction of the MMF sub-harmonics of a 16/18 pole/slot combination WRSM on the performance of the machine by applying a phase-shifting winding technique, is studied. Ideally, a −20° electrical phase displacement is required between the currents of the coils to obtain a winding factor of unity of the main harmonic. To overcome the feasibility of applying this displacement practically, a −30° phase shift was selected which yields a winding factor close to unity. The phase shift was implemented by applying a star-delta connection between the coils of each phase. Although the wye-delta application is not new, the technique has not been applied to a 16/18 pole/slot combination before and the non-overlap winding structure is maintained. Many other techniques used to reduce the MMF harmonic content of a non-overlap winding change the final winding

structure to that of an overlap winding. This is not ideal because the advantages of the non-overlap winding are then diminished.

The harmonic content analysis of the 16/18 combination shows that the first and second MMF harmonics are greatly reduced without reducing the working harmonic. The winding factor of the main harmonic is increased by the phase-shift. This has improved the 16/18 machine's torque and power density. The minimization of sub- and higher-order harmonics is especially noted in the reduced torque ripple and increased efficiency of the phase-shifted winding machine. One of the disadvantages of the phase-shifted non-overlap winding is the small increase in the rotor core losses because of the increased 5th harmonic. However, the overall losses are reduced because the total sub-harmonic content is decreased.

A 3 kW prototype 16/18 WRSM with the proposed wye-delta phase-shifted non-overlap winding is manufactured and tested. The practical performance tests of this small machine indicate that the phase-shifted winding prototype has a good efficiency of over 90% for a wide power range from 0.2–1.0 per unit power. Additionally, the good full-load torque quality of the machine is confirmed by measurements. This all is expected from the reduction of sub- and higher-order harmonics in the MMF harmonic spectrum. Finally, the concern of possible high circulating current in the delta winding is studied from the measured delta current waveforms. The relatively low percentage THD found of the delta current from no-load to full load shows that this aspect is not a problem. In its entirety, the paper shows that the proposed non-overlap wye-delta phase-shift winding can be used with significant improvement by the industry for multiples of 8/9 pole-slot combination WRSMs.

## References

1.  REN 21. Renewables 2019 Global Status Report (Paris: REN21 Secretariat). 2019. Available online: www.ren21.net/gsr (accessed on 10 October 2021).
2.  Dajaku, G.; Spas, S.; Dajaku, X.; Gerling, D. An Improved Fractional Slot Concentrated Winding for Low-Poles Induction Machines. In Proceedings of the 19th International Conference for Electrical Machines, Lausanne, Switzerland, 4–7 September 2016; pp. 116–121.
3.  Alberti, L.; Bianchi, N. Design and tests on a fractional-slot/induction machine. In Proceedings of the IEEE Energy Conversion Congress and Exposition (ECCE), Raleigh, NC, USA, 15–20 September 2012; pp. 166–172.
4.  Heller, F.; Kauders, W. The Görges Polygon (Das Görgessche Durchflutungspolygon). *Arch. Elektrotechnik* **1925**, *29*, 599–616. [CrossRef]
5.  Cistelecan, M.V.; Ferreira, F.J.T.E.; Popescu, M. Three phase tooth-concentrated multiple-layer fractional windings with low space harmonic content. In Proceedings of the 2010 IEEE Energy Conversion Congress and Exposition (ECCE), Atlanta, GA, USA, 12–16 September 2010; pp. 1399–1405.

6.    Dotz, B.; Gerling, D. Windings with various numbers of turns per phasor. In Proceedings of the 2017 IEEE International Electric Machines and Drives Conference (IEMDC), Miami, FL, USA, 21–24 May 2017; pp. 1–7.

7.    Dajaku, G.; Xie, W.; Gerling, D. Reduction of low space harmonics for the fractional slot concentrated windings using a novel stator design. *IEEE Trans. Magn.* **2014**, *50*, 1–12. [CrossRef]

8.    Dajaku, G.; Gerling, D. A novel 24-slots/10-poles winding topology for electric machines. In Proceedings of the 2011 IEEE International Electric Machines Drives Conference (IEMDC), Niagara Falls, ON, Canada, 15–18 May 2011; pp. 65–70.

9.    Zhu, S.; Shaohong, S.; Cox, T.; Xuand, Z.; Gerada, C. Novel 24-slots 14-poles fractional-slot concentrated winding topology with low-space harmonics for electrical machine. *J. Eng.* **2019**, *17*, 3784–3788. [CrossRef]

10.   Bekka, N.; Trichet, D.; Bernard, N.; Zaïm, M. Application of Phase Shifting Technique for Reducing the Magnetomotive Force Space Harmonics of Tooth Concentrated Windings. *Electr. Power Compon. Syst.* **2016**, *44*, 1707–1720. [CrossRef]

11.   Garner, K.S.; Kamper, M.J. Reducing MMF harmonics and core loss effect of non-overlap winding wound rotor synchronous machine (WRSM). In Proceedings of the IEEE Energy Conversion Congress and Exposition (ECCE), Cincinnati, OH, USA, 1–5 October 2017; pp. 1850–1856.

12.   Ockhuis, D.K.; Kamper, M.J. Grid Connection Power Converter and Speed Controller for Slip-Synchronous Wind Generators. In Proceedings of the 2019 IEEE Energy Conversion Congress and Exposition (ECCE), Baltimore, MD, USA, 29 September–3 October 2019; pp. 6741–6748.

13.   Kloppers, C.; Garner, K.S.; Kamper, M.J. Design and optimisation of a 16/18 wound rotor wind synchronous generator with non-overlap winding. In Proceedings of the 26th Southern African Universities Power and Engineering Conference, Johannesburg, South Africa, 24–26 January 2018; pp. 1–6.

*Article*

# Characteristic Analysis and Experimental Verification of Electromagnetic and Vibration/Noise Aspects of Fractional-Slot Concentrated Winding IPMSMs of e-Bike

**Young-Geun Lee, Tae-Kyoung Bang, Jeong-In Lee, Jong-Hyeon Woo, Sung-Tae Jo and Jang-Young Choi \***

Department of Electrical Engineering, Chungnam National University, Daejeon 34134, Korea; 201502206@o.cnu.ac.kr (Y.-G.L.); bangtk77@cnu.ac.kr (T.-K.B.); lji477@cnu.ac.kr (J.-I.L.); dnwhd0@cnu.ac.kr (J.-H.W.); jst4900@o.cnu.ac.kr (S.-T.J.)
* **Correspondence: choi_jy@cnu.ac.kr**

**Abstract:** In this study, we performed the electromagnetic and mechanical characteristic analyses of an 8-pole 12-slot interior permanent magnet synchronous motor (IPMSM). Permanent magnet synchronous motors are classified into surface permanent magnet synchronous motor and interior permanent magnet synchronous motors according to the type of rotor. The IPM type is advantageous for high-speed operation because of the structure where the permanent magnet is embedded inside the rotor, and it has the advantage of having a high output density by generating not only the magnetic torque of the permanent magnet, but also the reluctance torque. However, such a motor has more vibration/noise sources than other types, owing to changes in reluctance. The sources of motor noise/vibration can be broadly classified into electromagnetic, mechanical, and aerodynamic sources. Electromagnetic noise sources are classified into electromagnetic excitation sources, torque pulsations, and unbalanced magnetic forces (UMFs). Vibration and noise cause machine malfunctions and affect the entire system. Therefore, it is important to analyze the electromagnetic vibration source. In this study, the electromagnetic characteristics of an IPMSM were analyzed through the finite element method to derive the UMF. Vibration and noise analyses were performed by electromagnetic–mechanical coupling analysis, and vibration and noise characteristics based on electromagnetic noise sources were analyzed.

**Keywords:** IPMSMs; electromagnetic characteristic; vibration/noise source; electromagnetic–mechanical coupled analysis

## 1. Introduction

Recently, owing to the increasing public concern about environmental problems, such as global climate change, various technologies have been considered for this challenge. Particularly, ecofriendly mobility has attracted increasing attention because it contributes to reducing global warming. For the dissemination of ecofriendly mobility, it is necessary to develop high-performance traction motors that exhibit high torque at low speed, and constant output characteristics over a wide range. Considering this, interior permanent magnet synchronous motors (IPMSMs) are the most suitable traction motors for ecofriendly mobility.

In the electromagnetic aspect, IPMSMs produce reluctance torque, which is an additional torque, from the difference in inductances in the d and q axes. Furthermore, a permanent magnet mechanically inserted in the rotor prevents magnet scattering at high speeds and exhibits equal mechanical and electrical air-gap length [1,2]. Therefore, IPMSMs have a wider operating range through flux-weakening control compared to other types. However, the operating range differs according to the flux-weakening (FW) control range, which in turn depends on parameters such as the d- and q-axes inductance of the motor

and the electrical saliency. Additionally, the FW control range, which is essential for motor design and optimization, can be predicted from the flux vector diagram of the motor [3–7].

In the vibration/noise aspect, IPMSMs suffer from more vibration/noise sources than other types of motors owing to changes in reluctance. Vibration and noise can cause motor eccentricity, bearing defects, and misalignments. Electromagnetic vibration sources are roughly classified into torque pulsations and electromagnetic forces [8]. Torque pulsation is classified as torque because of the interaction between the permanent magnets of the rotor and the stator slots of a permanent magnet machine (cogging torque) and load pulsation, owing to the interaction between the input current and the back-electromotive force (back-EMF) (torque ripple), and the difference between the d- and q-axes air-gap reluctance (reluctance torque). Electromagnetic force is classified as magnetic pull force (MPF) owing to the distribution of magnetic flux density generated by the slot structure and winding pattern and unbalanced magnetic force (UMF) generated according to the change in magnetic flux density [9–15]. MPF indicates the magnitude and distribution of the magnetic force density, which affects the motor based on the magnitude of the force, and not the distribution of the force. Additionally, the MPF distribution changes depending on the combination of the motor pole-slots, and the MPF distribution should be symmetrical to obtain motor stability. The electromagnetic vibration of the motor is mainly generated by the radial force, which is one of the components of the UMF [16–19]. The radial force is proportional to the square of the air-gap magnetic flux density, and as the torque density of the motor increases, the air-gap flux density also increases. Therefore, in the case of an electric motor with a high torque density, such as a PMSMs, the rate of electromagnetic vibration increases. Moreover, the spatial distribution of the radial force is affected by the stator and rotor, and its magnitude changes with time; thus, the radial force generates a vibration frequency that affects the vibration. This makes it possible to predict the electromagnetic noise/vibration characteristics generated by the motor [20–24]. If the noise and vibration characteristics of the motor are predicted through this method, not only the noise and vibration characteristics of the motor can be identified in the design stage, but also a more mechanically robust design can be made. In addition, as sensors and electronic components increase as the system becomes electronics, disturbance caused by the motor to the external system may be reduced in the design stage.

Therefore, in this study, dynamic modeling of the IPMSM was performed to predict the operation characteristics based on the electromagnetic characteristics and parameter analysis results of the model using the finite element method (FEM). Additionally, based on electromagnetic characteristic data, the vibration source generated in the stator was analyzed through the circumferential mode of the radial force, which is the electromagnetic vibration source, and the fast Fourier transform (FFT) analysis. Figure 1 shows the analysis flow of this study, and Table 1 lists the design specifications of the analysis model.
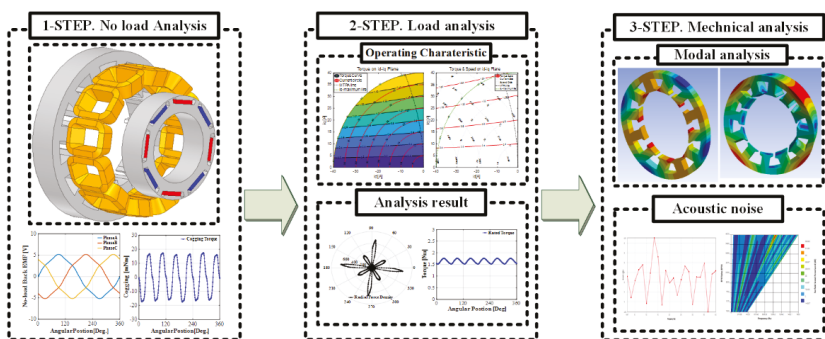


**Figure 1.** Analysis flow.

**Table 1.** Specification of analysis model.

| Specification | IPMSM | Unit |
|---|---|---|
| Rated output power | 180 | W |
| Rated speed | 1745 | RPM |
| Pole/Slot | 8/12 | - |
| Stator OD | 116 | mm |
| Rotor OD | 71 | mm |
| Total magnet volume | 6249.6 | mm$^3$ |

## 2. Electromagnetic Analysis

### 2.1. No-Load Analysis

The no-load back-EMF of a permanent magnet machine is the electromotive force induced by the interaction between the field magnetic flux and the armature winding. The no-load back-EMF waveform when controlling the IPMSM is realized as the basis for determining the accessibility of the control. That is, the closer the no-load back-EMF is to a sine wave, the easier it is to control the IPMSM. Moreover, electrical equipment generates cogging torque because of non-uniform air gap transmittance owing to the tooth slot structure, and this should be checked during no-load analysis.

The cogging torque is the torque component generated by the tendency of the stator and rotor to align in the direction that maximizes the permeance of the magnetic circuit in a permanent magnet machine. As shown in Equation (1), it can be expressed as a function of the magnetic flux density ($B_{rg}$, $B_{\theta g}$) in the radial and tangential directions of the air gap, the length in the axial direction ($l_{stk}$), and the distance to the air gap ($r$). The cogging torque acts on the rotor without applying an input current (in a no-load state). Because there is no input current, the average torque is zero; thus, it is not recognized as an active ingredient that generates power. Additionally, the cogging torque generates torque ripple, velocity ripple, and vibration/noise. The harmonic component of the cogging torque is represented by a function of the number of poles and the least common multiple of the number of slots; the electric harmonic frequency of the cogging torque is as shown in Equation (2). $f_e$ represents the frequency of the motor, $LCM(2p, Q_s)$ represents the least common multiple of the number of poles and slots, and $p$ denotes the number of pole pairs.

Figure 2a,b shows the magnitude and waveform of the no-load back electromotive force (EMF) and FFT analysis results of the no-load back-EMF. The total harmonic distortion (THD) of the no-load back-EMF was 5.17%. Figure 2c–e shows the no-load back-EMF of the experiment result, the magnitude and waveform of the cogging torque, and the FFT analysis results of the cogging torque.

$$T = r^2 \frac{l_{stk}}{\mu_0} \int_0^{2\pi} B_{rg} B_{\theta g} d\theta \tag{1}$$

$$f_{cog} = f_e LCM(2p, Q_s)/p \tag{2}$$

The peak-to-peak value of the cogging torque is 34.9 mNm, and as a result of FFT analysis, the main harmonic order is interpreted as 6th, which is also consistent with the result of Equation (2).
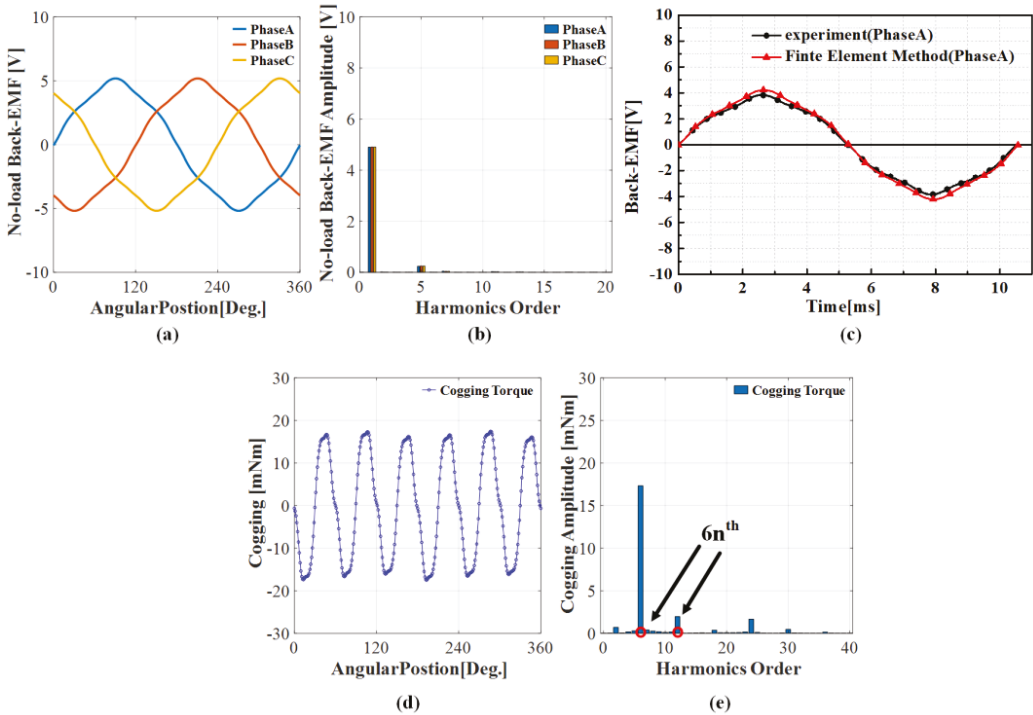
**Figure 2.** No-load Analysis result of no-load back EMF and Cogging Torque: (**a**) waveform of no-load back-EMF, (**b**) FFT of no-load back EMF, (**c**) experiment results of no-load back-EMF, (**d**) waveform of cogging torque, and (**e**) FFT of cogging torque.

### 2.2. Parameter Calculation

As mentioned in the introduction, the IPMSM has different d- and q-axes inductances because permanent magnets are embedded inside the rotor core. Therefore, both magnetic torque and reluctance torque occur, and they have reverse saliency. The IPMSM operation region is generally divided into a constant torque region where the torque is constant as the speed increases and a constant output region where the output is constant when the speed increases. The maximum torque per ampere (MTPA) control and flux weakening (FW) control are applied according to each region. However, the operating range differs based on the FW control range, which depends on parameters such as the d- and q-axes inductance of the motor and the electrical saliency. Additionally, the FW control range, which is essential for motor design and optimization, can be predicted from the flux vector motor diagram.

Figure 3a,b shows the general operating characteristics of the IPMSM, and a vector diagram, respectively. The blue line in Figure 3a represents the torque curve, and the red line represents the power curve.

$$i_d = -I_a \sin \beta, \ i_q = I_a \cos \beta \tag{3}$$

$$L_d = \frac{\lambda_o \cos \alpha - \lambda_f}{i_d}, L_q = \frac{\lambda_o \sin \alpha}{i_q} \tag{4}$$

$$\zeta = \frac{L_q}{L_d} \tag{5}$$

$$V_{ds} = R_s i_{ds} + L_{ds}\frac{di_{ds}}{dt} - \omega_r L_{qs} i_{qs} \tag{6}$$

$$V_{qs} = R_s i_{qs} + L_{qs}\frac{di_{qs}}{dt} - \omega_r(L_{ds} i_{ds} + \lambda_f) \tag{7}$$
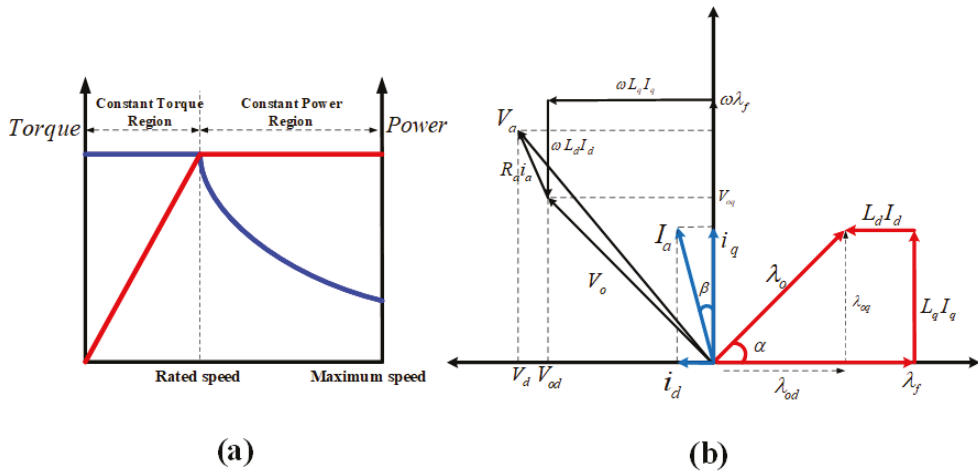


**Figure 3.** IPMSMs operating region and vector diagram: (**a**) characteristic of IPMSMs and (**b**) vector diagram according to d- and q-axis.

The important parameters of the IPMSM can be derived using vector diagrams that represent the electromagnetic relationship through the IPMSM d- and q-axes parameters and FEM analysis results.

$\alpha$ is the phase difference between the no- and on-load magnetic flux linkages. $\beta$ is the phase angle of the current. If we derive the $\alpha$ and $\beta$, we can derive the saliency $\zeta$ that expresses rate of d- and q-axes inductances. $\lambda_f$ and $\lambda_0$ are the no- and on-load flux linkages, respectively. The magnitude and phase of no-load magnetic flux linkage were derived through no-load analysis without current, and the magnitude and phase of the load magnetic flux linkage were derived by applying the rated current. $I_a$ represents the maximum current applied to the stator. The stator current $I_a$ is again divided into a d- and q-axes currents, as shown in Equation (5). Additionally, the d- and q-axes inductances and saliency of an IPMSM can be expressed by Equations (4) and (5) because of the relationship between the d- and q-axes currents, and armature magnetic flux linkage. The magnitudes of the d- and q-axes inductances differ depending on the phase angle of the current. Therefore, a process of searching for the phase angle that generates the maximum torque is required. Finally, by deriving the d- and q-axes voltage Equations (6) and (7), the main parameter calculations using the vector diagram were completed.

Figure 4 shows the no-, on-load flux linkage, and phase difference calculated based on vector diagrams and FEM analysis data, and the d- and q-axes inductances based on the current phase angle.
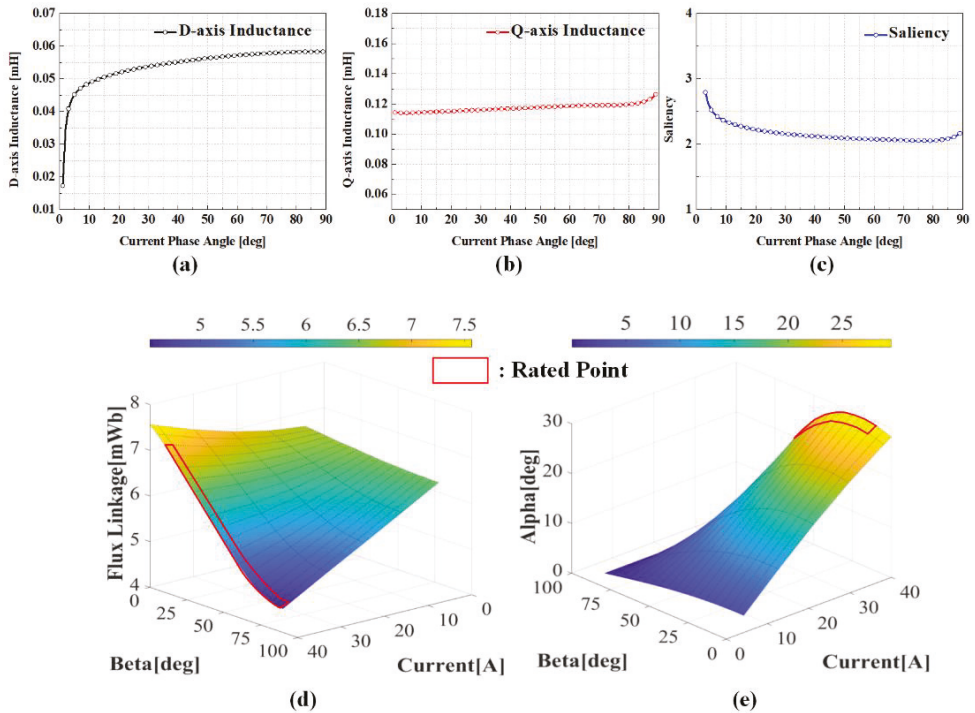
**Figure 4.** Calculation of d-, q-axis inductance, flux linkage, and phase difference at no-, on-load flux linkages according to input current and current angle. (**a**) d-axis inductance, (**b**) q-axis inductance, (**c**) saliency, (**d**) flux linkage, and (**e**) flux linkage phase difference angle.

### 2.3. Load Analysis

The IPMSM torque equation can be expressed by Equation (8). In Equation (8), the first term represents the magnetic torque generated by the permanent magnet, and the second term represents the reluctance torque generated by the difference between the d- and q-axes reluctances. As shown in the torque equation, the magnetic torque is proportional to the current and the amount of armature magnetic flux linkage owing to the permanent magnet. Further, the reluctance torque is proportional to the d- and q-axes currents, and the multiple of the d- and q-axes inductance difference. Further, the magnetic and reluctance torques vary in magnitude depending on the phase angle of the current, and the IPMSM torque implies that there is a current phase in which the generated torque can be maximized for the same current magnitude.

$$T_{total} = \frac{P}{2}\frac{3}{2}[\lambda_f i_q + (L_d - L_q)i_d i_q] \tag{8}$$

Therefore, the maximum torque/current control method was used to generate the maximum torque, and the optimum current phase and current vector for creating this condition can be derived as shown in Equations (9)–(12).

$$i_s = \sqrt{i_d{}^2 + i_q{}^2} \tag{9}$$

$$V_s = \sqrt{(R_s i_d - \omega L_q i_q)^2 + (R_s i_q + \omega L_d i_d + \omega \lambda_f)^2} \tag{10}$$

$$i_d = \frac{-\lambda_f + \sqrt{(\lambda_f{}^2 + 8(L_d - L_q)^2 I_s{}^2}}{4(L_d - L_q)} \tag{11}$$

$$\beta = \sin^{-1}\left[\frac{-\lambda_f + \sqrt{(\lambda_f{}^2 + 8(L_d - L_q)^2 I_s{}^2}}{4(L_d - L_q)I_s}\right] \tag{12}$$

In the above equation, the stator applied current ($i_s$) should be less than or equal to the current limit value ($i_{am}$), and the current limit value corresponds to the rated current during continuous operation. Similarly, the back-EMF ($V_s$) of the motor should be equal to or less than the maximum output voltage ($V_{am}$) of the inverter.

Considering the current and voltage limits, the range of selectable current vectors is highly limited. Therefore, to satisfy this limitation and operate the motor through maximum output control, appropriate current control based on the motor speed is required.

If the motor is driven by the maximum torque control per unit current, the back-EMF of the motor approaches the speed (base speed) at which the maximum output voltage of the inverter is reached. In the speed range above the base speed, it is necessary to consider both the current and voltage limits. As a result, FW control is required for operation in the high-speed region. In this case, the operation was performed based the d- and q-axes current commands that generate the maximum torque with the allowable current, as in the case of MTPA control for the same loss minimum operation. Above the base speed, the magnitude of the applied current was the same as the current magnitude below the base speed. The voltage was controlled such that the maximum output voltage of the inverter and the voltage of the motor are equal. Therefore, the current was controlled until the current-limiting source matches the maximum torque control line per unit magnetic flux. In relation to the parameters, if there is no maximum torque control curve per unit magnetic flux inside the current limit circle, it can be operated until the output becomes zero.

Both the voltage and current limits should be met when operating the IPMSMs. When both of these limiting conditions are achieved, the controllable current region is considered as the common region of the voltage-limiting ellipse and the current-limiting circle. Therefore, the current command cannot be controlled unless it is located inside the common area.

Figures 5 and 6 show the current and torque characteristics based on the IPMSM operating region derived from the above equation. Clearly, the maximum torque was generated when there is a phase angle of the current at 25 A, which is the current condition for generating the maximum torque, and the size of the voltage-limiting ellipse decreases as the speed increases. There is a point where the reduced voltage-limiting ellipse, current-limiting circle, and torque curve meet, and the intersection of these three curves becomes the next operating point. Theoretically, the analysis model in this study can run to the intersection of the d-axis and the current-limiting circle, because the voltage-limiting ellipse is not included in the current-limiting circle. These conditions allow the load characteristics to be derived using an IPMSM load simulation [25,26]. The back-EMF of a motor is generated by a variation in the magnetic flux density that varies depending on the position of the rotor in the air gap. Therefore, the mode of variation in the magnetic flux density affects the back-EMF of the motor. Additionally, when the THD of the back-EMF increases, the input current for generating the same torque increases, and the motor has a low-torque density characteristic; thus, the motor does not operate efficiently. Figure 7 shows the results of the load analysis and the experimental results of the efficiency map.

$$f_{ripple} = 6 \cdot n \cdot f_e \tag{13}$$
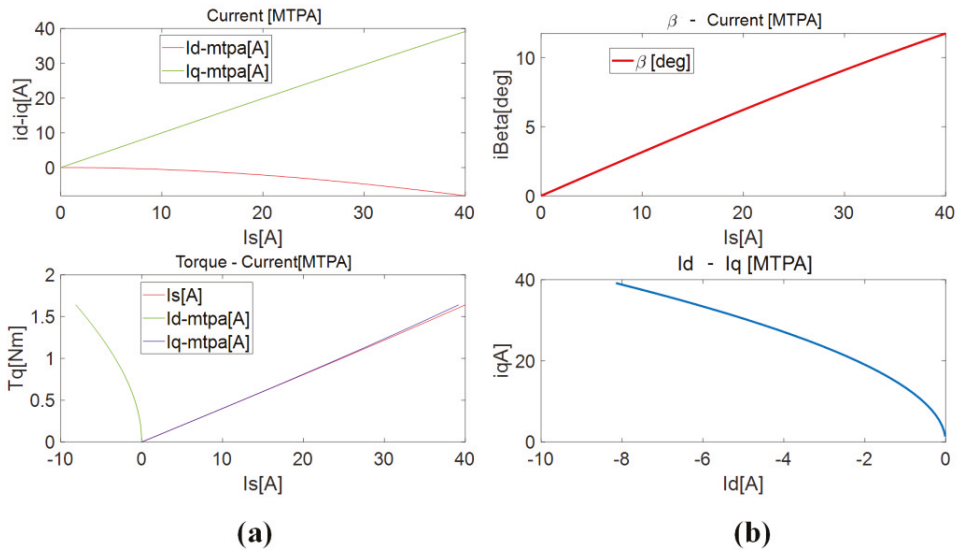
**Figure 5.** Current according to torque and current phase angle of IPMSM: (**a**) current and torque according to MTPA control and (**b**) current phase angle characteristic according to $I_s$.
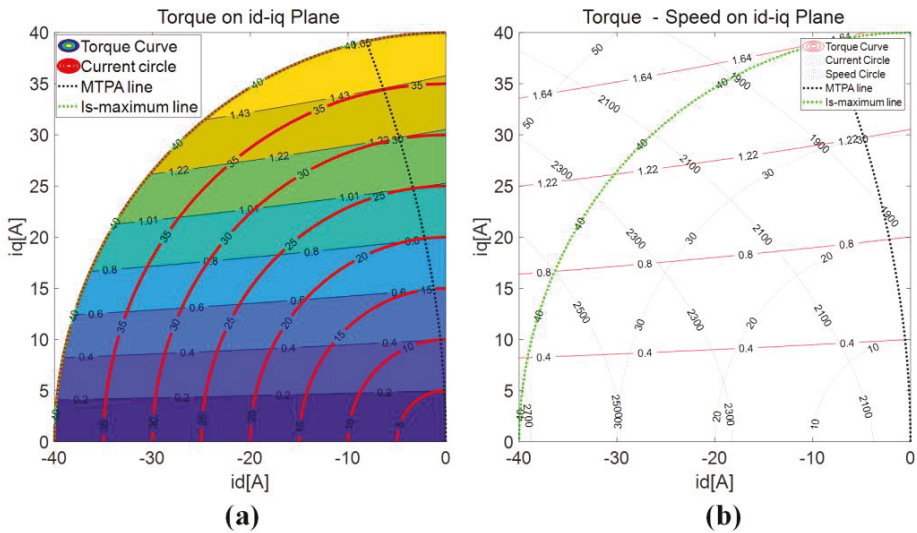


**Figure 6.** Characteristic curve of IPMSM: (**a**) Torque on $I_d$, $I_q$ plane. (**b**) Torque and speed on $I_d$, $I_q$ plane.
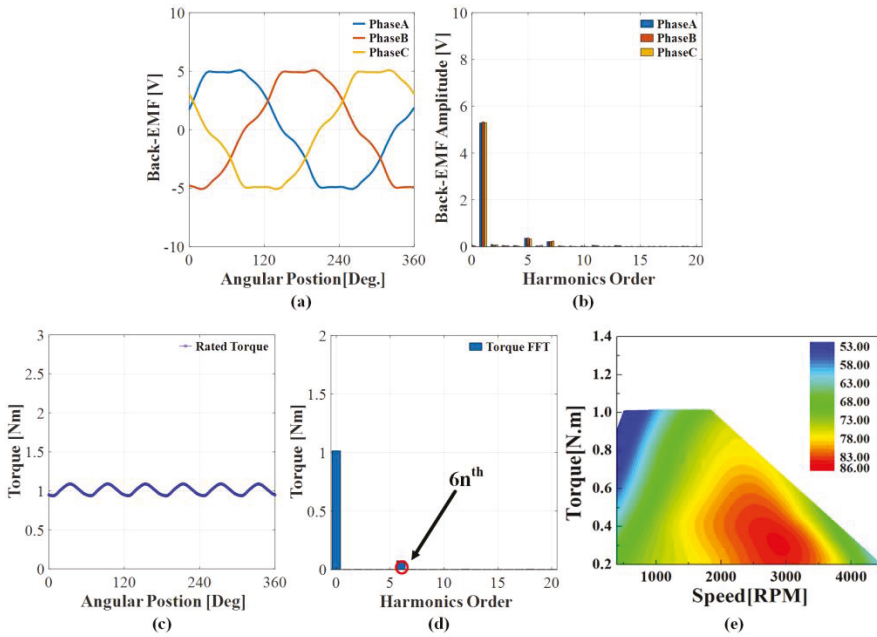
**Figure 7.** Load analysis result: (**a**) load back EMF waveform, (**b**) load back EMF FFT result, (**c**) torque waveform, (**d**) torque FFT result, and (**e**) efficiency map.

The electromagnetic torque is represented by the products of back-EMF and applied current, and the rate of change that occurs periodically in torque is called torque ripple. Therefore, because the harmonic components of the back-EMF and the applied current affect the torque ripple, it is necessary to analyze the harmonic components of the back-EMF to predict the vibration/noise. The relationship between torque ripple and frequency is expressed by Equation (13), and clearly, the results of the main harmonics confirmed by the FFT analysis of torque are in agreement. Figure 7 shows the results of the load analysis.

The UMF and electromagnetic force acting on the motor are obtained through load analysis. In this study, we used the Maxwell stress tensor method to derive the electromagnetic force or UMF generated by the motor. The stress vector per unit area is expressed by Equation (14).

$$F = \frac{1}{\mu_0}\left(B_n^2 - \frac{1}{2}|B|^2\right)i_n - \frac{1}{\mu_0}B_n B_t i_t \tag{14}$$

where $B$ is the magnetic flux density, and $n$ and $t$ represent the normal and tangential components in the coordinate system, respectively. Assuming that the magnetic permeability of the stator and rotor is infinite, the force densities in the radial and tangential directions acting on the surface of the stator are expressed by Equation (15). $B_r$ and $B_t$ represent the magnetic flux density in the radial and tangential directions, respectively.

Figure 8a,b shows the force density in the radial and tangential directions derived from Equation (15). Generally, the symmetry of the force density distribution can be used to determine its influence on vibration. Therefore, it can be confirmed that the force density of this analysis model is symmetrically distributed.

$$f_r = \frac{1}{\mu_0}\left(B_r^2 - B_\theta^2\right),\ f_\theta = \frac{1}{2\mu_0}B_r B_\theta \tag{15}$$
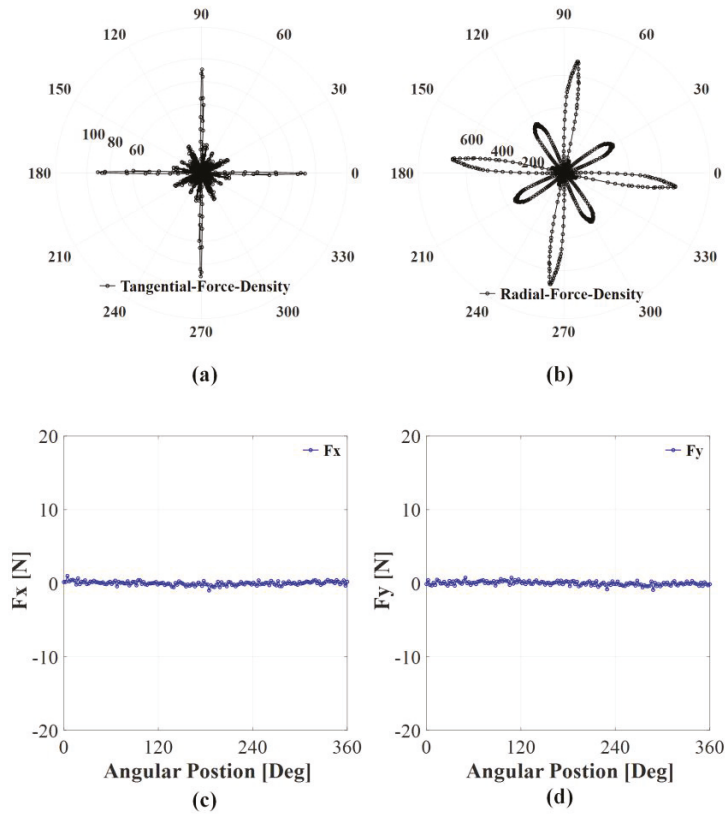
**Figure 8.** Force density and UMF result: (**a**) tangential distribution, (**b**) radial distribution, (**c**) x-component, and (**d**) y-component.

Equation (15) is converted into a Cartesian coordinate system, which is expressed as in Equation (16).

$$f_x = f_r \cos\theta - f_\theta \sin\theta, \ f_y = f_r \sin\theta + f_\theta \cos\theta \tag{16}$$

The components of the magnetic unbalanced force exerted on the stator center are calculated over a circular surface of radius normally in the middle of the air gap region, as shown in Equations (17) and (18).

$$F_x = \frac{rl_{stk}}{2\mu_0} \int_0^{2\pi} [(B_\theta{}^2 - B_r{}^2)\cos\theta - 2B_\theta B_r \sin\theta]d\theta \tag{17}$$

$$F_y = \frac{rl_{stk}}{2\mu_0} \int_0^{2\pi} [(B_\theta{}^2 - B_r{}^2)\sin\theta + 2B_\theta B_r \cos\theta]d\theta \tag{18}$$

Figure 8c,d shows UMF derived from Equations (17) and (18). The UMF result of the integral relationship with force density indicates that the value of UMF is close to zero, because the spatial distribution of the force density is symmetric. Therefore, it is considered that UMF does not significantly affect the vibration and noise characteristics of the analysis model.

### 3. Mechanical Analysis

*3.1. Modal Analysis*

Resonance occurs when the force imbalance, which is a radial force acting as a source of electromagnetic vibration of the motor, and the frequency owing to torque ripple and cogging torque are in a region close to the natural frequency of the motor. Resonance wears parts and reduces the drive performance of the motor, in addition to adversely affecting other systems. Moreover, the stator natural-vibration frequency plays a dominant role in vibration and resonance; therefore, a modal analysis of the stator should be performed. Therefore, it is important to confirm the natural frequency and mode shape, which are the mechanical characteristics of the electrical machine, at the design stage.

Free vibration is generated by the force inherent in the system itself when there is no external force. As for free vibration, the system oscillates at one or more natural frequencies, which are the natural characteristics of the dynamic system determined by the distribution of mass and stiffness. The mode represents a unique dynamic aspect of a system constituting the vibrator; when the stator vibrates by a force with a certain frequency, the shape of the stator is a unique mode with a frequency band of the force.

Figure 9 shows the free vibration of the 8-pole 12-slot motor model analyzed without a vibration source, that is, the natural frequency of the stator and the three mode shapes for each natural frequency. The red part contains a high resonance value. Based on the mode analysis, the frequency (natural frequency) of the first, second, and third modes of each model was higher than the operating frequency. Because this analysis is a structural analysis of a single motor, it is a mode analysis that proceeds without any restrictions. Notably, the amount of strain of a specific length itself is not meaningful, and there is a difference in the magnitude of vibration by that proportion. Basically, it is important to observe where and how often the deformation owing to vibration occurs with the amount of strain, and it can be expected that vibration based on the resonance of the stator structure owing to the natural frequency will not occur.
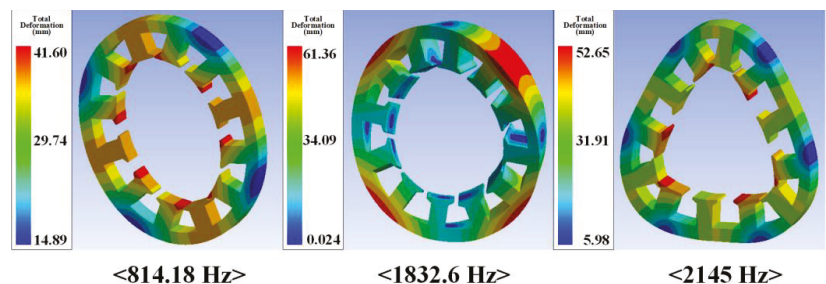


**Figure 9.** Modal analysis result.

*3.2. Acoustic Noise Analysis*

The vibration data used for the NVH characteristic analysis of PMSM were derived using 3D FEM considering the previously analyzed electromagnetic characteristic results. Figure 10 presents a waterfall diagram showing the NVH characteristic analysis results of the 8-pole 12-slot (8P12S) IPMSM to which an electromagnetic source was applied. This waterfall diagram was performed according to conditions of rotational speed. Here, the rotational speed conditions are 870, 1745, 2600, and 3490 rpm, respectively, and the load torque was selected at rated torque. In addition, as the analysis results are derived based on the mechanical 1 cycle in this NVH characteristic analysis, the characteristics of the electromagnetic vibration source of the motor for the mechanical 1 cycle should be considered.
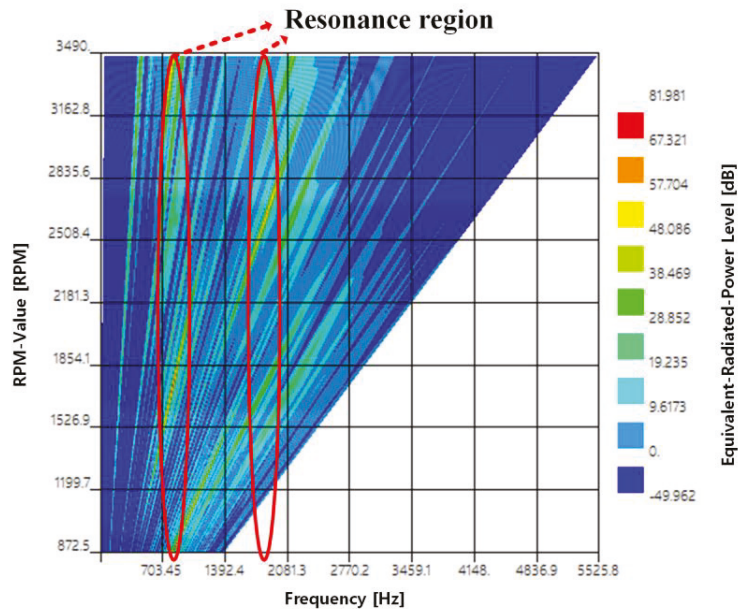
**Figure 10.** NVH Analysis result.

As aforementioned, the unbalanced electromagnetic force generated by the stator tip is close to zero; thus, other sources of vibration generate noise and vibration. Therefore, the level of vibration and noise was determined based on electromagnetic vibration sources, such as cogging torque and torque ripple. Of the torque-pulsation components, the cogging torque was mainly composed of the 6th harmonic component, and the torque ripple was mainly composed of the fundamental wave and the 6th order. The back-EMF under load was mainly in the harmonic order of 1, 5, and 7. Although the harmonic component of back-EMF was derived as a 1st, 5th, and 7th harmonic component, this harmonic component eventually appears as a harmonic component of torque ripple by interaction with the harmonic component of the applied current. Therefore, we need to focus on the FFT analysis result of the torque ripple.

Clearly from Figure 10, this corresponds to the FFT analysis results of cogging torque and torque ripple classified as electromagnetic vibration sources. In the case of cogging torque, the mechanical frequency 24th harmonic was the largest harmonic order, and in the case of torque ripple, the mechanical frequency was the largest in the order of 24th, 48th, and 8th harmonic order. Therefore, the noise level is higher in the frequency domain of the 1st, 8th, and 24th components than in the other regions. However, it is clear that the frequency at which the maximum noise is generated is larger in the resonance frequency region than in the harmonic region of the electromagnetic vibration/noise source.

## 4. Experiment Results

We performed experiments using a power analyzer and WT3000 manufactured by yaskawa in JAPAN, and the experimental results were validated by comparing them with the analysis results. Figure 11 shows the experiment setting.
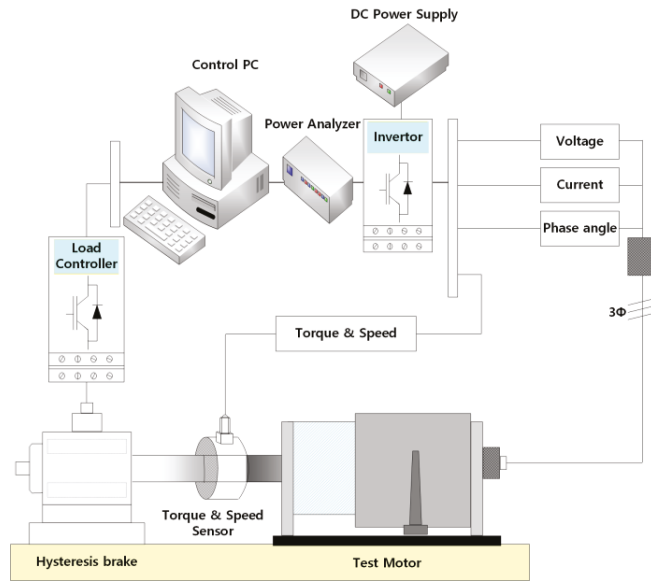
**Figure 11.** Concept of experimental system.

The back-EMF voltage induced in a stator winding because of the magnet flux crossing the air gap is given by the rate of change in flux linkage with respect to time. Figure 2c shows the back-EMF of the manufactured model under the no-load condition. As shown in Figure 2c, the predicted results mostly agree with the measurements in both waveform and amplitude. The effects on the leakage flux occurred in the end turn of the winding, fabrication error, and losses such as bearing friction, windage, and stray loss.

The torque obtained from the experiment was slightly lower than the FEM under identical conditions because the torque constant is proportional to the amplitude of the back-EMF. Figure 7b shows the characteristic performance and efficiency map of the analysis model under the rated load condition. These results were obtained under a variety of speed conditions at the rated load.

Based on the electromagnetic experiment data, the electromagnetic analysis performed in this study and the electromagnetic analysis were in good agreement; thus, the validity of the electromagnetic analysis was verified. As the validity of electromagnetic characteristics analysis was verified through experiments, it was confirmed whether the frequency was matched with the NVH analysis result based on the data derived through finite element analysis. It was confirmed that the harmonic order of the electromagnetic vibration source and the harmonic order of the mechanical vibration analysis result correspond. In addition, it was confirmed that the vibration/noise generated by mechanical resonance was greater than the vibration/noise component caused by electromagnetic vibration sources.

## 5. Conclusions

In this study, we predicted the noise and vibration generated by 8P12S IPMSMs through electromagnetic analysis. At the electromagnetic characteristics analysis step, we calculated important parameters based on the results of FEM and Vector diagram and identified operation characteristics according to the operation area. We also performed vibration/noise analysis and verified the results using electromagnetic experiments. We classified the electromagnetic vibration sources into several causes owing to torque pulsation and electromagnetic forces, analyzed the FFT analysis and waveform for the characteristics that affect vibration and noise, and verified their validity through experiments. Further, vibration and noise generated by the motor through electromagnetic-mechanical

coupling analysis were simulated using an FEM tool. As a result, if there is no mechanical vibration or noise source such as bearing faults and eccentricities, it is possible to predict the noise/vibration generated in the motor, even if only the electromagnetic characteristic analyses of the motor to be analyzed are accurate.

**Author Contributions:** J.-Y.C.: conceptualization, review and editing; Y.-G.L.: analysis, original draft preparation; J.-I.L.: experiment and motor control algorithm; T.-K.B.: experiment, motor control algorithm and co-simulation; J.-H.W.: co-simulation; S.-T.J.: experiment and motor control algorithm. All authors have read and agreed to the published version of the manuscript.

**Institutional Review Board Statement:** Not applicable.

**Informed Consent Statement:** Not applicable.

**Data Availability Statement:** The data presented in this study are available on request from the corresponding author.

**Conflicts of Interest:** The authors declare no conflict of interest.

## References

1. Tomigashi, Y.; Ueta, T.; Yokotani, K.; Ikegami, K. Reducing Cogging Torque of Interior Permanent Magnet Synchronous Motor for Electric Bicycles. In Proceedings of the IEEE European Conference on Power Electronics and Applications, Dresden, Germany, 11–14 September 2005.
2. Yang, Z.; Shang, F.; Brown, I.P.; Krishnamurthy, M. Comparative Study of Interior Permanent Magnet, Induction, and Switched Reluctance Motor Drives for EV and HEV Applications. *Proc. IEEE Trans. Transp. Electrif.* **2015**, *1*, 245–254. [CrossRef]
3. Bae, J.N. Permanent Magnet Synchronous Machine Design through and Automatic Selection of the Specific Loadings. Ph.D. Thesis, Hanyang University, Seoul, Korea, 2010.
4. Cho, S.; Jung, K.; Choi, J. Design Optimization of Interior Permanent Magnet Synchronous Motor for Electric Compressors of Air-Conditioning Systems Mounted on EVs and HEVs. *IEEE Trans. Magn.* **2018**, *54*, 1–5. [CrossRef]
5. Shin, K.; Choi, J.; Cho, H. Characteristic Analysis of Interior Permanent-Magnet Synchronous Machine with Fractional-Slot Concentrated Winding Considering Nonlinear Magnetic Saturation. *IEEE Trans. Appl. Supercond.* **2016**, *26*, 5200404. [CrossRef]
6. Kim, S.; Lee, G.; Hong, J.; Jung, T. Design Process of Interior PM Synchronous Motor for 42-V Electric Air-Conditioner System in Hybrid Electric Vehicle. *IEEE Trans. Magn.* **2008**, *44*, 1590–1593.
7. Kim, S.H. *DC, AC, BLDC Motor Control*; Bokdoo Press: Seoul, Korea, 2012.
8. Gieras, J.F.; Wang, C.; Lai, J.C. *Noise of Poly-Phase Electric Motors*, 2nd ed.; Taylor & Francis: New York, NY, USA, 2006.
9. Zhu, Z.Q.; Xia, Z.P.; Wu, L.J.; Jewell, G.W. Influence of slot and pole number combination on radial force and vibration modes in fractional slot PM brushless machines having single-and double-layer windings. In Proceedings of the IEEE Energy Conversion Congress and Exposition (ECCE), San Jose, CA, USA, 20–24 September 2009; pp. 3443–3450.
10. Zhu, Z.Q.; Xia, Z.P.; Wu, L.J.; Jewell, G.W. Analytical modeling and finite element computation of radial vibration force in fractional-slot permanent-magnet brushless machines. *IEEE Trans. Ind. Appl.* **2010**, *46*, 1908–1918. [CrossRef]
11. Im, D.H.; Chang, J.H.; Park, S.C.; Kwon, B.I.; Hong, J.P.; Kim, B.T. Analysis of radial force as a source of vibration in an induction motor with skewed slots. *IEEE Trans. Magn.* **1997**, *33*, 1650–1653. [CrossRef]
12. Kobayashi, T.; Tajima, F.; Ito, M.; Shibukawa, S. Effects of slot combination on acoustic noise from induction motors. *IEEE Trans. Magn.* **1997**, *33*, 2101–2104. [CrossRef]
13. Studer, C.; Keyhani, A.; Sebastian, T.; Murthy, S.K. Study of cogging torque in permanent magnet machines. In Proceedings of the 1997 IEEE Industry Applications Society (IAS '97), New Orleans, LA, USA, 4–9 October 1997; pp. 42–49.
14. Kim, B.-T.; Kwon, B.-I.; Park, S.-C. Reduction of electromagnetic force harmonics in asynchronous traction motor by adapting the rotor slot number. *IEEE Trans. Magn.* **1999**, *35*, 3742–3744.
15. Bianchi, N.; Bolognani, S. Design techniques for reducing the cogging torque in surface-mounted PM motors. *IEEE Trans. Ind. Appl.* **2002**, *38*, 1259–1265. [CrossRef]
16. Dai, M.; Keyhani, A.; Sebastian, T. Torque ripple analysis of a PM brushless DC motor using finite element method. *IEEE Trans. Energy Convers.* **2004**, *19*, 40–45. [CrossRef]
17. Mori, D.; Ishikawa, T. Force and vibration analysis of induction motors. *IEEE Trans. Magn.* **2005**, *41*, 1948–1951. [CrossRef]
18. Sung, S.; Jang, G.; Kang, K. Noise and vibration due to rotor eccentricity in a HDD spindle system. *Microsyst. Technol.* **2014**, *20*, 1461–1469. [CrossRef]

19. Seo, B.; Sung, S.; Kang, K.; Song, J.; Jang, G. Unbalanced magnetic force and cogging torque of PM motors due to the interaction between PM magnetization and stator eccentricity. *Microsyst. Technol.* **2016**, *22*, 1249–1255. [CrossRef]
20. Chen, Q.; Liu, G.; Gong, W.; Qu, L.; Zhao, W.; Shen, Y. Design of a spoke-type permanent-magnet motor with optimal winding configuration for electric vehicle applications. *J. Appl. Phys.* **2012**, *111*, 07E710. [CrossRef]
21. Meessen, K.J.; Paulides, J.J.H.; Lomonova, E.A. Force calculations in 3-D cylindrical structures using Fourier analysis and the Maxwell stress tensor. *IEEE Trans. Magn.* **2012**, *49*, 536–545. [CrossRef]
22. Hur, J.; Reu, J.-W.; Kim, B.; Kang, G.-H. Vibration reduction of IPM-type BLDC motor using negative third harmonic elimination method of air-gap flux density. *IEEE Trans. Ind. Appl.* **2011**, *47*, 1300–1309.
23. Fang, L.; Jung, J.; Hong, J.-P.; Lee, J.-H. Study on high-efficiency performance in interior permanent-magnet synchronous motor with double-layer PM design. *IEEE Trans. Magn.* **2008**, *44*, 4393–4396. [CrossRef]
24. Jung, J.-W.; Lee, S.-H.; Lee, G.-H.; Hong, J.-P.; Lee, D.-H.; Kim, K.-N. Reduction design of vibration and noise in IPMSM type integrated starter and generator for HEV. *IEEE Trans. Magn.* **2010**, *46*, 2454–2457. [CrossRef]
25. Ge, H.; Yu, M.; Berker, B.; Babak, N.-M.; Ali, E. Speed Range Extended Maximum Torque Per Ampere Control for PM Drives Considering Inverter and Motor Nonlinearities. *IEEE Trans. Power Electron.* **2017**, *32*, 7151–7159. [CrossRef]
26. Mohamed, Y.A.-R.I.; Lee, T.K. Adaptive self-tuning MTPA vector controller for IPMSM drive system. *IEEE Trans. Energy Convers.* **2006**, *21*, 636–644. [CrossRef]

*Communication*

# Optimal Design of a BLDC Motor Considering Three-Dimensional Structures Using the Response Surface Methodology

**Seong-Tae Jo, Hyo-Seob Shin, Young-Geun Lee, Ji-Hun Lee and Jang-Young Choi ***

Department of Electrical Engineering, Chungnam National University, Daejeon 305-764, Korea; jst4900@o.cnu.ac.kr (S.-T.J.); shs1027@cnu.ac.kr (H.-S.S.); 201502206@o.cnu.ac.kr (Y.-G.L.); ljh@o.cnu.ac.kr (J.-H.L.)
* Correspondence: choi_jy@cnu.ac.kr

**Abstract:** In this paper, the optimal design of a brushless direct current motor with a three-dimensional (3D) structure using the response surface methodology (RSM) is presented. There were two optimization goals: reduction of the cogging torque and maintenance of the back electromotive force to prevent performance degradation. For motors with a 3D structure, a 3D finite element method analysis is essential, though it requires considerable computation time. Therefore, to reduce the optimal design time, the 3D structure was placed on the 2D plane. Thereafter, a 2D corrected model was applied to the RSM. For the validity of the technique, the analysis results of the initial 3D model, 2D model, and 2D corrected model were compared, and the results of the optimal design 3D model, 2D corrected model, and experiment were compared.

**Keywords:** BLDC motor; magnet overhang; housing-integrated rotor; 2D equivalent; response surface methodology; computation time

## 1. Introduction

With the development of technology, the mechanical commutation device of a DC motor was changed to an electrical commutation device, and a brushless DC (BLDC) motor was developed. In a DC motor, permanent magnets (PMs) are present in the external stator. However, PMs in BLDC motors are in the rotor. They are divided into outer and inner rotor types [1]. The outer-rotor-type BLDC motor has a large PM; therefore, it can increase the torque, and its inertia is large, which is advantageous for constant-speed operation [2,3]. Because of these characteristics, the outer-rotor-type BLDC motors are typically used in fan and pump applications [4–6]. Meanwhile, the noise and vibration of a BLDC motor affect the life of the device and cause inconvenience to users. Electromagnetic vibration sources that affect noise and vibration include cogging torque, torque ripple, back electromotive force (EMF), and total harmonic distortion (THD). Recently, studies on noise and vibration optimization through the reduction of cogging torque have been actively conducted [7,8]. In this study, the optimal design of cogging torque reduction, which is one of the electromagnetic vibration sources, was carried out.

Three-dimensional structures, such as the magnet overhang and housing-integrated rotor, are used to increase the power density. When a housing-integrated rotor is applied, the magnetic flux path is secured, and the radial thickness of the yoke can be reduced. When a magnet overhang is applied, the air gap flux density can be increased [9,10].

In general, the electromagnetic analysis of motors is performed using finite element method (FEM) analysis. However, motors with three-dimensional (3D) structures, such as magnet overhang and housing-integrated rotors, are difficult to analyze accurately with two-dimensional (2D) FEM analysis. Therefore, motors with 3D structures require 3D FEM analysis, which is unsuitable for optimal designs that require a lot of analysis and long computation times. To this end, a method of interpreting a 3D structure's 2D equivalent has

been previously studied [11,12]. In the case of the magnet overhang, the magnetic energy decreases as the volume of the PM decreases when converting from 3D to 2D. Therefore, to maintain the magnetic energy equally, properties, such as coercive force and remanence, are adjusted [13,14]. When an equivalent housing-integrated rotor is used, flux saturation due to flux path reduction should be considered. The volume in the 3D structure is equivalent to increasing the radial direction thickness of the yoke in a 2D structure.

In general, motors have a trade-off relationship. When one characteristic is improved according to the control of a variable, the other characteristics deteriorate. Therefore, several characteristics must be satisfied simultaneously. Multi-objective optimization allows a user to select the optimal point through a family of variables [15–17]. For example, electromagnetic characteristics, such as cogging torque, torque ripple, torque average value, back EMF, and efficiency, may be classified and optimized so that they are minimized and maximized, respectively.

The response surface methodology (RSM) is a type of multi-objective optimization that creates a surrogate model by defining the relationship between variables and response values based on response values derived from multiple analysis points. The RSM selects an analysis point within a set variable range, predicts a surrogate model, and derives the desired optimal point by applying the goal and desirability function of each response value [18–22]. Unlike the global optimization technique that directly analyzes all points to derive the optimal point, the result of the point selected through the surrogate model has an error relative to the actual analysis result. As the number of objective functions increases, the accuracy of the response surface decreases; therefore, two to four objective functions are usually applied to the RSM [21,23,24].

In this study, a BLDC motor with a 3D structure was optimally designed based on the RSM. The purpose of the optimal design was to reduce the cogging torque and maintain the back EMF to sustain the electromagnetic characteristics of the motor [25,26]. During optimization, winding specifications and things that are not factors were not changed. Inductance is the ratio of flux linkage per current, and the no-load back EMF is proportional to the time-varying magnetic flux linkage. Therefore, maintaining the no-load back EMF means maintaining the inductance and flux linkage. Additionally, because things that are not factors and no-load back EMF were not changed, efficiency and losses are similar to the initial model. Therefore, they were not included in the objective function. The RSM with a 3D structure requires considerable computation time; the optimal design time can be shortened by proceeding with a 2D equivalent of the 3D structure during the optimal design process. For the validity of the technique in this study, the 3D and 2D FEM analysis results of the initial design were compared. Moreover, the 3D and 2D FEM analyses and experimental results of the optimal design were compared.

## 2. The 3D Structure and Its 2D Equivalent

### 2.1. Analysis Model

Figure 1 shows the analysis model used in this study. It was an 8-pole, 12-slot BLDC motor and had two 3D structures with a magnet overhang and a housing-integrated rotor.

### 2.2. Magnet Overhang

Because ferrite magnets have weaker magnetism than rare earth magnets, a larger magnet volume is required to increase the output. The magnet overhang is a structure that increases the axial length of the PM, reducing the magnetic flux leakage and increasing the air gap magnetic flux density. The model to which the magnet overhang is applied is not a plane structure. Therefore, it is indispensable to analyze the model as a 3D FEM. However, because 3D FEM analysis requires considerable analysis time, it is efficient to analyze models using a 2D equivalent for optimal design.
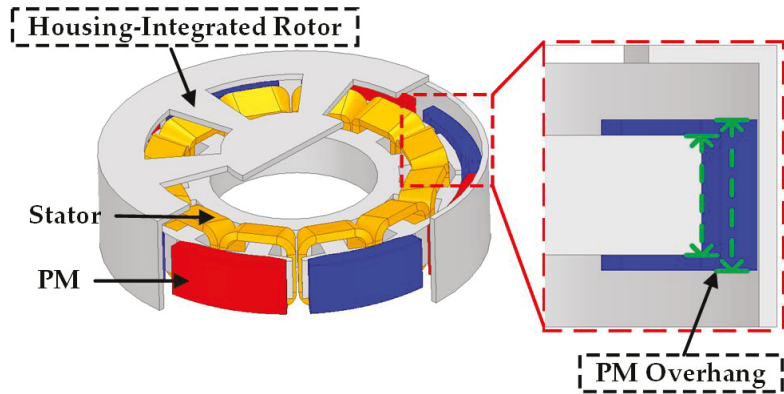
**Figure 1.** The 3D structures of the analysis model.

Through the following equation, it is possible to derive a condition that allows the magnet overhang to have the same magnetic energy, even though the volume decreases when represented in 2D.

$$W_H = \frac{1}{2} B_{m1} H_{m1} V_1 = \frac{1}{2} B_{m2} H_{m2} V_2 \tag{1}$$

Equation (1) is about the magnetic energy of a PM $W_H$ as a function of magnetic flux density, magnetic field strength, and volume. In Equation (1), $B_{m1}$, $H_{m1}$, and $V_1$ are the magnetic flux density, magnetic field strength, and volume at the operating point of the PM in the existing model, respectively. $B_{m2}$, $H_{m2}$, and $V_2$ are the magnetic flux density, magnetic field strength, and volume at the operating point of the PM in the 2D corrected model, respectively. $B_{m1}$, $H_{m1}$, and $V_1$ are specified values in the 3D model, and when converted to 2D, $V_1$ decreases to become $V_2$; therefore, $B_{m2}$ and $H_{m2}$ should increase. To equalize the degree of energy flow when adjusting the operating point, the operating point $P_1(B_{m1}, H_{m1})$ of the 3D model's PM should be the operating point $P_2(B_{m2}, H_{m2})$ of the $P_c$, which is the permeance coefficient, in the load line, as shown in Figure 2 [13,14,27].

$$P_c = \frac{B_m}{\mu_0 |H_m|} = \frac{\mu_{rec} B_m}{B_r - B_m} = \frac{1}{f_{leakage}} \times \frac{L_m}{L_g} \times \frac{A_g}{A_m} \tag{2}$$

$$B_{m1} = B_r + \mu_0 \mu_{rec} H_{m1} \tag{3}$$
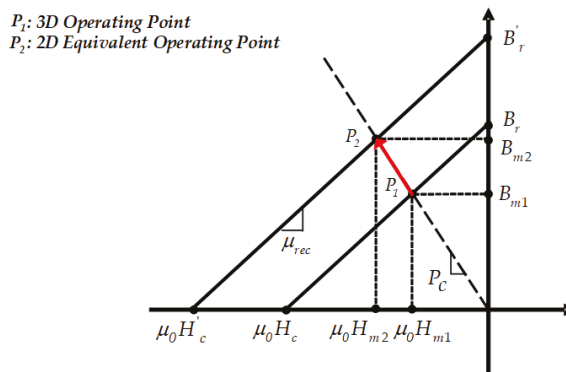


**Figure 2.** Demagnetization curve of a PM.

Equation (2) is about the permeance coefficient as a function of $B_m$ and $H_m$. In Equation (2), $f_{leakage}$ is a leakage coefficient with a value usually between 0.85 and 0.95; in this study, it was set to 0.9. $\mu_{rec}$ is the relative permeability, $B_r$ is the remanence, $L_m$ is the magnet axial length, $L_g$ is the air gap length, $A_g$ is the area of the air gap, and $A_m$ is the area of the magnet. Equation (3) represents the demagnetization curve in Figure 2.

Equation (4) represents the operating point $P_1$, which can be derived from Equations (2) and (3).

$$B_{m1} = \frac{P_c}{P_c + \mu_{rec}} B_r, \ H_{m1} = \frac{B_{m1} - B_r}{\mu_0 \mu_{rec}} \tag{4}$$

The operating point $P_2(B_{m2}, H_{m2})$ can be derived through Equations (1) and (2) and the driving point $P_1(B_{m1}, H_{m1})$.

$$B_{m2} = \sqrt{B_{m1} H_{m1} \frac{V_1}{V_2} \mu_0 P_c}, \ H_{m2} = \frac{B_{m2}}{\mu_0 P_c} \tag{5}$$

*2.3. Housing-Integrated Rotor*

The housing-integrated rotor is a 3D structure that is applied to secure the magnetic flux path and reduce the size of the device. As shown in Figure 3, when analyzing the 3D FEM, the magnetic flux flows not only in the yoke but also in the housing part. It is impossible to consider the housing part of the housing-integrated rotor in 2D when performing a 2D FEM analysis. When only the 3D yoke part is expressed in 2D, the rotor is significantly saturated.
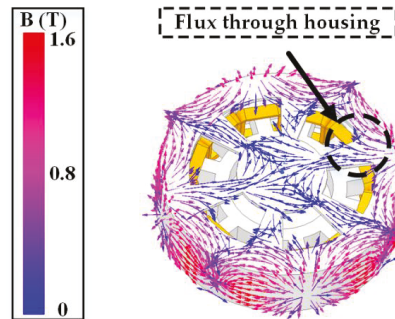


**Figure 3.** Magnetic flux density through the housing part.

The required values can be derived when the housing-integrated rotor is converted to 2D through the following equation:

$$V_{housing} + V_{yoke} = \left( r_{ro}^2 - r_{ri}^2 \right) \pi l_s \tag{6}$$

In Equation (6), $V_{housing}$ is the volume of the housing part; $V_{yoke}$ is the volume of the yoke part; $r_{ro}$ and $r_{ri}$ are the outer and inner diameters of the rotor in 2D, respectively; and $l_s$ is the axial length of the stator.

The rotor volume in the 3D model and the rotor volume in the 2D corrected model were equated by extending the radial direction of the rotor in the 2D corrected model.

**3. Design of Experiments (DOE)**

The cogging torque, the optimization object of this study, is affected by the shape of the motor, including the stator, rotor, and magnet. If there are many variables that can be adjusted, unnecessary analysis points are created and the optimization period is increased. Therefore, it is necessary to select and proceed with the most influential variables when producing an optimal design.

DOE is a technique for finding the optimal point with a small number of experiments for the optimization target model. Because DOE derives a local solution within the range of the desired solution, the DOE can select the optimal point relatively quickly within the constraints. If DOE is applied, the influence of each factor on the model can be identified and an optimization point can be determined by defining the relationship with the objective function.

In general, factors that are significant in the objective function are selected through factorial design, and the optimal point is determined by applying the selected factors to the RSM.

### 3.1. Design Variables Affecting Cogging Torque

Cogging torque is a pulsation torque caused by a tendency to align the reluctance to a minimum in a magnetic circuit composed of a stator, rotor, PM, and air gap of a model. The cogging torque affects the torque ripple and adversely affects the performance of the motor; therefore, it should be considered in an optimal design. The cogging torque can be estimated using the following equation:

$$C_T = \frac{P \cdot Q}{LCM(P,Q)} \tag{7}$$

In Equation (7), $C_T$ is the goodness factor, $P$ is the number of poles, $Q$ is the number of slots, and $LCM(P,Q)$ is the least common multiple of $P$ and $Q$. The goodness factor is a measure for estimating the size of the cogging torque and is inversely proportional to $LCM(P,Q)$. The model in this study was an 8-pole, 12-slot model, and the cogging torque was large because the least common multiple was small [6,28,29]. To reduce the cogging torque, variables related to the shape of the rotor, stator, and magnet should be applied. As shown in Figure 4, the factors to be applied to the DOE in this study were three variables for the stator and two variables for the PM.
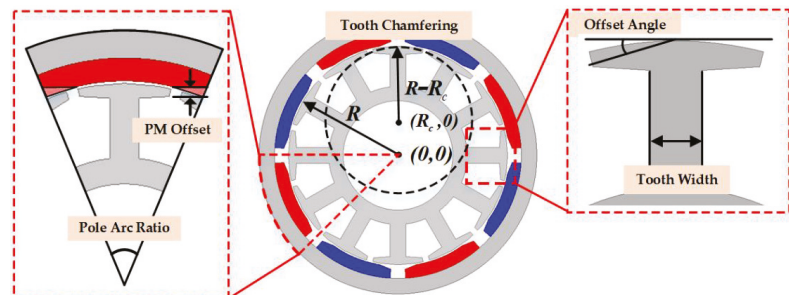


**Figure 4.** Design variables.

### 3.2. Factorial Design

Before proceeding with the RSM by applying the presented factors, meaningful factors should be selected through factorial design. Applying the factorial design can select factors that significantly affect the objective function and shorten the unnecessary optimization time. In particular, in the multi-objective optimization method, the effect on each objective function can be analyzed and selected according to the purpose. In this study, the $2^k$ factorial design is used; the coefficient represents the number of levels and the exponent represents the number of factors. In the two-level factorial design, the level of all factors was two, and the relational expression between factors and response values can be expressed simply and efficiently. Figure 5 shows the relationship between the cogging torque and back EMF, which were the objective functions of this study, and the variables. As the goal of this study was to reduce the cogging torque while maintaining the back EMF, variables that had a small influence on the back EMF and had a large influence on the cogging torque

were advantageous. As shown in Figure 5, the PM offset, stator offset, and tooth width were selected because the pole arc ratio has a significant influence on the back EMF, and chamfering has little effect on either objective function.
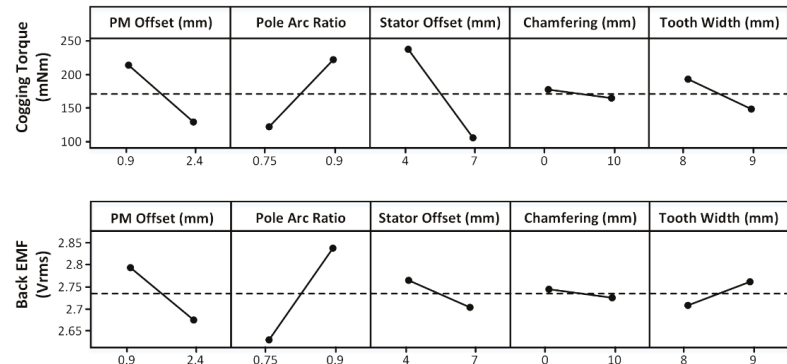


**Figure 5.** Effect of variables on the cogging torque and back EMF.

### 3.3. Factorial Design with Center Point

The RSM proceeds when the analysis result in the factorial design is near the optimal point. The optimal point exists where there is a curvature on the response surface, where it is located by adding a center point to the factorial design as a method to search for the curvature. The evidence of curvature exists when the response values at the center point are not included in the response surface in the factorial design.

### 3.4. Response Surface Method

When evidence of curvature is found in the factorial design with the center point, the RSM is performed to determine the optimal point. In this study, the central composite design (CCD), which is generally used among RSMs, was applied. Figure 6a,b shows the CCD when two and three factors are applied, respectively. As shown in Figure 6, the CCD considers the response value at the center and axial points, unlike the factorial design. Because the response values of the central and axial points exist, the curvature at the response surface and the quadratic terms of the response function can be estimated.

$$f(x) = a_0 + a_1 x_1 + a_2 x_2 + a_3 x_1 x_2 + a_4 x_1^2 + a_5 x_2^2 \tag{8}$$
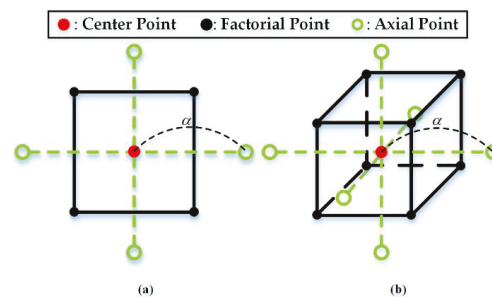


**Figure 6.** Central composite design with (**a**) two variables and (**b**) three variables.

Equation (8) is the response function of the two-factor RSM. $f(x)$ is a response function, $a$ is an estimation coefficient, and $x_1$ and $x_2$ are the factor values of each variable. $\alpha$, shown in Figure 6, represents the distance from the central point to the axial point. If the axial point and factorial point are designed to exist at an equal distance from the center point,

the analysis model has rotationality, resulting in equal variance and improved algorithm stability. The position of the axial point is generally determined by $\alpha = \sqrt[4]{n_f}$, where $n_f$ is the number of factorial points.

Table 1 lists the optimization ranges of each factor. Each point is the position of the axial point, and the value of $\alpha$ is 1.681 [30].

**Table 1.** Range of variables.

| Variables | Lower Limit | Upper Limit |
|---|---|---|
| PM Offset | 1 mm | 2 mm |
| Stator Offset | 4.5 mm | 6.5 mm |
| Tooth Width | 8.5 mm | 9.1 mm |

Table 2 shows the analysis points at the center, factorial, and axial points of the RSM. The response values at each analysis point are shown, and the 1st to 8th analysis points represent the axial points, the 9th to 14th analysis points represent the factorial points, and the 15th analysis point represents the center point.

$$y_1 = 4907.97 + 544.668 * x_1 + 44.7990 * x_2 - 1052.21 * x_3 - 58.5907 * x_1{}^2$$
$$-15.0979 * x_2{}^2 + 59.6963 * x_3{}^2 - 58.5878 * x_1 * x_2 \tag{9}$$
$$+4.80467 * x_2 * x_3$$

$$y_2 = 0.500444 + 0.0524745 * x_1 + 0.0536581 * x_2 + 0.465951 * x_3$$
$$-0.0266451 * x_1{}^2 - 0.00396127 * x_2{}^2 - 0.0217918 * x_3{}^2 \tag{10}$$
$$-0.00424264 * x_1 * x_2 - 0.00377124 * x_2 * x_3$$

**Table 2.** Design variables and responses of the RSM.

| Run | PM Offset (mm) | Stator Offset (°) | Tooth Width (mm) | Cogging Torque (mNm) | Back EMF (Vrms) |
|---|---|---|---|---|---|
| 1 | 1.20270 | 4.90540 | 8.62162 | 297.904 | 2.8869 |
| 2 | 1.79730 | 4.90540 | 8.62162 | 210.677 | 2.8488 |
| 3 | 1.20270 | 6.09460 | 8.62162 | 205.006 | 2.8602 |
| 4 | 1.79730 | 6.09460 | 8.62162 | 123.946 | 2.8224 |
| 5 | 1.20270 | 4.90540 | 8.97838 | 280.799 | 2.9078 |
| 6 | 1.79730 | 4.90540 | 8.97838 | 181.924 | 2.8687 |
| 7 | 1.20270 | 6.09460 | 8.97838 | 190.720 | 2.8794 |
| 8 | 1.79730 | 6.09460 | 8.97838 | 96.452 | 2.8408 |
| 9 | 1 | 5.5 | 8.8 | 258.151 | 2.8946 |
| 10 | 2 | 5.5 | 8.8 | 118.949 | 2.8295 |
| 11 | 1.5 | 4.5 | 8.8 | 273.221 | 2.8880 |
| 12 | 1.5 | 6.5 | 8.8 | 12.980 | 2.8415 |
| 13 | 1.5 | 5.5 | 8.5 | 228.151 | 2.8500 |
| 14 | 1.5 | 5.5 | 9.1 | 188.990 | 2.8835 |
| 15 | 1.5 | 5.5 | 8.8 | 206.225 | 2.8688 |

Equations (9) and (10) are the response functions estimated through the RSM. $y_1$ and $y_2$ are the cogging torque and back EMF, respectively; $x_1$, $x_2$, and $x_3$ are the PM offset, stator offset, and tooth width, respectively. The tendency of the response value according to the change in the factor value is determined by the linear, quadratic, and alternating terms of each factor.

Figure 7 shows the contour plot of the response value according to the changes in the factors. All the response surfaces have a curvature. As shown in Equations (9) and (10) and Figure 7, when the PM offset and stator offset increased, the cogging torque and back EMF decreased, and when the tooth width increased, the cogging torque decreased and the back EMF increased.
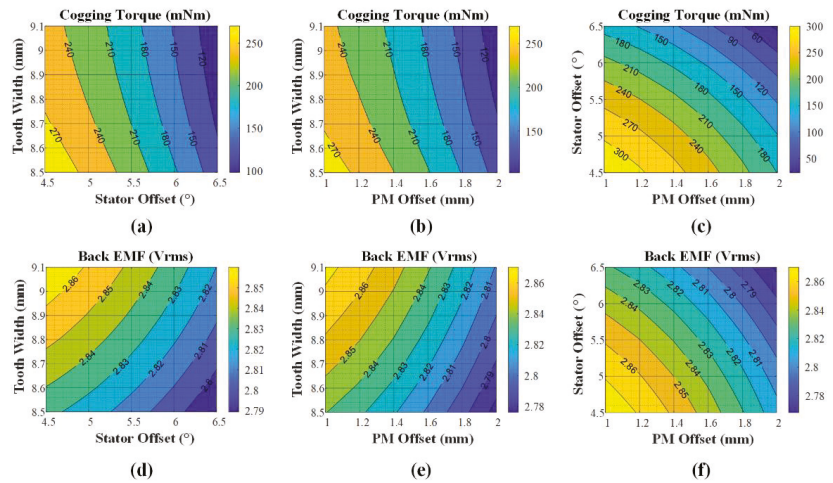
**Figure 7.** Contour plot of the cogging torque with (**a**) tooth width and stator offset, (**b**) tooth chamfering and stator offset, (**c**) tooth chamfering and tooth width, and BEMF with (**d**) tooth width and stator offset, (**e**) tooth chamfering and stator offset, and (**f**) tooth width and stator offset.

When using the response surface, the optimal point is selected using the goal and desirability function of each response value. The goal was to maintain 2.84 $V_{rms}$, which was the back EMF of the initial model, and to minimize the cogging torque. The desirability function can assign importance to each target value by selecting a weight between 0.1 and 10, as shown in Figure 8. When the weight is close to 0.1, high satisfaction is derived even if the response value is far from the target value, and when the weight is close to 10, high satisfaction is derived near the target value. In this study, since the reduction in the cogging torque and the maintenance of the back EMF are equally important values, the weights of the two response values were set to 1. Figure 9 shows the result of selecting the optimal point based on the relationship between each variable and the response values. Table 3 shows the inductances and the flux linkages in each analysis model, and the inductances and flux linkages of the two models were similar.

**Table 3.** Inductance and flux linkage of each analysis model.

| Analysis Model | Initial Corrected Model | Optimal 2D Corrected Model |
|---|---|---|
| Phase Inductance | 86.07 µH | 87.28 µH |
| Flux Linkage | 0.0096 Wb | 0.0097 Wb |
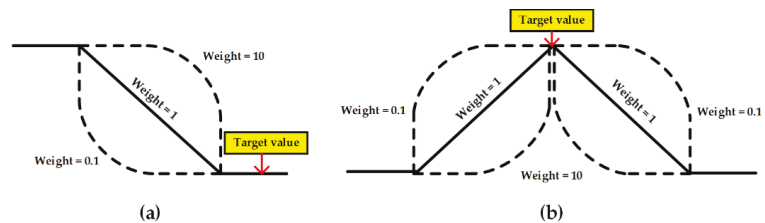


**Figure 8.** Desirability function for (**a**) smaller the better characteristics and (**b**) nominal is the best characteristics.
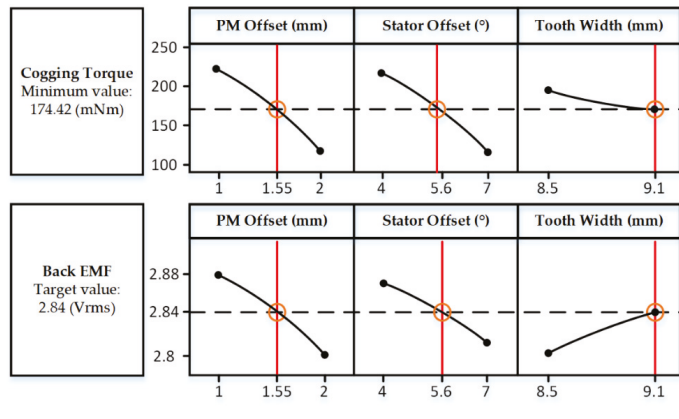
**Figure 9.** Set optimal point based on the initial parameter.

## 4. Results

Figure 10 shows the manufactured optimization model, housing-integrated rotor, and magnet overhang.
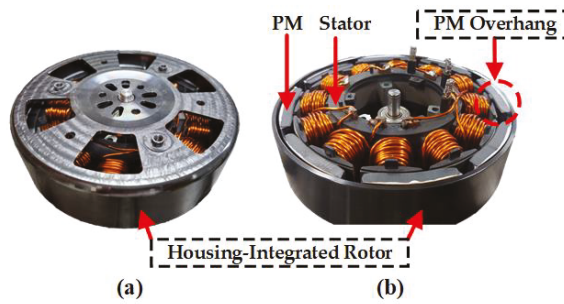


**Figure 10.** Manufactured analysis model (**a**) upper view and (**b**) lower view.

Figure 11a,b shows the cogging torque and back EMF results when the 3D structure was converted to 2D, respectively, and the results of the 3D initial and 2D initial models are also included; "2DC" in Figures 11 and 12 means 2D corrected. The values of the cogging torque and back EMF in the 2D initial model were smaller than the values of the 3D initial model. This was because the volume of the magnet decreased and the energy decreased; the volume of the yoke decreased so that the magnetic flux path could not be secured. By deriving the operating point of the magnet according to Equations (1)–(5) and adjusting the B–H curve, the energy held by the PM was the same. In addition, the thickness was increased so that the yoke was not saturated. Figure 11 shows that the analysis results of the 2D corrected model were close to those of the 3D initial model.

Figure 12a,b shows the cogging torque and back EMF of the 2D corrected model, respectively, when multi-objective optimization of the motor was performed by applying the RSM, and the results of the 3D optimization model and the manufactured model are shown. Figure 12a shows that the cogging torques of the experiment, optimized 3D model, and 2D corrected model were approximate. Figure 12b shows that the back EMFs of the experiment, optimized 3D model, and 2D corrected model are approximate.
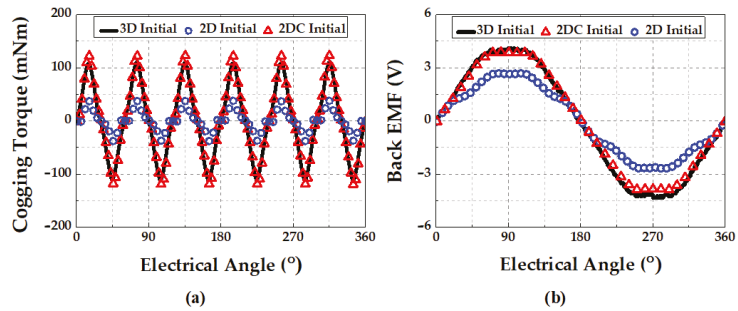
**Figure 11.** The 2D corrected model analysis results for the (**a**) cogging torque and (**b**) back EMF.
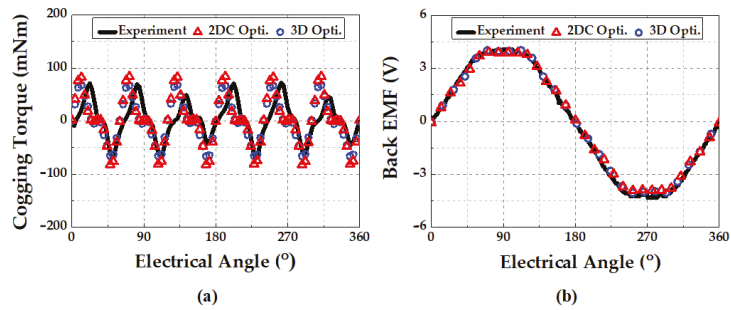


**Figure 12.** RSM results for the (**a**) cogging torque and (**b**) back EMF.

Table 4 shows the analysis results of the 2D corrected model under different load conditions, when calculating the efficiency, the mechanical loss was set to 3%. Table 5 shows the experimental results under different load conditions of the manufactured model.

**Table 4.** Analysis results of the 2D corrected model.

| Load Torque (Nm) | Output Power (W) | Core Loss (W) | Copper Loss (W) | Efficiency (%) |
|---|---|---|---|---|
| 0.5 | 139.1 | 11.74 | 3.46 | 87.44 |
| 1 | 274.2 | 13.31 | 12.32 | 88.71 |
| 1.5 | 408.9 | 14.64 | 25.88 | 88.25 |
| 2 | 548.0 | 16.10 | 44.60 | 87.33 |
| 2.42 | 669.7 | 17.65 | 64.59 | 86.39 |

**Table 5.** Experiment results of the manufactured model.

| Load Torque (Nm) | Output Power (W) | Core + Mechanical Loss (W) | Copper Loss (W) | Efficiency (%) |
|---|---|---|---|---|
| 0.5 | 137 | 25.4 | 3.91 | 82.76 |
| 1 | 274 | 27.3 | 12.34 | 88.05 |
| 1.5 | 411 | 33.7 | 26.18 | 88.28 |
| 2 | 548 | 44.1 | 45.92 | 87.17 |
| 2.38 | 651 | 54.2 | 64.81 | 87.58 |

Table 6 shows the analysis time of the 2D corrected model and the 3D model. It can be seen that the times for the no-load and load analyses of the 2D corrected model were significantly shorter than the analysis time for the 3D model. The specifications of the CPU, RAM, cores, and mesh, which is the total number of elements, are shown for the validity of the analysis results.

**Table 6.** Analysis time.

|  | 2D Corrected Model | 3D Model |
|---|---|---|
| No-load analysis (s) | 71 | 39,381 |
| Load analysis (s) | 5891 | 142,958 |
| Mesh | 10,253 | 809,367 |
| CPU | Intel Core i9-11900K @3.50 GHz | |
| RAM | 128 GB | |
| Cores | 4 of 8 | |

## 5. Conclusions

In this paper, the optimal design of a BLDC motor with a 3D structure through RSM is presented. To improve the performance of the motor, reducing the cogging torque and maintaining the back EMF were selected as the objective functions. Because it is difficult to perform 2D FEM on models with 3D structures and 3D FEM analysis takes considerable time, 3D structures were analyzed by using an equivalent 2D structure. The magnet overhang was equated by adjusting the B–H curve to have the same magnetic energy when the volume of the magnet changed. The housing-integrated rotor increased the thickness of the yoke in the 2D model to maintain the total volume in the 3D structure by considering flux saturation. When comparing the cogging torque and back EMF of the initial 2D model, initial 2D corrected model, and initial 3D model, the results of the initial 2D corrected model were close to those of the initial 3D model.

The RSM was applied as the model optimization technique, and a two-level five-factorial design was used to select the variables to be applied to the RSM. The PM offset, stator offset, and tooth width were selected as factors because out of the two objective functions since they affect the cogging torque more. Before advancing with the RSM, a factorial design with a center point was performed to check whether the factors were suitable for proceeding with the RSM, and a curvature appeared on the response surface of the cogging torque and back EMF. Therefore, a CCD was performed using three selected factors as variables. The response surface was derived according to the values of each variable through linear, quadratic, and alternating terms estimated through the CCD. After that, by selecting the optimal point, the 2D corrected model was inversely equivalent to the 3D structure model, and it was confirmed that the electromagnetic characteristics were similar. Because the electromagnetic characteristics were maintained after optimization, the validity of the optimal design technique of this study was verified. Therefore, the time to optimize the BLDC with 3D structures was shortened by using a 2D corrected model. By using the 2D equivalent technique of this study, it will be possible to reduce the load analysis time of the BLDC of the 3D structure, which consumes considerable computation time. In addition, because the RSM requires few analysis points, it will be possible to optimize the electromagnetic characteristics under load faster than other techniques.

## References

1. Kim, S.H. *Motor Control-DC, AC, BLDC*; D.B.Info.: Seoul, Korea, 2017.
2. Kai, Y.; Yaojing, F. Design of Novel Spiral Magnetic Poles and Axial-Cooling Structure of Outer-Rotor PM Torque Motor. *IEEE Trans. Appl. Supercond.* **2010**, *20*, 838–841. [CrossRef]
3. Wang, Y.; Chau, K.T.; Chan, C.C.; Jiang, J.Z. Transient analysis of a new outer-rotor permanent-magnet brushless DC drive using circuit-field-torque coupled time-stepping finite-element method. *IEEE Trans. Magn.* **2002**, *38*, 1297–1300. [CrossRef]
4. Tang, Z.-H.; Chen, Y.-T.; Liou, Y.-K.; Liang, R.-H. Axial Magnetic Force Analysis and Optimized Design for Single-Phase BLDC Slim Fan Motors. *IEEE Trans. Ind. Electron.* **2021**, *68*, 6840–6848. [CrossRef]
5. Youssef, M.Z. Design and Performance of a Cost-Effective BLDC Drive for Water Pump Application. *IEEE Trans. Ind. Electron.* **2014**, *62*, 3277–3284. [CrossRef]
6. Leitner, S.; Gruebler, H.; Muetze, A. Innovative Low-Cost Sub-Fractional HP BLDC Claw-Pole Machine Design for Fan Applications. *IEEE Trans. Ind. Appl.* **2019**, *55*, 2558–2568. [CrossRef]
7. Lee, C.-M.; Seol, H.-S.; Lee, J.Y.; Lee, S.H.; Kang, D.-W. Optimization of Vibration and Noise Characteristics of Skewed Permanent Brushless Direct Current Motor. *IEEE Trans. Magn.* **2017**, *53*, 1–5. [CrossRef]
8. Park, Y.-U.; Cho, J.-H.; Kim, D.-K.; Young-Un, P. Cogging Torque Reduction of Single-Phase Brushless DC Motor with a Tapered Air-Gap Using Optimizing Notch Size and Position. *IEEE Trans. Ind. Appl.* **2015**, *51*, 4455–4463. [CrossRef]
9. Lee, T.-Y.; Seo, M.-K.; Kim, Y.-J.; Jung, S.-Y. Motor Design and Characteristics Comparison of Outer-Rotor-Type BLDC Motor and BLAC Motor Based on Numerical Analysis. *IEEE Trans. Appl. Supercond.* **2016**, *26*, 1–6. [CrossRef]
10. Chun, Y.-D.; Lee, J.; Wakao, S. Overhang effect analysis of brushless DC motor by 3-D equivalent magnetic circuit network method. *IEEE Trans. Magn.* **2003**, *39*, 1610–1613. [CrossRef]
11. Shin, H.-S.; Shin, K.-H.; Jang, G.-H.; Cho, S.-K.; Jung, K.-H.; Choi, J.-Y. Experimental Verification and 2D Equivalent Analysis Techniques of BLDC Motor with Permanent Magnet Overhang and Housing-Integrated Rotor Core. *IEEE Trans. Appl. Supercond.* **2020**, *30*, 1–5. [CrossRef]
12. Chun, Y.; Wakao, S.; Kim, T.; Jang, K.; Lee, J. Multiobjective Design Optimization of Brushless Permanent Magnet Motor Using 3D Equivalent Magnetic Circuit Network Method. *IEEE Trans. Appl. Supercond.* **2004**, *14*, 1910–1913. [CrossRef]
13. Kim, K.-C.; Lee, J. The dynamic analysis of a spoke-type permanent magnet generator with large overhang. *IEEE Trans. Magn.* **2005**, *41*, 3805–3807. [CrossRef]
14. Kim, K.-C.; Koo, D.-H.; Lee, J. The Study on the Overhang Coefficient for Permanent Magnet Machine by Experimental Design Method. *IEEE Trans. Magn.* **2007**, *43*, 2483–2485. [CrossRef]
15. Jolly, L.; Jabbar, M.; Qinghua, L. Design optimization of permanent magnet motors using response surface methodology and genetic algorithms. *IEEE Trans. Magn.* **2005**, *41*, 3928–3930. [CrossRef]
16. Rao, K.S.R.; Bin Othman, A.H. Design optimization of a BLDC motor by Genetic Algorithm and Simulated Annealing. In Proceedings of the 2007 International Conference on Intelligent and Advanced Systems, Kuala Lumpur, Malaysia, 25–28 November 2007; pp. 854–858. [CrossRef]
17. Han, K.J.; Cho, H.-S.; Cho, D.-H.; Jung, H.-K. Optimal core shape design for cogging torque reduction of brushless DC motor using genetic algorithm. *IEEE Trans. Magn.* **2000**, *36*, 1927–1931. [CrossRef]
18. Li, J.; Liu, Z.; Jabbar, M.; Gao, X. Design Optimization for Cogging Torque Minimization Using Response Surface Methodology. *IEEE Trans. Magn.* **2004**, *40*, 1176–1179. [CrossRef]
19. Park, J.; Kim, S.; Hong, J.; Lee, J. Rotor Design on Torque Ripple Reduction for a Synchronous Reluctance Motor with Concentrated Winding Using Response Surface Methodology. *IEEE Trans. Magn.* **2006**, *42*, 3479–3481. [CrossRef]
20. Fang, L.; Jung, J.-W.; Hong, J.-P.; Lee, J.-H. Study on High-Efficiency Performance in Interior Permanent-Magnet Synchronous Motor with Double-Layer PM Design. *IEEE Trans. Magn.* **2008**, *44*, 4393–4396. [CrossRef]
21. Si, J.; Zhao, S.; Feng, H.; Cao, R.; Hu, Y. Multi-objective optimization of surface-mounted and interior permanent magnet synchronous motor based on Taguchi method and response surface method. *Chin. J. Electr. Eng.* **2018**, *4*, 67–73. [CrossRef]
22. Im, Y.-H.; Hwang, S.-I.; Choi, J.-Y.; Jang, S.-M.; Choi, J.-H. Analysis of Torque Pulsation Considering Interior Permanent Magnet Rotor Rib Shape Using Response Surface Methodology. *IEEE Trans. Magn.* **2012**, *48*, 979–982. [CrossRef]
23. Kim, S.-I.; Hong, J.-P.; Kim, Y.-K.; Nam, H.; Cho, H.-I. Optimal design of slotless-type PMLSM considering multiple responses by response surface methodology. *IEEE Trans. Magn.* **2006**, *42*, 1219–1222. [CrossRef]
24. Lee, B.-H.; Hong, J.-P.; Lee, J.-H. Optimum Design Criteria for Maximum Torque and Efficiency of a Line-Start Permanent-Magnet Motor Using Response Surface Methodology and Finite Element Method. *IEEE Trans. Magn.* **2012**, *48*, 863–866. [CrossRef]
25. Koh, C.S.; Yoon, H.S.; Nam, K.W.; Choi, H.S. Magnetic pole shape optimization of permanent magnet motor for reduction of cogging torque. *IEEE Trans. Magn.* **1997**, *33*, 1822–1827. [CrossRef]
26. Islam, M.; Mir, S.; Sebastian, T. Issues in Reducing the Cogging Torque of Mass-Produced Permanent-Magnet Brushless DC Motor. *IEEE Trans. Ind. Appl.* **2004**, *40*, 813–820. [CrossRef]
27. Hendershot, J.R.; Miller, T.J.E. *Design of Brushless Permanent Magnet Machines*; Motor Design Books: Venice, FL, USA, 2010.
28. Hwang, S.-M.; Eom, J.-B.; Hwang, G.-B.; Jeong, W.-B.; Jung, Y.-H. Cogging torque and acoustic noise reduction in permanent magnet motors by teeth pairing. *IEEE Trans. Magn.* **2000**, *36*, 3144–3146. [CrossRef]

29. Zhu, Z.Q.; Howe, D. Influence of design parameters on cogging torque in permanent magnet machines. *IEEE Trans. Energy Convers.* **2000**, *15*, 407–412. [CrossRef]
30. Garroi, J.-J.; Goos, P.; Sörensen, K. A variable-neighbourhood search algorithm for finding optimal run orders in the presence of serial correlation. *J. Stat. Plan. Inference* **2009**, *139*, 30–44. [CrossRef]

# Comparative Design and Performance Analysis of 10 kW Rare-Earth and Non-Rare Earth Flux Reversal Wind Generators

**Manne Bharathi** [1,*], **Udochukwu Bola Akuru** [2,*] **and Malligunta Kiran Kumar** [1]

[1] Electrical and Electronic Engineering, Koneru Lakshmaiah Educational Foundation, Guntur 522502, India; mkkumar@kluniversity.in

[2] Department of Electrical Engineering, Tshwane University of Technology, Pretoria 0183, South Africa

\* Correspondence: bharathi.manne1994@gmail.com (M.B.); AkuruUB@tut.ac.za (U.B.A.); Tel.: +91-70-755-50797 (M.B.)

**Abstract:** Generators are a key technological element of the wind energy generation system. Currently, there is an increasing interest in adopting non-conventional stator-mounted permanent magnet generators, e.g., flux reversal generators (FRGs), which is a good alternative to conventional synchronous generators for medium-speed wind turbine generator applications. The usage of FRG with rare-earth (RE) permanent magnets (PMs) is increasing due to their high efficiency and high power density factors. However, RE PMs are unattractive to wind generators in terms of their cost and unpredictable market supply. In this paper, an attempt is made to study the potential of FRG with non-rare earths (ferrite PMs) for wind generators. The three-phase, 6/8 pole FRG is designed and compared with RE and NRE PMs for wind generator application at 375 r/min, 10 kW. Using 2D FEA, both the generators are compared in terms of their power generating performance with excellent overload capability. It shows that the average efficiency of the generators is approximately similar, but the torque density of NRE-FRG is only 51% that of RE-FRG. The NRE-FRG design is heavier, with the total active mass being 2.6 times higher than the RE-FRG, but with the estimated total active material cost of both generators almost the same. Moreover, the toque ripple for RE-FRG is 64% higher than for NRE-FRG. The demagnetization risk analysis was performed, and it is found that at higher temperatures, RE-FRG structures are prone to higher demagnetization risks, while it is much lower in NRE-FRGs. In summary, it is found that NRE-FRG is a suitable alternative to RE-FRG for medium-speed wind turbine generator applications in the 10-kW power range.

**Keywords:** finite element analysis (FEA); flux reversal generator (FRG); medium-speed; non-rare earth (NRE); permanent magnet (PM); rare earth (RE); wind turbine generator

## 1. Introduction

Generators are a key technological element of the wind energy generation system. Recently, there has been an increasing growth and prominence of wind energy generation development, which has dominated the overall renewable power generating capacity and is considered one of the fastest growing renewable energy sources with an installed capacity of 651 GW by the end of 2020 [1]. This encourages researchers' interest in designing and manufacturing wind generators for various power levels [2]. Wind energy generators acquire various types of AC generators, such as induction generators, permanent magnet synchronous generators (PMSG), and non-conventional stator PM generators. Permanent magnet synchronous generators (PMSG) with permanent magnets on the rotor are attractive for high power wind energy generation applications because of their high energy yield compared to other induction and electrical-electrical synchronous generators [3].

Stator-mounted PM machines have been recently experimented for wind generator applications [4,5]. With a simple and robust rotor, these machine variants provide ease of cooling since active parts are stator mounted, as well as reduced risk of demagnetization [6]. The flux reversal machine (FRM) is a typical non-conventional stator-mounted PM machine,

in which both PMs and armature windings are located on the stator, leaving the rotor simple and robust as it resembles that of the switched reluctance machine (SRM). Then, the PMs are mounted on the stator pole shoe of the FRM with potentials for high power density compared to similar PM machines [7–10].

The traditional design of FRM uses rare earth (RE) PM options such as Nd-Fe-B, N38SH, and Sm-Co. RE PMs are expensive and their supply uncertainty has forced researchers to find alternatives, e.g., non-rare earth (NRE) PMs. NRE-PMs are several times cheaper, and the resources and extraction are more mature across various countries of the world compared to RE, but they carry greater demagnetization risks due to lower coercive force [11]. Nevertheless, FRG is shown to possess unique characteristics that reduce the demagnetization risks at rated load conditions [12].

Numerous FRG structures have been proposed in the past few years for wind/generator applications. For the first time, the single phase 2/3 pole FRG with Sm-Co magnet structure was proposed as a high-speed claw-pole alternator in 1997 [13]. Then, the direct and quantitative performance comparisons are made with other competing brushless generators by using the flux-mmf diagram technique, which is superior to the generalized generator modeling techniques in this class. It was shown under experimentation that FRG possesses a unique flux nature and small inductance variation with rotor position. Based on the structure best suitable for high-speed and high-power applications, this is the most competitive among other brushless generators.

In [14], the study considered the comparison of PM FRGs based on commonly used concentrated winding as against distributed winding; the superiority of later in terms of voltage quality, with smoother and much lower total harmonic distortion, was clearly emphasized. It must be said that the PM material used for the study in [14] is based on RE technology. In [15], the simple and rugged construction of FRGs, with high power density and fault-tolerant capability, was exploited for roof-top wind and aircraft generators. To this end, a novel ring outer rotor FRG with the inner bridge is proposed to improve the power factor, voltage regulation, and flux leakages inherent in FRGs. It was conclusively shown that the inner bridge PM ring FRG, improves the average air-gap flux density and reduces cogging torque while reducing flux leakage and thereby improving the power factor compared to conventional 6/14 pole outer rotor topology.

In [16], it was explained that the high specific torque characteristics and simple rotor topology of a 2.4 kW three-phase 6/14 pole 214 r/min FRG make it suitable for low-speed direct-drive wind power generation systems, no thanks to their high number of poles. The study also compared the outer and inner rotor configurations, showing that the outer rotor FRG exhibit a higher power density of up to 1.25 times that of the inner rotor variant.

In [17], a soft magnetic composite (SMC) core material FRG is designed for gearless wind generator mode at 0.6 kW and 650 r/min. The SMC core is still RE-based, only that it is cheaper and can be easily magnetized and demagnetized. The findings from the study revealed that the active mass of the SMC FRM is reduced by 21% compared to the one whose rotor is purely contrived by steel laminations. The efficiency of the former is also improved by 7% due to reduction of the rotor losses. In [18], a novel 4-phase FRG with DC electromagnet excitation is proposed for wind power generation. When compared with a corresponding PM FRG design, the overarching advantages are that the DC design can vary its airgap flux density under varying wind resource conditions and is cheaper.

The research trend in FRG design and applications clearly shows that NRE materials are emerging. Such studies abound in other stator-mounted brushless machines [19,20]. Based on this research, ferrites (NRE) materials are appearing as suitable replacements for RE-type machines. To this end, the main motivation of this study is to expose the potential of NRE over RE PM material in FRG for geared medium-speed wind power generator applications. This is ideal for wind turbine generator designs because, just as other ferrite electrical generators, it reduces overall generator costs while also allowing easily accessible ferrite raw materials to be used for the machine's excitation system. Furthermore, the existing literature has not highlighted the design of NRE FRG using ferrite PMs, indicating

a need to investigate the performance comparison of NRE versus RE FRGs. The selection of the medium-speed range is thanks to its competitive generator performance to cost index compared to geared high-speed and gearless systems [19].

In this study, a three-phase, 6/8 pole FRG designed with RE and ferrites PM, with similar parameters and characterization for a 10-kW power scale, is investigated using finite element analysis (FEA). The proposed 10 kW power range being investigated is clearly a niche power level of lower power limit small wind turbines, the so-called micro wind power generation units [2,21,22]. Further, both machines, NRE and RE FRGs, are compared in terms of their electromagnetic operating performance such as output voltage, torque density, power factor, torque ripple, as well as efficiency at either no-load or rated conditions. Thereafter, mass and cost estimates, as well as demagnetization risk analysis of the associated PM FRG variants are studied and compared in FEA for medium-speed wind power generation.

## 2. Design Sizing and Analytical Formulation

The design of an electrical generator procedure is different from that of a motor. In the case of generator operating conditions, characterized by varying the external load, whereas in motor design, a predefined maximum torque point ($I_d = 0$) under AC brushless operation. Then the generator is not practicable for designing under an AC brushless operating mode, much like a motor action. Therefore, the generator performance is characterized using the co-simulation method, connecting the generator with an external load. In this regard, the generator with rare earth and ferrites PMs is designed under the same specifications with a rated output power of 10 kW and at a rated speed of 375 r/min. FRGs are modeled in direct and quadrature (dq) axis references to proclaim the steady-state. dq equations are used to analyze both the generators' performances. Both generators' power generating capabilities are thoroughly investigated in terms of power and torque density, overload capability, cogging torque, torque ripple, efficiency, and power factor.

### 2.1. Basic Structure and FEA Model Formulation

The three-phase 6/8 pole stator-slot ($N_s$)/rotor-pole ($N_r$) combinations achieve symmetrical phase back electromotive force (EMF) with higher torque density. A reduced number of stator-slot/rotor pole numbers is preferred for reduced iron losses and manufacturing difficulty, whereas a lower number of poles causes a reduction in the amplitude of back-EMF [23]. Considering all the limitations, a compromise between high back EMF and standard (50 Hz) frequency operation, a 6/8 FRG structure is chosen. Based on the generator rated speed (n) and rotor poles ($N_r$), open circuit EMF frequency ($f_e$) and the flux pattern speed in terms of supply frequency ($n_f$) as expressed by

$$f_e = \frac{n * N_r}{60} \tag{1}$$

$$n_f = 60 * f_e \tag{2}$$

The two-pole pitch span angle ($\tau$) resembles two PMs poles of oppositive polarities placed on the stator poles expressed as

$$2\tau_{PM} = \frac{\pi D_r}{N_r} \tag{3}$$

The main design specifications of RE-FRG and NRE-FRG with the same power level are given in Table 1. The sizing equation used to model the FRG [24] is given as

$$D_r = \sqrt[3]{\frac{2P_b}{\pi f_t \lambda \omega_r J \eta}} \tag{4}$$

$P_b$ = rated power, $f_t$ = tangential force density (2.1 N/cm$^2$), $\lambda$ is the ratio of stack length to rotor diameter ($D_r$); $\omega_r$ = rotor speed (rad/s); J = current density and $\eta$ = machine efficiency. The medium value of $\lambda$ is 1.2, justified for 6 stator slots [10].

**Table 1.** Design specifications/dimensions of RE-FRG and NRE-FRG.

| Parameter/Dimension | RE-FRG | NRE-FRG |
|---|---|---|
| Stator outer diameter ($D_{out}$), mm | 253 | 272 |
| Number turns per coil ($N_t$) | 80 | 80 |
| Stack length ($l_{stack}$), mm | 165 | 280 |
| Airgap (g), mm | 0.5 | 0.5 |
| Magnet thickness ($h_{pm}$), mm | 4 | 8 |
| Outer rotor diameter ($D_r$), mm | 156 | 165 |
| Rotor pole span angle ($\alpha = \beta$), deg | 22.5 | 22.5 |
| Rotor pole height ($h_{pr}$), mm | 44 | 52 |
| Stator pole width ($w_{ts}$), mm | 57 | 71 |
| Slot opening width ($l_{wi}$), mm | 70 | 92 |
| Stator back iron thickness ($B_{cs}$), mm | 11 | 24 |
| Shaft diameter ($D_{sh}$), mm | 46 | 46 |
| Current density (J), (A/mm$^2$) | 5 | 5 |
| Rated speed ($\omega_r$), (r/min) | 375 | 375 |
| Fill factor ($k_{fill}$) | 0.4 | 0.4 |
| Rated frequency ($f_e$), (Hz) | 50 | 50 |

In the FRG, energy conversion occurs by virtue of the interaction between the stator coil MMF and PM fields. $N_s/3$ is the number of stator poles per phase with coils in series, while the induced EMF per phase ($E_m$) and electromagnetic torque ($T_e$) are given as [24]

$$E_m = \frac{N_s}{3}.\frac{n_p}{2}.N_t.2\pi\omega_r.l_{stack}.\pi D_r.K_{fringe}.B_{PMi} \tag{5}$$

$$T_e = \frac{3E_m I_{rms}}{\sqrt{2}\,(2\pi n)} \tag{6}$$

where $N_s$ is number of stator slots, $n_p$ is number of PM pole pairs, $N_t$ is the number of turns per coil, $l_{stack}$ is stack length, $K_{fringe}$ is flux fringing factor, $B_{PMi}$ is airgap flux density and $I_{rms}$ is RMS value of the current.

The sub-optimal major design dimensions of FRG such as pole width ($w_{ts}$), pole height ($h_{ps}$), slot opening ($l_{wi}$), and stator outer diameter ($D_{out}$) are expressed as

$$w_{ts} = \frac{\lambda_{pmmax}}{B_{ps}l_{stack}} \tag{7}$$

$$h_{ps} = \frac{2N_t I_{rms}}{JK_{fill}l_{wi}} \tag{8}$$

$$l_{wi} = \frac{2\pi D_r}{N_r} - w_{ts} \tag{9}$$

$$D_{out} = D_r + 2h_m + 2h_{sa} + 2h_{ps} + 2B_{cs} \tag{10}$$

where $\lambda_{pmmax}$ is maximum flux per pole of the 6/8 pole FRG structure having 8 rotor poles and 8 interpoles; $B_{ps}$ is stator pole flux density, $h_m$ is PM thickness, $h_{sa}$ is stator pole shoe height, $h_{ps}$ is stator pole height, and $B_{cs}$ is stator back iron thickness. The conceived FRG design specifications and parameters are listed in Table 1, while the basic structural view of a 3-phase, 6/8 pole FRG and dimensions are shown in Figure 1. The angles subtended by the rotor pole ($\alpha$) and interpoles ($\beta$) are $\pi/8$ [23]. The interpole space is rounded off to reduce fringing near rotor back iron. In the general basic design of permanent magnet flux reversal machines, $B_{cs}$ and rotor back iron thickness ($B_{cr}$) are assumed to be equal [24]. To improve the torque density and reduce the cogging torque effects in the air gap, a pseudo-

optimum parametric variation of design dimensions is undertaken in FEA. Based on the design structure of RE-FRG, the NRE-FRG is designed by increasing the cross-section of the machine and stack length to get 10 kW power range. This slightly increases the size, losses, and active material mass of the NRE-FRG of machine, while maintaining other parameters to be the same as the RE-FRG.
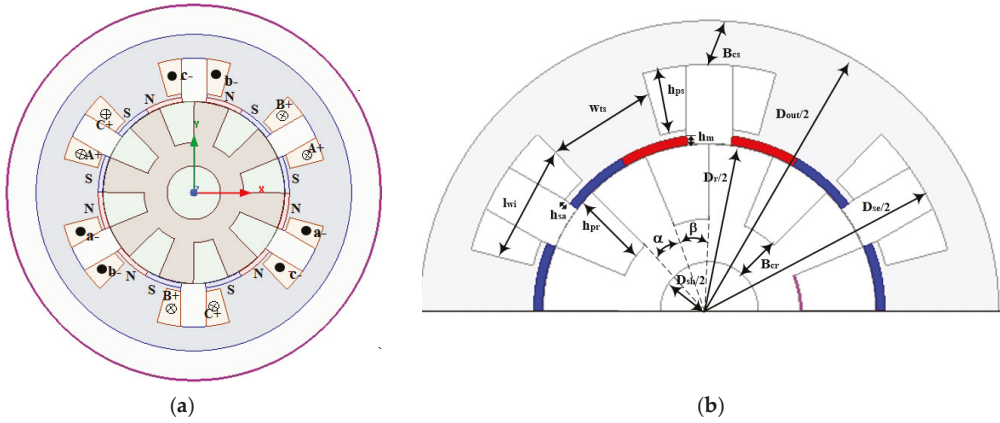


**Figure 1.** FRG concepts of 3-phase 6/8 pole FRG: (**a**) structural view, and (**b**) generic dimensions.

### 2.2. DQ-Axes Modelling

The 3-phase 6/8 FRG structure is transformed into traditional dq axes reference frames that are revolving at rotor speed. The static and steady-state behavior of the FRG is investigated using dq equivalent circuits and phasor diagrams, as shown in in Figure 2. In the case of FRG, rotor speed, and flux pattern speeds are different, not as in traditional synchronous machines, so that the rotor speed is $N_r$ times less than the flux pattern speed from (1) and (2). The variation in these speeds is represented by k. It is the ratio of rotor speed to the flux pattern speed. The generalized equation of k is as follows:

$$k = \frac{N_r}{(P_{eq}/2)} \tag{11}$$

where $P_{eq}$ is the number of effective flux pattern poles. With 6/8 pole FRG structure, k value is 8. Stator voltage and flux linkage equations under dq reference frames with positive current flowing out are expressed as

$$V_d = -R_s I_d + \omega_r L_q I_q \tag{12}$$

$$V_q = -R_s I_q - \omega_r L_d I_d + \omega_r \lambda_m \tag{13}$$

$$\lambda_q = L_q I_q \tag{14}$$

$$\lambda_d = L_d I_d + \lambda_m \tag{15}$$

where $\lambda_m$ mutual flux linkage due to PMs, $V_d$, $V_q$, $I_d$, $I_q$, $L_d$, $L_q$, $\lambda_d$, and $\lambda_q$ are the dq axis voltage, currents, inductances, and flux linkages, respectively.

The electromagnetic torque ($T_e$) in terms of dq reference frame is expressed as

$$T_e = \frac{3}{2} * \frac{P_{eq}}{2} * k\left(\lambda_m I_q + I_d I_q \left(L_q - L_d\right)\right) \tag{16}$$
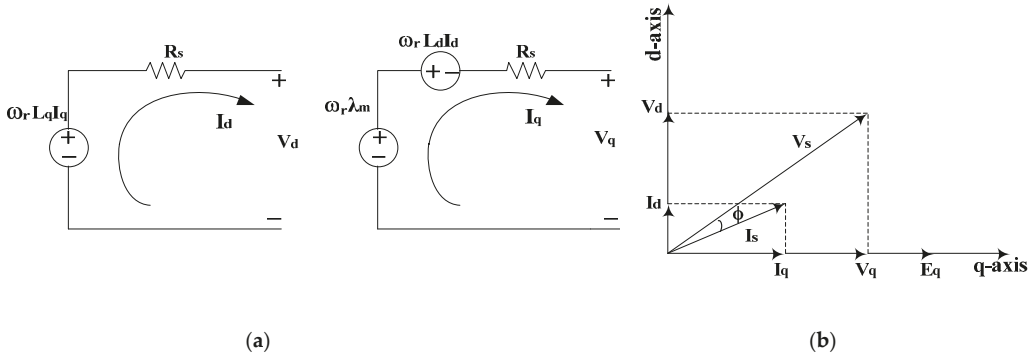
**Figure 2.** Dq modeling of FRG: (**a**) equivalent circuit, and (**b**) phasor diagram.

The stator phase winding resistance is evaluated according to machine slot phase winding information expressed as [25]

$$R_s = \frac{4\rho_{cu}N_t^2\left(l_{stack} + l_{end}\right)}{A_{coil}} \tag{17}$$

where $\rho_{cu}$ is the resistivity of the copper material at room temperature, $A_{coil}$ is the area of the coil per phase, $l_{end} = (w_{ts} + l_{wi})$ is end winding length of the machine.

The winding copper losses of the generator at the rated condition and the core losses of the machine are estimated through FEA from the Steinmetz empirical equation as

$$P_{cu} = \frac{3}{2}\left(I_d^2 + I_q^2\right) * R_s \tag{18}$$

$$P_{core} = K_e f^a B_i^b G \tag{19}$$

where $K_e$ is Steinmetz material coefficient, a is the exponent of machine electrical frequency, b is the exponent of peak airgap flux density, and G is the mass of the laminated material.

The output power ($P_o$), efficiency ($\eta$), power factor (PF), and torque density ($T_d$) of the FRGs, while ignoring friction and windage losses are expressed as

$$P_o = 1.5 * \left(V_q I_q + V_d I_d\right) \tag{20}$$

$$\eta = \left(\frac{P_o}{P_o + P_{core} + P_{cu}}\right) * 100\% \tag{21}$$

$$PF = \frac{\left(V_q I_q + V_d I_d\right)}{\left(\left(\sqrt{V_q^2 + V_d^2}\right) * \left(\sqrt{I_q^2 + I_d^2}\right)\right)} \tag{22}$$

$$T_d = \frac{4T_{avg}}{\pi D_{out}^2 l_{stk}} \tag{23}$$

The torque ripple factor at load condition is expressed as

$$K_{rp} = \left(\frac{T_{max} - T_{min}}{T_{avg}}\right) * 100\% \tag{24}$$

where $T_{avg}$ is average load torque, $T_{max}$, $T_{min}$ is maximum and minimum instantaneous torque values at load condition.

The mass (M) of various parts of the generators are estimated by

$$M = \left( \int \int_o^{l_{stack}} A \, dz \right) D \tag{25}$$

where A is the surface area the object, D is the density of the material.

The temperature dependence of demagnetization coefficients is modeled by

$$B_{ri}(T) = B_{r,20°C} \left( 1 + C_1 \left( T - 20^0 \right) \right) \tag{26}$$

$$H_{cj}(T) = H_{c,20°C} \left( 1 + C_2 \left( T - 20^0 \right) \right) \tag{27}$$

where $B_{ri}$ and $H_{cj}$ are induction and coercive forces, $C_1$ and $C_2$ are the temperature coefficients of $B_{ri}$ and $H_{cj}$, respectively, and T is the temperature on the object.

### 3. Generators Performance Evaluation

Many researchers have studied and developed various FRG structures for wind generator applications. Most of the designs are low power scale with RE type FRG structures [15–18]. Here, in this study, a 6/8 pole, 10 kW RE-FRG, and NRE-FRG are designed and implemented in 2D FEA ANSYS Maxwell for medium-speed wind turbine generators. Both the generators are designed with a rated speed of 375 r/min and have similar dimensional parameters. The power density, torque density, efficiency, and power factor of the generators are analyzed and compared, mostly in dq reference frame. Therefore, in this study, the analysis part is divided into four subsections, where in the first sub-section, transient no-load analysis is carried out to study the flux linkages, induced voltages, and cogging torques for both the machines. Thereafter, in the second sub-section, on-load transient analysis is conducted to further study the electromagnetic performances of both machines. In the third sub-section, a comparative analysis of mass and cost estimation of both machines is undertaken. Finally, in the fourth sub-section, the investigation and comparison of the demagnetization risks are undertaken by setting the temperatures under rated load conditions for both the generators, while the flux density variations under different temperatures are observed.

### 3.1. No-Load Analysis

In this section, the RE-FRG and NRE-FRG machines are under open-circuit conditions based on 2D FEA. Under no-load conditions, phase flux linkages, back EMF, and cogging torque are obtained. In static analysis, when no-load is applied to the armature winding, the EMF induced at the open winding terminals are compared in both machines. From Figures 3 and 4, the open circuit analysis reveals that the phase flux linkages and fundamental EMF magnitude of the NRE-FRG structure are lower than for the RE-FRG because the remanence flux density and coercive forces of the ferrite PMs are much lower.

Under no-load, both machines exhibit cogging torque, which results in acoustic noise and vibration. The peak-to-peak cogging torque is thus evaluated for both the generators. From Figure 5, it is revealed that the peak-to-peak cogging torque of RE-FRG is twice that of the NRE-FRG because it has higher coercive force, reducing the cogging torque of RE-FRG [26,27]. The cogging torque characteristics should invariably impact the pulsation in the instantaneous torque.
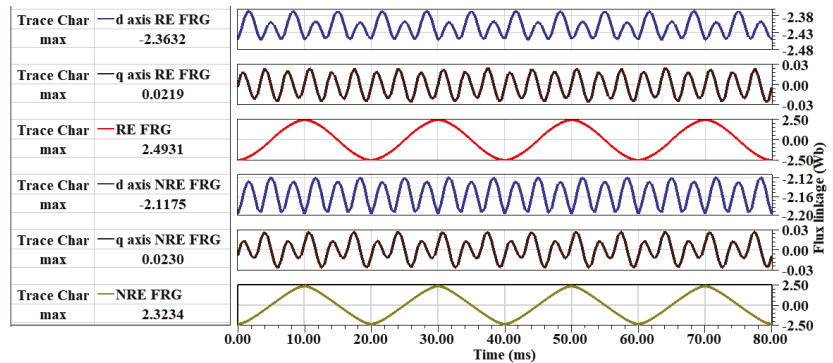
**Figure 3.** No-load dq- and phase flux linkage waveforms.
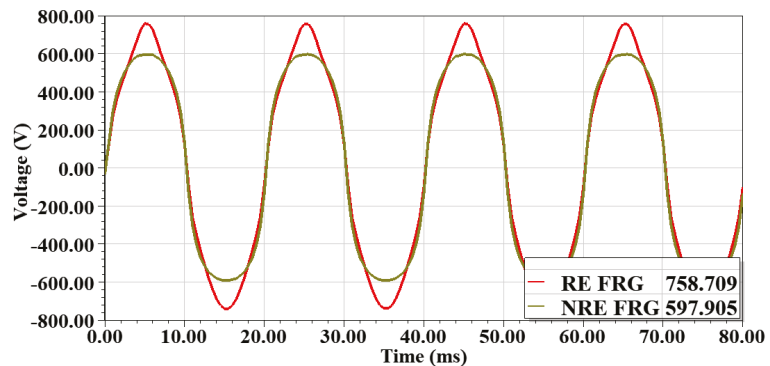


**Figure 4.** No-load voltage comparison at 375 r/min.
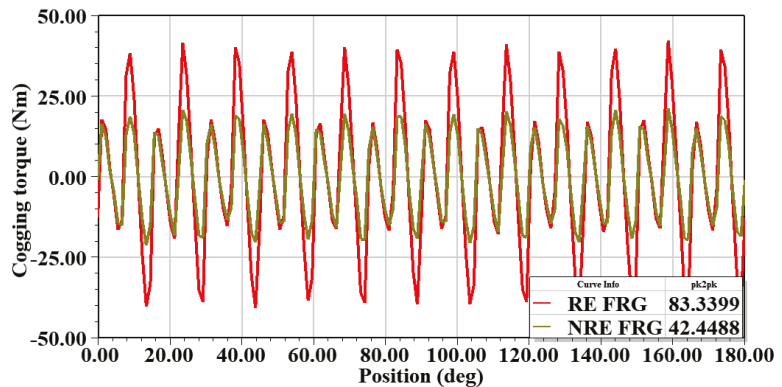


**Figure 5.** Cogging torque comparison under no-load.

*3.2. On-Load Analysis*

On-load power generating performances include torque ripple, efficiency, losses, power factor, and power density of the RE-FRG and NRE-FRG. In the first case, both generators are operated at 375 rpm under varying load current in 2D FEA, while in the second case, the load current is fixed at rated while generator speed is varied. Hence, based on the rated voltage of each phase, rated power, and impedance triangle, the calculated

rated load is 63 + j34 Ω. Figure 6 shows the flux density plot of RE-FRG and NRE-FRG under rated load conditions. The generator load profile is demonstrated by varying the phase current against the real output power for both the generators, analyzed up to 2.5 times the rated load as presented in Figure 7a. In all cases under load analysis, the wind generators are pushed up to 250% of their rated load to exhibit their overload profile. In Figure 7b, the output is now compared at varying generator speeds. The active power of RE-FRG is somewhat higher than that of NRE-FRG for a wide range operating point, with a linear profile conceived up to 2.5 pu in Figure 7a, demonstrating that both generators are designed with excellent overload capability. Overall, the performance comparison analysis of RE-FRG and NRE-FRG under 2D FEA is summarized in Table 2.

**Table 2.** Performance comparison of 10 kW RE-FRG and NRE-FRG based on 2D FEA.

| Parameter | RE-FRG | NRE-FRG |
|---|---|---|
| Output real electrical power at rated load condition (W) | 9840.9 | 9806.3 |
| Input electromechanical power at rated condition (W) (375 r/min, torque 268.4 Nm) | 10,542 | 10,558 |
| Required AC-DC converter power VA | 11,277 | 12,256 |
| Torque ripple under half-rated load, % | 7.26 | 4.19 |
| Torque ripple under rated load, % | 12.46 | 4.4 |
| Torque ripple, % | 9.86 | 4.29 |
| Efficiency at normal load (0.5 times of rated load), % | 91.9 | 92 |
| Efficiency at rated load, % | 93.4 | 92.9 |
| Average efficiency, % | 92.7 | 92.4 |
| Total losses at rated load, W | 701.4 | 753.8 |
| Power factor | 0.87 | 0.81 |
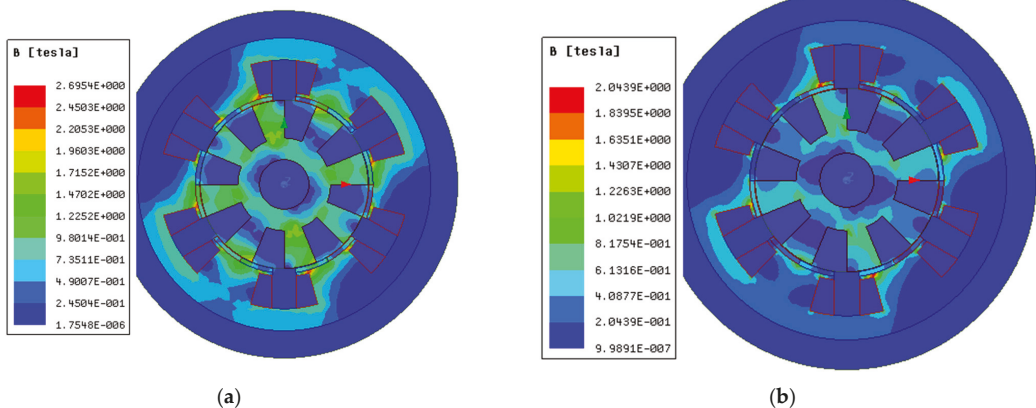


**Figure 6.** Rated load flux density plot of 10 kW FRGs: (**a**) RE-FRG and (**b**) NRE-FRG.

The phase currents versus efficiency variation of RE-FRG and NRE-FRG are presented in Figure 8a, while the generator speed is varied with efficiency in Figure 8b. The efficiency of RE-FRG is seen to be generally higher in both figures. The losses in the generators considered are stator core loss and winding loss (of armature winding) excluding windage loss and fiction losses (mechanical losses). Total losses of NRE-FRG are higher than RE-FRG by 7% at rated condition due to increased copper losses. Electromechanical power versus total loss variations are investigated in Figure 9. Torque ripple at rated load of both generators is analyzed and evaluated based on (24) and is shown in Figure 10; it is discovered that RE-FRG has 64.7% higher torque ripple compared to NRE-FRG. The power factor load curve is demonstrated in Figure 11a by varying the phase current against power factor for both the generators up to 2.5 times of rated load, while the generator speed is

varied against power factor in Figure 11b. The full load power factor of NRE-FRG and RE-FRG are evaluated as 0.81 and 0.87, respectively. The RE-FRG always exhibit superior power factor quality compared to the NRE-FRG in both figures, indicating higher cost premium on power electronic converter costs for the latter.

### 3.3. Mass and Cost Estimation

Mass and cost estimation are two key parameters for wind generators. The mass calculation of each active material used for the generator can be evaluated using field calculus as in (25). An estimation of the surface area of each object, such as rotors, stators, magnets, etc., is undertaken for both machines. Thereafter, it is multiplied with axial length ($l_{stk}$) and respective material mass density of each object, as well as evaluation of mass of the required material stated in Equation (26). Finally, the total cost is estimated by multiplying the weight by its corresponding material unit rate. From an economic standpoint, the total PM cost of ferrites is approximately seven times lower than rare earth, based on quotations in Table 3 [28]. At a closer look, it is observed that NRE-FRG requires at least two times the total active mass and 2.7 times (ferrite PM thickness is a little bit high) of the PM mass of RE-FRG in Table 4. Because of the higher market price of RE PMs, the cost of NRE-FRG is almost the same as that of RE-FRG. Based on (23), the torque density of the RE-FRG design is seen to be 1.96 times higher than NRE-FRG as indicated in Table 4.



(a)



(b)
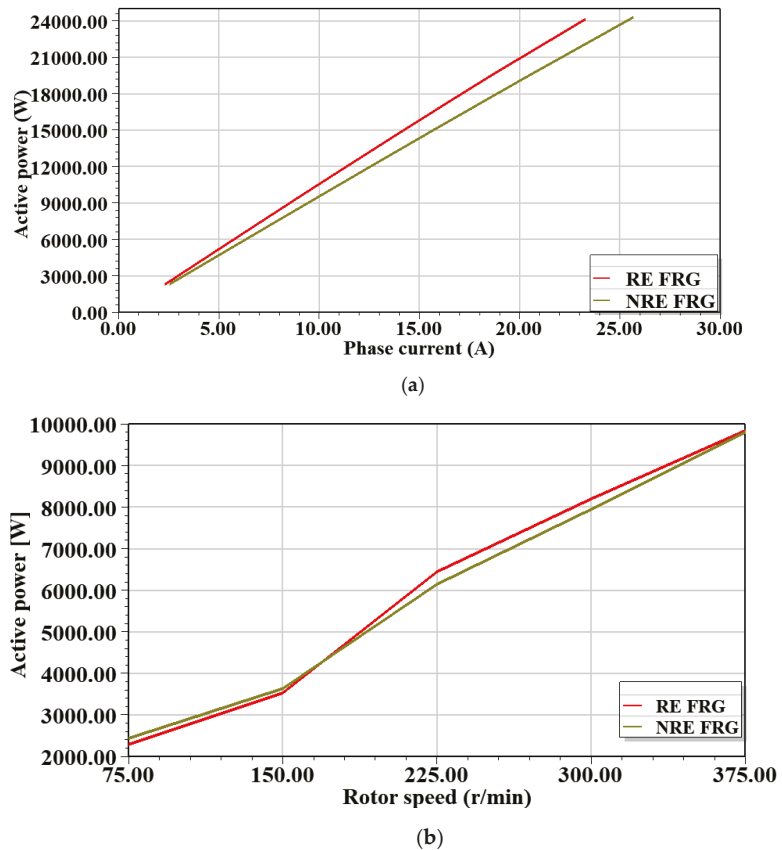
**Figure 7.** (**a**) On-load phase current vs. active power at 375 r/min; (**b**) generator speed vs. active power at rated load current.
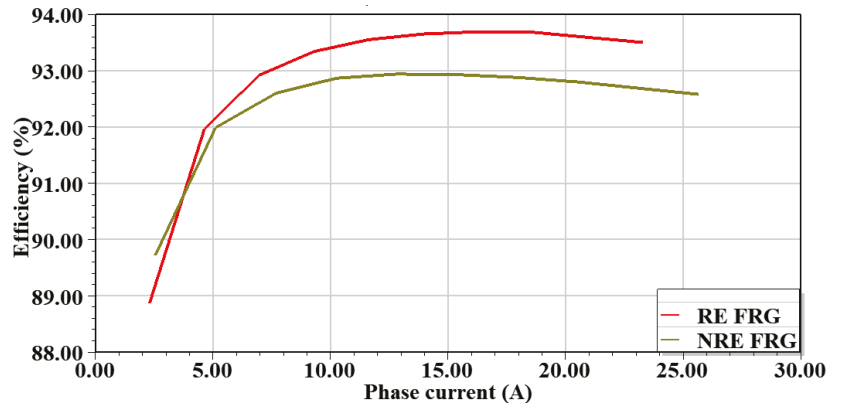
(**a**)
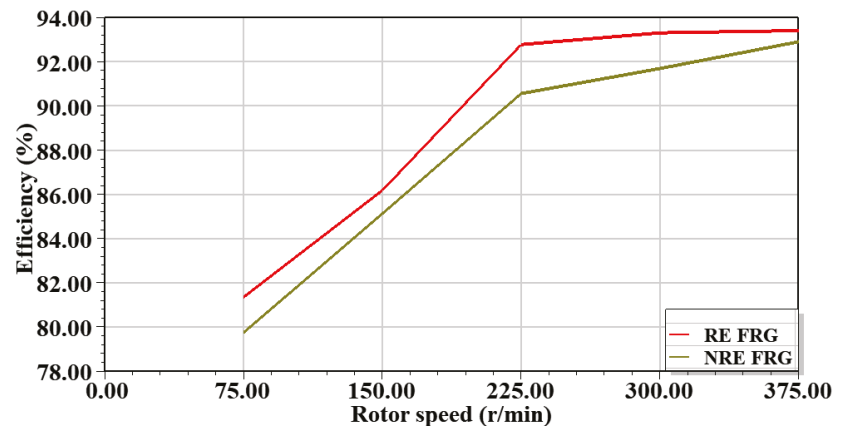


(**b**)

**Figure 8.** (**a**) On-load phase current vs. efficiency at 375 r/min; (**b**) generator speed vs. efficiency at rated load current.
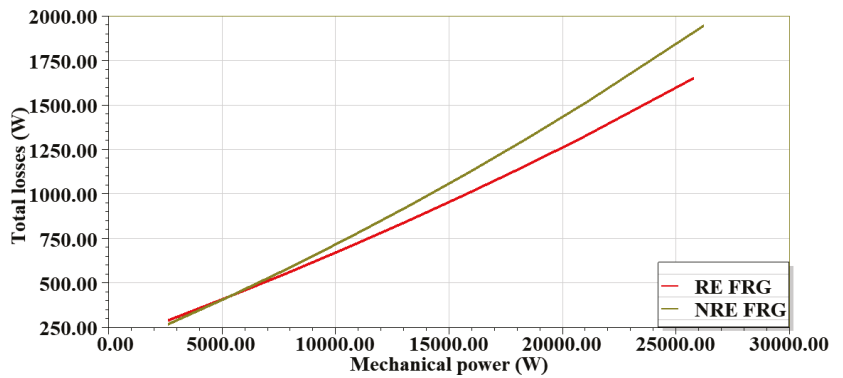


**Figure 9.** Input mechanical power against total losses comparison at 375 r/min.
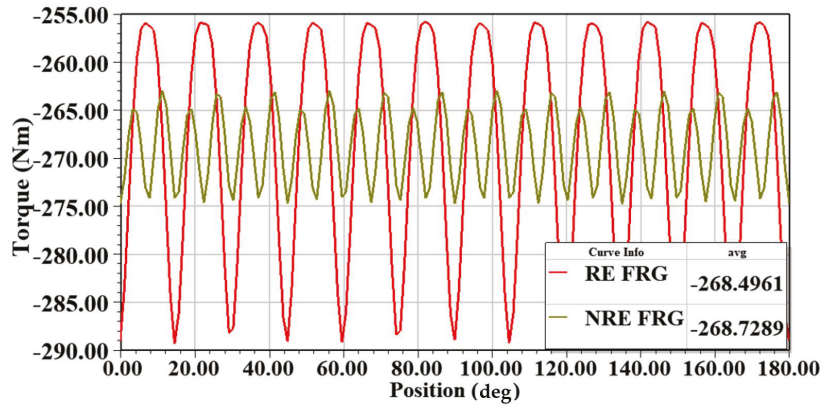
**Figure 10.** Comparison of torque ripple effect under load.
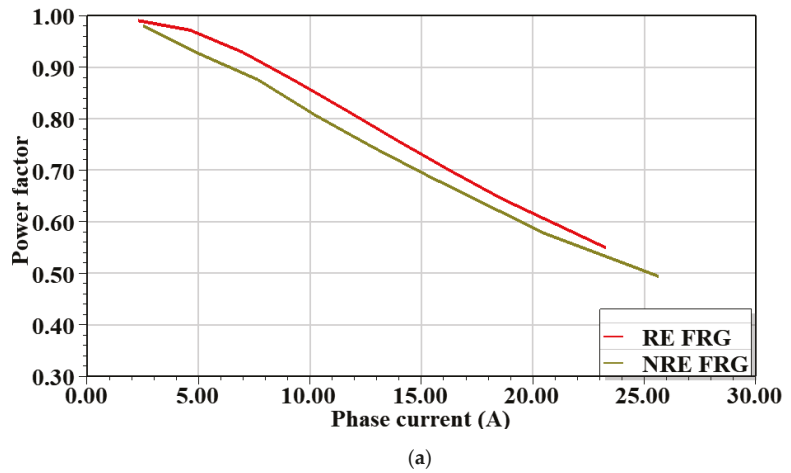


(**a**)
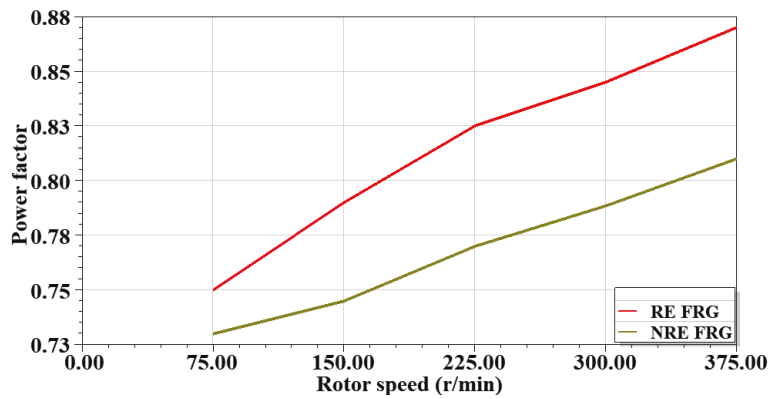


(**b**)

**Figure 11.** (**a**) Comparison of phase current against power factor; (**b**) generator speed against power factor at rated load current.

**Table 3.** Unit prices of active materials of RE-FRG and NRE-FRG [28].

|  | Cost (USD/kg) |
|---|---|
| Steel laminations | 1 |
| Copper | 7 |
| Sr-Fe (Ferrites) | 18.46 |
| Nd-Fe35 (Rare earths) | 126.6 |

**Table 4.** Mass/cost analysis.

| Parameter | RE-FRG | NRE-FRG |
|---|---|---|
| Mass of the stator core, kg | 58.16 | 160.9 |
| Mass of the rotor core, kg | 23.82 | 59.89 |
| Mass of the magnets, kg | 3.12 | 8.47 |
| Mass of the copper, kg | 14.6 | 29.77 |
| Mass of the total machine, kg | 99.7 | 259.01 |
| Torque density (kNm/m$^3$) | 32.356 | 16.515 |
| Torque/PM mass (Nm/kg) | 86.1 | 31.727 |
| Torque/Active mass (Nm/kg) | 2.693 | 1.04 |
| Active material cost, $ | 579.2 | 585.5 |

*3.4. Demagnetization Risks*

Demagnetization can weaken the magnetic properties of the magnet at high temperatures and lead to a reduction in the performance of the generator. A general characteristic of PM and their demagnetization susceptibility is that they are inversely related to the absolute temperature or extreme currents in the winding. The coercivity ($H_c$) of typical (rare earth) PMs is generally negative temperature coefficients, but this generalization does not apply to ferrites PMs due to their positive temperature coefficients [29].

In the PMs, the minimum radial flux density position is to be considered as a demagnetization point for a given FEA solution for both the generators. Investigating the RE-FRG and NRE-FRG designs, the demagnetization withstand capability to appraise the impact of temperature rise on the remanence of the PM materials is undertaken by using 2D FEA, in ANSYS Maxwell. Here, the RE-FRG design, Nd-Fe-B type PMs are employed, which is under the grade of N35SH, and its remanence flux density is 1.2T. Demagnetization occurs below 0.25 T. Then, for NRE-FRG, Sr-Fe type PMs are used, with a grade of Y32, and the remanence flux density is 0.4 T, then the demagnetization knee point occurs below 0.1 T [30,31]. In this sub-section, an investigation on the demagnetizing risks is done by varying from minimum room temperature (20 °C) to a high temperature (120 °C) and then analyzing the corresponding impact on radial PM flux density ($B_{ri}$) and power factor. Temperature coefficients, residual induction ($C_1$), and residual coercive force ($C_2$) are taken from respected grades of PMs used for RE-FRG and NRE-FRG designs as indicated in Table 5 based on (26) and (27).

The radial flux density of PMs is examined for RE-FRG when it becomes lower than 0.25 T ($B_{ri} > 0.25$) and for NRE-FRG when it becomes lower than 0.1 T ($B_{ri} > 0.1$), both at a maximum temperature of 120 °C. Figure 12, based on the evaluated profile, shows the RE-FRG is unable to satisfy the safety limits at the temperatures above 60 °C. However, for NRE-FRG, it satisfies its demagnetization safety limits and the performance is good at above room temperature. PMs demagnetization points at 20 °C and 120 °C for both RE-FRG and NRE-FRG with their power factor values are depicted in Figures 13 and 14, respectively. Overall, it can be said that the NRE-FRG design structure performance is better at high temperatures than with RE-FRG for 10 kW, which translates to minimum demagnetization risks for the former. Hence, deep demagnetization risk occurs for the RE-FRG above 60 °C with the power factor worsening at 120 °C.

**Table 5.** Material specifications.

| | Rare Earth | Ferrites |
|---|---|---|
| Grade | N35SH | Y32 |
| Relative permeability ($\mu_r$) | 1.09 | 1.09 |
| Remanent flux density ($B_r$), T | 1.2 | 0.4 |
| Coercive force ($H_C$) kA/m; | 900 | 300 |
| Mass density D, kg/m$^3$ | 7500 | 5000 |
| Temperature coefficients ($C_1$), %/°C | −0.12 | −0.2 |
| Temperature coefficients ($C_2$), %/°C | −0.55 | 0.40 |
| Laminations | Electrical steel: steel_1008 | Electrical steel: steel_1008 |
| Stator windings | Copper: $\rho_{cu} = 2.1 \times 10^{-8}$ Ωm | Copper: $\rho_{cu} = 2.1 \times 10^{-8}$ Ωm |
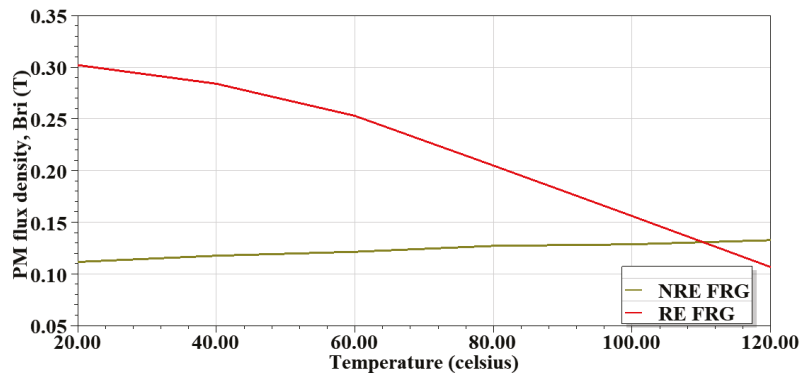


**Figure 12.** Average PM flux density under various temperatures.



(**a**)　　　　　　　(**b**)
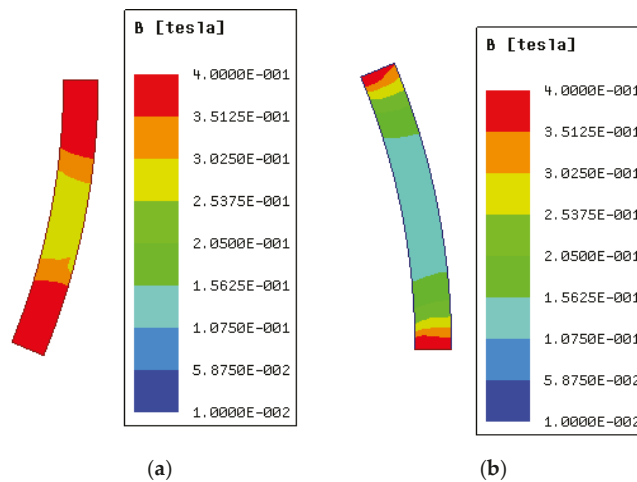
**Figure 13.** Demagnetization indicated by flux densities of RE-FRG structure when the temperature variation: (**a**) at 20 °C, PF = 0.89; (**b**) at 120 °C, PF = 0.59.
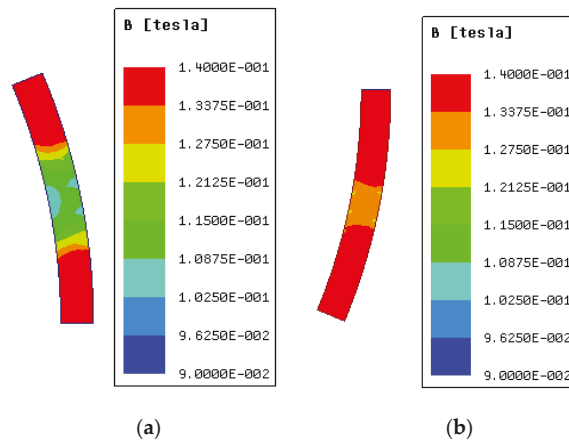
**Figure 14.** Demagnetization indicated by flux densities of NRE-FRG structure when the temperature variation: (**a**) at 20 °C, PF = 0.76; (**b**) at 120 °C, PF = 0.843.

## 4. Conclusions

In this paper, two three-phase, 6/8 pole FRG structures (designed with rare earth and ferrite PMs) were analyzed and compared in 2D FEA for wind turbine generator applications, at 375 r/min and 10 kW power levels. Detailed analyses are performed under no-load and on-load power generating performances. Based on the similar performance requirements, the average efficiencies of both the machines are approximately similar, with excellent overload capability. The average torque ripple for RE-FRG under load is 64.7% higher compared to the NRE-FRG. However, the torque density of the NRE-FRG is only about 51% that of the RE-FRG, at approximately the same cost since the former is 2.6 times heavier. It is also found that for the RE-FRG design, a higher demagnetization risk occurs at higher temperatures, thereby reducing the power factor values and lowering the performance of the generator. Unlike RE-FRG, the NRE-FRG design has a lower demagnetization risk while operating at higher temperatures. Overall, the NRE-FRG structure is shown as an attractive alternative to the RE-FRG for micro kW medium-speed wind turbine generator applications.

**Author Contributions:** Conceptualization, U.B.A. and M.B.; methodology, M.B. and U.B.A.; software, M.B.; validation, M.B. and U.B.A.; formal analysis, M.B. and U.B.A.; investigation, M.B.; resources, M.K.K.; data curation, M.B.; writing—original draft preparation, M.B. and U.B.A.; writing—review and editing, M.B., U.B.A. and M.K.K.; visualization, M.B.; supervision, U.B.A. and M.K.K.; project administration, M.B. and M.K.K.; funding acquisition, U.B.A. All authors have read and agreed to the published version of the manuscript.

## References

1. REN 21. Renewables 2020 Global Status Report (Paris: REN21 Secretariat). Available online: http://www.ren21.net/gsr (accessed on 10 October 2020).
2. Potgieter, J.H.J.; Kamper, M.J. Double PM-Rotor, Toothed, Toroidal-Winding Wind Generator: A Comparison with Conventional Winding Direct-Drive PM Wind Generators Over a Wide Power Range. *IEEE Trans. Ind. Appl.* **2016**, *52*, 2881–2891. [CrossRef]

3.  Polinder, H.; van der Pijl, F.F.A.; de Vilder, G.J.; Tavner, P. Comparison of direct-drive and geared generator concepts for wind turbines. *IEEE Trans. Energy Convers.* **2006**, *21*, 725–733. [CrossRef]
4.  Ojeda, J.; Simoes, M.G.; Li, G.; Gabsi, M. Design of a flux-switching electrical generator for wind turbine systems. *IEEE Trans. Ind. Appl.* **2012**, *48*, 1808–1816. [CrossRef]
5.  Akuru, U.B.; Kamper, M.J. Optimisation and Design Comparison of 10 kW and 3 MW PM Flux Switching Machines for Geared Medium-Speed Wind Power Generators. *Electr. Eng.* **2018**, *100*, 2509–2525. [CrossRef]
6.  Shao, L.; Hua, W.; Soulard, J.; Zhu, Z.; Wu, Z.; Cheng, M. Electromagnetic Performance Comparison Between 12-Phase Switched Flux and Surface-Mounted PM Machines for Direct-Drive Wind Power Generation. *IEEE Trans. Ind. Appl.* **2020**, *56*, 1408–1422. [CrossRef]
7.  Zhao, Y.; Kou, B.; Zhao, X. A Study of Torque Characteristics of a Novel Flux Reversal Machine. In Proceedings of the 22nd International Conference on Electrical Machines and Systems (ICEMS), Harbin, China, 11–14 August 2019; pp. 1–5.
8.  Gao, Y.; Qu, R.; Li, D.; Li, J. Torque Performance Analysis of Three-Phase Flux Reversal Machines. *IEEE Trans. Ind. Appl.* **2017**, *53*, 2110–2119. [CrossRef]
9.  Gao, Y.; Li, D.; Qu, R.; Ding, H. Synthesis of Novel Flux Modulation Machine with Permanent Magnets on Both Stator and Rotor. In Proceedings of the IEEE International Electric Machines & Drives Conference (IEMDC), San Diego, CA, USA, 12–15 May 2019; pp. 678–685.
10. Zhang, J.; Cheng, M.; Hua, W.; Zhu, X. New approach to power equation for comparison of doubly salient electrical machines. In Proceedings of the IEEE Industry Applications Annual Meeting, Tampa, FL, USA, 8–12 October 2006; pp. 1178–1185.
11. Tahanian, H.; Aliahmadi, M.; Faiz, J. Ferrite Permanent Magnets in Electrical Machines: Opportunities and Challenges of a Non-Rare-Earth Alternative. *IEEE Trans. Magn.* **2020**, *56*, 1–20. [CrossRef]
12. Shin, H.K.; Kim, T.H. A Study on the Iron Loss and Demagnetization Characteristics of an Inset-type Flux-Reversal Machine. *J. Magn.* **2013**, *18*, 297–301.
13. Deodhar, R.P.; Andersson, S.; Boldea, I.; Miller, T.J.E. The flux reversal machine: A new doubly salient permanent magnet machine. *IEEE Trans. Ind. Appl.* **1997**, *33*, 925–934. [CrossRef]
14. Ghasemian, M.; Tahami, F.; Rezazadeh, G. A comparative analysis of permanent magnet flux reversal generators with distributed and concentrated winding. In Proceedings of the IECON-43rd Annual Conference of the IEEE Industrial Electronics Society, Beijing, China, 29 October–1 November 2017; pp. 1657–1661.
15. Sharma, A.; Sashidhar, S. A Novel Ring Permanent Magnet Flux Reversal Machine for a Direct-Drive Wind Generator. In Proceedings of the IECON the 46th Annual Conference of the IEEE Industrial Electronics Society, Singapore, 18–21 October 2020; pp. 838–843.
16. More, D.S.; Kalluru, H.; Fernandes, B.G. Outer rotor flux reversal machine for rooftop wind generator. In Proceedings of the 2008 IEEE Industry Applications Society Annual Meeting, Edmonton, AB, Canada, 5–9 October 2008; pp. 1–6.
17. Dmitrievskii, V.A.; Prakht, V.A.; Kazakbaev, V.M. Design and Mathematical Modeling of Gearless SMC Flux Reversal Generator for Wind Turbine. In Proceedings of the XIII International Conference on Electrical Machines (ICEM), Alexandroupoli, Greece, 3–6 September 2018; pp. 2079–2084.
18. Lee, C.H.T.; Chau, K.T.; Liu, C. Design and analysis of a cost-effective magnetless multiphase flux-reversal DC-field machine for wind power generation. *IEEE Trans. Energy Convers.* **2015**, *30*, 1565–1573. [CrossRef]
19. Pavel, C.C.; Lacal-Arántegui, R.; Marmier, A.; Schüler, D.; Tzimas, E.; Buchert, M.; Jenseit, W.; Blagoeva, D. Substitution strategies for reducing the use of rare earths in wind turbines. *Resour. Policy* **2017**, *52*, 349–357. [CrossRef]
20. Akuru, U.B.; Kamper, M.J. Intriguing Behavioral Characteristics of Rare-Earth-Free Flux Switching Wind Generators at Small- and Large-Scale Power Level. *IEEE Trans. Ind. Appl.* **2018**, *54*, 5772–5782. [CrossRef]
21. Szabó, L. A Survey on Modular Variable Reluctance Generators for Small Wind Turbines. *IEEE Trans. Ind. Appl.* **2019**, *55*, 2548–2557. [CrossRef]
22. Shrestha, G.; Polinder, H.; Ferreira, J.A. Scaling laws for direct drive generators in wind turbines. In Proceedings of the 2009 IEEE International Electric Machines and Drives Conference, Miami, FL, USA, 3–6 May 2009; pp. 797–803.
23. Boldea, I.; Wang, C.; Nasar, S.A. Design of a three-phase flux reversal machine. *Electr. Mach. Power Syst.* **1999**, *27*, 849–863.
24. Boldea, I.; Zhang, J.; Naser, S.A. Theoretical characterization of flux reversal machine in low-speed servo drives-the pole-PM configuration. *IEEE Trans. Ind. Appl.* **2002**, *37*, 1549–1556. [CrossRef]
25. Akuru, U.B.; Kamper, M.J. Formulation and Multi-objective Design Optimization of Wound-Field Flux Switching Machines for Wind Energy Drives. *IEEE Trans. Ind. Electron.* **2018**, *65*, 1828–1836. [CrossRef]
26. Manne, B.; Malligunta, K.K.; Akuru, U.B. Design and Performance Assessment of a Small-Scale Ferrite-PM Flux Reversal Wind Generator. *Energies* **2020**, *24*, 5565. [CrossRef]
27. Akuru, U.B. An Overview on Cogging Torque and Torque Ripple Reduction in Flux Switching Machines. *Int. J. Energy Power Syst. (IJPES)* **2021**, *41*, 130–144. [CrossRef]
28. Prakht, V.; Dmitrievskii, V.; Kazakbaev, V.; Ibrahim, M.N. Comparison between rare-earth and ferrite permanent magnet flux-switching generators for gearless wind turbines. In Proceedings of the 7th International Conference on Power and Energy Systems Engineering, CPESE, Fukuoka, Japan, 26–29 September 2020.
29. Akuru, U.B.; Kamper, M.J. Design and Investigation of Low-cost PM Flux Switching Machine for Geared Medium-speed Wind Energy Applications. *Electr. Power Compon. Syst.* **2018**, *46*, 1084–1092. [CrossRef]

30. Liu, D.; Song, X.; Wang, X. Design Challenges of Direct-Drive Permanent Magnet Superconducting Wind Turbine Generators. In Proceedings of the International Conference on Electrical Machines (ICEM), Gothenburg, Sweden, 23–26 August 2020; pp. 640–646.
31. Zhang, K.; Huang, X.; Wu, L.; Fang, Y.; Cao, W. Stator Design Aspects for Permanent Magnet Superconducting Wind Power Generators. *IEEE Trans. Appl. Supercond.* **2019**, *29*, 1–5. [CrossRef]

*Review*

# A Review of the Advancements in the Design of Brushless Doubly Fed Machines

**Oreoluwa I. Olubamiwa and Nkosinathi Gule \***

Department of Electrical and Electronic Engineering, Stellenbosch University, Stellenbosch 7600, South Africa; 19469462@sun.ac.za

\* Correspondence: nathie@sun.ac.za

**Abstract:** Research interest on brushless doubly fed induction machines (BDFMs) is increasing, as they offer higher reliability compared to doubly fed induction generators (DFIGs) in wind turbines. At the moment, BDFMs do not have a definitive structure nor design process, as literature is rife with different approaches to designing BDFMs. In this paper, a comprehensive review of the design of BDFMs from available literature is conducted. The evolution of cascade induction machine systems to contemporary BDFMs is first illustrated. Pioneering research work in the evolution which have influences on modern BDFM designs are highlighted. Relevant research on different aspects of present day BDFM design are then discussed. BDFM design and optimization methodologies applied in available literature are also explored.

**Keywords:** wind power generation; brushless doubly fed machines; pole pair combinations; nested loop rotors

## 1. Introduction

Doubly fed induction generators (DFIGs) are the most widely employed generators in medium and large wind turbines. This is due to their low cost, variable speed operations, and the use of fractionally rated converters in their setup [1]. However, DFIG based wind turbines have the highest operational and maintenance (O&M) costs, because of DFIG slip ring and brush assembly failures [2]. This is further compounded in remote areas like offshore wind sites, which have low accessibility. It is worth noting that offshore wind power is getting increasing attention, and a significant expansion in offshore wind installations is projected in the coming years [3].

Brushless doubly fed machines (BDFMs) have similar advantages with DFIGs, and the absence of slip ring and brush assemblies in their setup increases their reliability [4]. As a result, the O&M costs of wind turbines using BDFMs would potentially be reduced. However, BDFMs have complex structures with lower power densities, compared to DFIGs [5]. There is also no consensus regarding certain critical aspects of BDFM design.

The development of BDFMs can be traced to machines preceding DFIGs, and these machines were mostly used for motoring purposes. In this paper, the historical evolution of BDFMs is first outlined to paint a clear picture of the development of BDFM design. The influence of the shift from cascade motoring to doubly fed generating operations on BDFM features is discussed. A thematic review of published literature considering the design of contemporary BDFMs is then presented. The different BDFM components are comprehensively examined, as well as design and optimization procedures employed in literature. The overarching aim of this paper is to provide perspective on contemporary BDFM structures, and a comprehensive overview of BDFM design.

It is recognized that general reviews on BDFMs are available in literature such as [6–8]. These reviews cover a broad array of subjects like brief histories, electromagnetic design, modelling techniques, modes of operation, and control strategies. Consequently, the BDFM design considerations in these reviews are not exhaustive. Doubly fed reluctance machines

are also discussed in these reviews. However, in this paper, there is a comprehensive focus on the design of BDFMs, and the procedures involved. Doubly fed machines with reluctance rotors, hybrid rotors and dual stators are not considered.

This paper is divided into two main sections:

1. The evolution of cascaded IMs to contemporary BDFM topologies. In this section, significant contributions to the present day BDFM topologies are highlighted, with the underlying reasons for these design developments.
2. Discussions on the aspects of BDFM design. A comprehensive run-down of recent developments and approaches employed in the design of BDFMs, are presented in this section.

## 2. Development of BDFMs from Cascade Induction Motors

At the turn of the 19th century, polyphase induction motors (IMs) were increasing in industry usage, due to their simplicity and reliability [9]. Squirrel cage induction motors (SCIMs) were preferred in environments like mining industries, where rough and rigorous handling of equipment were required [10]. However, SCIMs were only relevant for constant speed and moderate starting torque operations. This was before the advent of power electronics, and variable speed motoring operations commonly employed direct current motors [11,12]. Wound rotor (slip ring) induction motors using rheostatic control also seem to have been used for variable speed applications at the time [13,14]. Slip ring IM setups with rheostatic control had performances analogous to shunt motors [12], however with significant losses [15].

Cascade motors were developed in the pursuit of the robustness of SCIMs, and the variable speed functionality of slip ring IMs with rheostatic controls [10,14]. Cascade motor origins can be traced to cascade systems, which consisted of two or more motors having a common connecting shaft. A good example of these cascade systems is the Steinmetz cascade IM system, which was patented in 1897 [16]. These motors were connected according to different configurations to achieve different speed and power configurations. Examples of these connections are illustrated in Figure 1. In Figure 1a, the stator of the secondary motor is connected to the rotor of the primary motor. By this connection, a starting torque almost double one of the motors is achievable without the losses common with rheostatic controls. The connection in Figure 1b enables speed control capabilities similar to the series-parallel control of DC motors; Figure 1c likewise, with more options [16].
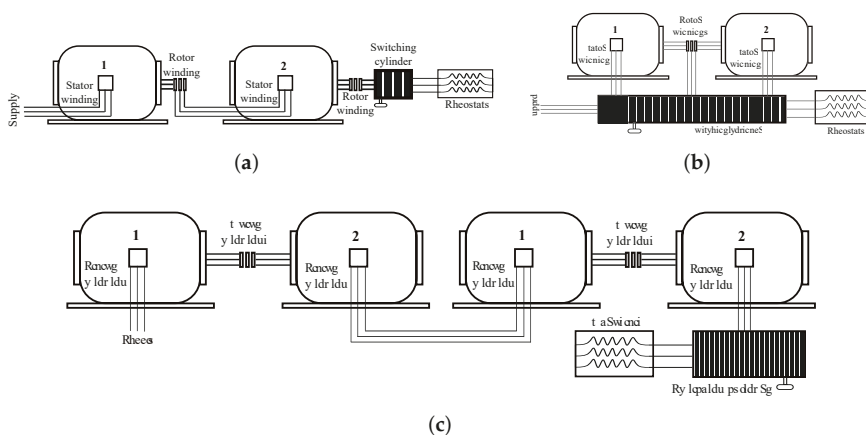


**Figure 1.** Steinmetz cascade system examples: (**a**) two motors with rotor of primary motor connected to secondary stator, (**b**) two motors with both rotors connected to each other, and (**c**) four motors [16].

Cascade systems however had disadvantages of high cost, low efficiency, low power factor, and poor overload capacity [14]. Over time, different machines were designed with inspiration from cascade systems, from which modern day BDFMs were eventually developed. In the following subsections, distinct pioneering machines are highlighted, with their major contributions to the development of BDFMs underscored. A summary of the shift from cascade operations to synchronous doubly fed operations is also given.

### 2.1. The Thompson Motor

A motor patented by S. Thompson in 1901, was highlighted in [14] as essentially being equivalent to a two motor cascade. The stator was divided into segments occupied by the primary and secondary windings. Alternate segments had different windings preventing mutual induction, as illustrated in Figure 2. The primary windings were connected directly to the main supply, while the secondary windings were connected to regulating resistances. The rotor had a wave winding which coupled with the primary stator field and induced a field on the secondary stator winding. Placing all the windings on one core was to reduce the setup cost, as opposed to two separate machines connected in cascade. The Thompson motor helped shape the shift from multiple motors in a cascade system to a single motor with cascaded operations.
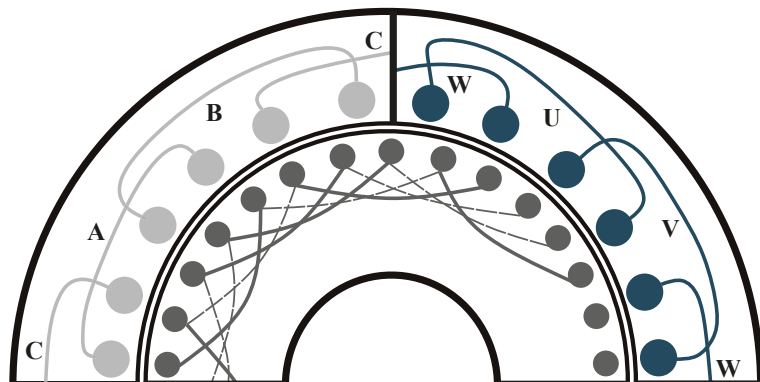


**Figure 2.** Thompson motor winding illustration [14].

### 2.2. The Lydall Motor

A patent for a polyphase motor which could be operated at three speeds without rheostatic loss, was accepted in 1903 [13]. This motor was developed by the Siemens brothers & Co. Limited and Francis Lydall, with two stator windings which had different pole numbers preventing direct inductive coupling. The rotor also had two windings wound in similar fashion as the stator, with connections made possible by slip rings. A schematic illustration of the Lydall motor is given in Figure 3. In reality, the "switching controller" in Figure 3 consisted of 3 barrel switches used to achieve desired connections.

The synchronous speed of S1 was achieved by connecting the supply to S1, S2 to R1, and R2 to the starting rheostats; the synchronous speed of S2 was achieved by swapping these connections (S2 to the supply, S1 to R2, R1 to rheostats). A cascade speed was achieved by connecting S1 to the supply, shorting S2 and R2, and connecting R1 to the starting rheostats.
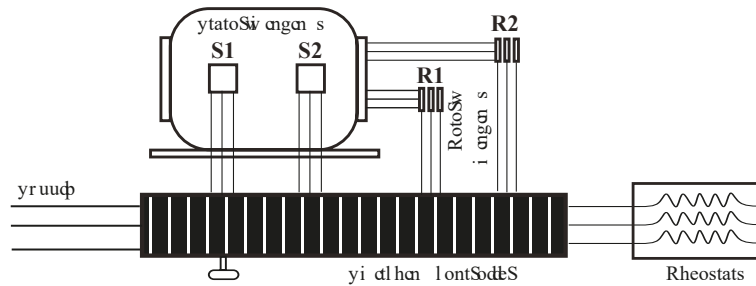
**Figure 3.** Schematic representation of the Lydall motor [13].

The difference in pole numbers made segmentation of the stator windings unnecessary, as one could be placed on top the other. However, there was increased copper losses from the two sets of windings (on the stator and rotor), and increased magnetic leakage due to deeper slots, especially from the winding farthest from the air-gap [14]. Despite this, it should be noted that present day BDFMs use the Lydall type of stator, with windings of different pole numbers; one on top of the other.

*2.3. The Hunt Motor*

L.J. Hunt introduced a cascade motor in [14], with single stator and rotor windings. This motor had regulating resistances connected to tappings on the stator winding, and did not need slip rings. Slip rings could however be employed if more efficient speeds were desired. The special stator winding allowed for reduction of magnetic leakage and copper losses incurred by the two stator windings in prior cascade motors. Hunt continued to work on the development of this motor, fine tuning the design and making it more practical.

Upon the successful construction and usage of large numbers of these machines, another paper [10] was published in 1914. This paper gave more details as to the design of the hunt motor, and also notably a brief guide into the selection of the number of poles on the stator. In Figure 4, the coil group connections to obtain 4 poles, 8 poles, and (4 + 8) poles configurations from a star wound single stator are illustrated. In 1921, F. Creedy published a paper [17], which shed more light on the pole number selections, paving the way for new combinations. Improved rotor and stator winding designs for this type of cascade motor were also discussed in [17]. The works of L.J. Hunt and F. Creedy were foundational for the selection of suitable pole pair combinations for BDFM stator windings.
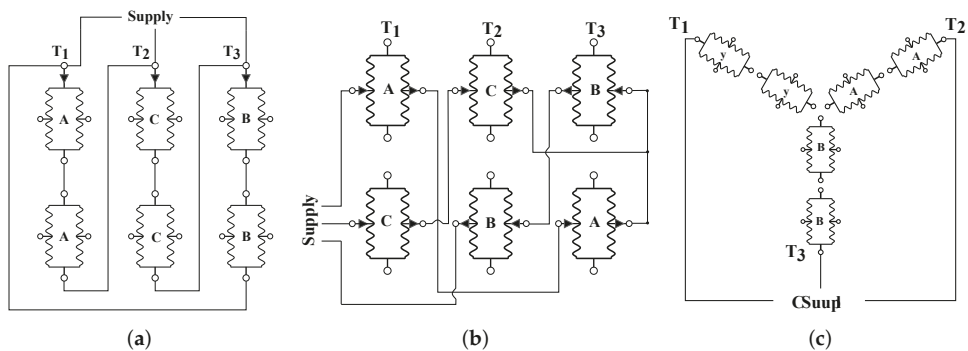


**Figure 4.** Hunt motor stator connections: (**a**) 4 poles, (**b**) 8 poles, and (**c**) (4 + 8) poles [10].

## 2.4. The Broadway & Burbridge Motor

In [18], Broadway and Burbridge sought to design cascade motor rotors that were simpler compared to the irregularly grouped double layer wound rotors in the Hunt/Creedy motors. Two single layer winding rotors, the graded winding rotor and the multicircuit winding rotor, were investigated. The winding arrangements of these rotors are illustrated in Figure 5. Although, the coils of the graded winding rotor in Figure 5a are not short circuited together, the graded winding rotor prototype in Figure 6a has a common end-ring for all the coils. The graded winding rotor in Figure 6a is built for a (6 + 2) poles cascade machine. A multicircuit rotor for a (18 + 12) poles machine is also built in [18], as shown in Figure 6b. These rotors presented in [18], which are now more commonly called the nested loops (NL) and cage+NL rotors respectively, are currently the most widely used rotors in contemporary BDFMs.
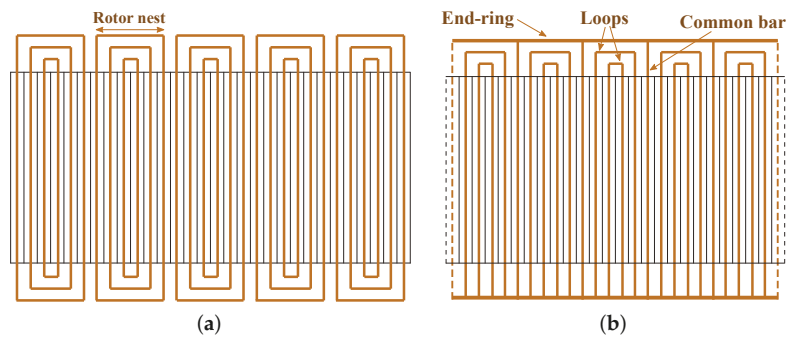
**Figure 5.** Broadway & Burbridge rotor winding arrangements: (**a**) Graded winding rotor and (**b**) multicircuit winding rotor [18].
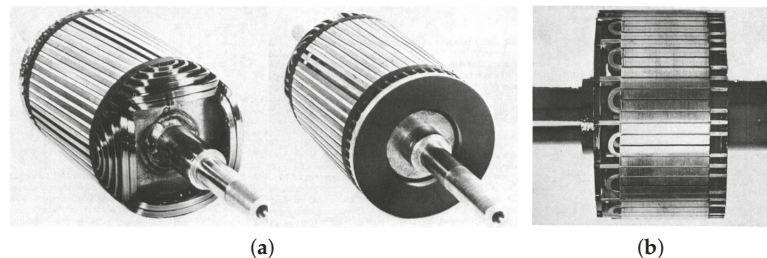
**Figure 6.** Broadway & Burbridge rotor prototypes: (**a**) Graded winding rotor for (6 + 2) poles machine, and (**b**) multicircuit rotor for (18 + 12) poles machine [18].

## 2.5. Cascade Systems to Brushless Doubly Fed Operations

The cascade IM systems/cascade motors were conceived at a time before power electronic converters. Early cascade systems/motors were developed to achieve efficient motor operations at different (usually low) speeds. The cascade motors were also developed with the view of obtaining robustness and reliability similar to SCIMs [14,18].

The synchronous operation of machines similar to S. Thompson's motor, were detailed by B.H. Smith in 1966-7 [19,20]. These motors used by B.H. Smith, were at the time called twin stator induction machines, and the stator windings were both fed with three phase supplies at different frequencies. This was the first of analyses of what were hitherto cascade motors, operating similarly to doubly fed induction machines. Slip frequency excitation from a low power frequency converter was discussed for harnessing slip power from the machine rotors.

In 1970 [18], Broadway and Burbridge also discussed the synchronous operations of cascade machines. However, these synchronous operations were limited to the machine synchronous speed, such that AC was applied to one stator winding, and DC to the other. Full load performances of the cascade machines in synchronous operations were notably superior to asynchronous operations of equivalent multipole IMs. Also, there was an increase in power factor compared to asynchronous operations.

The first traceable mention of the term "brushless doubly fed machine (BDFM)" is in [21], a 1989 paper about a dynamic model of BDFMs. In 1994, Brune et al. tested the possibilities of using BDFMs in a variable speed wind turbine in [22]. The use of a BDFM in a wind turbine was an attempt to obtain the benefits of a DFIG in with a more robust structure, which is still the main reason for the recent push in research about BDFMs. A 1.5 kW prototype was built to demonstrate the viability of BDFM based wind turbines. In the following sections, the discussion is shifted to recent (mainly post 90s) developments in the design of BDFMs. Research challenges with the design and approaches to solving these issues are also discussed.

## 3. Recent BDFM Design Development

In a push towards commercial MW rated BDFMs, the authors in [23] presented a 250 kW rated BDFM. This being the largest BDFM/BDFIG tested to date, showed expected performances and stable control, and thus the viability of the technology.

Although the BDFM is not yet at a commercial scale of implementation, the prospects of usage in wind turbines have piqued the interests of several research groups globally. As a result, a number of notable developments in the design of BDFMs have occurred. A large portion of these developments have had focusses on suitable pole pair combinations and optimum rotor design. Maximizing the power density and reduction of harmonics have also received their fair share of attention. Furthermore, different design approaches of BDFMs have been presented, and all these aspects are discussed in the subsequent sections.

### 3.1. Stator Winding Development

Up until around 1989, the L.J. Hunt type of stator windings [10] were used for BDFMs, in which coil groups were interconnected in a way to accommodate two AC supplies (or pole pairs) [21]. However in [24], it was suggested that the L.J. hunt type of stator winding was better suited for applications in which only one set of terminals were connected to a power source at a time.

For synchronous BDFM operations, with two AC supplies connected to the terminals, there are unbalances in the Hunt type of stator, which lead to internal circulating currents. Therefore, reverting to isolated stator windings like in the Lydall motor was recommended in [24]. This helped in avoiding the circulating currents, while affording greater simplicity and flexibility.

Consequently, contemporary BDFM stators have two isolated windings, the power winding (PW) and the control winding (CW). The stator windings do not couple directly, but are cross-coupled by a special rotor (see Section 3.2). As already suggested in [14], the winding which is farthest from the airgap has increased leakage. Placing the PW at the bottom layer would have significant effects on the converter ratings, as higher leakage would increase the difficulty in controlling the grid side power factor as noted in [25]. Thus, the PW with $p_1$ pole pairs typically occupies the bottom layer (closest to the airgap) of the stator slots, while the CW with $p_2$ pole pairs occupies the top layer. This type of stator for a $p_1/p_2 = 2/3$ BDFM, is illustrated in Figure 7.
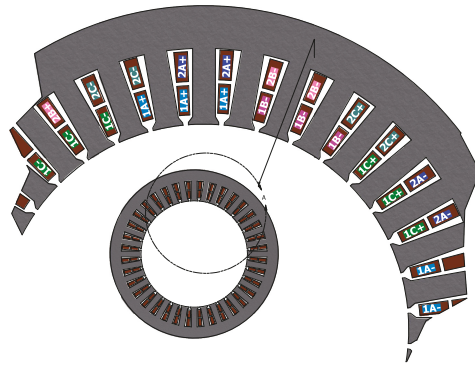
**Figure 7.** Stator winding arrangement of a BDFM with $p_1/p_2 = 2/3$.

3.1.1. Relative Winding Pole Size

Typically, $p_1$ is lower than $p_2$ for a number of reasons. A significant reason for using the lower pole as $p_1$ is the higher magnetizing requirements with increasing poles [26–28]. Thus higher poles for $p_1$ can increase the power ratings of the converters used. Furthermore, the lower pole number for $p_1$ affords better winding distribution, as the PW and CW occupy the same number of slots, and this helps reduce unwanted harmonics.

The BDFM torque breaks down at the synchronous speed of a $p_1$ machine, thus favouring a lower $p_1$ for a wider operating speed range [27]. However, this hardly applies to BDFMs with regards to being alternatives to DFIGs in wind turbines. To use fractionally rated converters, the BDFM maximum speed will typically be lower than the synchronous speed of the higher pole [29].

The rotor field frequency ($\omega_{r_f}$) is calculated from the formula in [30,31],

$$\omega_{r_f} = \omega_1 - p_1\omega_r = -\omega_2 + p_2\omega_r, \tag{1}$$

where, $\omega_1$ & $\omega_2$ are the electrical angular speeds of the PW and CW respectively, while $\omega_r$ is mechanical angular speed of the rotor. It can be observed that $\omega_{r_f}$ is higher if $p_1$ is lower than $p_2$. This leads to higher core losses [32,33], and rotor impedances considering that skin effect is lower at lower frequencies. The disparity between $p_1$ and $p_2$ should not be too high to reduce copper losses due to skin effect [32].

3.1.2. Unbalanced Magnetic Pull and Magnetic Coupling

In [34], it was established that when a $x$-pole pair field is combined with a $(x + y)$-pole pair field, a force imbalance occurs when $y = 1$. This imbalance, now commonly called an unbalanced magnetic pull (UMP), was then illustrated (Figure 8) with a 2/3 pole pair combination. It can be observed from the force diagram in Figure 8, that a strong force zone is directly opposite to a weak zone, giving rise to the imbalance. If $y > 1$, there will be equal $y$ strong and weak zones [34], and UMPs can be avoided.

The harmonics generated by the PW and CW are given respectively as

$$\begin{aligned} h_{pw} &= p_1(2t - 1), \quad t \in \mathbb{N}, \\ h_{cw} &= p_2(2t - 1), \quad t \in \mathbb{N}. \end{aligned} \tag{2}$$

If the windings have no common harmonic, they do not couple inductively. A bit more nuance about selecting pole pair combinations towards ensuring non coupling is provided in [30]. However, the rules given in [30] only apply when series windings are used. The use of parallel coil group connections can enable direct coupling of the PW and CW, which produces circulating currents. Practical connections of coil groups in parallel

while avoiding direct coupling are discussed in [35], and these parallel paths can help mitigate UMPs.
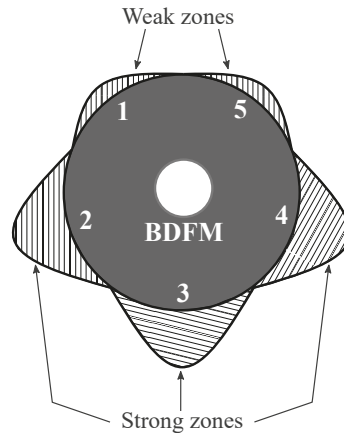


**Figure 8.** Force diagram for $p_1/p_2 = 2/3$ (adapted from [34]).

3.1.3. Commonly Used Pole Pair Combinations

Pole pair combinations which do not produce UMPs were tested using 2D FE BDFM models in [36] to highlight suitable combinations. Although the $p_1/p_2 = 2/4$ pole pair combination is used for a 250 kW BDFM prototype in [37], the results in [36] suggest that the $p_1/p_2 = 4/6$ combination is more suitable in terms of power, efficiency and torque ripple. However, optimization results in [38] indicate that the $p_1/p_2 = 2/4$ combination performs better than the $p_1/p_2 = 4/6$ combination for a BDFM in a D180 frame size. Analytical estimations in [29] also point to better performance from the $p_1/p_2 = 2/4$ combination, compared to the $p_1/p_2 = 4/6$ in terms of power and efficiency.

In spite of these, the $p_1/p_2 = 2/3$ is the preferred combination for the D180 frame BDFM in [38,39], as it produces the best performance in terms of efficiency and generated torque. The $p_1/p_2 = 2/3$ combination in [38] also has considerably lower torque ripple and time harmonic distortions, compared to the $p_1/p_2 = 2/4$ combination. Concerns of UMP with the $p_1/p_2 = 2/3$ combinations were considered minor in [38], due to the small size of the machine. In [40], the $p_1/p_2 = 4/6$ is the preferred combination for a 3.2 MW BDFM, due to the less coupling of higher space harmonics compared to the $p_1/p_2 = 2/4$ combination, and the absence of UMP, which is present in the $p_1/p_2 = 2/3$ combination. The lower harmonic content in the 4/6 combination relative to the 2/4 combination is also alluded to in [41], however the PW has the higher pole number. A summary of the relative performances of the 2/3, 2/4 and 4/6 pole pair combinations as described in literature, is given in Table 1.

**Table 1.** Relative performance of popular BDFM pole pair combinations.

| Parameters | Pole Pair Combinations ($p_1/p_2$) | | |
| --- | --- | --- | --- |
| | 2/3 | 2/4 | 4/6 |
| Power density [29,38,39] | High | Medium | Low |
| Efficiency [29,38,39] | High | Medium | Low |
| Torque ripple [38] | Low | High | Low |
| Harmonic distortion [40,41] | Low | High | Low |
| UMP [35,36] | Present | - | - |

### 3.2. Rotor Winding Development

The nested loop (NL) and cage+NL rotors, whose origins are traced to [18], are currently deemed the most suitable for BDFMs [6,30,42]. The NL rotor winding arrangement and a prototype are shown in Figure 9a,b respectively. The cage+NL rotor winding arrangement has already being illustrated in Figure 5b, and a prototype is shown in Figure 9c. The winding arrangement in Figure 9a differs from that in Figure 5a by the presence of a common end ring, with the rotor illustrated in Figure 5a now sometimes called an isolated loop (IL) rotor [30]. These (NL, IL, & cage+NL) rotor types have robust builds with better torque performance and lower losses, compared to wound rotors [6].

A rotor similar to the NL rotor, but with double layers of bars, is highlighted in [30]. It is suggested that this double layer bar rotor has a larger torque envelope than the NL rotor; also higher efficiency due to less excess harmonic reactance. However, the increased complexity has manufacturing and control implications. The double layer bar rotor winding arrangement is illustrated in Figure 10a, while a prototype is shown in Figure 10b.

Whilst considering the high harmonic reactance and potential considerable skin effect in large BDFMs using NL rotors, series wound (SW) rotors are compared with NL rotors in [42]. The winding arrangement of the SW rotor is illustrated in Figure 11a, with a prototype shown in Figure 11b. Although the SW rotor has lower harmonic content and no skin effect issues, it has higher impedance and develops lower torque. Despite this, the performance of the SW rotor is deemed acceptable. It is also indicated that with similar slot fill factors, the SW and NL rotors will have similar torque performance due to identical referred rotor resistance. Also in [43], details of the design of a 60 kW BDFM with a special "double-sine" rotor are given. This rotor was designed as a potential BDFM rotor with greatly reduced harmonic content.

Although, the cage+NL rotor has similar advantages with the NL rotor, the NL configuration is more commonly used [6]. In [44,45], the NL and cage+NL rotors are compared based on their rotor equivalent circuit parameters, and it is suggested that the cage+NL rotors provide better performance due to their lower impedances. This advantage of cage+NL rotors is shown in [46] to be more evident when the disparity between $p_1$ and $p_2$ is greater. In cases where the $p_1$ value is close to $p_2$, the NL rotor may perform better due to lower leakage inductance.

Initial guidelines for loop design of the NL and cage+NL rotors are given in [47]. It is suggested that loops with spans closer to the pitch of the higher pole number in the BDFM, are more efficient and effective in torque production. It is also suggested in [47], that loops with small spans have minor contributions to torque production, similar to suggestions in [44,48,49].
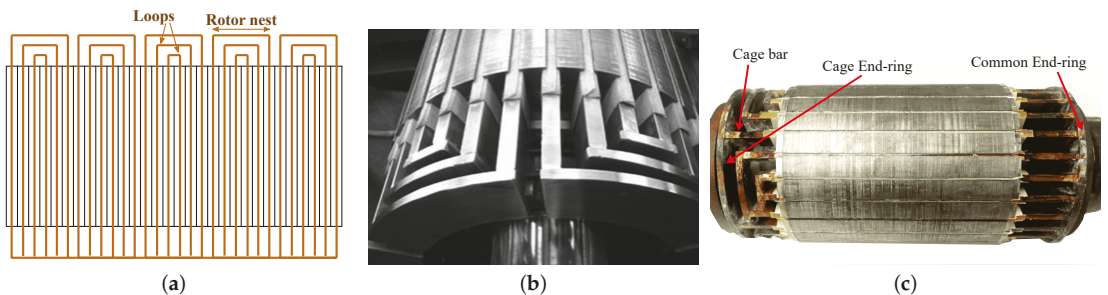


**Figure 9.** Widely used BDFM rotors: (**a**) NL rotor winding arrangement for $p_1 + p_2 = 5$, (**b**) NL rotor prototype [42], and (**c**) Cage + NL rotor prototype.
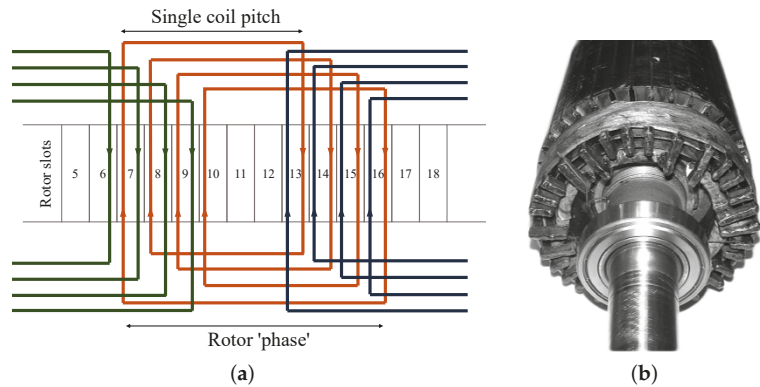
**Figure 10.** Double layer bar rotor: (**a**) Winding arrangement for $p_1/p_2 = 2/4$, and (**b**) prototype [30].
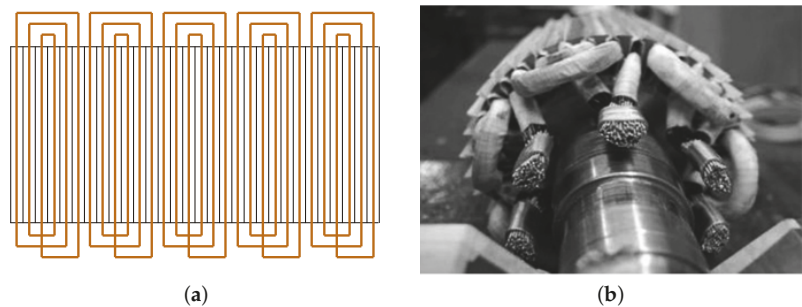


**Figure 11.** SW rotor: (**a**) Winding arrangement for $p_1 + p_2 = 5$, and (**b**) prototype [42].

Observations in [44,47,48] indicate that the rotor loops should not necessarily be evenly spaced, and the width of the outer loops should be maximized. An increase in rotor loops per nest helps to mitigate space harmonics in BDFMs [27,48], and helps with better current distribution in BDFM rotors [27].

### 3.3. BDFM Sizing and Power Ratings

By analyzing the stator magnetic fields in BDFMs using a per phase equivalent circuit, a composite magnetic loading based on the stator fields is derived in [5]. Expressions for the BDFM power rating as a function of the pole pairs, stack length, airgap radius, electric and magnetic loadings, are given in [5]. The magnetic loading derivation in [5] was further modified in [27], as the loading derived in [5] was deemed too conservative, leading to over-sizing. Other aspects of the BDFM geometric sizing such as the slot teeth width and core height/depth are given in [27].

The BDFM power ratings expression in [5] is used to predict about a quarter reduction of the power rating in BDFMs, compared to conventional DFIGs of the same size. The influence of pole pair combinations on this disparity in power between BDFMs and DFIGs is investigated in [29]. It is suggested that combinations with lower $(p_1/p_2)$ pole ratios have slight reduction in this disparity. These observations are somewhat echoed in [50], however, the analysed MW rated BDFMs have more than a quarter increase in mass when compared with DFIGs of similar power and operating speed. BDFMs also suffer a reduction in efficiency compared to DFIGs, as they have more windings, and consequently higher winding losses [6].

The impact of pole combination choices on the BDFM core depth is also characterized in [29]. For the pole pair combinations investigated in [29], it is observed that the BDFM core

depths are at least two times bigger than DFIG core depths. However, it is also observed that as $p_1$ gets closer to $p_2$, the core depth ratio between BDFMs and DFIGs of similar speeds gets smaller. Also, it is demonstrated in [51], how sections of an NL rotor core which do not contribute to the rotor magnetic circuit can be removed for weight reduction.

The effects of rotor leakage inductances on inverter ratings are illustrated in [25]. An increase in the rotor leakage inductance reduces the inverter ratings required for crowbar-less low voltage ride through (LVRT) requirements, but reduces the power factor management abilities. A trade-off between LVRT and power factor management requirements is therefore advocated in the choice and design of BDFM rotors. The use of magnetic wedges in optimizing inverter ratings is also discussed in [37,52]. However, it is worth noting that magnetic wedges are brittle and less reliable than non-magnetic wedges.

### 3.4. Vibrations and Harmonics Mitigation

In [53], it is affirmed that the combination of two magnetic fields of different poles in BDFMs produces extra vibrations not present in single field induction machines. It is further revealed that the bending forces on the stator back iron, which are significantly dependent on the pole pair combinations, contribute greatly to these vibrations. Apparently, combinations with pole numbers which are close, tend to produce higher vibrations. A method to mitigate these vibrations is also given, such that the machines are "stiffened" by increasing the stator core depth. This solution would have to be applied with caution, as BDFMs already have longer core depths compared to DFIGs [29].

In [54], it is stated that the most significant source of torque ripple in BDFMs is the winding distribution space harmonics; the excessive space harmonics present in the nested loop rotor structure being a major culprit. In [41,44,48], it is suggested that increasing the rotor loop spans helps in reducing harmonic content in BDFMs. Also, an increase in rotor loops per nest helps to mitigate space harmonics in BDFMs [27,48]. Using a coupled circuit (CC) model, the effect on torque ripple of NL and cage+NL rotor loop spans relative to the PW and CW pole pitches, is illustrated in [49]. It is shown how the CC model can be used to find suitable rotor designs for specific BDFM applications.

Slot types have effects on torque ripple [54]. Also, a double layer CW is expected to reduce torque ripple according to [55]. It is shown analytically in [56], that rotor skews help to reduce torque ripple. The effects of rotor skewing are further investigated in [57], and it is determined that skewing has little effects on losses, however, there is a slight reduction in the average torque.

As noted in Section 3.1, suitable pole pair combinations are investigated for torque ripple and harmonic content in [36,38,40]. Pole pair combinations that are multiples of the 2/3 combination have low harmonic content [6,36,38,40], however, the 2/3 combination itself suffers from UMP.

### 3.5. BDFM Design and Optimization Procedures

A proposed design procedure for a 6 MW BDFM is presented in [4], as illustrated in Figure 12. The power rating is selected because the largest DFIG generators used in wind turbines are rated similarly. In the design process, the BDFM equivalent circuit in [58] is used to obtain an initial design from the determined machine specifications. A coupled circuit (CC) BDFM model is then employed to evaluate the designed nested loop rotor. Finite element analysis (FEA) of the design is conducted to investigate the peak flux densities in the different iron parts, and obtain a close estimate of the magnetizing current. Thermal evaluation of the BDFM design is also recommended, alongside discussions with machine manufacturers, to aid practicality. System performances such as dynamics, control stability and LVRT capabilities are then considered in a fine-tuning of the design. This design procedure was reportedly employed for the 250 kW built and tested in [23].
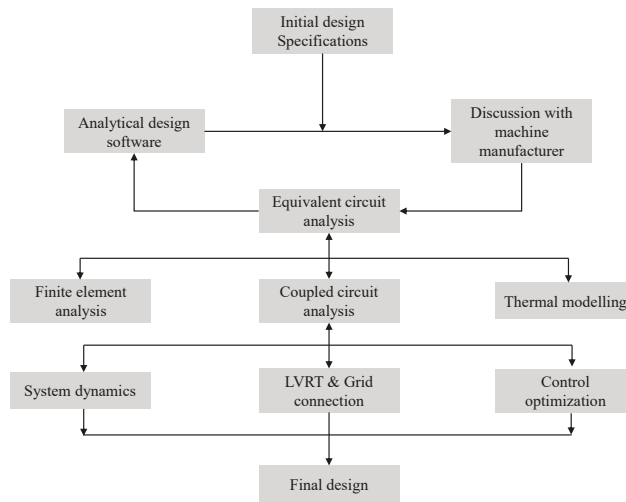
**Figure 12.** Proposed design procedure for a 6-MW BDFM [4].

Available BDFM electric equivalent circuit (EEC) models are limited in evaluating saturation, and FEA models are computationally costly. In light of these, a design approach for BDFMs using an EEC alongside a magnetic equivalent circuit (MEC) model is presented in [59]. The MEC developed in [60], is used to determine the flux distribution by the PW and CW, while the EEC model uses the MEC results to determine the machine performance.

It was noted in [61], that investigations on the design of BDFMs are limited in available literature. To that effect, a comprehensive BDFM design procedure considering the electromagnetic and thermal aspects of the BDFM, is presented in [61], with details of some of the models used given in [62]. A flowchart of the design procedure is given in Figure 13a. An EEC model is used to evaluate stator and rotor currents, while a static MEC as presented [62], is used to analyze the flux density distributions and core loss caused by these currents.

Temperature analysis is conducted in the design process in [61] using a lumped parameter thermal model illustrated in Figure 13b. The machine sections are designated as resistances, with the losses identified as heat sources. The description of the thermal model components are given in Table 2. A simple vibration analysis is also used to estimate vibrations in designs, and the optimization results are verified using 2-D FEA.

An optimization process using the imperialist competitive algorithm is used to maximize the power to weight ratio, efficiency, power factor, while minimizing the voltage regulation and rotor differential leakage inductance in [61]. Feasibility of different aspects of the BDFM design are monitored, such as the stator and rotor slots, the airgap length, shaft diameter etc. However, it is the CW power factor that was being maximized. The CW is also seemingly placed closest to the airgap.

An iterative (Tabu search) method is used to optimize the stator of a 180 frame size BDFM based on its per phase equivalent circuit model in [63]. The optimization was used to demonstrate how appropriate division of the stator slot area between the PW and CW, can enable BDFM operation at the magnetic and electric loading limits. This maximizes the power output, as was demonstrated by the 21 % increase in power from the original design. This method of optimization is also applied to a D160 frame BDFM in [64], to optimize the electric and magnetic loadings. The maximum motoring torque with a lower limit on the PW power factor of 0.75 is used for machine evaluation in the optimization process.

(**a**)             (**b**)
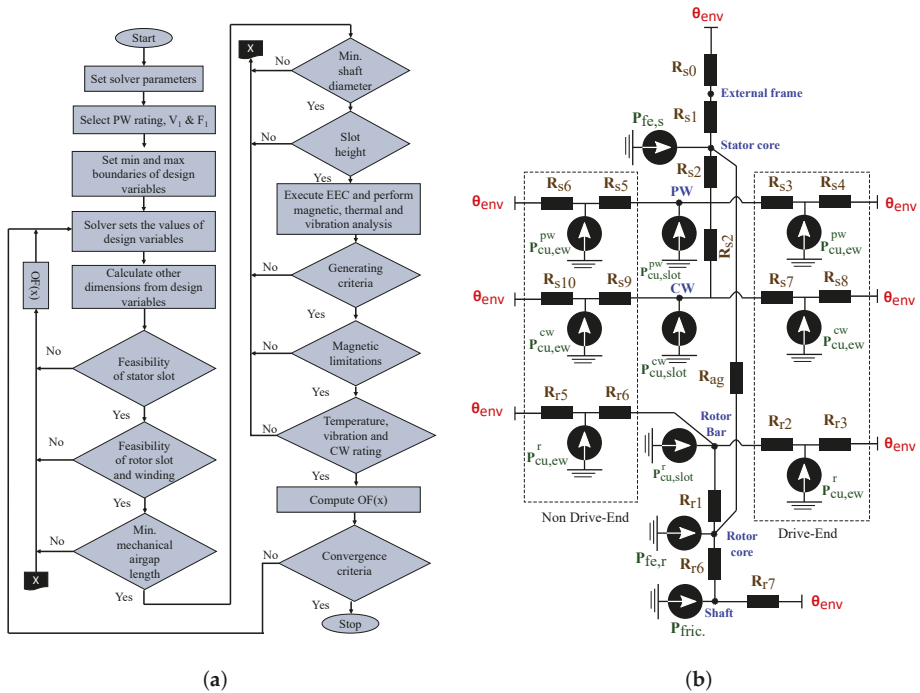
**Figure 13.** Design process and thermal model in [61]: (**a**) Design flow chart, and (**b**) Radial equivalent thermal network of a BDFM.

**Table 2.** Resistance descriptions in thermal model [61].

| Component | Description |
|---|---|
| $R_{s0}$ | Thermal resistance between external frame and environment with thermal resistance of external frame |
| $R_{s1}$ | Thermal resistance of stator core |
| $R_{s2}$ | Thermal resistance of coil insulator |
| $R_{s3}/R_{s5}$ $R_{s7}/R_{s9}$ | Thermal resistance of PW & CW end-winding to middle of slot at drive end/non-drive end sections |
| $R_{s4}/R_{s6}$ $R_{s8}/R_{s10}$ | Thermal resistance between PW & CW end-winding and environment at drive end/non-drive end sections |
| $R_{ag}$ | Thermal resistance between rotor and stator |
| $R_{r1}$ | Thermal resistance of rotor slot insulator |
| $R_{r2}/R_{r4}$ | Thermal resistance of rotor end-winding to middle of slot at drive end/non-drive end sections |
| $R_{r3}/R_{r5}$ | Thermal resistance between rotor end-winding and environment at drive end/non-drive end sections |
| $R_{r6}$ | Thermal resistance of rotor core |
| $R_{r7}$ | Thermal resistance between shaft and environment |
| $P_{fe,(s/r)}$, $P_{fric}$ | Stator/rotor iron, frictional losses |
| $P_{cu,ew}$, $P_{cu,slot}$ | End-winding, slot copper losses |

A magnetostatic FE BDFM model is presented in [39,65] to enable computationally efficient and accurate optimization processes. The non-dominated sorting genetic algorithm (NSGA-II) is used in [39] alongside the magnetostatic FE model to optimize the torque and efficiency of a BDFM designed for a D180 frame size. Geometric variables such as the stator inner radius and the ratios of slot/yoke height are used in the optimization process. The NSGA-II is also used in an optimization process in [40] to optimize the material cost and efficiency of a 3.2 MW BDFM. Similar geometric variables and magnetostatic FE models like in [39], are used in the optimization process in [40].

Both optimization processes in [39,40] are illustrated in Figure 14; A & B representing the optimized BDFM performances in [39,40] respectively. Different pole pair combinations ($p_1/p_2$ = 1/3, 2/3, 2/4 & 4/6) are tested in the optimization process in [39], with the 2/3 combination having the superior performance. However the 4/6 pole pair combination is used for the 3.2 MW BDFM in [40], because of the effects of the presence of UMP using the 2/3 combination. It is worth noting that the machines in [39,40] are optimized at the maximum torque operation points.

In [66], the authors of this paper presented a BDFM design process. A modified version of that process is presented here. The design process of a BDFM is represented with two intertwined processes; the geometric and winding design process illustrated in Figure 15a, and the power density optimization process illustrated in Figure 15b. The geometric process is used for each design iteration in the optimization process. Given the absence of specific values for the stack aspect ratio, electric and magnetic loadings in literature, practical values are identified during an optimization process, and these values are used in the final geometric and winding design of the BDFM.

In this design process, the CC model developed in [49] is used to determine the appropriate rotor type and structure (number of loops) for individual design applications. The optimization process which also employs the NSGA-II is used to maximize the efficiency and power density at power output constraints. It is demonstrated in [67], how the power output of BDFMs varies with PW power factor, such that the maximum generated power from a design may be much larger than the power generated at PW unity power factor. As a result, power output at PW unity power factor is used in the optimization process in [66]. A response surface approximation (RSA) developed from 2-D transient FEA results is used with the NSGA-II. The RSA is used to enable computational efficiency in the optimization process. A summary of the listed design and optimization procedures is given in Table 3.
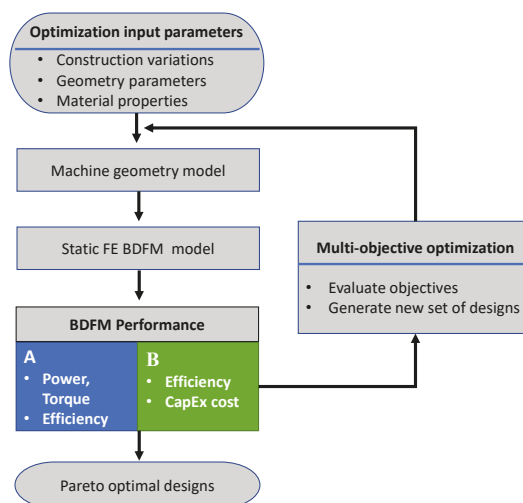


**Figure 14.** NSGA-II optimizations flow chart. Optimization processes in [39,40].
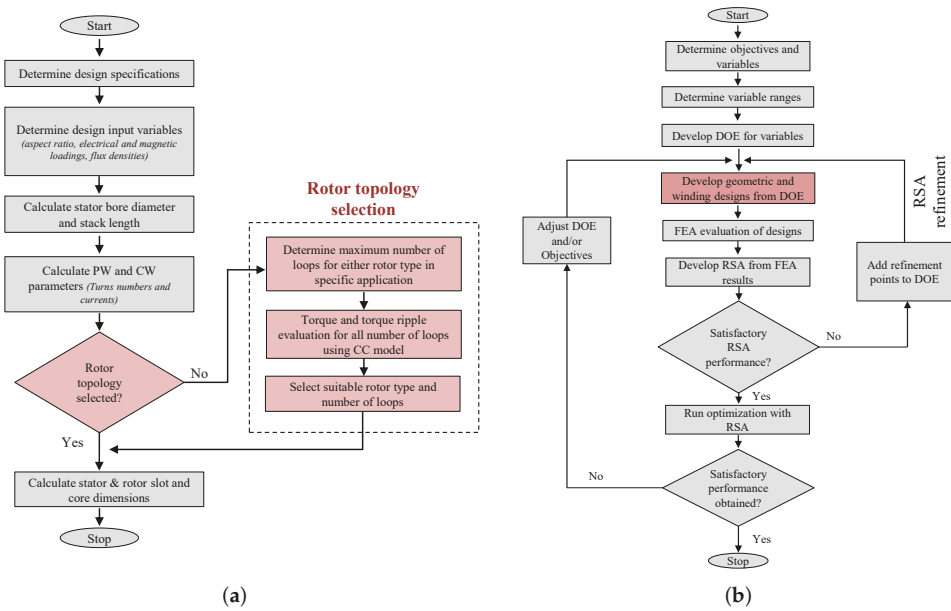
**Figure 15.** Design process proposed by authors: (**a**) Geometric and winding design process and (**b**) optimization process.

**Table 3.** Summary of design and optimization procedures.

| Description | Relevant References | Models/Analytical Methods | Applications/Advantages | Limitations |
|---|---|---|---|---|
| 6 MW BDFM design | [4,23,58] | Equivalent circuit models, CC models, FEA | Comprehensive MW rated BDFM design | Impractical for smaller designs |
| BDFM design with EEC and MEC models | [59,60] | EEC and MEC models | Computationally cheap | Limited functionality |
| Electromagnetic and thermal design of BDFMs | [61,62] | EEC, MEC & thermal models, vibration analysis, 2D FEA, imperialist competitive algorithm | Robust design procedure; broad functionality | Complex implementation |
| BDFM rotor design and power density optimization | [49,66,67] | CC model, Transient FEA, NSGA-II, Response surface approximations | Rotor type selection; Systematic power output evaluation; computationally cheap optimization | No thermal considerations; slightly complex implementation |
| Electric and magnetic loading optimization | [63,64] | Equivalent circuit model, Tabu search method | Maximizing power output, easy implementation | Power factor constraint too low |
| Multi-objective optimizations | [39,40,65] | Magnetostatic FEA, NSGA-II | Computationally cheap optimizations; material cost, efficiency & torque optimizations | No power factor consideration |

## 4. Conclusions and Future Research

This review on the design of BDFMs can be divided into two parts; the evolution of cascade motors to BDFMs, and the recent developments in BDFM design. BDFMs have a rich history in terms of development, which has been laid out. The evolution was detailed in a way to provide the reader with perspective on BDFM development by highlighting pioneering designs and prototypes. Contemporary developments in the design of BDFMs are also described. These recent developments have revolved around the stator winding pole pair combinations, rotor topology and performance optimizations.

Recurring themes in recent BDFM design related articles include the selection of suitable pole pair combinations for the stator windings, vibrations & harmonic mitigation, and optimization of machine power density & efficiency. The stator structure design seems to be settled on the electrically isolated windings occupying different layers in the stator slots, with the PW typically closest to the airgap, and the CW closer to the core. However, there is no clear candidate for the pole pair combinations of these windings. Researchers are split between the 2/4 and 4/6 combinations for different reasons which are detailed. Thus, further insight on suitable pole pair combinations is crucial. The use of fractionally distributed windings for harmonics mitigation also needs to be further investigated.

On the other hand, a lot of research is still being conducted on the type and structure of BDFM rotors. Two rotor types, the NL and cage+NL rotors, are the leading choices of rotor types. The number of loops per nest for either rotor type is not fixed, and varies for reasons like harmonics, vibrations and torque performance. There is a possibility of significant skin effect in large BDFMs using NL or cage+NL rotors, and this needs to be investigated. Also, a comprehensive performance comparison between the NL, IL and cage+NL rotors is important.

BDFM sizing is detailed in available literature. However, the equations used for parameters like the airgap flux density or core depths are not definitive. To this effect, investigations across different power ratings may be required to identify the saturation tolerances of BDFMs. This will also help provide a more accurate basis for power density comparisons between BDFMs and DFIGs.

Different models have been used for design purposes, giving researchers interested in BDFM designs a variety of options. However, many require individual implementation, as they are unavailable in software form for public use, or in commercial software packages. This generally makes the design of BDFMs a longer process than conventional machines. Different design procedures have also been presented, and these provide useful insight into the design of BDFMs. Finally, it is reckoned that a robust design process for BDFMs would involve both machine and converter designs.

## Abbreviations

The following abbreviations are used in this manuscript:

| | |
|---|---|
| BDFM | Brushless doubly fed machine |
| CC | Coupled circuit |
| CW | Control winding |
| DFIG | Doubly fed induction generator |
| EEC | Electric equivalent circuit |
| FEA | Finite element analysis |
| IL | Isolated loops |
| IM | Induction machine |
| LVRT | Low voltage ride through |
| MEC | Magnetic equivalent circuit |
| NL | Nested loops |
| NSGA-II | Non dominated sorting genetic algorithm |
| O&M | Operational and maintenance |
| $p_1$ | PW pole pairs |
| $p_2$ | CW pole pairs |
| PW | Power winding |
| RSA | Response surface approximation |
| SCIM | Squirrel cage induction motor |
| SW | Series wound |
| UMP | Unbalanced magnetic pull |

## References

1. Polinder, H.; Ferreira, J.A.; Jensen, B.B.; Abrahamsen, A.B.; Atallah, K.; McMahon, R.A. Trends in Wind Turbine Generator Systems. *IEEE J. Emerg. Sel. Top. Power Electron.* **2013**, *1*, 174–185. [CrossRef]
2. Carroll, J.; McDonald, A.; Dinwoodie, I.; McMillan, D.; Revie, M.; Lazakis, I. Availability, operation and maintenance costs of offshore wind turbines with different drive train configurations. *Wind Energy* **2017**, *20*, 361–378. [CrossRef]
3. Global Wind Energy Council (GWEC). *Global Wind Report 2021*; Technical Report; GWEC: Brussels, Belgium, 2021.
4. Abdi, E.; Tatlow, M.R.; McMahon, R.A.; Tavner, P. Design and performance analysis of a 6 MW medium-speed Brushless DFIG. In Proceedings of the 2nd IET Renewable Power Generation Conference (RPG 2013), Beijing, China, 9–11 September 2013; pp. 1–4. [CrossRef]
5. McMahon, R.A.; Roberts, P.C.; Wang, X.; Tavner, P.J. Performance of BDFM as generator and motor. *IEE Proc. Electr. Power Appl.* **2006**, *153*, 289–299. [CrossRef]
6. Strous, T.D.; Polinder, H.; Ferreira, J.A. Brushless doubly-fed induction machines for wind turbines: Developments and research challenges. *IET Electr. Power Appl.* **2017**, *11*, 991–1000. [CrossRef]
7. Zhang, F.; Yu, S.; Wang, H.; Wang, Y.; Wang, D. Overview of research and development status of brushless doubly-fed machine system. *Chin. J. Electr. Eng.* **2016**, *2*, 1–13. [CrossRef]
8. Han, P.; Cheng, M.; Ademi, S.; Jovanovic, M.G. Brushless doubly-fed machines: Opportunities and challenges. *Chin. J. Electr. Eng.* **2018**, *4*, 1–17. [CrossRef]
9. Bell, L. Some Facts about Polyphase Motors. *Trans. Am. Inst. Electr. Eng.* **1894**, *11*, 559–569. [CrossRef]
10. Hunt, L.J. The "cascade" induction motor. *J. Inst. Electr. Eng.* **1914**, *52*, 406–426. [CrossRef]
11. Adams, A.D. Motor Speed Regulation. *Trans. Am. Inst. Electr. Eng.* **1899**, *16*, 443–445. [CrossRef]
12. Scott, C.F. Variable Speed Motor Control. *Trans. Am. Inst. Electr. Eng.* **1902**, *20*, 111–114. [CrossRef]
13. Siemens Brothers & Co. Ltd.; Lydall, F. Improvements in Polyphase Induction Motors. British Patent 16839, 23 July 1903.
14. Hunt, L.J. A new type of induction motor. *Electr. Eng. J. Inst.* **1907**, *39*, 648–667. [CrossRef]
15. Leonard, H.W. Volts vs. Ohms; Speed Regulation of Electric Motors. *Trans. Am. Inst. Electr. Eng.* **1896**, *13*, 373–386. [CrossRef]
16. Steinmetz, C.P. Operating alternating motors. U.S. Patent 587340 A, 3 August 1897.
17. Creedy, F. Some developments in multi-speed cascade induction motors. *Electr. Eng. J. Inst.* **1921**, *59*, 511–532. [CrossRef]
18. Broadway, A.R.W.; Burbridge, L. Self-cascaded machine: A low-speed motor or high-frequency brushless alternator. *Electr. Eng. Proc. Inst.* **1970**, *117*, 1277–1290. [CrossRef]
19. Smith, B.H. Theory and Performance of a Twin Stator Induction Machine. *IEEE Trans. Power Appar. Syst.* **1966**, *PAS-85*, 123–131. [CrossRef]
20. Smith, B.H. Synchronous Behavior of Doubly Fed Twin Stator Induction Machine. *IEEE Trans. Power Appar. Syst.* **1967**, *PAS-86*, 1227–1236. [CrossRef]
21. Wallace, A.K.; Spee, R.; Lauw, H.K. Dynamic modeling of brushless doubly-fed machines. In Proceedings of the Conference Record of the IEEE Industry Applications Society Annual Meeting, San Diego, CA, USA, 1–5 October 1989; pp. 329–334. [CrossRef]

22. Brune, C.S.; Spee, R.; Wallace, A.K. Experimental evaluation of a variable-speed, doubly-fed wind-power generation system. *IEEE Trans. Ind. Appl.* **1994**, *30*, 648–655. [CrossRef]

23. Abdi, E.; Mcmahon, R.; Malliband, P.; Shao, S.; Mathekga, M.E.; Tavner, P.; Abdi, S.; Oraee, A.; Long, T.; Tatlow, M. Performance analysis and testing of a 250 kW medium-speed brushless doubly-fed induction generator. *IET Renew. Power Gener.* **2013**, *7*, 631–638. [CrossRef]

24. Rochelle, P.; Spee, R.; Wallace, A.K. The effect of stator winding configuration on the performance of brushless doubly-fed machines in adjustable speed drives. In Proceedings of the Conference Record of the 1990 IEEE Industry Applications Society Annual Meeting, Seattle, WA, USA, 7–12 October 1990; pp. 331–337. [CrossRef]

25. Oraee, A.; Abdi, E.; McMahon, R.A. Converter rating optimisation for a brushless doubly fed induction generator. *IET Renew. Power Gener.* **2015**, *9*, 360–367. [CrossRef]

26. McMahon, R.A.; Abdi, E.; Malliband, P.D.; Shao, S.; Mathekga, M.E.; Tavner, P.J. Design and testing of a 250 kW medium-speed Brushless DFIG. In Proceedings of the 6th IET International Conference on Power Electronics, Machines and Drives (PEMD 2012), Bristol, UK, 27–29 March 2012; pp. 1–6. [CrossRef]

27. McMahon, R.A.; Mathekga, M.E.; Wang, X.; Tatlow, M.R. Design considerations for the brushless doubly-fed (induction) machine. *IET Electr. Power Appl.* **2016**, *10*, 394–402. [CrossRef]

28. Rüncos, F.; Carlson, R.; Sadowski, N.; Kuo-Peng, P. Performance analysis of a doubly fed twin stator cage induction generator. *Recent Developments of Electrical Drives*; Springer: Dordrecht, The Netherlands, 2006; pp. 361–373.

29. Oraee, A.; McMahon, R.; Abdi, E.; Abdi, S.; Ademi, S. Influence of Pole-pair Combinations on the Characteristics of the Brushless Doubly Fed Induction Generator. *IEEE Trans. Energy Convers.* **2020**, *35*, 1151–1159. [CrossRef]

30. Roberts, P.C. A Study of Brushless Doubly-Fed (Induction) Machines. Ph.D. Thesis, University of Cambridge, Cambridge, UK, 2004.

31. Roberts, P.C.; Long, T.; Mcmahon, R.A.; Shao, S.; Abdi, E.; Maciejowski, J.M. Dynamic modelling of the brushless doubly fed machine. *IET Electr. Power Appl.* **2013**, *7*, 544–556. [CrossRef]

32. Kusko, A.; Somuah, C.B. Speed Control of a Single-Frame Cascade Induction Motor with Slip-Power Pump Back. *IEEE Trans. Ind. Appl.* **1978**, *IA-14*, 97–105. [CrossRef]

33. Gorginpour, H.; Oraee, H.; Abdi, E. Calculation of Core and Stray Load Losses in Brushless Doubly Fed Induction Generators. *IEEE Trans. Ind. Electron.* **2014**, *61*, 3167–3177. [CrossRef]

34. Chapman, F. The production of noise and vibration by certain squirrel-cage induction motors. *J. Inst. Electr. Eng.* **1922**, *61*, 39–48. [CrossRef]

35. Abdi, S.; Abdi, E.; McMahon, R. A Study of Unbalanced Magnetic Pull in Brushless Doubly Fed Machines. *IEEE Trans. Energy Convers.* **2015**, *30*, 1218–1227. [CrossRef]

36. Van der Blij, N.H.; Strous, T.D.; Wang, X.; Polinder, H. A novel analytical approach and finite element modelling of a BDFIM. In Proceedings of the 2014 International Conference on Electrical Machines (ICEM), Berlin, Germany, 2–5 September 2014; pp. 346–352. [CrossRef]

37. Abdi, E.; Oraee, A.; Abdi, S.; McMahon, R.A. Design of the Brushless DFIG for optimal inverter rating. In Proceedings of the 7th IET International Conference on Power Electronics, Machines and Drives (PEMD 2014), Manchester, UK, 8–10 April 2014; pp. 1–6. [CrossRef]

38. Strous, T.D.; Wang, X.; Polinder, H.; Ferreira, J.A.B. Finite element based multi-objective optimization of a brushless Doubly-Fed Induction Machine. In Proceedings of the 2015 IEEE International Electric Machines Drives Conference (IEMDC), Coeur d'Alene, ID, USA, 10–13 May 2015; pp. 1689–1694. [CrossRef]

39. Wang, X.; Strous, T.D.; Lahaye, D.; Polinder, H.; Ferreira, J.A. Modeling and Optimization of Brushless Doubly-Fed Induction Machines Using Computationally Efficient Finite-Element Analysis. *IEEE Trans. Ind. Appl.* **2016**, *52*, 4525–4534. [CrossRef]

40. Wang, X.; Polinder, H.; Lahaye, D.; Ferreira, J.A. FE based multi-objective optimization of a 3.2 MW brushless doubly-fed induction machine. In Proceedings of the 2017 IEEE Workshop on Electrical Machines Design, Control and Diagnosis (WEMDCD), Nottingham, UK, 20–21 April 2017; pp. 89–94. [CrossRef]

41. Strous, T.D.; Wang, X.; Polinder, H.; Ferreira, J.A. Evaluating Harmonic Distortions in Brushless Doubly Fed Induction Machines. *IEEE Trans. Magn.* **2017**, *53*, 1–10. [CrossRef]

42. Mcmahon, R.; Tavner, P.; Abdi, E.; Malliband, P.; Barker, D. Characterising brushless doubly fed machine rotors. *IET Electr. Power Appl.* **2013**, *7*, 535–543. [CrossRef]

43. Xiong, F.; Wang, X. Design of a Low-Harmonic-Content Wound Rotor for the Brushless Doubly Fed Generator. *IEEE Trans. Energy Convers.* **2014**, *29*, 158–168. [CrossRef]

44. Logan, T.G.; McMahon, R.A.; Tavner, P.J.; Tohidi, S. A comparison of cage and nested-loop BDFM rotors. In Proceedings of the 6th IET International Conference on Power Electronics, Machines and Drives (PEMD 2012), Bristol, UK, 27–29 March 2012; pp. 1–6. [CrossRef]

45. Abdi, S.; Grace, A.; Abdi, E.; McMahon, R. A new optimized rotor design for brushless doubly fed machines. In Proceedings of the 20th International Conference on Electrical Machines and Systems (ICEMS), Sydney, NSW, Australia, 11–14 August 2017; pp. 1–6. [CrossRef]

46. Oraee, A.; Abdi, E.; Abdi, S.; McMahon, R.; Tavner, P.J. Effects of Rotor Winding Structure on the BDFM Equivalent Circuit Parameters. *IEEE Trans. Energy Convers.* **2015**, *30*, 1660–1669. [CrossRef]

47. Wallace, A.; Rochelle, P.; Spee, R. Rotor modeling and development for brushless doubly-fed machines. *Electr. Mach. Power Syst.* **1995**, *23*, 703–715. [CrossRef]
48. Wang, X.; Liu, D.; Polinder, H.; Lahaye, D.; Ferreira, J.A. Comparison of nested-loop rotors in brushless doubly-fed induction machines. In Proceedings of the 19th International Conference on Electrical Machines and Systems (ICEMS), Chiba, Japan, 13–16 November 2016; pp. 1–6.
49. Olubamiwa, O.I.; Gule, N.; Kamper, M.J. Coupled circuit analysis of the brushless doubly fed machine using the winding function theory. *IET Electr. Power Appl.* **2020**, *14*, 1558–1569. [CrossRef]
50. Strous, T.D.; Shipurkar, U.; Polinder, H.; Ferreira, J.A. Comparing the Brushless DFIM to other Generator Systems for Wind Turbine Drive-Trains. *J. Phys. Conf. Ser.* **2016**, *753*, 112014. [CrossRef]
51. Abdi, S.; Abdi, E.; Oraee, A.; McMahon, R. Optimization of Magnetic Circuit for Brushless Doubly Fed Machines. *IEEE Trans. Energy Convers.* **2015**, *30*, 1611–1620. [CrossRef]
52. Abdi, S.; Abdi, E.; Oraee, A.; McMahon, R.A. Investigation of magnetic wedge effects in large-scale BDFMs. In Proceedings of the 2nd IET Renewable Power Generation Conference (RPG 2013), Beijing, China, 9–11 September 2013; pp. 1–4. [CrossRef]
53. Logan, T.; Mcmahon, R.; Seffen, K. Noise and vibration in brushless doubly fed machine and brushless doubly fed reluctance machine. *IET Electr. Power Appl.* **2014**, *8*, 50–59. [CrossRef]
54. Strous, T.D.; Wang, X.; Polinder, H.; Ferreira, J.A.B. Brushless doubly-fed induction machines: Torque ripple. In Proceedings of the 2015 IEEE International Electric Machines Drives Conference (IEMDC), Coeur d'Alene, ID, USA, 10–13 May 2015; pp. 1145–1151. [CrossRef]
55. Chen, J.; Zhang, W. Harmonics in Brushless Doubly Fed Induction Generator for Torque Ripple Analysis and Modeling. *IEEE Trans. Magn.* **2014**, *50*, 1–4. [CrossRef]
56. Gorginpour, H.; Jandaghi, B.; Oraee, A.; Saket, M.A.; Ahmadian, M.; Oraee, H. Reduction of the torque ripple in Brushless Doubly-Fed Machine. In Proceedings of the 2011 3rd International Youth Conference on Energetics (IYCE), Leiria, Portugal, 7–9 July 2011; pp. 1–7.
57. Wang, X.; Strous, T.D.; Lahaye, D.; Polinder, H.; Ferreira, J.A. Effects of rotor skew on the performance of brushless doubly-fed induction machine. In Proceedings of the 2015 IEEE International Electric Machines Drives Conference (IEMDC), Coeur d'Alene, ID, USA, 10–13 May 2015; pp. 260–265. [CrossRef]
58. Roberts, P.C.; McMahon, R.A.; Tavner, P.J.; Maciejowski, J.M.; Flack, T.J. Equivalent circuit for the brushless doubly fed machine (BDFM) including parameter estimation and experimental verification. *IEE Proc. Electr. Power Appl.* **2005**, *152*, 933–942. [CrossRef]
59. Chang, Y.H.; Li, Y.T.; Lin, I.H.; Hsieh, M.F. A design approach integrating the magnetic circuit and electric circuit models for BDFIM. In Proceedings of the 2014 17th International Conference on Electrical Machines and Systems (ICEMS), Hangzhou, China, 22–25 October 2014; pp. 1685–1690. [CrossRef]
60. Hsieh, M.F.; Lin, I.H.; Hsu, Y.C.; McMahon, R.A. Design of Brushless Doubly-Fed Machines Based on Magnetic Circuit Modeling. *IEEE Trans. Magn.* **2012**, *48*, 3017–3020. [CrossRef]
61. Gorginpour, H.; Oraee, H.; McMahon, R.A. Electromagnetic-Thermal Design Optimization of the Brushless Doubly Fed Induction Generator. *IEEE Trans. Ind. Electron.* **2014**, *61*, 1710–1721. [CrossRef]
62. Gorginpour, H.; Oraee, H.; McMahon, R.A. A Novel Modeling Approach for Design Studies of Brushless Doubly Fed Induction Generator Based on Magnetic Equivalent Circuit. *IEEE Trans. Energy Convers.* **2013**, *28*, 902–912. [CrossRef]
63. Wang, X.; Roberts, P.C.; McMahon, R.A. Optimisation of BDFM stator design using an equivalent circuit model and a search method. In Proceedings of the 3rd IET International Conference on Power Electronics, Machines and Drives (PEMD 2006), Dublin, Ireland, 4–6 April 2006; pp. 606–610. [CrossRef]
64. Wang, X.; McMahon, R.A.; Tavner, P.J. Design of the Brushless Doubly-Fed (Induction) Machine. In Proceedings of the 2007 IEEE International Electric Machines Drives Conference, Antalya, Turkey, 3–5 May 2007; pp. 1508–1513. [CrossRef]
65. Wang, X.; Strous, T.D.; Lahaye, D.; Polinder, H.; Ferreira, J.A. Finite element modeling of brushless doubly-fed induction machine based on magneto-static simulation. In Proceedings of the 2015 IEEE International Electric Machines Drives Conference (IEMDC), Coeur d'Alene, ID, USA, 10–13 May 2015; pp. 315–321. [CrossRef]
66. Olubamiwa, O.I.; Gule, N. Design and optimization of a Cage + Nested loops rotor BDFM. In Proceedings of the 2020 International Conference on Electrical Machines (ICEM), Gothenburg, Sweden, 23–26 August 2020; pp. 1868–1874. [CrossRef]
67. Olubamiwa, O.I.; Gule, N. Prioritizing power factor in power density assessments of doubly fed induction generator alternatives. In Proceedings of the 2020 International Symposium on Power Electronics, Electrical Drives, Automation and Motion (SPEEDAM), Sorrento, Italy, 24–26 June 2020; pp. 47–52.

# Evaluation of Drive Cycle-Based Traction Motor Design Strategies Using Gradient Optimisation

**Stavros Pastellides \*, Stiaan Gerber, Rong-Jie Wang and Maarten Kamper**

Department of Electrical & Electronic Engineering, Stellenbosch University, Stellenbosch 7600, South Africa; sgerber@sun.ac.za (S.G.); rwang@sun.ac.za (R.-J.W.); kamper@sun.ac.za (M.K.)
\* Correspondence: 17509955@sun.ac.za

**Abstract:** In this paper, two design optimisation methods are evaluated using gradient-based optimisation for electric vehicle traction applications. A driving cycle-based approach is used to evaluate specific operational points for the design optimisation procedure. To determine the operational points, an energy centre of gravity (ECG) approach is used. Both optimisation methods are described, namely the point based method and the flux mapping method, with a focus on the flux mapping procedure. Within the flux mapping approach, an inner optimisation loop is defined in order to maintain the stability of gradient calculation for the gradient-based optimisation. An emphasis is placed on the importance of how the optimisation problem is defined, in terms of the objective function and constraints, and how it affects a gradient based optimisation. Based on a design case study conducted in the paper, it is found that the point-based strategy realised motor designs with a slightly lower overall cost (5.66% lower than that of the flux mapping strategy with 8 ECG points), whereas the flux mapping strategy found motor designs with a lower input energy (1.48% lower than that of the point-based strategy with 8 ECG points). This may be attributed to the difference in the definition and interpretation of constraints between these two methods. It is also shown that including more operational points from the driving cycle in the design optimisation leads to designs with reduced total input energy and thus better drive-cycle energy efficiency. This paper further illustrates the significant computational advantages of a gradient-based optimisation over a global optimisation method as it can be completed within a fraction of the time while still finding a global optimum, as long as the problem definition is correctly determined.

**Keywords:** design optimisation; drive cycle; electric vehicle; finite element analysis; gradient-based optimisation; permanent magnet machines

## 1. Introduction

There is a global increase in the use of electrified power trains within the transportation sector. Electric motors are one of the critical components in electric vehicle (EV) power trains. The design of these electric motors can be a challenging task as it involves multiple design considerations such as the efficiency, cost, size, weight, and torque quality or a combination of them [1–4]. Traditionally, the EV motor design mainly focuses on one or two key working points of the torque–speed envelope [5–7]. In recent years, driving cycle-based motor design optimisation, where the efficiency of the machine over the entire driving cycle is considered, has become increasingly popular. Several works have been carried out utilising finite element analysis (FEA) and driving cycle-based techniques to maximise the efficiency of the motor over a driving cycle. In [2], a system level design optimisation is conducted over multiple driving modes for a synchronous reluctance machine, while in [3], a design optimisation is undertaken which optimises the efficiency of the permanent magnet (PM) motor over a given driving cycle. The research conducted in these papers shows the significance of using equivalent working points from the driving cycle analysis, as well as how a design optimisation can be conducted for a driving-cycle based design.

As it is not feasible to optimize a motor design for every speed and torque point of the driving cycle, certain data segmentation and clustering techniques are required. There are many different methods to consider when determining these representative points. In [8], the equivalent representative points from the driving cycle are determined through a centre of gravity means. This method determines these points by breaking the driving cycle up into equivalent grids and using the equivalent centre of gravity for these points over the grid space. With this method, it was shown that an increase in overall efficiency is obtained compared to a key working point optimisation technique. However, this method has also a weakness—i.e., it may not fully encapsulate the primary working points at which the motor operates during the driving cycle.

In [1,9–12], the energy representative points are defined through an energy center of gravity approach from the driving cycle, which is used to maximise the energy efficiency of an EV's traction motor over the driving cycle. The energy centre of gravity is similar to the center of gravity method; however, it uses the equivalent energy distribution over the driving cycle instead of the speed–torque points. In [9], the maximum energy efficiency of an EV was defined and presented. A total of 12 equivalent operating points were used from the driving cycle with different energy distributions. The proposed design technique was further validated by a design case and measurement results. In [10], the influences of different driving cycles on design optimisations for PM motors are analysed. From the research conducted, it was shown that for all different driving cycles used, a high efficiency is achieved over a wide torque–speed range. This further proves the validity of the energy center of gravity approach.

In [11], an optimised torque distribution strategy of maximising the motor efficiency for a front and rear-wheel driven EV is described. By using the energy center of gravity method, an understanding was developed of the energy consumption during the low-torque region for a particular driving cycle. In [12], a hybrid approach of combining a data clustering and energy center approach was implemented. It was found in the research that the energy center of gravity and hybrid approaches both converged to similar results, which shows that either can be used when a drive cycle-based optimisation is required. These papers show the validity of the energy center of gravity approach and its use in determining equivalent working points from a driving cycle.

In [4,13], a k-means clustering algorithm is used in order to determine the most relevant points from an energy distribution of the driving cycle. From both papers, the k-means algorithm helped to locate the key areas where the greatest amount of energy is consumed from the driving cycle using a data mining algorithm. This method helps to define the most important working points that the motor operates at compared to a segmented approach. Further, an evaluation is conducted in [1] for different clustering and grouping methods of representative points from the driving cycle. It was shown that by considering these representative operating points, an improved efficiency can be found over a single operating point method. There is clearly an advantage for the drive cycle-based motor design approaches when compared with the traditional design approach.

It is further noted that using different optimisation and design techniques plays a vital role as well. Methods are used where the representative points of the driving cycle are simulated through finite element (FE) analysis, where the specified voltage and current are determined for each particular point. One method that can be taken into consideration is a simple point-based method. DQ currents of the motor for specific operating points are used to determine the output parameters of the motor at specified speed points. These parameters include the voltage, torque, current density, and flux-linkage. This is seen to be one of the easier methods to implement for design techniques. One other method which is considered is the use of flux-linkage mapping. This method simulates a flux-linkage map for a motor design. The map is then searched over in order to find the best operational parameters for the specified operating point [4,10,14–17]. An area that is not always clear for EV motor designers is the choice of suitable design strategies to use for FEA-based

design optimisation procedures. An understanding is required of the differences between the two methods, as well as their respective implementations.

In the above-discussed literature, global optimisation algorithms are almost exclusively used in machine design optimisations, which shows the popularity of the global optimisation algorithms in engineering designs [18]. Despite the advantages of these global optimisation algorithms, they are known to be computationally expensive when compared with their gradient-based counterparts. Gradient-based optimisation has been shown to be more computationally efficient than global optimisation methods, especially when many variables are being considered. Yet, the latter also suffers from finding local minima and its dependence of the starting values of variables [19]. In [20], a gradient-based optimisation was used for a grid-connected wound-rotor induction motor. It was shown that for the gradient based optimisation problem, the gradient-based algorithm needs to be carefully formulated to ensure a global minimum is found. Success was also shown in [21] using gradient-based optimisation; however, only a two-point method was used instead of the full driving cycle analysis. Furthermore, in [22], it was determined that the gradient-based optimisation method used was comparable to a global optimisation solution with the gradient method converging in a faster time.

In this paper, an evaluation is conducted of the two design techniques for traction motors—namely, the point-based design and the flux-linkage map methods—through gradient-based design optimisation. This is conducted in order to show the differences between both design techniques and to help to choose a technique to implement for traction design. Further, this paper shows that gradient-based design optimisation is still an attractive method for traction motor designs as it is computationally efficient and effective in locating a global optimum, provided that the design optimisation is carefully configured. The remaining part of the paper is organised as follows: in Section 2, the driving cycle is analysed and the equivalent representative points are determined. In Section 3, the different design optimisation techniques are elaborated on. In Section 4, an evaluation is conducted for both techniques, and the design and simulation of a case study machine is conducted. Lastly, relevant conclusions are drawn in Section 5.

## 2. Drive Cycle Analysis

In this section, the motor torque–speed envelope based on the specifications of the studied electric vehicle and the world-wide harmonised light-duty vehicle test procedure (WLTP) drive cycle for a class 3 vehicle is described. The motor energy consumption distribution over the WLTP drive cycle is analysed and is then used to determine certain representative points through clustering techniques. These representative points are important for formulating a drive cycle-based optimisation process.

### 2.1. Electric Vehicle and Motor Design Specifications

An electric vehicle with the capabilities of being able to operate in suburban areas is investigated for a drive cycle-based optimisation in this paper. The power train topology of the vehicle is shown in Figure 1, where a PM motor is coupled to the front axial of the vehicle via a differential. The power and torque capabilities of the motor are derived through fundamental analytical vehicle load equations, which take into account the vehicle's resistances and acceleration [23,24]. The specifications and properties of the investigated EV and motor are given in Table 1, with wind resistance being regarded as negligible for this case study.

### 2.2. Determining Representative Points from the Driving Cycle

The torque and speed demand required by the vehicle is analysed over the WLTP drive cycle. This driving cycle procedure is predominately used to measure fuel consumption, $CO_2$ emissions, pollutant emissions, and the energy consumption of alternative power trains such as electric vehicles [25]. The driving cycle has a duration of 1800 s, with a distance of 23,266 m. The driving cycle is divided up into four different sub-systems, with

each simulating an urban, suburban, rural, and highway driving scenario, respectively. The maximum speed required by the cycle is 131.3 km/h. The speed profile of the WLTP is shown in Figure 2.
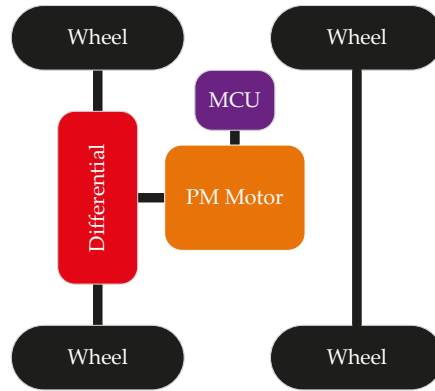


**Figure 1.** The power train of the light EV.

**Table 1.** Specifications of proposed EV Design.

|  | Parameters | Value |
|---|---|---|
| Electric | Wheel radius (m) | 0.27 |
| Vehicle | Vehicle frontal area (m$^2$) | 2.5 |
|  | Aerodynamic drag coefficient ($C_d$) | 0.3 |
|  | Rolling resistance coefficient ($C_r$) | 0.013 |
|  | Vehicle mass (kg) | 1000 |
|  | Differential gear ratio | 6:1 |
|  | Maximum vehicle speed (km/h) | 131.3 |
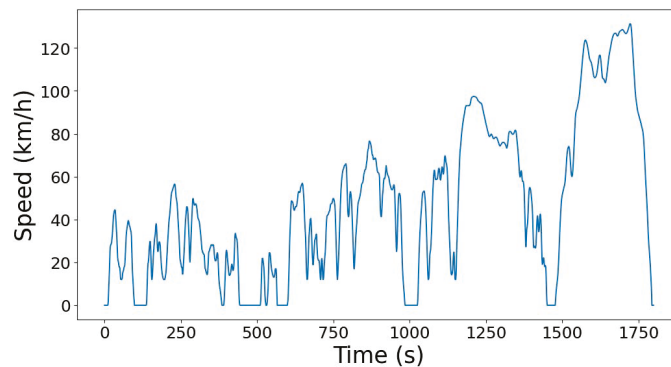


**Figure 2.** Motor speed over the WLTP range.

Using the vehicle dynamics model in [23,24], the required traction efforts for the given wheel radius and differential gear ratio can be determined [3,8]. The torque requirements over the driving cycle range can be readily calculated and mapped as shown in Figure 3. As the motor is designed and optimised for motor operation, regenerative braking is not considered. The torque distributions over the entire motor speed range (constant torque and constant power) for the WLTP driving cycle are given in Figure 4.
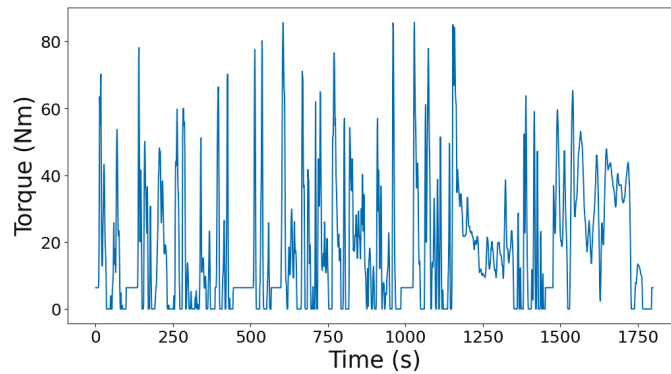
**Figure 3.** Motor torque over the WLTP drive cycle.
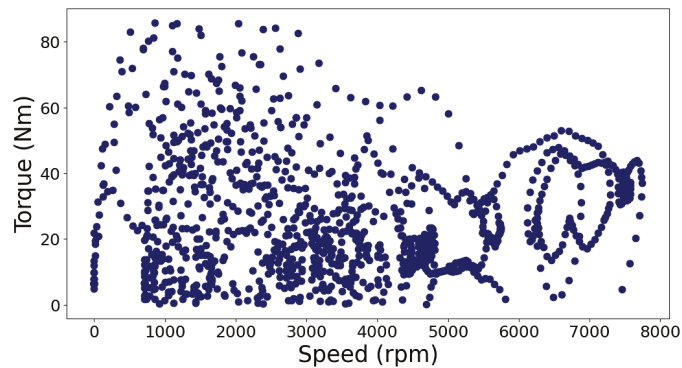


**Figure 4.** Vehicle torque profile for the WLTP speed range.

Several different methods are used to determine the representative operating points from a driving cycle for the design optimisation process. In [8,26], the geometric center of gravity method is used, which is based on the geometric representation of torque distribution points within an area of the driving cycle. Essentially, this method focuses on the greatest amount of time for which the motor operates within a given area specified by the user. Another method used to determine the operating points for a driving cycle is the use of the distribution of energy consumed during a driving cycle. Figure 5 shows the energy load profile of the motor in joules, which is determined from the product of torque and speed in Figure 4 over a time period for each torque and speed point. Determining the representative points from the load energy distribution can be done in multiple ways. In [1,9–12,27], the energy center of gravity (ECG) method is used, which is based on the energy distribution of points within a region of the driving cycle. This method considers the amount of energy used within each region and the weight of the energy for the representative points. Another method is the use of clustering methods. Different types of clustering techniques can be used in order to determine the representative points [1,4,12,13,28]. An evaluation of different methods of choosing the representative points and their respective impact on the design optimisations is reported in [1,12].

For this study, the ECG method is used. The load energy density of the drive cycle is divided up into $i$ clusters. The energy, $E_i$, of the $i$th cluster or region is calculated as

$$E_i = \sum_{j=1,2\ldots}^{N_i} E_{j,i} \tag{1}$$

where $N_i$ is the number of operating points within each *i*th cluster and *j* is the number of clusters chosen. The calculated representative torque and speed points within each region, $T_{eq,i}$ and $\omega_{eq,i}$, are given as follows:

$$T_{eq,ij} = \frac{1}{E_i} \sum_{j}^{N_i} E_{ij} T_{ij} \tag{2}$$

$$\omega_{eq,i} = \frac{1}{E_i} \sum_{j=1}^{N_i} E_{ij} \omega_{ij} \tag{3}$$
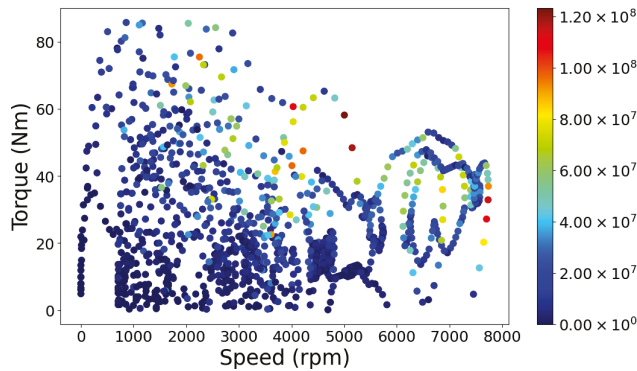


**Figure 5.** Load energy consumption over the WLTP drive cycle

In order to account for the magnitude of each representative point calculated, a weighting factor is required for the optimisation design. These weighting factors are determined according to the amount of required energy during the driving cycle process. These weighting factors of the representative points are calculated according to the ratio of energy consumed by all the operating points during the driving cycle, given as [1]

$$W_{E,i} = \frac{E_i}{\sum_{k=1,2\ldots} E_k} \tag{4}$$

where *k* is each operating point of the drive cycle. By using Equations (1)–(4) and specifying the number of clusters to be 8, the representative points shown in Figure 6 are defined in Table 2. The motor parameters can be deduced and are given in Table 3.

**Table 2.** Summary of representative points.

| Region | Point | Weighting of Energy $W_E$ |
|---|---|---|
| 0–2000 rpm 0–42.8 Nm | 1345.9 rpm 26.01 Nm | 4.64% |
| 0–2000 rpm 42.8–85.8 Nm | 1351 rpm 60.1 Nm | 10.15% |
| 2001–4000 rpm 0–42.8 Nm | 3182.5 rpm 24.69 Nm | 20.93% |
| 2001–4000 rpm 42.8–85.8 Nm | 2806.6 rpm 56.27 Nm | 15.1% |
| 4001–6000 rpm 0–42.8 Nm | 4861.8 rpm 26.02 Nm | 14.36% |

**Table 2.** *Cont.*

| Region | Point | Weighting of Energy $W_E$ |
|---|---|---|
| 4001–6000 rpm 42.8–85.8 Nm | 4601.7 rpm 53.5 Nm | 5.88% |
| 6001–8000 rpm 0–42.8 Nm | 7014.1 rpm 29.42 Nm | 19.42% |
| 6001–8000 rpm 42.8–85.8 Nm | 6897.2 rpm 44.48 Nm | 9.53% |
| Base Speed Maximum Torque | 3000 rpm 118.7 Nm | N/A |
| Maximum Speed Torque | 8000 rpm 44.5 Nm | N/A |
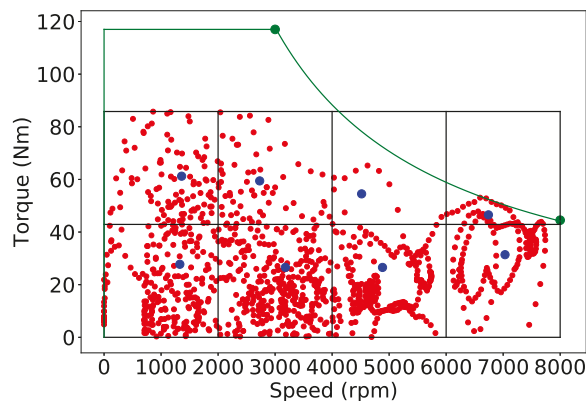


**Figure 6.** Representative points from ECG.

**Table 3.** Specifications of proposed motor design.

| Parameters | Value |
|---|---|
| Nominal power (kW) | 37.28 |
| Motor base speed (r/min) | 3000 |
| Motor maximum speed (r/min) | 8000 |
| Maximum torque (maximum speed) (Nm) | 44.5 |
| Peak torque (base speed) (Nm) | 118.7 |
| CPSR | 2.66 |

## 3. Design Optimisation Procedure

The motor topology considered for this study is a 24-slot, 8-pole V-shaped interior permanent magnet (IPM) machine. For the finite element based design, a parametric 2D model is shown in Figure 7 with the relevant design parameters that are used for the design optimisation. For each design consideration, a rather conservative slot fill factor of 0.35 is assumed with the temperature of the stator windings and the PM being 120 °C and 80 °C, respectively. Further, given the power rating and the space constraints of the motor, the maximum current density allowed is set to be 10 A/mm$^2$ in the design, which means that the motor is required to be water cooled. More detailed motor design specifications are tabulated in Table 4.

To evaluate the motor capabilities for the optimisation procedures, the torque and voltage are required for each operating point as given by (5)–(7), where $v_d$, $v_q$, $i_d$, $i_q$, $L_d$, and $L_q$ are the $d$ and $q$-axis voltages, currents, and inductances, respectively, $R_s$ is the phase

resistance, $\lambda_{PM}$ is the PM's flux-linkage, $\omega_e$ is the electric angular speed, $p$ is the number of pole pairs, and $T_e$ is the electromagnetic torque, as described in [29].

$$T_e = \frac{3}{2}p[\lambda_{PM} + (L_d - L_q)i_d]i_q \tag{5}$$

$$v_d = R_s i_d - \omega_e L_q i_q \tag{6}$$

$$v_q = R_s i_q + \omega_e(L_d i_d + \lambda_{PM}) \tag{7}$$
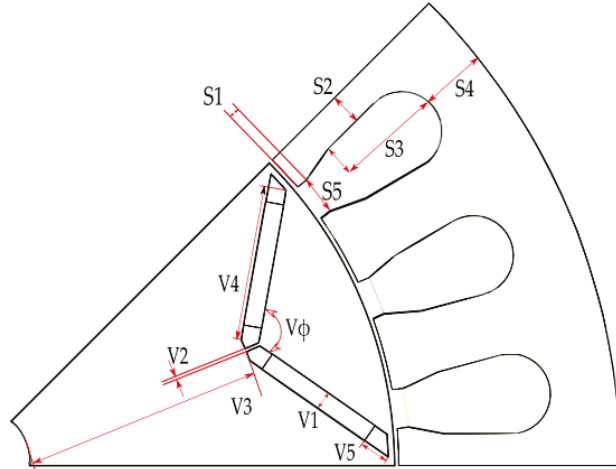


**Figure 7.** Cross section of motor parameters .

**Table 4.** Motor design specifications.

| Parameters | Value |
|---|---|
| Number of pole pairs | 4 |
| Number of slots | 24 |
| Air-gap length | 1 mm |
| Winding fill factor | 0.35 |
| Lamination steel | M19_26G |
| PM material and grade | NdFeB N48H |
| Maximum Line voltage | 310 V |
| Maximum phase current | 75 A |
| Maximum current density | 10 A/mm$^2$ |

Further, in order to calculate the efficiency of all the representative points of the driving cycle, Equations (8)–(10) can be used, where the windage and friction losses are not considered. The core losses ($P_{core}$) in Equation (9) are computed by employing time-step FE solutions and the Steinmetz-based equation [30]. The copper losses are calculated using the finite element mesh in the copper area on a per element basis.

$$P_{copper} = \sum_{e=1}^{n} \frac{J^2 k_f A_e L(1 + k_{ew})}{\sigma} \tag{8}$$

where $n$ is the number of elements in the copper area, $J$ is the RMS current density, $k_f$ is the copper fill factor, $A_e$ is the area of element $e$, $L$ is the active stack length of the machine, $k_{ew}$ is the ratio of end-winding length to stack length, and $\sigma$ is the conductivity of copper.

$$\eta = \frac{T_e \cdot \omega}{T_e \cdot \omega + P_{copper} + P_{core}} \tag{9}$$

$$\eta_{eng} = \sum_{i=1}^{N} \eta_i \cdot \omega_{eq,i} \tag{10}$$

By using the $\eta_{eng}$ value as the average efficiency, which takes into account the weighting of energy, and ensuring a constraint is added to this, an overall high efficiency can be maintained for the motor's operating range. Within the optimisation methods discussed further, the minimum constraint of $\eta_{eng}$ is chosen to be 94% due to the allowed cooling capabilities and loss restrictions for the specified case study motor.

### 3.1. Optimisation Strategies

The optimisation algorithm used within each method of this study is the sequential least squares programming algorithm (SLSQP) [31], which is a gradient-based optimisation method. The SLSQP algorithm minimises a single objective function of multiple variables, subject to both equality and inequality constraints. Both optimisation strategies implemented are conducted using an in-house 2D FE package. Although gradient-based algorithms are more efficient than global methods for electrical machine design with many design variables, they are susceptible to becoming trapped into a local optimum and numerical noise [32]. While the former can be mitigated by using different starting points, the latter can still affect the accuracy and stability of the gradient evaluation for gradient-based optimisation. For this study, a unique implementation of a gradient-based optimisation procedure is applied, which employs a mesh reshaping technique described in [33]. This technique shows significant improvements on the performance of gradient-based optimisation, as it helps with the stability of the gradient calculation while maintaining the mesh quality over a large design space.

#### 3.1.1. Point Based Optimisation Strategy

The first optimisation method considered is the point-based optimisation strategy. This method evaluates the motor design along $-n$ points specified from the driving cycle. By evaluating the motor along these design points, it ensures the motor is within the constant power speed range (CPSR) limits set by the user. The motor design is evaluated through an optimisation loop which adjusts both the rotor and stator geometric variables, as well as the dq-currents at each operating point, inherently adjusting the optimal current angle. This process is shown in Figure 8. This method begins by the user setting the initial geometric and operating point parameters. The geometric parameters are given boundaries, and constraints are assigned to the operating point parameters. It is possible to include a relatively large number of design points in the optimisation loop within an efficient time span.

The optimisation problem is formulated as

$$
\begin{aligned}
\text{Minimise:} \quad & F(\mathbf{X}) = C_{\text{total}} \\
\text{Subject to:} \quad & T_x \geq T_{min} \,(\text{Nm}) \\
& V_{LLx} \leq V_{max} \,(\text{V}) \\
& I_{\phi x} \leq I_{max} \,(\text{A}) \\
& \eta_{\text{eng}} \geq \eta_{engmin} \\
& B_{MMx} \geq B_{max} \,(\text{T}) \\
& J_x \leq J_{max} \,(\text{A/mm}^2)
\end{aligned}
\tag{11}
$$

where $\mathbf{X}$ represents the vector of design variables, which includes the geometric variables and $dq$-currents for each operating point of the machine. $C_{\text{total}}$ is the cost of the active material of the machine, which includes PM material, copper, and steel. The costs of

materials used are given in Table 5. $T_{min}$ is the minimum torque for each operating point, $V_{LLx}$ and $I_{\phi x}$ are the maximum allowable voltage and current for each operating point, respectively, $B_{MMx}$ is the demagnetisation margins of the magnets at each operating point, and $J_{max}$ is the maximum current density allowed. The intrinsic value of this method is the rapid computational time when few points are selected from the driving cycle, as well as the simplicity of the optimisation process.
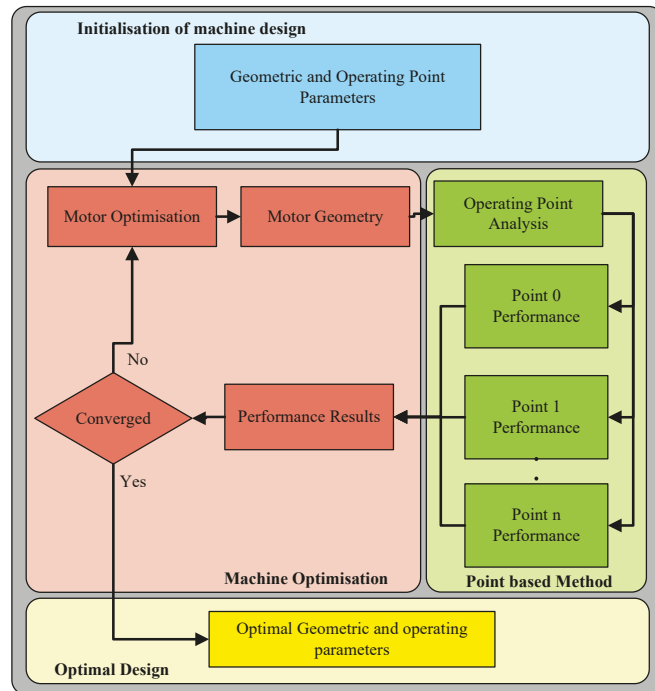


**Figure 8.** Point-based optimisation flow chart.

**Table 5.** Costs of materials.

| Material | Cost |
| --- | --- |
| PM | $50/kg |
| Silicon steel | $2/kg |
| Copper | $6.67/kg |

### 3.1.2. Flux Mapping Optimisation Strategy

The second optimisation strategy considered is the flux mapping strategy. The process of using flux maps for the optimisation is where the flux linkages on the *dq*-axis are formulated across multiple points, and an interpolation of these points is mapped out. The flow diagram of this method is shown in Figures 9 and 10. A single geometric design is evaluated over multiple points set by the user, similar to the point-based method. However, a look up map of the entire *dq*-parameters is generated. The formulation of a flux map is seen to be less computationally efficient compared to the point-based method due to each *dq*-current point being simulated. However, it has the advantage of the algorithm determining the best fit current curve for each geometric design on all operating points specified, known as the maximum torque per ampere (MTPA) curve. This further allows the user to discern the full capabilities of the motor. An example of the *d*- and *q*-axis

flux-linkage map of a motor design is shown in Figure 11, which is used to determine the torque map in Figure 12.
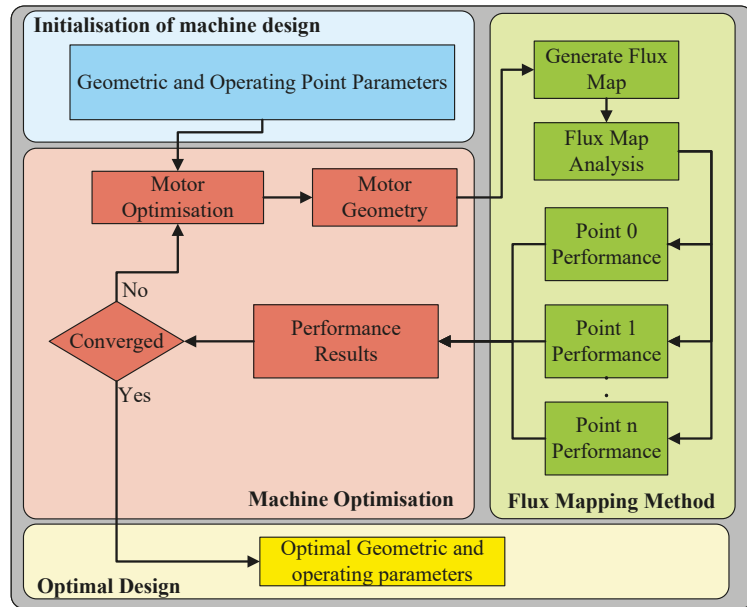


**Figure 9.** Flux mapping optimisation flow chart.
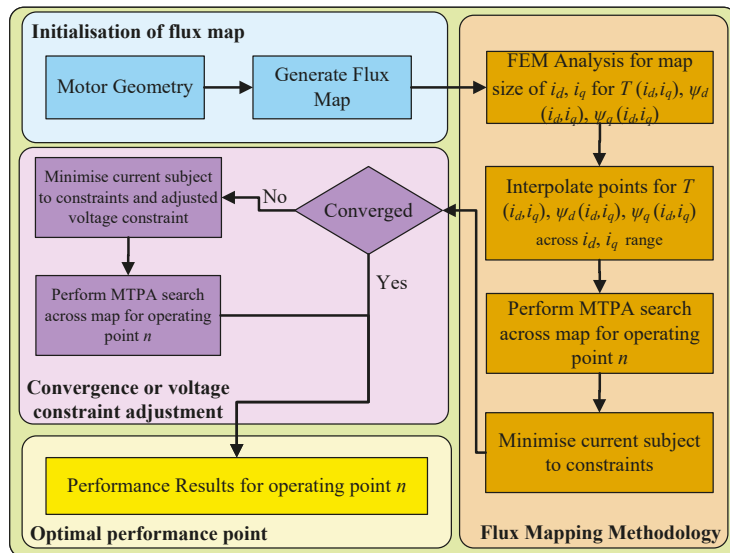


**Figure 10.** Flux mapping methodology.

(**a**)



(**b**)
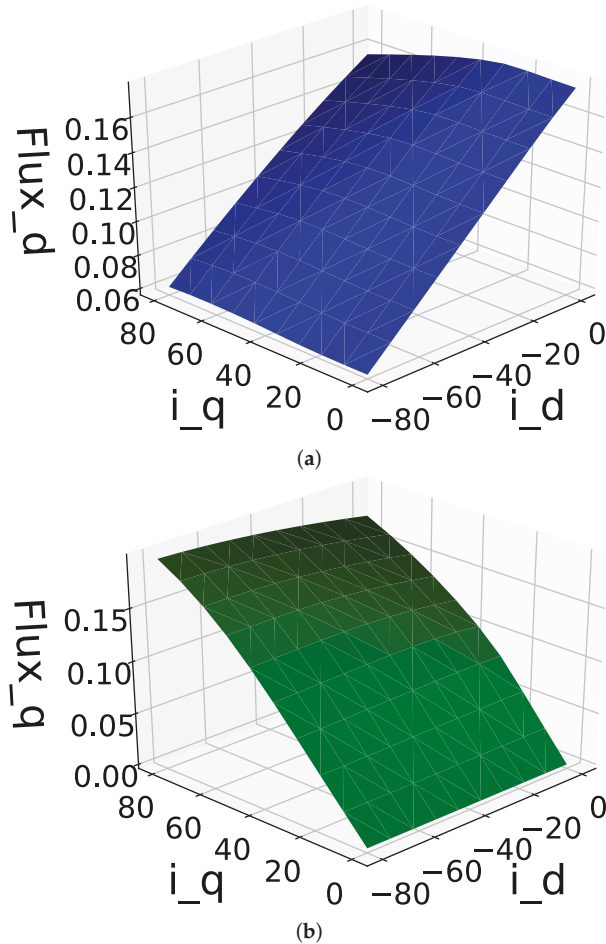
**Figure 11.** Flux-linkage maps with dq-axis currents (**a**) *d*-axis flux-linkage (**b**) *q*-axis flux-linkage.

In order to evaluate the MTPA on the flux map for each of the operating points, the SLSQP is used once more. This method searches along the flux map while keeping to the specifications set for the *dq*-currents, as shown in Figure 10. The bound and constraints for each operating point on the outer optimisation loop (where the geometric parameters of the machine are optimised) are defined as

$$
\begin{aligned}
\text{Minimise:} \quad & F(\mathbf{X}) = C_{\text{total}} \\
\text{Subject to:} \quad & T_x \geq T_{point} \text{ (Nm)} \\
& V_{LLx} \leq V_{max} \text{ (V)} \\
& I_{\phi x} \leq I_{max} \text{ (A)} \\
& \eta_{\text{eng}} \geq \eta_{engmin} \\
& B_{MMx} \geq B_{max} \text{ (T)} \\
& J_x \leq J_{max} \text{ (A/mm}^2)
\end{aligned}
\tag{12}
$$

where **X** represents the vector of design variables of the machine. $T_{point}$ is the minimum torque for each operating point.
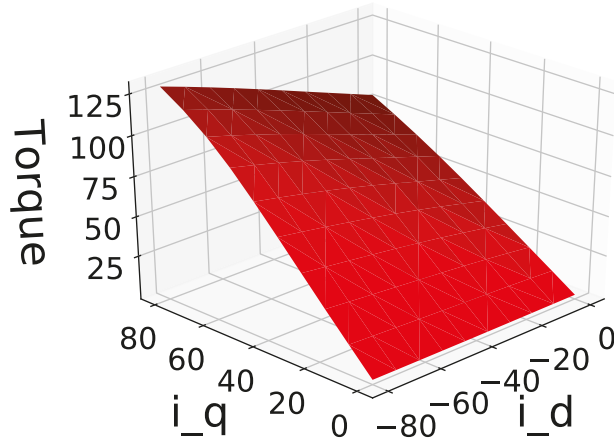
**Figure 12.** Torque flux map with *dq*-axis currents.

For the inner optimisation loop, where the operating point is evaluated according to the MTPA point on the flux map, the optimisation problem is formulated as

$$
\begin{aligned}
\text{Minimise:} \quad & F(\mathbf{X}) = I_\phi \ (\text{A}) \\
\text{Subject to:} \quad & T_x \geq T_{point} \ (\text{Nm}) \\
& V_{LL} \leq V_{max} \ (\text{V})
\end{aligned}
\tag{13}
$$

where **X** represents the vector of the *dq*-currents as well as the constant of the specified speed for the evaluated operating point. $T_x$ is the set torque value for each operating point. By finding the MTPA point, the output parameters and *dq*-currents are returned to the outer optimisation loop for the geometric design, as shown in Figures 9 and 10.

However, during the design optimisation process, certain outcomes may arise during the outer optimisation process. When a design with certain geometric parameters is simulated, various parameters, such as $V_{LL_x}$, may not be within the constraints of $V_{max}$ for any *dq*-currents specified. This may occur when the magnet thickness is sizeable and a large flux linkage is evident. This generates a significant back-EMF in the motor. From this, the inner optimisation algorithm (MTPA) may not able to satisfy the constraints being violated for these points, which either results in the optimisation algorithm failing and terminating or resulting in large gradients occurring during the outer optimisation loop. This further causes the gradient-sensitive optimisation to be incapable of finding the correct minimum cost. In [17], the voltage constraints were handled by formulating an optimisation objective function using Lagrange multipliers. However, the applied on–off gate function may negatively impact the accuracy and stability of the gradient calculations, which is not ideal for gradient-based optimisations. To ensure that the objective and constraints are relatively smooth functions, an optimisation inner-loop shown in Figure 10 has been formulated to deal with these non-convergence cases; i.e.,

$$
\begin{aligned}
\text{Minimise:} \quad & F(\mathbf{X}) = \alpha^2 \\
\text{Subject to:} \quad & V_{LL} \leq V_{LL_{max}} (1 + \alpha)^2 \ (\text{V}) \\
& T_x \geq T_{point} \ (\text{Nm}) \\
& I_\phi \leq I_{max} \ (\text{A})
\end{aligned}
\tag{14}
$$

where **X** represents the vector of the *dq*-currents, as well as the constant of the specified speed for the evaluated operating point. $\alpha$ is chosen as a variable parameter that adjusts the maximum voltage constraint during each iteration of the optimisation loop. During the

inner optimisation loop search across the flux map, the constraints given may be violated. From here, this variable parameter is adjusted, which shifts the maximum voltage of the design. Therefore, the constraints may be further improved with each iteration, until a valid design is found. The objective of this optimisation is still tasked with minimising the current on the flux map subject to the constraints; however, the added parameter is also required to be set at a minimum to ensure that the voltage constraint is not overly inflated. This allows the outer optimisation loop to have a smoother gradient for each iteration where a non valid design is found, which improves the gradient-based optimisation of the SLSQP.

## 4. Evaluation of Optimisation Strategies

A summary of the optimisation results for different numbers of ECG points is given in Table 6. For each design variation that is developed with different ECG points, the base speed and maximum speed points are also required to be evaluated to ensure that the correct operating parameters are able to be reached. From the results of Table 6, it is seen that the multi-point method generally has a better output result in terms of the objective function of costing when compared to the flux mapping method, with a note regarding the difference in cost for 8 ECG points, with the multi-point method being 5.66% less than the flux mapping method. The number of ECG points included in the optimisation has a greater influence on the optimum results from the flux mapping method than those from the multi-point method.

**Table 6.** Evaluation of optimisation method results.

| Number of ECGs | Parameters | Multi-Point | Flux Mapping |
|---|---|---|---|
| 2 | Total cost ($) | 108.26 | 109.2 |
| | Total mass (kg) | 21.57 | 21.83 |
| | PM mass (kg) | 0.726 | 0.771 |
| | Copper mass (kg) | 6.48 | 6.11 |
| | Steel mass (kg) | 14.36 | 14.95 |
| 4 | Total cost ($) | 108.21 | 115.94 |
| | Total mass (kg) | 26.87 | 24.09 |
| | PM mass (kg) | 0.604 | 0.881 |
| | Copper mass (kg) | 5.45 | 5.46 |
| | Steel mass (kg) | 20.81 | 17.75 |
| 6 | Total cost ($) | 108.62 | 111.83 |
| | Total mass (kg) | 21.59 | 23.965 |
| | PM mass (kg) | 0.748 | 0.735 |
| | Copper mass (kg) | 6.32 | 6.13 |
| | Steel mass (kg) | 14.51 | 17.1 |
| 8 | Total cost ($) | 106.23 | 112.42 |
| | Total mass (kg) | 23.93 | 25.66 |
| | PM mass (kg) | 0.61 | 0.63 |
| | Copper mass (kg) | 6.26 | 6.66 |
| | Steel mass (kg) | 17.06 | 18.37 |

Figures 13–16 show the efficiency maps of the optimum designs, with two ECGs and eight ECGs for both optimisation methods. It is evident that the more ECG points are added, the greater the increase in the overall efficiency range. The flux mapping method has a slightly better performance in terms of the efficiency range for both two ECG and eight ECG cases. This is further elaborated upon in Table 7, which shows that the drive cycle energy consumption for the designs generated from the flux mapping method is invariably lower than that of the multi-point designs. The difference for the flux mapping method for two ECG points and eight ECG points is a reduction in total input energy by 1.25%, whereas for the multi-point method, it is only 0.07%. In contrast, the flux mapping method with eight ECG points is 1.48% lower in terms of the total input energy for the

eight ECG points. The total input energy given is determined by taking all the points of the driving cycle in Figure 5, and determining from the MTPA algorithm an efficiency map and the efficiency at each point. The total output energy from Equation (1) is used and the corresponding efficiency is incremented, allowing the total input energy required to be given. A pseudo-code is shown in Figure 17 of this process.
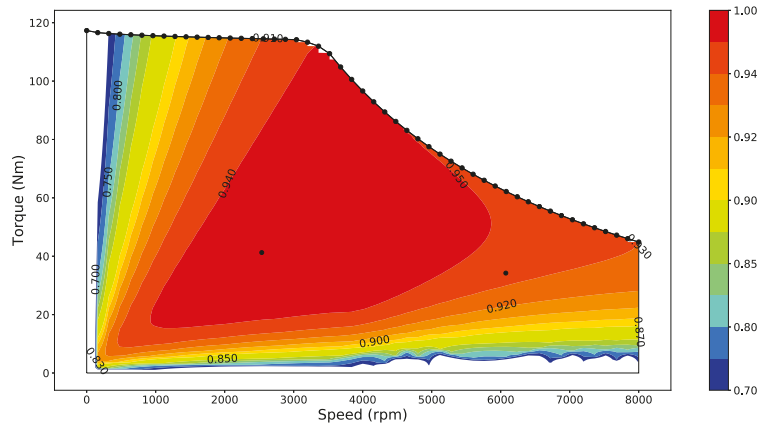


**Figure 13.** Efficiency map of two ECG points with multi-point method.
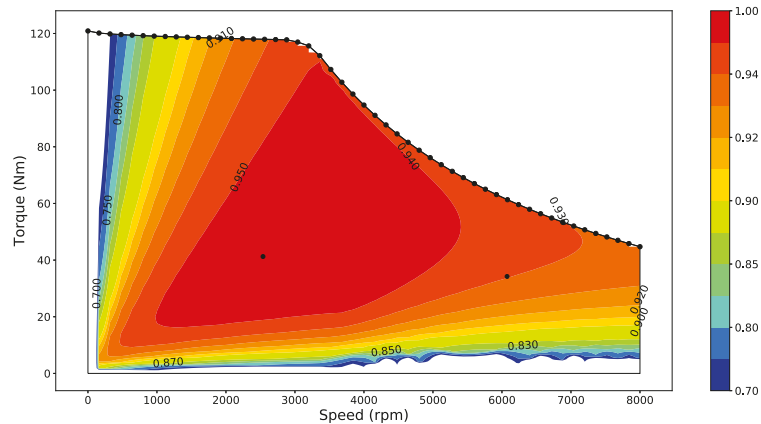


**Figure 14.** Efficiency map of two ECG points with flux map method.

The reason that the flux mapping method realises more globally efficient designs when more ECG points are used may be explained as follows. For the multi-point method, the *dq*-currents are specified as variables in the optimisation loop. If these currents satisfy a constraint for an operating point, the optimisation determines this to be valid. This results in the optimisation finding a minimum costing machine, but not necessarily at the MTPA for each operating point. Further, the global $\eta_{eng}$ constraint defined is determined intrinsically by the *dq*-currents. This therefore means that if the constraint is met through the optimisation, the most optimal energy efficiency may not be found, but the ideal costing will be. For the flux mapping method, the MTPA for each operating point is determined. This causes the total input energy to be lower compared to the multi-point method, as the MTPA *dq*-current points are optimally determined for each iteration cycle. This leads to a more globally efficient machine design, but not necessarily the lowest-cost design.
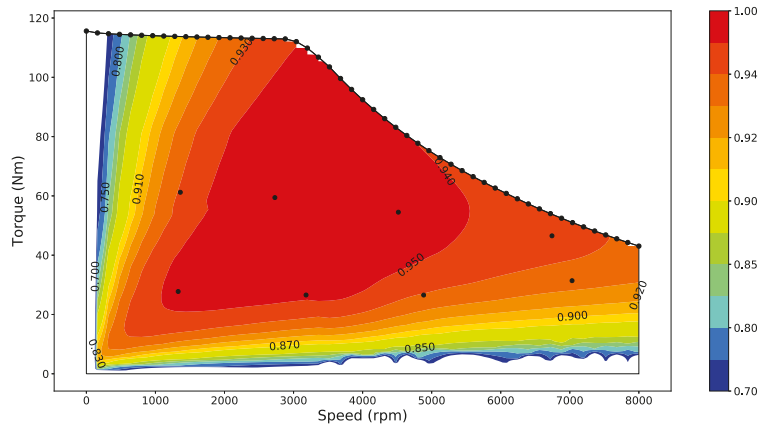
**Figure 15.** Efficiency map of eight ECG points with multi-point method.
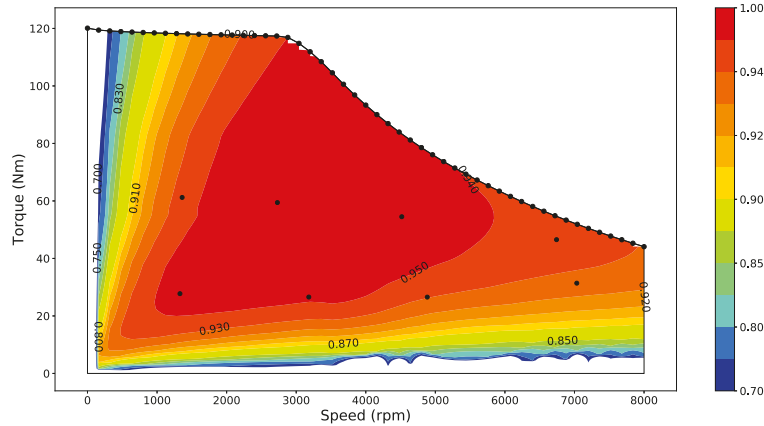


**Figure 16.** Efficiency map of eight ECG points with flux map method.

**Table 7.** Comparison of drive-cycle energy consumption of the optimum motor designs.

| Number of ECGs | Multi-Point | Flux Mapping |
|:---:|:---:|:---:|
| 2 | 16.934 GJ | 16.882 GJ |
| 4 | 16.931 GJ | 16.793 GJ |
| 6 | 16.931 GJ | 16.778 GJ |
| 8 | 16.921 GJ | 16.673 GJ |

The cross-sections of the optimum designs from both the multi-point and flux mapping methods with two ECG points and eight ECG points are shown in Figures 18 and 19. Their respective optimised motor geometric parameters are summarised in Table 8. Clearly, the optimum designs obtained from both methods are very similar to each other.

Figure 20 displays the computational time of both multi-point and flux mapping methods with different numbers of ECG points. It is observed that for the multi-point method, there is an increase of 8 times in time from 2 ECG points to 8 ECG points, whereas the flux mapping method only has an increase of 1.5 times. Further, for 8 ECG points, the multi-point method took up to 7397 s whereas the flux mapping method took 3028 s. This shows that the flux mapping method has the potential of being 2.4 times faster than

the multi-point method when many ECG points are used. In order to show the rationale of selecting the gradient-based design optimisation procedure for this study, multi-point optimisation using the differential evolution (DE) method was also conducted. The time taken for the DE design is also shown on the same graph. It can be seen that the DE optimisation using only two ECG points takes weeks to complete, whereas the gradient-based design needs only a few minutes. This clearly shows the huge computational advantages that the gradient-based optimisation can offer.
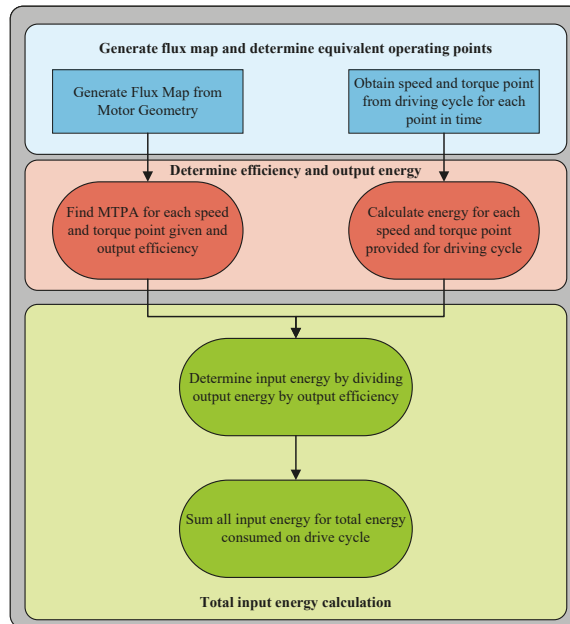


**Figure 17.** Pseudo-code for drive cycle energy consumption calculation.

**Table 8.** Comparison of multi-point and flux mapping optimum designs with two and eight ECG points.

| Parameter | Number of ECGs: 2 | | Number of ECGs: 8 | |
|---|---|---|---|---|
| | Multi-Point | Flux Mapping | Multi-Point | Flux Mapping |
| S1 (mm) | 2.79 | 2.81 | 2.76 | 2.81 |
| S2 (mm) | 6.1 | 6.22 | 7.34 | 7.55 |
| S3 (mm) | 31.13 | 30.17 | 24.74 | 25.8 |
| S4 (mm) | 13.85 | 14.49 | 14.63 | 15.53 |
| S5 (mm) | 7.29 | 7.24 | 9.09 | 9.33 |
| V1 (mm) | 6.98 | 6.16 | 4.17 | 4.28 |
| V2 (mm) | 0.5 | 0.5 | 0.5 | 0.78 |
| V3 (mm) | 42.98 | 42.72 | 55.33 | 57.1 |
| V4 (mm) | 22.37 | 22.94 | 39.24 | 36.98 |
| V5 (mm) | 7.55 | 6.7 | 2.94 | 3.54 |
| $V\theta°$ | 115.51 | 115.1 | 114.8 | 114.61 |
| R (mm) | 137.14 | 136.17 | 151.6 | 156.07 |
| L (mm) | 45.43 | 46.82 | 40.33 | 40.73 |
| Coil turns | 12 | 12 | 11 | 11 |

It can also be seen that when the number of ECG points is greater than 4, the flux mapping method becomes computationally more efficient. This is because the multi-point

method has an increase of two design variables, namely the $dq$-currents for each specific point, as the number of ECG points increases. This drastically increases the amount of time taken as the search space for the optimal design becomes much larger. However, for the flux mapping method, the search space remains the same, with only an increase in the amount of points to find on the actual interpolated map.
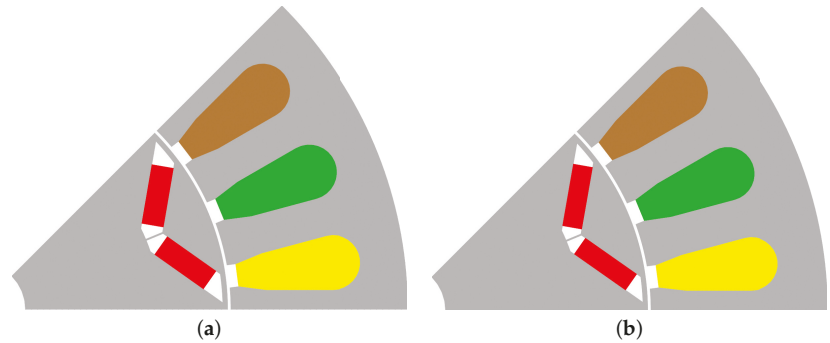


**Figure 18.** Cross-section of optimum designs from (**a**) multi-point method and (**b**) flux map method, all with two ECG points.
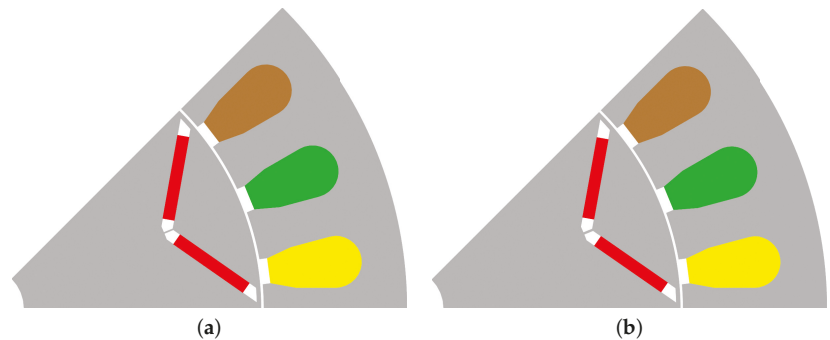


**Figure 19.** Cross-section of optimum designs from (**a**) multi-point method and (**b**) flux map method, all with eight ECG points.

The multi-point method is relatively simple to implement for a designer compared to the flux mapping method. The flux mapping method requires the user to implement interpolation and MTPA analysis, while for the multi-point method, only the $dq$-currents are required in order to analyse the motor's performance. Another issue of the flux mapping method is the search space of the flux map. By creating a large map that is densely populated and takes longer to generate, a more accurate MTPA search can be conducted. On the contrary, with a small and less densely populated flux map, the flux mapping technique is computationally faster with a reduced accuracy. This shows the flux mapping method is sensitive to the size of the flux map, and there is a trade-off between speed and accuracy.

A factor that also needs to be considered is the core losses of the machine. For larger machines, core losses have a much larger effect on the design of the motor. This would need to be included within the constraint function, dependent on the particular motor design. For traction applications, the torque ripple is also an important design consideration, which is not part of the design study in this paper. However, this can be easily included in the design optimisation with either method and further constrained according to the design specifications.
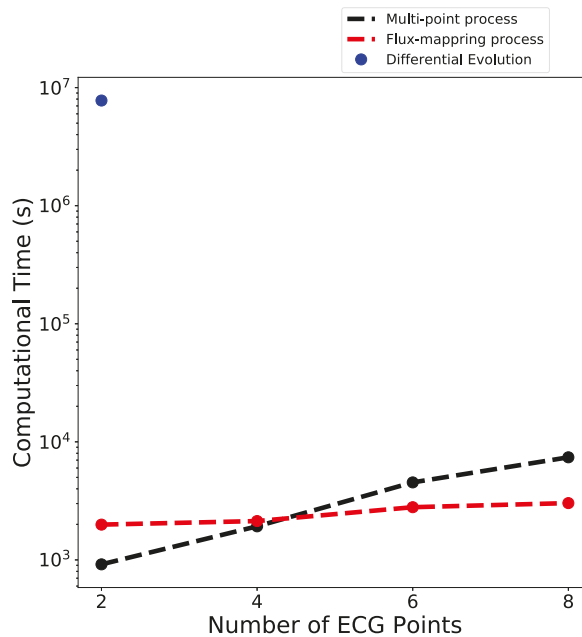
**Figure 20.** Computational time comparison of optimisation processes.

It is up to the designer to determine which method is best suited for their application. If the MTPA is required for each operating point, a more globally efficient machine design can be found when using the flux mapping method. However, if material costing is the goal of the design, the multi-point method is the best strategy, and few operating points are required.

## 5. Conclusions

An evaluation of design optimisation techniques for gradient-based optimisation is conducted in this paper. Using a drive cycle-based approach for motor design optimisation, an increase in overall efficiency can be achieved for the specified drive cycle. A weighting of energy method can be used when analysing the drive cycle, which is further implemented in the design strategies. The methods evaluated are the multi-point-based approach and a flux mapping method. The multi-point-based method is shown to have an advantage in terms of costing, computational efficiency, and ease of implementation when few operational points are used; however, it becomes less attractive when more operational points are used, due to the significantly increased time requirement to complete a design optimisation process. The other design optimisation technique, flux mapping, is more complicated to implement and use; however, when many operational points are used from the driving cycle, it is seen to be computationally more efficient, and a greater global efficiency can be found at the detriment of a slightly higher cost of the machine.

This paper shows how either methodology can be implemented and which may be more beneficial for the designer according to the design requirements. It further shows the importance of the problem definition for a gradient-based design optimisation problem. Compared with a global optimisation method, a gradient-based optimisation method is still very attractive because of its superior computational speed. This topic can be further researched in terms of adding more parameters to the design specifications, such as including core losses and torque ripple analysis. Given the scope of the work, the proposed optimisation strategies are only evaluated based on a typical design case study. It

is necessary to further compare and verify the suitability of these design strategies with more case studies and even practical validations.

## References

1.  Salameh, M.; Brown, I.P.; Krishnamurthy, M. Fundamental Evaluation of Data Clustering Approaches for Driving Cycle-Based Machine Design Optimization. *IEEE Trans. Transp. Electrif.* **2019**, *5*, 1395–1405. [CrossRef]
2.  Diao, K.; Sun, X.; Lei, G.; Bramerdorfer, G.; Guo, Y.; Zhu, J. System-Level Robust Design Optimization of a Switched Reluctance Motor Drive System Considering Multiple Driving Cycles. *IEEE Trans. Energy Convers.* **2021**, *36*, 348–357. [CrossRef]
3.  Li, Q.; Fan, T.; Wen, X.; Li, Y.; Wang, Z.; Guo, J. Design optimization of interior permanent magnet sychronous machines for traction application over a given driving cycle. In Proceedings of the IECON 2017—43rd Annual Conference of the IEEE Industrial Electronics Society, Beijing, China, 29 October–1 November 2017; pp. 1900–1904. [CrossRef]
4.  Fatemi, A.; Demerdash, N.A.; Nehl, T.W.; Ionel, D.M. Large-scale design optimization of PM machines over a target operating cycle. *IEEE Trans. Ind. Appl.* **2016**, *52*, 3772–3782. [CrossRef]
5.  Mai, H.; Dubas, F.; Chamagne, D.; Espanet, C. Optimal design of a surface mounted permanent magnet in-wheel motor for an urban hybrid vehicle. In Proceedings of the 2009 IEEE Vehicle Power and Propulsion Conference, Dearborn, MI, USA, 7–10 September 2009; pp. 481–485.
6.  Dutta, R.; Rahman, M. Design and analysis of an interior permanent magnet (IPM) machine with very wide constant power operation range. *IEEE Trans. Energy Convers.* **2008**, *23*, 25–33. [CrossRef]
7.  Jolly, L.; Jabbar, M.; Qinghua, L. Optimization of the constant power speed range of a saturated permanent-magnet synchronous motor. *IEEE Trans. Ind. Appl.* **2006**, *42*, 1024–1030. [CrossRef]
8.  Carraro, E.; Morandin, M.; Bianchi, N. Traction PMASR Motor Optimization According to a Given Driving Cycle. *IEEE Trans. Ind. Appl.* **2016**, *52*, 209–216. [CrossRef]
9.  Lazari, P.; Wang, J.; Chen, L. A computationally efficient design technique for electric-vehicle traction machines. *IEEE Trans. Ind. Appl.* **2014**, *50*, 3203–3213. [CrossRef]
10. Chen, L.; Wang, J.; Lazari, P.; Chen, X. Optimizations of a permanent magnet machine targeting different driving cycles for electric vehicles. In Proceedings of the 2013 International Electric Machines & Drives Conference, Chicago, IL, USA, 12–15 May 2013; pp. 855–862.
11. Yuan, X.; Wang, J. Torque distribution strategy for a front-and rear-wheel-driven electric vehicle. *IEEE Trans. Veh. Technol.* **2012**, *61*, 3365–3374. [CrossRef]
12. Korta, P.; Iyer, L.V.; Lai, C.; Mukherjee, K.; Tjong, J.; Kar, N.C. A novel hybrid approach towards drive-cycle based design and optimization of a fractional slot concentrated winding SPMSM for BEVs. In Proceedings of the 2017 IEEE Energy Conversion Congress and Exposition (ECCE), Cincinnati, OH, USA, 1–5 October 2017; pp. 2086–2092. [CrossRef]
13. Fatemi, A.; Ionel, D.M.; Popescu, M.; Chong, Y.C.; Demerdash, N.A. Design optimization of a high torque density spoke-type PM motor for a formula E race drive cycle. *IEEE Trans. Ind. Appl.* **2018**, *54*, 4343–4354. [CrossRef]
14. Liu, K.; Feng, J.; Guo, S.; Xiao, L.; Zhu, Z.Q. Identification of flux linkage map of permanent magnet synchronous machines under uncertain circuit resistance and inverter nonlinearity. *IEEE Trans. Ind. Inform.* **2017**, *14*, 556–568. [CrossRef]
15. Mohammadi, M.H.; Lowther, D.A. A computational study of efficiency map calculation for synchronous AC motor drives including cross-coupling and saturation effects. *IEEE Trans. Magn.* **2017**, *53*, 1–4. [CrossRef]
16. Chen, L.; Chen, X.; Wang, J.; Lazari, P. A computationally efficient multi-physics optimization technique for permanent magnet machines in electric vehicle traction applications. In Proceedings of the 2015 IEEE International Electric Machines & Drives Conference (IEMDC), Coeur d'Alene, ID, USA, 10–13 May 2015; pp. 1644–1650.

17. Wang, G.; Chen, X.; Xing, Y.; Liu, H.; Tian, D. Optimal design of an interior permanent magnet in-wheel motor for electric off-road vehicles. In Proceedings of the 2018 IEEE International Conference on Electrical Systems for Aircraft, Railway, Ship Propulsion and Road Vehicles & International Transportation Electrification Conference (ESARS-ITEC), Nottingham, UK, 7–9 November 2018; pp. 1–5.

18. Menzel, G.; Och, S.H.; Mariani, V.C.; Moura, L.M.; Domingues, E. Multi-objective optimization of the volumetric and thermal efficiencies applied to a multi-cylinder internal combustion engine. *Energy Convers. Manag.* **2020**, *216*, 112930. [CrossRef]

19. Raminosoa, T.; Rasoanarivo, I.; Sargos, F.; Andriamalala, R. Constrained optimization of high power synchronous reluctance motor using non linear reluctance network modeling. In Proceedings of the Conference Record of the 2006 IEEE Industry Applications Conference Forty-First IAS Annual Meeting, Tampa, FL, USA, 8–12 October 2006; Volume 3, pp. 1201–1208.

20. Mabhula, M.; Kamper, M. Gradient-based Multi-objective Design Optimisation Formulation of Grid-connected Wound-rotor Induction Motors. In Proceedings of the 2020 International Conference on Electrical Machines (ICEM), Gothenburg, Sweden, 23–26 August 2020; Volume 1, pp. 163–169.

21. Turker, H. Design optimization ofan interior permanent magnet synchronous machine (IPMSM) for electric vehicle application. In Proceedings of the 2016 IEEE International Conference on Renewable Energy Research and Applications (ICRERA), Birmingham, UK, 20–23 November 2016; pp. 1034–1038.

22. Msaddek, H.; Mansouri, A.; Brisset, S.; Trabelsi, H. Design and optimization of PMSM with outer rotor for electric vehicle. In Proceedings of the 2015 IEEE 12th International Multi-Conference on Systems, Signals & Devices (SSD15), Mahdia, Tunisia, 16–19 March 2015; pp. 1–6.

23. Ehsani, M.; Gao, Y.; Emadi, A. *Modern Electric, Hybrid Electric, and Fuel Cell Vehicles: Fundamentals, Theory, and Design*, 2nd ed.; Power Electronics and Applications Series; CRC Press: Boca Raton, FL, USA, 2010.

24. Chau, K.T. *Electric Vehicle Machines and Drives*; Wiley: Hoboken, NJ, USA, 2015; Chapter 1–4.

25. United Nations. *Concerning the Adoption of Harmonized Technical United Nations Regulations for Wheeled Vehicles, Equipment and Parts Which Can Be Fitted and/or Be Used on Wheeled Vehicles and the Conditions for Reciprocal Recognition of Approvals Granted on the Basis of These United Nations Regulations*; United Nations: New York, NY, USA, 2021.

26. Li, Q.; Fan, T.; Li, Y.; Wang, Z.; Wen, X.; Guo, J. Optimization of external rotor surface permanent magnet machines based on efficiency map over a target driving cycle. In Proceedings of the 2017 20th International Conference on Electrical Machines and Systems (ICEMS), Sydney, Australia, 11–14 August 2017; pp. 1–5. [CrossRef]

27. Wei, D.; He, H.; Li, J. A Computationally Efficiency Optimal Design for a Permanent Magnet Synchronous Motor in Hybrid Electric Vehicles. In Proceedings of the 2020 IEEE 9th International Power Electronics and Motion Control Conference (IPEMC2020-ECCE Asia), Nanjing, China, 29 November–2 December 2020; pp. 43–47.

28. Sarigiannidis, A.G.; Beniakar, M.E.; Kladas, A.G. Fast adaptive evolutionary PM traction motor optimization based on electric vehicle drive cycle. *IEEE Trans. Veh. Technol.* **2016**, *66*, 5762–5774. [CrossRef]

29. Pastellides, S.; Gerber, S.; Wang, R.J.; Kamper, M.J. Design of a Surface-Mounted PM Motor for Improved Flux Weakening Performance. In Proceedings of the 2020 International Conference on Electrical Machines (ICEM), Gothenburg, Sweden, 23–26 August 2020; Volume 1, pp. 1772–1778.

30. Reinert, J.; Brockmeyer, A.; De Doncker, R. Calculation of losses in ferro- and ferrimagnetic materials based on the modified Steinmetz equation. *IEEE Trans. Ind. Appl.* **2001**, *37*, 1055–1061. [CrossRef]

31. Kraft, D.; Schnepper, K. SLSQP—A nonlinear programming method with quadratic programming subproblems. *DLR Oberpfaffenhofen* **1989**, *545*.

32. Venter, G. Review of optimization techniques. In *Encyclopedia of Aerospace Engineering*; Blockley, R., Shyy, W., Eds.; Wiley and Sons: New York, NY, USA, 2010.

33. Gerber, S.; Wang, R.J. Traction Motor Optimization Using Mesh Reshaping for Gradient Evaluation. In Proceedings of the 2020 International Conference on Electrical Machines (ICEM), Gothenburg, Sweden, 23–26 August 2020; Volume 1, pp. 2546–2552. [CrossRef]

*Article*

# Novel Design of Six-Phase Spoke-Type Ferrite Permanent Magnet Motor for Electric Truck Application

Hoyun Won [1], Yang-Ki Hong [1,*], Minyeong Choi [1], Jonathan Platt [1], Briana Bryant [1], Seungdeog Choi [2], Shuhui Li [1], Hwan-Sik Yoon [3], Timothy A. Haskew [1], Jongkook Lee [4], Taegyu Lee [4] and Tae-Won Lim [4]

1　Department of Electrical and Computer Engineering, The University of Alabama, Tuscaloosa, AL 35487, USA; hwon@crimson.ua.edu (H.W.); mchoi11@crimson.ua.edu (M.C.); jtplatt@crimson.ua.edu (J.P.); bmbryant1@crimson.ua.edu (B.B.); sli@eng.ua.edu (S.L.); thaskew@eng.ua.edu (T.A.H.)
2　Department of Electrical Engineering, Mississippi State University, Starkville, MS 35762, USA; seungdeog@ece.msstate.edu
3　Department of Mechanical Engineering, The University of Alabama, Tuscaloosa, AL 35487, USA; hyoon@eng.ua.edu
4　Institute of Fundamental and Advanced Technology (IFAT), Hyundai Motor Company, Uiwang-si 16082, Korea; samemind@hyundai.com (J.L.); xorb9@hyundai.com (T.L.); twlim@hyundai.com (T.-W.L.)
*　Correspondence: ykhong@eng.ua.edu

**Abstract:** This paper proposes a 300 kW 24-slot/10-pole 6-phase stator-shifted fractional-slot concentrated winding spoke-type ferrite permanent magnet machine for electric truck applications. The proposed motor consists of a stator with dual three-phase windings positioned 75 degrees apart to reduce higher-order MMF harmonic order, and a rotor with an inexpensive and high-resistance ferrite permanent magnet in the spoke configuration. The simulated result of the stator-shifted machine is compared with a fabricated stator-shifted machine, and the results show good agreement with each other. To further reduce the torque ripple from 2.5 to 0.9% while maintaining a high maximum torque of 2980 Nm, circular voids with a diameter of 11 mm are embedded in the rotor. The proposed motor is evaluated for irreversible demagnetization, mechanical and thermal stability, and fault tolerant ability. To assess the proposed motor performance, the electric truck simulation model is constructed using MATLAB/Simulink and used to compare with the reported 12-slot/10-pole rare-earth permanent magnet-based machine. Compared to a previously reported six-phase rare-earth permanent magnet based flat-type machine, the proposed motor can save 4.3 kWh of energy with a USD 2512 lower cost while retaining a similar motor performance.

**Keywords:** phase-shift; rare-earth free permanent magnet; six-phase winding; spoke-type motor

## 1. Introduction

Throughout the world, many municipal governments have announced the replacement of diesel transit buses with electric buses to reduce the air pollution in cities [1–3]. Eliminating diesel exhaust emissions from the diesel transit buses by replacing them with electric buses not only improves the air quality by eliminating 2 million tons of greenhouse gas emissions each year, but also delivers financial benefits, including reduced maintenance and fuel cost by USD 200,000 over the lifetime of the bus, and societal benefits, including reduced health care expenses caused by air pollutants [1–3]. It is reported that air pollutants can cause heart attacks, premature deaths, asthma, and other severe health issues. The transit bus is classified as class-7 heavy-duty truck (HDT), which also covers most of the city vehicles, such as street sweepers, garbage, beverage, and furniture trucks. Accordingly, electrifying the class-7 HDTs is essential to substantially reduce air pollution in the city.

Among the reported electric motors used for HDTs, multi-phase rare-earth permanent magnet (RE-PM)-based synchronous machines are widely utilized due to their high

torque and power density, maximum speed, and efficiency [1]. For multi-phase machines, fractional-slot concentrated winding (FSCW) is generally utilized because the FSCW provides the inherent fault-tolerant capability, higher winding factor, and lower cogging torque than distributed winding [4–6]. However, the FSCW produces unwanted space harmonics in the stator magnetomotive force (MMF), resulting in high eddy current losses in permanent magnet (PM), localized core saturation, and difficulty to produce high reluctance torque from interior-mounted rotor topology [7,8].

To suppress the stator MMF harmonics, various methods, including PM segmentation [4,5], multilayer winding design [9], coils with a different number of turns per coil side [10], and stator-shifting [11], have been reported. Among these MMF harmonic suppression methods, the stator-shifting concept reduces both sub- and high-order stator MMF harmonics effectively without increasing manufacturing costs and material usage [4–6,11]. This concept has been validated with various rotor topologies, including surface-mounted and interior-mounted single- and multi-layer V-type rotor topologies [4–6]. However, this concept has not been validated for interior-mounted spoke-type rotor topology yet.

For HDTs, rare-earth NdFeB magnets are widely used for permanent magnet synchronous machines (PMSMs) to achieve high torque density, efficiency, and maximum speed by exploiting its high maximum energy product $(BH)_{max}$. However, NdFeB RE-PM suffers from high and volatile cost, unstable supply, complicated manufacturing processes, and low electrical resistivity [12,13]. The traction motors of HDTs need PMs with a lower price and more stable supply than the motors used in light-duty vehicles because a high peak power rating in the range from 300 to 360 kW is required for HDTs [1]. The motor must be large enough to produce such a high peak power, requiring a large PM volume. Further, the high electrical resistivity of PM is essential for the motor employing the FSCW winding to minimize the temperature of the PM. The PM temperature rises by the eddy current loss caused by higher-order space harmonics. Thereby, a cost-effective and high electrical resistive PM is demanded to address the above issues.

Among such PMs, hard ferrite shows the most viable solution. Ferrite has USD 86–93 lower cost and 6667-times higher electrical resistivity than NdFeB PM [14]. However, the ferrite-based PM motors suffer from low torque density due to the relatively low magnetization. One of the ways to address this drawback is to employ spoke-type interior-mounted rotor topology. This topology arranges the ferrite PMs in oriented planes to increase the air-gap flux by focusing the PM flux and increasing the reluctance torque [15]. However, this design results in significant flux density distortion in the air gap, causing a high torque ripple. Although many methods, from design-based to control-based, have been reported to minimize the torque ripple, they either decrease the maximum torque or increase an unbalanced axial electromagnetic force [16].

In the previous paper [17], we reported a novel 24-slot/10-pole 6-phase stator-shifted FSCW spoke-type ferrite interior PMSM (6Φ-SS-FSCW-Fer-SIPMSM), exhibiting a peak power of 250 kW, peak torque of 2150 Nm, and torque ripple of 4.1%. The circular-notch torque ripple reduction method and the stator-shift concept were introduced and explained.

In this paper, the proposed 6Φ-SS-FSCW-Fer-SIPMSM is scaled up to produce a peak power of 300 kW, peak torque of 2980 Nm, and torque ripple of 0.9% for quantitative comparison with the reported 300 kW 12-slot/10-pole 6-phase FSCW NdFeB-based flat-type IPMSM (6Φ-FSCW-Nd-FIPMSM) [3]. The circular-notch torque ripple reduction method and stator-shift concepts are further advanced and quantitatively analyzed via winding-function theory, harmonic spectrum analysis, and flux distributions in the motor. In addition, the proposed 6Φ-SS-FSCW-Fer-SIPMSM performance is compared with the conventional 12-slot/10-pole 6-phase FSCW spoke-type ferrite interior PMSM. Lastly, the electric truck model, constructed with MATLAB/Simulink, is used to evaluate the proposed motor performance and efficiency, and for comparison with the reported 6Φ-FSCW-Nd-FIPMSM.

## 2. Initial Motor Design and Validation

Recently, Morozov et al. evaluated the performance of five 12-slot/10-pole 6Φ-FSCW-Nd-FIPMSM, having various power ratings of 150, 200, 250, 300, and 350 kW, with 4 gearboxes from 3- to 6-speed [3]. Class-7 HDT simulation was performed under various drive cycles. The simulation result show that a 300 kW 12-slot/10-pole 6Φ-FSCW-Nd-FIPMSM with a 3-speed gearbox satisfies the required performance goals of 27 s acceleration time from 0 to 60 mph, 30% starting grade, and 113 km/h top speed with good energy efficiency [3]. Thus, the reported 300 kW 12-slot/10-pole 6Φ-FSCW-Nd-FIPMSM was chosen as a benchmark motor in this paper and investigated more thoroughly.

Table 1 shows the specification of the benchmark motor [3], while Figure 1a shows the schematic of the reported benchmark motor. With the given specification in Table 1, the reported 6Φ-FSCW-Nd-FIPMSM was designed and simulated using ANSYS Maxwell 2D finite-element-analysis (FEA) v.18.1 to validate the reported motor performance. Because the reported literature did not provide a specific grade of Nd-Fe-B PM, the reported 6Φ-FSCW-Nd-FIPMSM with various grades of the Nd-Fe-B PM was first simulated to determine the grade of Nd-Fe-B PM used in the literature. The simulation results show that N42UH grade Nd-Fe-B PM, which has remanent flux density of 1.28 T and coercivity of 955 kA/m at room temperature [18], produces same maximum torque of 3110 Nm as reported by the authors of [3].

**Table 1.** Specifications of benchmark motor. Data from [3].

| Parameter | Value |
|---|---|
| Stator outer/inner diameter [mm] | 550/366 |
| Rotor outer/inner diameter [mm] | 362/196 |
| Stack length [mm] | 300 |
| Number of slots/poles | 12/10 |
| Number of turns | 64 |
| Number of parallel paths | 8 |
| Rated/peak current density [A/m$^2$] | 6.3/16.4 |
| Rated/peak current [A$_{rms}$] | 250/636 |
| Copper mass [kg] | 135 |
| Maximum torque [Nm] | 3110 |
| Soft iron core material | M19–29G |

Phase A   Phase B   Phase C   Phase D   Phase E   Phase F



(a)   (b)
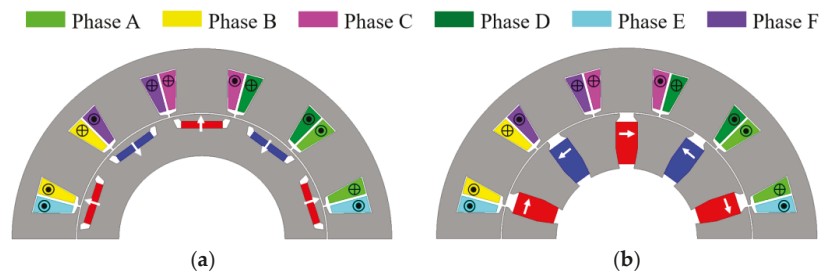
**Figure 1.** Schematic of 6-phase 12-slot/10-pole (**a**) reported flat-type IPMSM and (**b**) proposed spoke-type IPMSM.

To observe the effect of the ferrite PM on motor performance, the reported 6Φ-FSCW-Nd-FIPMSM was simulated with Hitachi's NMF-12G ferrite PM, which has a remanent flux density of 0.45 T and coercivity of 334 kA/m at room temperature. Due to lower magnetic properties of the ferrite PM than Nd-Fe-B PM, the torque at peak current was significantly reduced from 3110 to 1550 Nm (50% reduction), as shown in Figure 2. In order to improve the torque, four different rotor topologies, including PM-assisted synchronous reluctance machine (PMASynRM), V-type PMSM, surface-mounted PMSM (SPM), and

spoke-type PMSM, were simulated and investigated under the same motor specifications, operating conditions, and NMF-12G ferrite PM as in our previous studies [17]. The simulation results show that among the above topologies, the spoke-type topology, which is shown in Figure 1b, delivered the highest torque of 2320 Nm and relatively low back EMF at 3000 rpm, but suffered from high torque ripple. Compared to the reported flat-type topology, the spoke-type topology increased the maximum torque from 1550 to 2320 Nm (49.7% improvement), as shown in Figure 2. This is mainly attributed to the flux concentration effect of the spoke type topology [19] and increased PM volume. The motor, having this spoke-type rotor topology, and the FSCW winding were simulated and verified experimentally by the authors of [19], who showed that the rotor sustained its operation up to 14,000 rpm without mechanical breakdown.
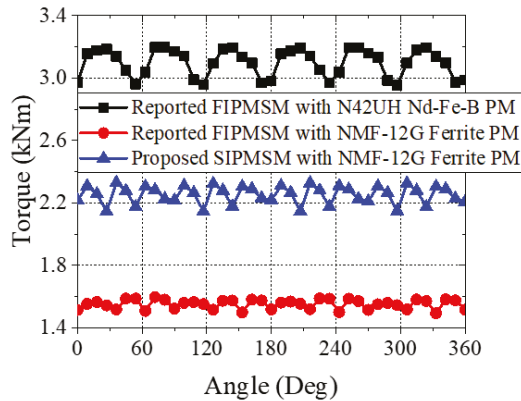


**Figure 2.** Maximum torque performance of the reported FIPMSM with N42UH Nd-Fe-B PM and NMF-12G ferrite PM and proposed SIPMSM with NMF-12G ferrite PM.

### 2.1. Winding Configuration

A typical dual 3Φ 12-slot/10-pole configuration with a double layer winding is shown in Figure 3a. According to the authors of [4], the most detrimental MMF harmonics are those close to the torque-producing harmonic. For the five pole-pair motor, the detrimental MMF harmonics are the first and seventh harmonic, whereas the torque-producing harmonic is the fifth harmonic. It was reported that when the phases of the two three-phase windings are shifted by 30°, all harmonics below the torque-producing harmonic can be canceled [20]. However, the harmonics above the torque-producing harmonic, which is the seventh harmonic, remain.

Thus, the concept of stator-shifting was employed to minimize the seventh harmonic by shifting one of the dual three-phase windings with a specific mechanical angle ($\alpha$) against another three-phase winding, as illustrated in Figure 4. The number of slots and coil pitches must be doubled from 12 to 24 and from 1 to 2, respectively, to accommodate the shifted 3-phase winding. The number of turns was halved from 64 to 32 to maintain the same total copper volume. An optimal $\alpha$ that minimizes the seventh harmonic can be calculated using a winding function theory [16]. Based on the winding function theory, the MMF of the unshifted and $\alpha$-shifted three-phase winding are:

$$F_1(\theta, t) = \sum_{k=1,-5,7}^{\infty} \frac{12 N_c I_m}{k\pi} \sin\left(\frac{k\pi}{12}\right) \cdot \sin\left(\frac{(k-1)\pi}{12}\right) \cdot \sin\left(k\theta - \omega t - \frac{(k-1)\pi}{12}\right) \tag{1}$$

$$F_2(\theta, t) = \sum_{k=1,-5,7}^{\infty} \frac{12 N_c I_m}{k\pi} \sin\left(\frac{k\pi}{12}\right) \cdot \sin\left(\frac{(k-1)\pi}{12}\right) \cdot \sin\left(k\theta - \omega t - k\alpha - \frac{(k-1)\pi}{12}\right) \tag{2}$$

where $N_c$ is the number of turns, $I_m$ is the peak phase current, and $k$ is the harmonic order. The negative $k$ for the fifth harmonic is required to account for the harmonic sequence

direction. Since $N_c$ and $I_m$ were the same for both windings, the total MMF ($F_t$) was calculated by adding $F_1$ and $F_2$, resulting in Equation (3).

$$F_t(\theta, t) = F_1(\theta, t) + F_2(\theta, t) = \sum_{k=1,-5,7}^{\infty} \frac{24 N_c I_m}{k\pi} \sin\left(\frac{k\pi}{12}\right) \cdot \sin\left(\frac{(k-1)\pi}{12}\right) \cdot \cos\left(\frac{k\alpha}{2}\right) \cdot \sin\left(k\theta - \omega t - \frac{k\alpha}{2} - \frac{(k-1)\pi}{12}\right) \quad (3)$$

where the sum to product trigonometric identifies for sine is used to simplify the equation. As Equation (3) suggests, one of the simple and effective ways to cancel the seventh harmonic is to find the $\alpha$ that can make the term $\cos(k(\alpha/2))$ equal to zero for $k = 7$. The optimal $\alpha$ is 77.14°. However, realizing such $\alpha$ requires an uneven tooth width. Instead, the $\alpha$ closest to the optimal $\alpha$ and in multiples of tooth pitch, i.e., multiplication of $360°/24 = 15°$, meet the requirement. The closest value to the optimal angle of 77.14° and yielding an integer multiple to tooth pitch is 75°, which corresponds to five slots apart from each winding. Figure 3b illustrates the proposed 24-slot/10-pole 6Φ-SS-FSCW-Fer-SIPMSM with an $\alpha$ of 75°.
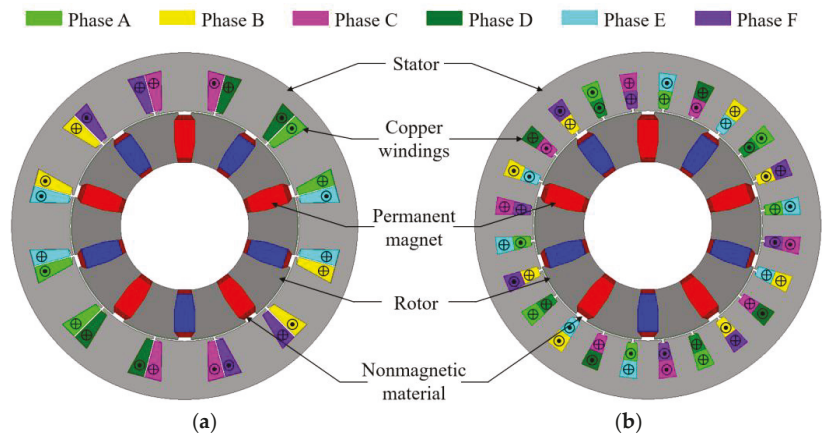


**Figure 3.** Schematic of 6-phase (**a**) 12-slot/10-pole unshifted and (**b**) 24-slot/10-pole stator-shifted FSCW winding layout.
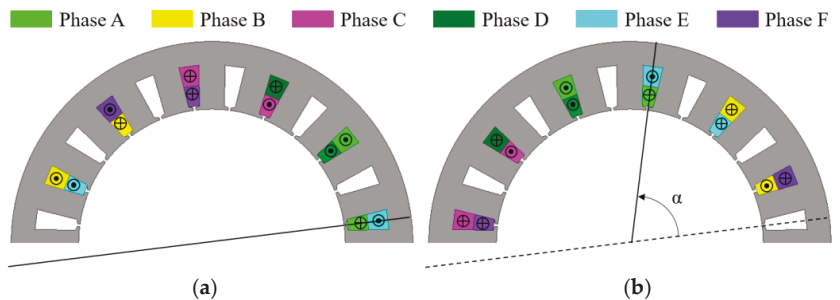


**Figure 4.** Design of (**a**) first and (**b**) second set of the 12-slot/10-pole winding layout.

The MMF distribution and corresponding harmonic spectrum of the conventional 12-slot/10-pole unshifted and the proposed 24-slot/10-pole shifted 6-phase PM machine are shown in Figure 5. As Figure 5b indicates, the stator-shifting design significantly decreased not only the 7th harmonic from 0.79 to 0.1 (87.3% reduction), but also other higher-order harmonics, such as the 17th harmonic, from 0.375 to 0.03 (92% reduction), the 19th harmonic from 0.36 to 0.26 (27.8% reduction), and the 29th harmonic from 0.2 to 0.16

(20% reduction). Hence, the corresponding winding layout with a 75° shift was selected and employed throughout this paper.
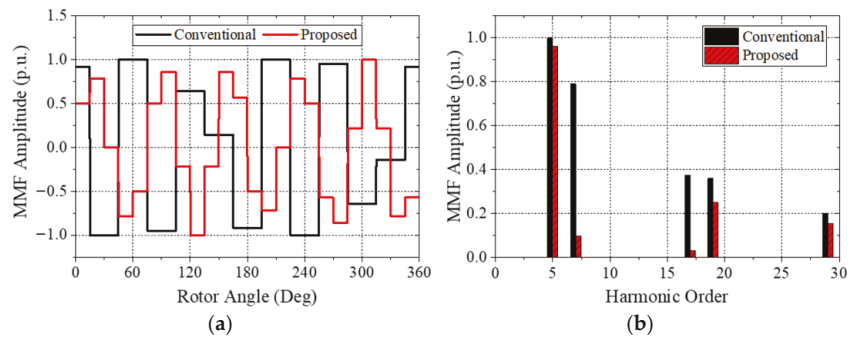


**Figure 5.** Total MMF distribution (**a**) profile and (**b**) harmonic spectrum of the conventional and proposed FSCW motor.

To validate the simulation results of the proposed 24-slot/10-pole 6Φ-SS-FSCW-Fer-SIPMSM, the reported 6-phase 18-slot/8-pole V-type IPMSM with a 20° electrical phase shift between two three-phase windings [4] was designed and simulated using ANSYS Maxwell 2D FEA v.18.1. Figure 6 shows the designed motor with a winding layout and prototype. The simulated back electromotive force (EMF) waveforms of the A-B-C windings at 2800 rpm using an in-house FEA tool were investigated and compared with the back EMF waveforms of the A-B-C windings that were measured and reported by the authors of [4]. Figure 7 shows the corresponding performance comparison. As shown, the simulated back EMF shows good agreement with the measured back EMF.
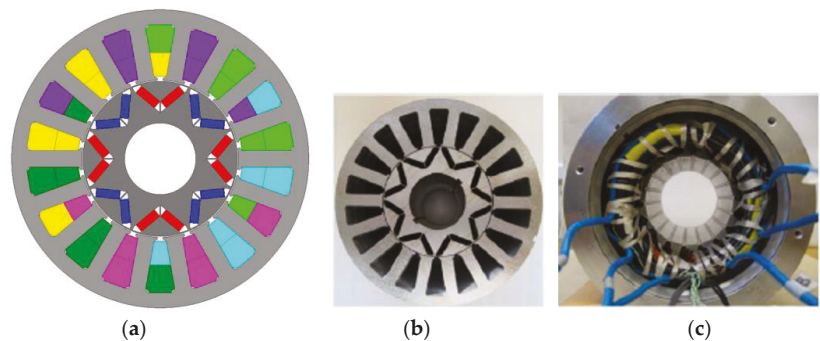


**Figure 6.** The 6-phase 18-slot/8-pole machine: (**a**) schematic with winding layout and top view of the motor, (**b**) without copper coil and PM, and (**c**) with copper coil and others [4]. ©IEEE. Reprinted with permission from Patel, V.; Wang, J.; Wang. W.; Chen, X. The 6-phase fractional-slot-per-pole-phase permanent-magnet machines with low space harmonics electric vehicle application. IEEE Transactions on Industry Application, vol. 50, no. 4, July 2014.
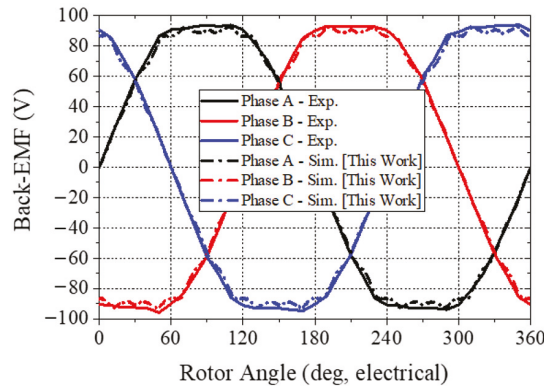
**Figure 7.** Comparison of measured [4] and simulated back EMFs of Phase A, B, and C windings at the base speed of 2800 rpm.

### 2.2. Electromechanical Performance Comparison

The maximum torque, torque ripple ($T_{rip}$), cogging torque ($T_{cog}$), and back-EMF harmonic spectrum of the conventional 12-slot/10-pole unshifted and the proposed 24-slot/10-pole shifted 6-phase spoke-type ferrite IPMSM were simulated and compared. The specifications of the conventional and proposed motors are summarized in Table 2. The simulated maximum torque, $T_{rip}$, $T_{cog}$, and total harmonic distortion (THD) of the back-EMF of the conventional and proposed motors are presented in Table 3. The $T_{rip}$ was calculated by Equation (4).

$$T_{rip} = \frac{T_{max} - T_{min}}{(T_{max} + T_{min})/2} \tag{4}$$

where $T_{max}$ and $T_{min}$ are the maximum and minimum torque magnitude, respectively. It is noted that the proposed stator-shifted machine increased the maximum torque from 2320 to 2970 Nm (28% improvement), and decreased the $T_{rip}$ from 10.9 to 2.5% (77.1% reduction) without affecting the $T_{cog}$ compared to the conventional unshifted machine. The significant increase in the maximum torque is mainly attributed to the increased air gap flux density. Figure 8 shows the air gap flux density at maximum current. Further, the $T_{rip}$ reduction of 77.1% may be attributed to the suppression of the 8th, 9th, 11th, 13th, 15th, and 17th harmonics in back-EMF, as shown in Figure 9. The suppression led to 11.3% less THD compared to the conventional unshifted motors.

**Table 2.** Specifications of the conventional and proposed motor.

| Parameter | Conventional | Proposed |
|---|---|---|
| Stator outer/inner diameter [mm] | | 550/366 |
| Rotor outer/inner diameter [mm] | | 362/196 |
| Stack length [mm] | | 300 |
| Number of slots/poles | 12/10 | 24/10 |
| Number of turns | 64 | 32 |
| Number of parallel paths | 8 | 8 |
| Coil pitch | 1 | 2 |
| Rated/peak current density [A/m$^2$] | | 6.3/16.4 |
| Rated/peak current [A$_{rms}$] | | 250/636 |

**Table 3.** Performance comparison between the conventional and proposed motor.

| Parameter | Conventional | Proposed |
|---|---|---|
| Maximum torque [Nm] | 2320 | 2970 |
| Torque ripple ($T_{rip}$) [%] | 10.9 | 2.5 |
| Cogging torque ($T_{cog}$) [Nm] | 3.3 | 3.3 |
| Total harmonic distortion (THD) of back-EMF at 2000 rpm [%] | 37.3 | 33.1 |
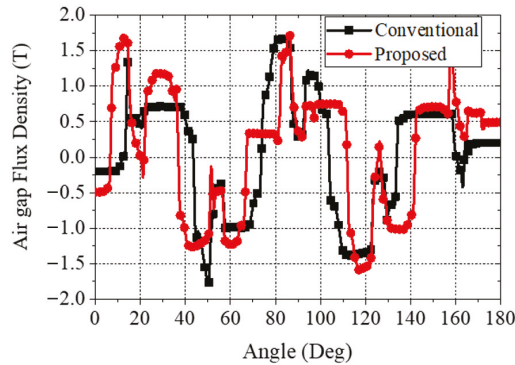


**Figure 8.** Air gap flux density at the maximum current.
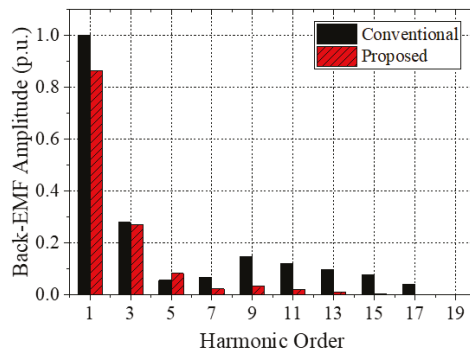


**Figure 9.** Comparison of normalized back-EMF space harmonic distribution profile of the conventional and proposed motor.

## 3. Optimal Motor Design and Specification

In this section, the $T_{rip}$ reducing circular notch method is discussed. The efficiency map with torque versus speed characteristics of the proposed 6Φ-SS-FSCW-Fer-SIPMSM was constructed and compared with the reported 6Φ-FSCW-Nd-FIPMSM. After the mechanical stress analysis at the maximum speed and the thermal analysis at the peak power, the irreversible demagnetization analysis was conducted to assess the reliability of the proposed motor at extremely low temperature of −40 °C and regular temperature at 80 °C.

### 3.1. Torque Ripple Reducing Circular Notch

Despite the small 2.5% $T_{rip}$ of the proposed motor, the $T_{rip}$ needs to be further decreased to reduce any stress affecting mechanical parts of the motor. One circular notch, having a diameter of 10 mm, was introduced on the edge of the rotor near the air gap to achieve $T_{rip}$ reduction, as shown in Figure 10. A nonmagnetic shaft with a rectangular notch was

also introduced to hold the rotor in one piece and rotate it. The performances of 6Φ-SS-FSCW-Fer-SIPMSM with and without the circular notch and a rectangular cavity-based nonmagnetic shaft are summarized in Table 4. A circular notch, having a diameter of 10 mm on the rotor, significantly decreased the $T_{rip}$ from 2.5 to 1.2% (53% reduction) while retaining the maximum torque. This is mainly attributed to the 0.3–0.4 T increased flux density in the blue dashed rectangular region in Figure 11b compared to the flux density in the blue dashed rectangular area in Figure 11a. This high flux density results in a 10.8% reduction in THD of back-EMF, which may be the main reason for the 53% reduction in the $T_{rip}$.
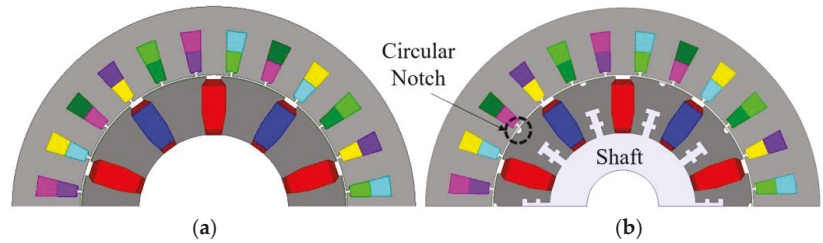


**Figure 10.** Design of 6Φ-SS-FSCW-Fer-SIPMSM (**a**) without and (**b**) with circular notch on the rotor and rectangular nonmagnetic shaft fixture.

**Table 4.** Performance comparison between conventional and proposed motor.

| Parameter | No Notch | Circular Notch on Rotor | Notch with Shaft |
|---|---|---|---|
| Torque [Nm] | 2970 | 2980 | 2980 |
| Torque ripple [%] | 2.5 | 1.2 | 1.2 |
| Torque ripple difference from no circular void [%] | - | 53 | 53 |
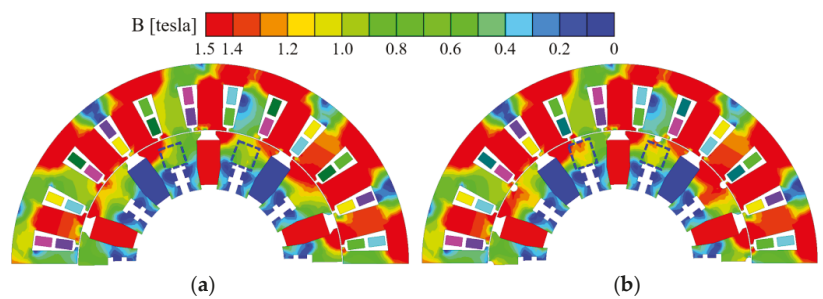


**Figure 11.** Flux density distribution of 6Φ-SS-FSCW-Fer-SIPMSM with (**a**) shaft only and (**b**) shaft and circular notch on the rotor.

A parametric study ws conducted to investigate the effects of circular notch diameter on the maximum torque and $T_{rip}$. Figure 12 shows the maximum torque, $T_{rip}$, and the $T_{cog}$ of the proposed 6Φ-SS-FSCW-Fer-SIPMSM as a function of the circular notch diameter. The maximum torque was unaffected by the circular notch diameter, as shown in Figure 12a, while the $T_{rip}$ showed a positive quadratic trend. The lowest $T_{rip}$ of 0.9% (64% reduction compared to that of the motor without notch) was observed for the motor having a circular notch with a diameter of 11 mm, which was also equivalent to 3.04% of outer rotor diameter. This reduction was mainly due to the lowest cogging torque at 11 mm diameter, as shown in Figure 12b. In summary, although the introduction of the circular notch may increase the manufacturing process and cost, the significant $T_{rip}$ of the motor can be reduced to 0.9%,

which can decrease the cost of shock absorbing materials and components. Figure 13 shows the detailed schematic of the proposed 6Φ-SS-FSCW-Fer-SIPMSM, while Table 5 shows the detailed machine dimensions.
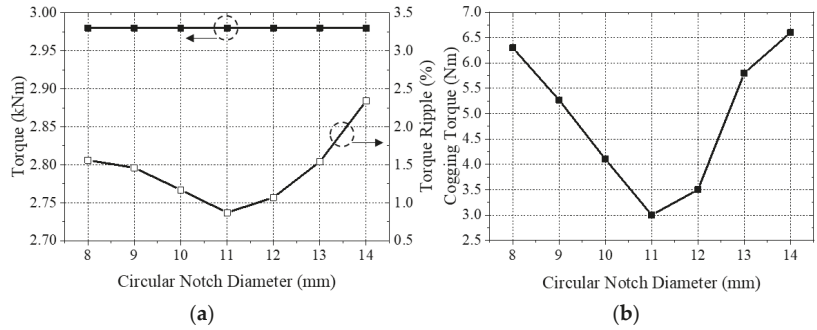


**Figure 12.** (**a**) Maximum torque and torque ripple performance and (**b**) cogging torque with respect to the diameter of the circular notch used on the rotor.
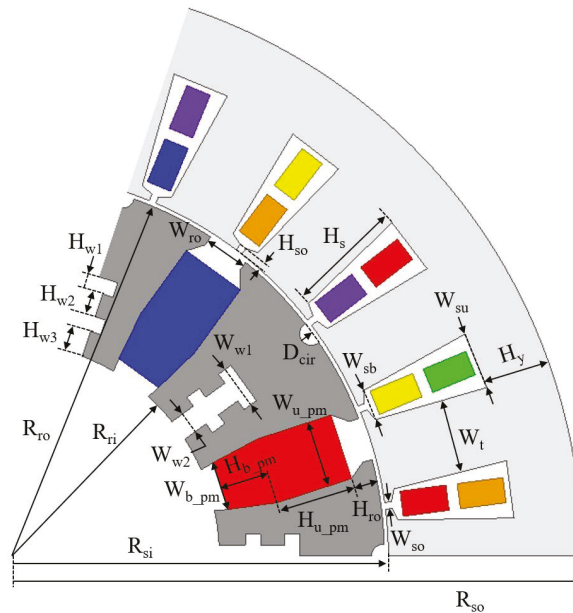


**Figure 13.** Geometrical parameters of the proposed 6Φ-SS-FSCW-Fer-SIPMSM.

**Table 5.** Machine dimensions of the proposed 6Φ-SS-FSCW-Fer-SIPMSM.

| Parameter | Symbol | Value [mm] |
|---|---|---|
| **Stator** | | |
| Yoke height | $H_y$ | 32 |
| Upper slot width | $W_{su}$ | 27.5 |
| Bottom slot width | $W_{sb}$ | 15 |
| Slot height | $H_s$ | 55 |
| Tooth width | $W_t$ | 36 |
| Slot opening height | $H_{so}$ | 3.3 |

**Table 5.** *Cont.*

| Parameter | Symbol | Value [mm] |
|---|---|---|
| **Stator** | | |
| Slot opening width | $W_{so}$ | 3.3 |
| Outer stator radius | $R_{so}$ | 275 |
| Inner stator radius | $R_{si}$ | 183 |
| **Rotor** | | |
| Rotor opening height | $H_{ro}$ | 12.1 |
| Rotor opening width | $W_{ro}$ | 20.5 |
| Rectangular cavity 1 height | $H_{w1}$ | 7.3 |
| Rectangular cavity 2 height | $H_{w2}$ | 11.4 |
| Rectangular cavity 3 height | $H_{w3}$ | 12.6 |
| Rectangular cavity 1 width | $W_{w1}$ | 20.8 |
| Rectangular cavity 2 width | $W_{w2}$ | 10.4 |
| Circular notch rotor | $R_{cir}$ | 5.5 |
| Outer rotor radius | $R_{ro}$ | 181 |
| Inner rotor radius | $R_{ri}$ | 98 |
| **Permanent Magnet** | | |
| Upper permanent magnet width | $W_{u\_pm}$ | 31.7 |
| Bottom permanent magnet width | $W_{b\_pm}$ | 23.3 |
| Upper permanent magnet height | $H_{u\_pm}$ | 37.1 |
| Bottom permanent magnet height | $H_{b\_pm}$ | 23.8 |

*3.2. Efficiency Map*

The efficiency map with the torque-speed characteristics was drawn to evaluate the proposed motor's base ($\omega_{base}$) and maximum speed ($\omega_{max}$) and power efficiency ($\eta$). The $\eta$ at the desired motor torque ($T_m$) and speed ($\omega_m$) is calculated by Equation (5).

$$\eta = \frac{P_{out}}{P_{in}} = \frac{T_m \omega_m}{T_m \omega_m + P_{cu} + P_{iron}} \tag{5}$$

where $P_{in}$ and $P_{out}$ are the input and output power, respectively, and $P_{cu}$ and $P_{iron}$ are the copper and iron loss, respectively. These losses are given by Equations (6) and (7),

$$P_{cu} = 6 I_{rms}^2 R_s \tag{6}$$

$$P_{iron} = K_h f B_m^2 + K_e f^2 B_m^2 \tag{7}$$

where $R_s$ is the stator winding resistance; $f$ is the frequency in Hz; $K_e$ and $K_h$ are the coefficient of eddy-current and hysteresis loss, respectively; and $B_m$ is the magnetic flux density. For $K_e$ and $K_h$, 0.409 and 164.2 were used, respectively.

The maximum torque per ampere (MTPA) control was utilized to find the optimal current and current angle to produce the maximum torque until $\omega_m$ reaches $\omega_{base}$. $\omega_{base}$ is a speed when the back-EMF of the motor reaches the maximum dc-link voltage ($V_{dc\_link}$), which can be calculated by Equation (8),

$$V_{dc\_link} = V_{bat} / \sqrt{3}, \tag{8}$$

where $V_{bat}$ is the battery dc voltage. Dividing $V_{bat}$ by a square root of 3 is needed because the space-vector pulse width modulation (SV-PWM) limits $V_{bat}$ at the expense of modulating voltage-fed inverter [21]. Above the base speed, the flux weakening control was applied to extend the motor operation until $\omega_m$ reached $\omega_{max}$. The motor reached its $\omega_{max}$ when both back-EMF and operating current reached a $V_{dc\_link}$ of 433 V and current limit of 636 A$_{rms}$.

By utilizing the above equations and control, the power efficiency map of the proposed 24-slot/10-pole 6Φ-SS-FSCW-Fer-SIPMSM was drawn, as shown in Figure 14a. The motor retained the constant maximum torque of 2980 Nm until the motor speed reached 1500 rpm, i.e., $\omega_{base}$, and sustained its operation until the speed reached 3750 rpm, i.e., $\omega_{max}$. The peak

$\eta$ was higher than 97% when the $\omega_m$ was between 250 to 2750 rpm, and the $T_m$ was below 600 Nm.
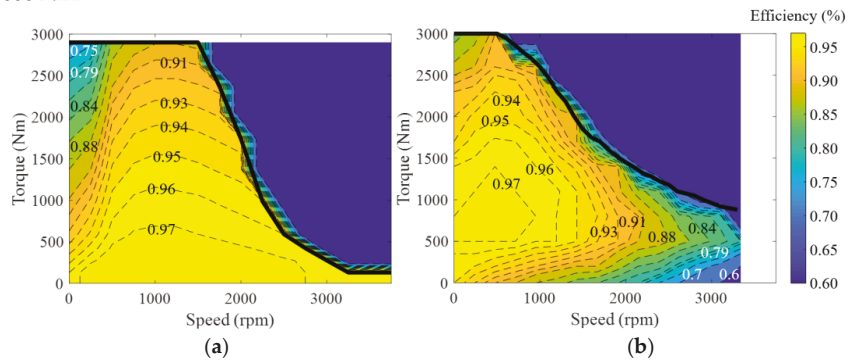


**Figure 14.** Efficiency map with torque-speed characteristic of (**a**) proposed 6Φ-SS-FSCW-Fer-SIPMSM and (**b**) conventional 6Φ-FSCW-Nd-FIPMSM.

For comparison, the efficiency map of the benchmark 300 kW 12-slot/10-pole RE-PM 6Φ-FSCW-Nd-FIPMSM was imported from [3] and plotted in Figure 14b. The motor exhibited a maximum torque of 3100 Nm, $\omega_{base}$ of 500 rpm, and $\omega_{max}$ of 3250 rpm, with a peak $\eta$ above 97% region for $\omega_m$ between 0 and 1000 rpm and $T_m$ between 500 and 1250 Nm. Compared to the benchmark RE-PM motor, the proposed ferrite motor exhibited 1000 rpm and 500 rpm higher $\omega_{base}$ and $\omega_{max}$, respectively, and 80% larger $\eta$ of 97% region with only 3.9% lower maximum torque.

### 3.3. Mechanical Analysis

Mechanical FEA analysis was conducted to validate the mechanical stability of the motor at the $\omega_{max}$ of 3750 rpm using ANSYS Mechanical. Figure 15 shows the Von Mises stress distribution in the rotor lamination, rotor shaft, and the bottom wedge of the proposed 6Φ-S-FSCW-Fer-SPMSM at 3750 rpm. As shown in Figure 15, the maximum stress occurred at the contact surface between the rotor lamination and the nonmagnetic shaft. The calculated Von Mises stresses in all these parts are well below the stress limit, which is 345 MPa for the $M19$ rotor lamination, 586 MPa for the CuBe alloy rotor shaft, and 138 MPa for the non-metallic composite rotor wedge.
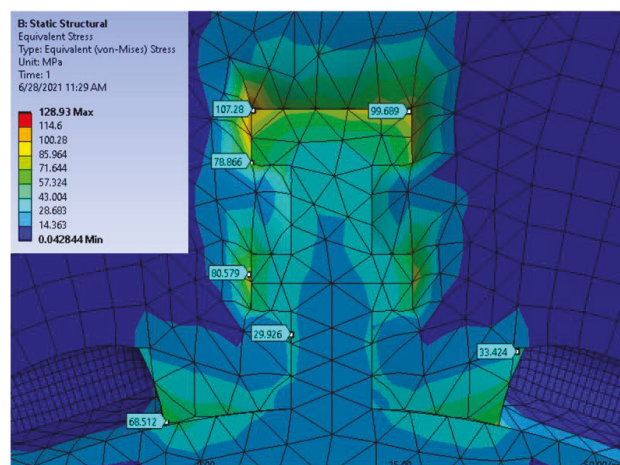


**Figure 15.** Mechanical analysis of the proposed 6Φ-S-FSCW-Fer-SPMSM at 3750 rpm.

*3.4. Thermal Analysis*

Thermal FEA analysis was conducted to validate the thermal stability of the motor at maximum power, where the current was at its peak of 690 $A_{rms}$ and speed was at its base speed of 1750 rpm. Table 6 summarizes the thermal conductivity of each component [19,22,23], while Table 7 shows the power loss density of each component. Due to the high resistance of the ferrite PM, the eddy-current loss of the PMs was negligible. Thus, the PM eddy-current loss was not included in the simulation. To cool the motor, the cooling system used in [19] was utilized. The details regarding the cooling system have been described by the authors of [19]. Figure 16 shows the FEA results at the maximum power. As clearly shown, the maximum temperature of the rotor was about 74–76 °C, which is well within the thermal limits of the permanent magnet. In comparison, the maximum temperature of the stator was around 180 °C, which occurred near the copper winding and is within the thermal limits of the class H insulation.

**Table 6.** Thermal conductivity of the components used in the simulation. Data from [19,22,23].

| Component | Thermal Conductivity [W/(mK)] | Material |
|---|---|---|
| Stator/Rotor | 48 | Silicon steel |
| Shaft | 105 | CuBe alloy |
| Winding | 387.6 | Copper |
| Air gap | 0.429 | Air |
| Permanent magnet | 1 | Ferrite |
| Rotor wedges | 0.1 | Non-metallic composite |

**Table 7.** Power loss density of the components at maximum power.

| Component | Power Loss Density [W/m$^3$] |
|---|---|
| Stator | 1,111,863 |
| Rotor | 83,169.6 |
| Winding | 1,744,287.42 |
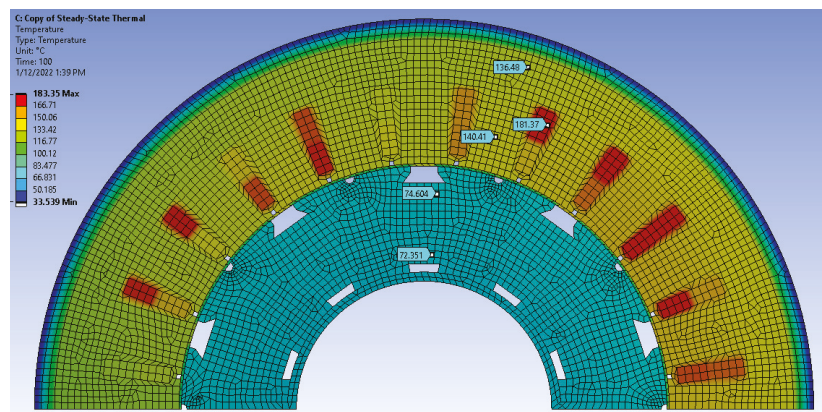


**Figure 16.** Thermal analysis of the proposed 6Φ-S-FSCW-Fer-SPMSM at maximum power.

*3.5. Demagnetization Analysis*

Due to the inherent low coercivity of the ferrite PM and positive temperature coefficient of the intrinsic coercivity, analyzing the irreversible demagnetization rate at the low (−40 °C) and high temperature (80 °C) is essential. Table 8 shows the magnetic properties of NMF-12G at −40 and 80 °C [24]. Further, it should be noted that the PM, whose flux density (*B*) or magnetic field (*H*) was below the knee point *B* value ($B_{thr}$) or exceeded knee

point H value ($H_{thr}$), was irreversibly demagnetized [14]. The $B_{thr}$ and $H_{thr}$ were 0.08 T and 330 kA/m at −40, and −0.1 T and 380 kA/m at 80 °C, respectively. Figures 17 and 18 show the $B$ and $H$ distribution of the ferrite PM under 2.6× and 2.8× rated current at −40 °C, and under 2.6× and 3.4× rated current at 80 °C. The simulation results show that the ferrite PM did not experience irreversible demagnetization, i.e., above $B_{thr}$ and below $H_{thr}$, under 2.6× rated current at both temperatures. When the current increased to 2.8× rated current at −40 °C and 3.4× rated current at 80 °C, the corner close to the airgap showed lower $B$ than $B_{thr}$ and higher $H$ than $H_{thr}$. This implies that NMF-12G ferrite PM can safely operate under a 2.8× rated current at −40 °C and 3.4× rated current at 80 °C.

**Table 8.** Magnetic properties of NMF-12G at −40 and 80 °C.

| Magnetic Property | −40 °C | 80 °C |
|---|---|---|
| Remanent flux density ($B_r$) [T] | 0.51 | 0.38 |
| Coercivity ($H_c$) [kA/m] | 345 | 299 |
| Intrinsic Coercivity ($H_{ci}$) [kA/m] | 350 | 414 |
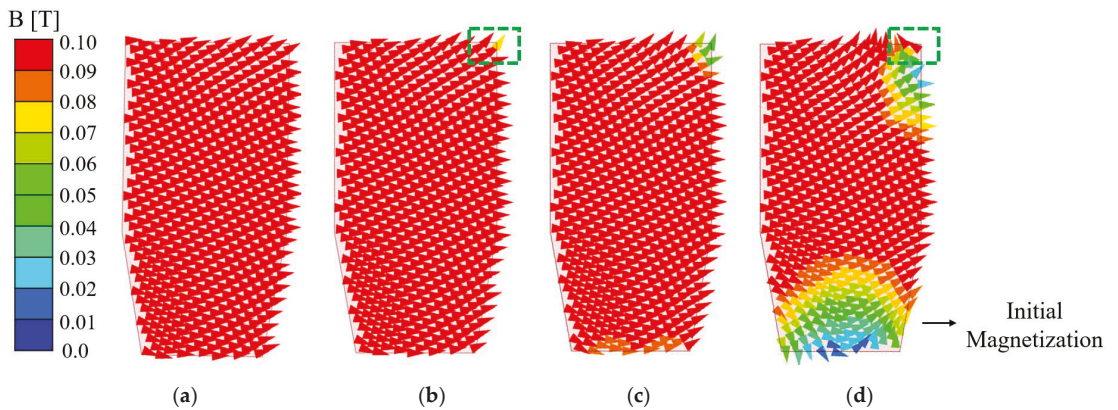


**Figure 17.** Flux density ($B$) distribution of 6Φ-SS-FSCW-Fer-SIPMSM at −40 °C when the motor current was (**a**) 2.6× and (**b**) 2.8× rated current, and 80 °C when the motor current was (**c**) 2.6× and (**d**) 3.4× rated current.
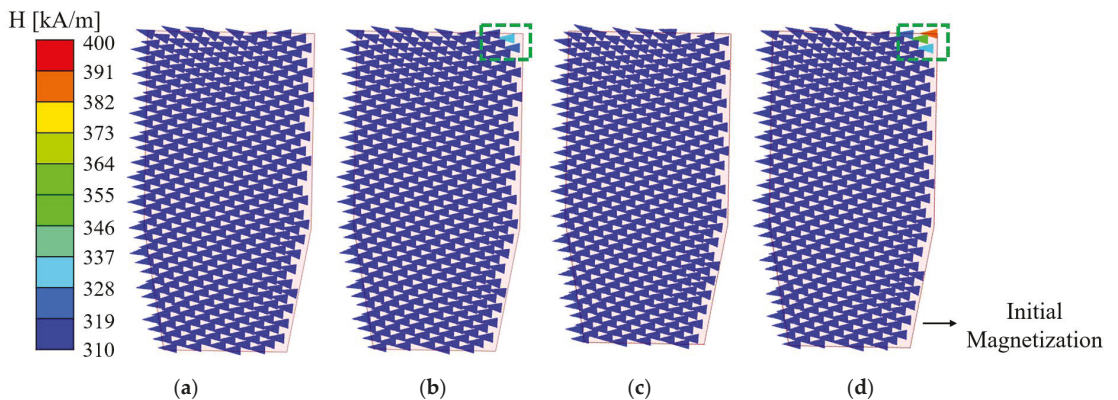


**Figure 18.** Magnetic field ($H$) distribution of 6Φ-SS-FSCW-Fer-SIPMSM at −40 °C when the motor current was (**a**) 2.6× and (**b**) 2.8× rated current, and 80 °C when the motor current was (**c**) 2.6× and (**d**) 3.4× rated current.

*3.6. Fault-Tolerant Capability*

One of the advantages of the six-phase winding configuration over the three-phase winding is the fault-tolerant capability [5]. To validate the fault-tolerant capability of the proposed six-phase machine, the motor was simulated when one of the six-phase windings was opened, i.e., I = 0. At the same time, other windings kept the same condition as a healthy case. Figure 19 shows the maximum torque profiles of the proposed machine for healthy and open-phase cases. Compared to the maximum torque for the healthy case, the average maximum torque for the open-phase case was reduced from 2.97 to 2.48 kNm, while the $T_{rip}$ was increased from 0.9 to 50%. On the other hand, the average maximum torque and $T_{rip}$ for the one-phase short-circuit case were increased from 2.97 to 3.2 kNm and from 0.9 to 32.5%, respectively. Although the one-phase open-circuit and short-circuit cause significant degradation in the maximum torque and $T_{rip}$, it is validated that the proposed motor can still operate even if one of the phases is opened and closed.
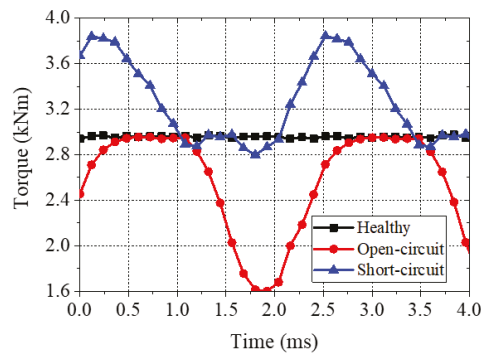


**Figure 19.** Torque performance of the proposed machine under healthy, 1-phase open-circuit, and 1-phase short-circuit.

**4. Electric Truck Simulation Model**

The dynamic model of an HDT was built and simulated using MATLAB/Simulink to assess the proposed motor performance under realistic HDT conditions. Figure 20 shows the block diagram for the HDT model, and Table 9 summarizes the vehicle specifications used in the simulation. A detailed description of each block in Figure 19 is presented below.
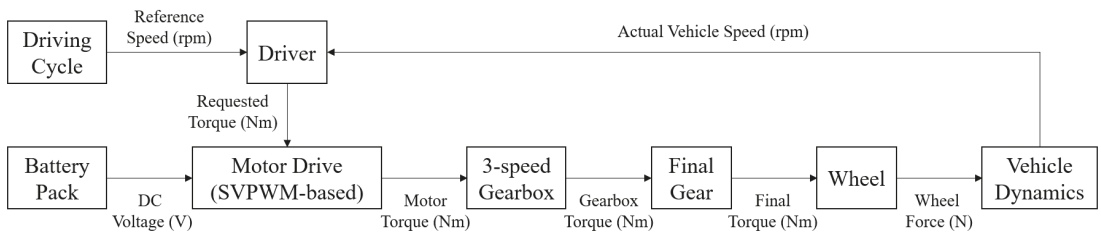


**Figure 20.** Overall block diagram for the dynamic model used in HDT simulation.

**Table 9.** Specification of the Class-7 Electric Truck Model. Data from [3].

| Parameter | Symbol | Value |
|---|---|---|
| Vehicle mass [kg] | $m_{veh}$ | 15,227 |
| Dynamic wheel radius [m] | $R_{wheel}$ | 0.488 |
| Rolling resistance coefficient | $C_{rr}$ | 0.008 |
| Coefficient of aerodynamic drag | $C_d$ | 0.6 |
| Vehicle frontal area [m²] | $A_v$ | 9.0 |

**Table 9.** *Cont.*

| Parameter | Symbol | Value |
|---|---|---|
| Initial State-of-Charge [%] | $SOC_{init}$ | 100 |
| Number of battery cell in parallel/series | $N_{parallel}/N_{series}$ | 53/225 |
| Final drive gear ratio | $G_{FDR}$ | 7.17 |

### 4.1. Driver

The main objective of this block is to convert the reference driving cycle to the required motor traction and braking torque to track the reference driving cycle. The required torque ($T_{req}$) was calculated by applying the reference and actual vehicle speed error to a proportional-integral (PI) controller. Then, the output of the PI controller, called the applied pedal position (APP), was converted to the $T_{req}$ by multiplying the output with the maximum motor torque of 2980 Nm.

### 4.2. Battery Pack

The main goal of the battery pack block is to calculate (1) the current state-of-charge ($SOC_{current}$), and (2) $V_{bat}$ from the motor current ($I_{mot}$) and calculated $SOC_{current}$. First, $SOC_{current}$ is calculated by Equation (9).

$$SOC_{current} = SOC_{init} - 100 \cdot \int \frac{I_{mot}}{3600 \cdot N_{parallel}} dt, \tag{9}$$

where $SOC_{init}$ is the initial $SOC$ of the battery pack, and $N_{cell\_parallel}$ is the number of battery cells in parallel. These values are listed in Table 9. Based on $SOC_{current}$, $V_{bat}$ is computed by Equation (10).

$$V_{bat} = N_{series} \left( V_{oc}(SOC_{current}) - \frac{R(SOC_{current}) \cdot I_{mot}}{N_{parallel}} \right) \tag{10}$$

where $V_{oc}$ and $R$ are the open-circuit cell voltage and resistance as a function of $SOC_{current}$, respectively, and $N_{series}$ is the number of battery cells in series. Figure 21 shows $V_{oc}$ and $R$ as a function of $SOC_{current}$. Since both $V_{oc}$ and $R$ change significantly at 10% of $SOC_{current}$, the simulation stops when $SOC_{current}$ reaches 15%.
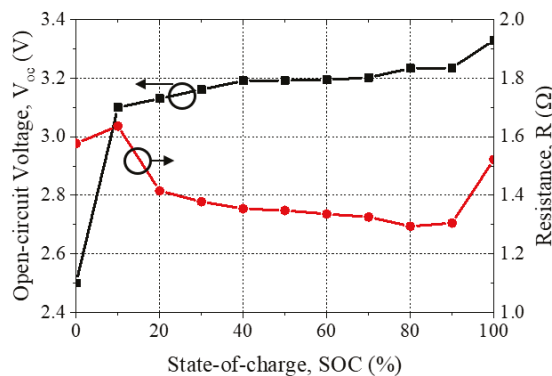


**Figure 21.** Open-circuit voltage and resistance versus state-of-charge.

### 4.3. Motor Drive

The motor drive block was used to calculate (1) $T_m$ from $T_{req}$ from the driver block, and (2) $I_{mot}$ to produce $T_m$. A lookup table determined $T_m$ with the maximum allowable torque at a given speed ($T_{thr}$), indicated by the solid black line shown in the motor efficiency map

in Figure 14. If $T_{req}$ is below $T_{thr}$, then $T_m$ equals $T_{req}$. On the other hand, if $T_{req}$ is higher than $T_{thr}$, then $T_m$ equals $T_{thr}$.

$I_{mot}$ is calculated by Equation (11).

$$I_m = \frac{T_m \omega_m}{\left(V_{dc}/\sqrt{3}\right) \cdot \eta_m} \tag{11}$$

where $\eta_m$ is each motor efficiency, as shown in Figure 14.

### 4.4. 3-Speed Gearbox and Final Gear

This block converted the $T_m$ and wheel speed ($\omega_{wheel}$) from the wheel block to the gear torque ($T_{gear}$) and $\omega_m$, respectively. $T_{gear}$ and $\omega_m$ were determined by Equations (12) and (13), respectively.

$$T_{gear} = T_m \cdot G_{1,2,3} \cdot G_{FDR}, \tag{12}$$

$$\omega_m = \omega_{wheel} \cdot G_{1,2,3} \cdot G_{FDR}, \tag{13}$$

where $G_{1,2,3}$ are the optimal three-speed gear ratios obtained in [3] under four drive cycles, and $G_{FDR}$ is the final drive ratio of 7.66. These gear ratios of the three-speed gearbox are listed in Table 10. Figure 22 describes the flowchart for the three-speed gear shifting strategy. The details of the drive cycles are presented in the following section.

**Table 10.** The 3-speed optimal gear ratio under the drive cycle.

| Drive Cycle | 1st | 2nd | 3rd |
|---|---|---|---|
| CILCC | 1.01 | 0.539 | 0.241 |
| OCC | 1.16 | 0.584 | 0.302 |
| UDDSHDV | 1.09 | 0.489 | 0.302 |
| HWFET | 1.01 | 0.416 | 0.259 |
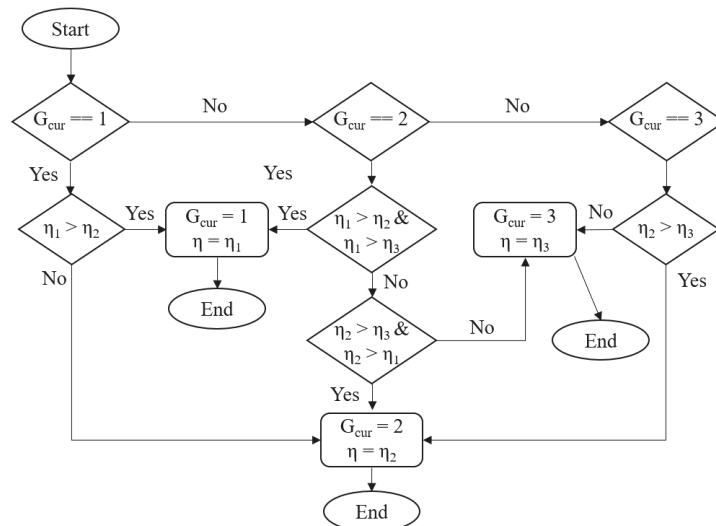


**Figure 22.** Flowchart for the 3-speed gear shifting strategy.

### 4.5. Wheel

The wheel block was used to convert (1) the $T_{gear}$ from the three-speed gearbox and final gear block to the traction force ($F_{trac}$), and (2) the vehicle speed ($V_{veh}$) from the vehicle dynamic block to the $\omega_{wheel}$. $F_{trac}$ and $\omega_{wheel}$ were calculated by Equations (14) and (15).

$$F_{trac} = T_{wheel}/R_{wheel}, \tag{14}$$

$$\omega_{wheel} = V_{veh}/R_{wheel}, \tag{15}$$

where $R_{wheel}$ is the wheel radius, listed in Table 9.

### 4.6. Vehicle Dynamics

Lastly, this subsystem converted $F_{trac}$ from the wheel block to the $V_{veh}$. The $V_{veh}$ was calculated using the following equations.

$$V_{veh} = \frac{1}{M_i} \int (F_{trac} - F_{loss})dt, \tag{16}$$

$$F_{loss} = \frac{1}{2}\rho A_v C_d (V_{veh})^2 + m_{veh}gC_{rr}, \tag{17}$$

where $g$ is the gravity (9.8 m/s$^2$), and $\rho$ is the air density (1.204 kg/m$^3$). Additional parameters are listed in Table 9.

## 5. Performance Evaluation of Proposed Motor in Electric Truck Simulation

### 5.1. Traction Performance

Generally, the class-7 HDTs are driven in two modes: city and inter-city. The city mode is driven like a utility service truck, requiring frequent start-stop operations, while the inter-city mode requires high-speed driving and few start-stop operations [3]. For the city mode, the Advanced Heavy Hybrid Propulsion Systems (AHHPS) program uses the combined international local and commuter cycle (CILCC) to evaluate HDTs [25]. The AHHPS is sponsored by the U.S. Department of Energy. To further evaluate in the city mode, the Urban Dynamometer Driving Schedule for Heavy Duty Vehicle (UDDSHDV) and Orange County Bus Cycle (OCC) were used. For the inner-city transportation, the Highway Fuel Economy Test (HWFET) was utilized. Figure 23 shows the driving cycles with the tracking performances of the reported and proposed PMSM. Both the reported and proposed PMSMs closely followed the reference driving cycles.
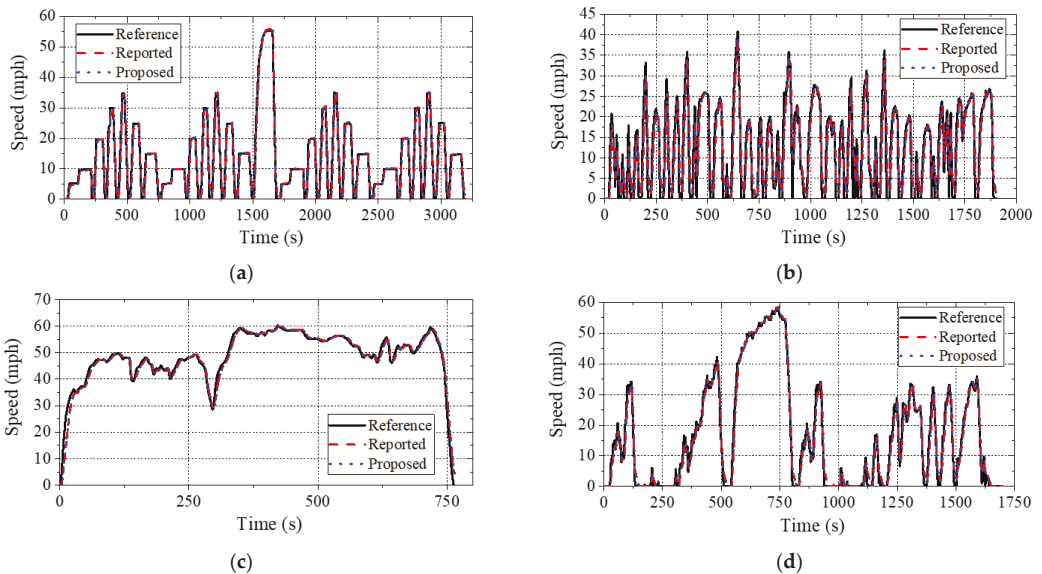


**Figure 23.** Tracking performance of the reported and proposed motor under (**a**) CILCC, (**b**) OCC, (**c**) HWFET, and (**d**) UDDSHDV.

### 5.2. Energy Consumption

Table 11 shows the energy consumption in Watt-hour (Wh) and Wh per km for the reported and proposed motor with the three-speed gearboxes. The proposed motor can save the energy by 55, 74, 28, and 90 Wh and 2.9, 5.9, 2.6, and 5.5 Wh per km in the CILCC, UDDSHDV, OCC, and HWFET driving cycle, respectively, compared to the reported motor. This implies that the proposed motor can save 1.8, 4.3, 1.9, and 3.7 kWh of energy when a 300 kWh battery is used. According to Bloomberg New Energy Finance, the average price of the battery per kWh in 2020 was USD 137 per kWh [26]. Based on this price and the calculated energy savings, the proposed motor can save USD 243.7, 589.3, 262.9, and 504 in the CILCC, UDDSHDV, OCC, and HWFET driving cycles, respectively.

**Table 11.** Energy consumption of the reported and proposed motor with a 3-speed gearbox under 4 drive cycles.

| Drive Cycle | Energy Consumption in Wh | | Energy Consumption in Wh/km | | Consumption Savings [%] |
|---|---|---|---|---|---|
| | Reported 6Φ-FSCW-Nd-FIPMSM | Proposed 6Φ-SS-FSCW-Fer-SIPMSM | Reported 6Φ-FSCW-Nd-FIPMSM | Proposed 6Φ-SS-FSCW-Fer-SIPMSM | |
| CILCC | 8485.7 | 8430.7 | 441.1 | 438.3 | 0.64 |
| OCC | 4719.6 | 4692.0 | 452.1 | 449.4 | 0.60 |
| UDDSHDV | 5658.0 | 5583.6 | 451.6 | 445.6 | 1.33 |
| HWFET | 452.0 | 446.5 | 452.0 | 446.5 | 1.22 |

### 5.3. Cost

A significant advantage of the ferrite motor over the RE-PM motor is the cost. Thereby, the costs of the reported RE-PM and proposed ferrite motor were compared to show the effectiveness of the proposed motor quantitatively. The motor cost was calculated by Equation (18):

$$\text{Machine Cost} = \left( A_{mag}\rho_{mag}C_{mag} + A_{ro}\rho_{M19}C_{M19} + A_{st}\rho_{M19}C_{M19} + A_{nm}\rho_{nm}C_{nm} \right)L + M_{cu}C_{cu}, \tag{18}$$

where $A$ denotes the area for each material, $\rho$ is the density, and $C$ is the material cost per kg. The subscripts correspond to $mag$ = magnet (NdFeB for the reported motor and NMF-12G for the proposed motor), $M19$ = M19–29G (non-oriented Si-steel), $Cu$ = copper, $nm$ = nonmagnetic wedge for the proposed motor only, $L$ = the stack length of the motor, and $M$ = the mass of the material. The cost and density of each material are listed in Table 12 [13,14]. The costs of the shaft, lamination between stacked cores, and housing with liquid cooling are excluded. Based on the prices listed in Table 12, the volume, weight, and cost of the reported and proposed motor are calculated and summarized in Table 13. These results show that the proposed motor can be fabricated not only 42 kg lighter but also with a USD 2512 lower cost than the reported motor. This cost reduction is mainly attributed to the significantly lower price of the ferrite PM than the RE-PM.

**Table 12.** Material cost and density.

| Material | Cost ($/kg) | Density (g/cm$^3$) |
|---|---|---|
| NdFeB | 100 | 7.5 |
| Ferrite | 7 | 5 |
| Copper | 7.03 | 8.96 |
| CuBe alloy | 165 | 1 |
| M19–29G | 1.0 | 7.85 |

**Table 13.** Volume, weight, and cost of the reported and proposed motor.

| Part | Reported | | | Proposed | | | Cost Savings [%] |
|---|---|---|---|---|---|---|---|
| | Volume [cm$^3$] | Weight [kg] | Cost [$] | Volume [cm$^3$] | Weight [kg] | Cost [$] | |
| Stator | 31,105 | 244.1 | 244 | 31,261 | 245.4 | 245 | 0 |
| Rotor | 19,819 | 155.6 | 156 | 14,234 | 111.8 | 112 | 28 |
| Magnet | 3570 | 26.8 | 2677 | 5467 | 27.4 | 191 | 92.9 |
| Coil | 15,066 | 135 | 949 | 15,066 | 135 | 949 | 0 |
| Wedges | 0 | 0 | 0 | 100.5 | 0.15 | 16.6 | −16,600 |
| Total | | 561 | 4026 | | 519 | 1514 | 62.4 |

## 6. Conclusions

This paper proposed a 6-phase (dual 3-phase) 24-slot/10-pole stator-shifted fractional-slot concentrated winding spoke-type ferrite permanent magnet motor for class-7 electric truck application. By adopting a stator-shifting concept and an 11 mm diameter circular notch embedded in the rotor, the proposed motor generated a maximum torque of 2980 Nm and a torque ripple of 0.9%. This low torque ripple is attributed to the significantly reduced MMF harmonic order of the 7th, 17th, 19th, and 29th, resulting in 86% torque ripple reduction with 28% torque improvement. The simulated results of the stator-shifted motor were in good agreement with the measured results of the stator-shifted prototype. The irreversible demagnetization and mechanical analysis showed that the proposed motor could operate up to the operating current of 3.8× of the rated current under extreme temperature and at its maximum speed of 3750 rpm without any issue. An electric truck model was constructed and simulated using MATLAB/Simulink to evaluate the proposed motor performance. The simulation results showed that compared to the reported NdFeB-based motor, the proposed ferrite motor could save not only the battery capacity of 2.6–5.9 Wh/km, which is equivalent to USD 244–589 when a 300 kWh battery is used, but also the motor cost of USD 2512 while showing similar motor performance.

## 7. Patents

The U.S. provisional patent entitled "Ferrite Spoke-type Permanent Magnet Synchronous Motor for Electric Truck" is under review by the U.S. patent office.

**Author Contributions:** Conceptualization, H.W. and Y.-K.H.; methodology, H.W.; software, H.W. and J.P.; validation, H.W. and J.P.; formal analysis, H.W.; investigation, H.W.; resources, Y.-K.H.; data curation, H.W.; writing—original draft preparation, H.W.; writing—review and editing, Y.-K.H., M.C., B.B., S.C., S.L., H.-S.Y. and T.A.H.; visualization, H.W.; supervision, Y.-K.H.; project administration, J.L., T.L. and T.-W.L.; funding acquisition, Y.-K.H. and T.-W.L. All authors have read and agreed to the published version of the manuscript.

**Institutional Review Board Statement:** Not applicable.

**Informed Consent Statement:** Not applicable.

**Data Availability Statement:** Data sharing not applicable.

**Conflicts of Interest:** The authors declare no conflict of interest.

## References

1. Smith, D.; Graves, R.; Ozpineci, B.; Jones, T.; Lustbader, J.; Kelly, K.; Walkowicz, K.; Birky, A.; Payne, G.; Sigler, C.; et al. *Medium-and Heavy-Duty Vehicle Electrification An Assessment of Technology and Knowledge Gaps; ORNL/SPR-2020/7*; Oak Ridge National Lab.(ORNL): Oak Ridge, TN, USA, 2019; pp. 1–60.
2. U.S. PIRG Education Fund, Environment America Research and Policy Center, Frontier Group. Available online: https://environmentamerica.org/feature/ame/electric-buses-america (accessed on 22 August 2021).

3.  Morozov, A.; Humphries, K.; Zou, T.; Rahman, T.; Angeles, J. Design, analysis and optimization of a multi-speed powertrain for class-7 electric truck. *SAE Int. J. Alt. Power.* **2018**, *7*, 27–42. [CrossRef]
4.  Patel, V.; Wang, J.; Wang, W.; Chen, X. Six-phase fractional-slot-per-pole-per-phase permanent-magnet machines with low space harmonics for electric vehicle application. *IEEE Trans. Ind. Appl.* **2014**, *50*, 2554–2563. [CrossRef]
5.  Abdel-Khalik, A.; Ahmed, S.; Massoud, A. A six-phase 24-Slot/10-pole permanent magnet machine with low space harmonics for electric vehicle applications. *IEEE Trans. Magn.* **2016**, *52*, 8700110. [CrossRef]
6.  Cheng, L.; Sui, Y.; Zheng, P.; Yin, Z.; Wang, C. Influence of stator MMF harmonics on the utilization of reluctance torque in six-phase PMA-SynRM with FSCW. *Energies* **2018**, *11*, 108. [CrossRef]
7.  Bianchi, N.; Bolognani, S.; Pre, M.; Grezzani, G. Design considerations for fractional-slot winding configuration of synchronous machines. *IEEE Trans. Ind. Appl.* **2006**, *42*, 907–1006. [CrossRef]
8.  Tangudu, J.; Jahns, T.; El-Refaie, A. Unsaturated and saturated saliency trends in fractional-slot concentrated-winding interior permanent magnet machines. In Proceedings of the IEEE Energy Conversion Congress and Exposition (ECCE), Atlanta, GA, USA, 12–16 September 2010.
9.  Alberti, L.; Bianchi, N. Theory and Design of Fractional-slot Multilayer Windings. *IEEE Trans. Ind. Appl.* **2013**, *49*, 841–849. [CrossRef]
10. Dajaku, G.; Gerling, D. Eddy current loss minimization in rotor magnets of PM machines using high-efficiency 12-teeth/10-slots winding topology. In Proceedings of the 2011 International Conference on Electrical Machines and Systems, Beijing, China, 20–23 August 2011.
11. Dajaku, G. Elektrische Maschine. German Patent DE 102008 057349 B3, 15 July 2010.
12. Jeong, C.; Hur, J. A novel proposal to improve reliability of spoke-type BLDC motor using ferrite permanent magnet. *IEEE Trans. Ind. Appl.* **2016**, *52*, 3814–3821. [CrossRef]
13. Won, H.; Hong, Y.; Choi, M.; Bryant, B.; Platt, J.; Choi, S. Cost-effectiveness hybrid permanent magnet assisted synchronous reluctance machine for electric vehicle. In Proceedings of the IEEE International Electric Machines and Drives Conference, Online, 17–20 May 2021.
14. Ma, Q.; ElRefaie, A.; Lequesne, B. Low-cost interior permanent magnet machine with multiple magnet types. *IEEE Trans. Ind. Appl.* **2020**, *56*, 1452–1463. [CrossRef]
15. Kimiabeigi, M.; Widmer, J.; Long, R.; Gao, Y.; Goss, J.; Martin, R.; Lisle, T.; Soler Vizan, J.; Michaelides, A.; Mecrow, B. On selection of rotor support material for a ferrite magnet spoke-type traction motor. *IEEE Trans. Ind. Appl.* **2016**, *52*, 2224–2233. [CrossRef]
16. Zhao, W.; Lipo, T.; Kwon, B. Torque pulsation minimizations in spoke-type interior permanent magnet motors with skewing and sinusoidal permanent magnet configurations. *IEEE Trans. Magn.* **2015**, *51*, 1–6.
17. Won, H.; Hong, Y.; Platt, J.; Choi, M.; Bryant, B.; Choi, S. Six-phase fractional-slot concentrated winding ferrite spoke-type permanent magnet synchronous motor for electric truck. In Proceedings of the IEEE International Electric Machines and Drives Conference, Online, 17–20 May 2021.
18. N42UH Arnold Magnetic Technologies. Available online: http://www.arnoldmagnetics.com/wp-content/uploads/2017/11/N42UH-151021.pdf (accessed on 23 February 2022).
19. El-Refaie, A.; Alexander, J.; Galioto, S.; Reddy, P.; Huh, K.; Bock, P.; Shen, X. Advanced high-power density interior permanent magnet motor for traction applications. *IEEE Trans. Ind. Appl.* **2014**, *50*, 3235–3248. [CrossRef]
20. Abdel-Khalik, A.; Ahmed, S.; Massoud, A. Low space harmonics cancellation in double layer fractional slot winding using dual multi-phase winding. *IEEE Trans. Magn.* **2015**, *51*, 8104710. [CrossRef]
21. Rashid, M. *Power Electronics: Circuits, Devices and Applications*, 3rd ed.; Prentice Hall: London, UK, 2004; pp. 919–923.
22. Li, Y.; Li, C.; Garg, A.; Gao, L.; Li, W. Heat dissipation analysis and multi-objective optimization of a permanent magnet synchronous motor using surrogate assisted method. *Case Stud. Therm. Eng.* **2021**, *27*, 101203. [CrossRef]
23. Ferrite Summary, TDK. Available online: https://product.tdk.com/en/system/files?file=dam/doc/product/ferrite/ferrite/ferrite-core/catalog/ferrite_summary_en.pdc (accessed on 23 February 2022).
24. Permanent Magnets, Hitachi. Available online: https://www.hitachimetals.com/materials-products/permanent-magnets/documents/Permanent_Magnets.pdf (accessed on 23 February 2022).
25. Zou, Z.; Davis, S.; Beaty, K.; O'Keefe, M.; Hendricks, T.; Rehn, R.; Weissner, S.; Sharma, V. A new composite drive cycle for heavy-duty hybrid electric class 4–6 vehicles. *SAE Trans. J. Eng.* **2004**, *113*, 771–778.
26. Green Car Reports. Available online: https://www.greencarreports.com/news/1132072_report-60-kwh-battery-pack-price-will-make-evs-cheaper-than-combustion (accessed on 22 August 2021).

# Semi-3D Analysis of a Permanent Magnet Synchronous Generator Considering Bolting and Overhang Structure

Ji-Su Hong [1], Hoon-Ki Lee [1], Junghyo Nah [1], Kyong-Hwan Kim [2], Kyung-Hun Shin [3] and Jang-Young Choi [1,*]

[1]  Department of Electrical Engineering, Chungnam National University, 99 Daehak-ro, Yuseong-gu, Daejeon 34134, Korea; hjs@o.cnu.ac.kr (J.-S.H.); lhk1109@cnu.ac.kr (H.-K.L.); jnah@cnu.ac.kr (J.N.)
[2]  Offshore Plant Research Division Korea Research Institute of Ships and Ocean Engineering, Daejeon 34103, Korea; kkim@kriso.re.kr
[3]  Department of Power System Engineering, Chonnam National University, 50 Daehak-ro, Yeosu 59626, Korea; kshin@jnu.ac.kr
*  Correspondence: choi_jy@cnu.ac.kr

**Abstract:** This study deals with the characteristic analysis of a permanent magnet synchronous generator (PMSG) with a bolting and an overhang structure. Bolting is applied to a PMSG to prevent the defects caused by scattering. To compensate the flux reduction caused by the end effect and bolting material, an overhang structure is used for the permanent magnet machine. Therefore, an overhang structure must be considered in the three-dimensional (3D) analysis of a PMSG; however, such an analysis is time-intensive. To reduce the initial analysis time, we performed a semi-3D analysis of a PMSG considering a bolting and an overhang structure. Subsequently, we compared the output results of the characteristic analysis with a 3D finite element method and experimental results under loading.

**Keywords:** semi-3D techniques; end effect; permanent magnet synchronous generator; PM overhang

## 1. Introduction

Generators are machines that convert mechanical energy into electrical energy. They are being actively studied in the design and analysis of devices for generating renewable energy owing to environmental issues. Among them, a permanent magnet synchronous generator (PMSG) uses a rare earth magnet having a high energy density. Therefore, it is advantageous for light-weighting and miniaturization compared with other generators, while achieving a high-generating efficiency. A PMSG is also utilized to convert power into energy using waves. Numerous systems are being studied to develop a wave power generator for renewable energy using PMSGs [1–4].

An oscillating water column system employed in a wave power generator should be designed to operate over a wide variable speed range [2,5–12]. Because a wave power generator endures continuous variation about speed under the effect of wave power, as such, when the power is generated at high speed due to the change in speed, the scattering of permanent magnets may occur. Therefore, methods such as sleeves and permanent magnet (PM) bolting are used to prevent the defects caused by scattering.

In this paper, the generator use a bolting. The bolting is more useful than sleeves in manufacturing processes. However, the magnetic flux is reduced by the bolting material characteristics. In addition, the end effect of PM machines also causes the leakage magnetic flux. To mitigate this problem, an overhang structure is used in which the axial length of the rotor is different from the length of the stator [6]. A PMSG with a bolting and an overhang structure should be considered as a complex three-dimensional (3D) structure. The 3D finite element method (FEM) is preferred to accurately consider and analyze these structural elements [6,13–15].

The FEM has been extensively used as a useful numerical method for analyzing complex generators in electromagnetics. The advantage of the FEM is that it enables precise analysis; therefore, the results of the characteristic analysis are similar to the experimental ones. However, it requires a long analysis time owing to various design variables, and a complex shape implies difficultly in dividing the elements [3]. One method to compensate this demerit of the FEM is the equivalent circuit method. In this method, the circuit parameters obtained from a PMSG form a semi-3D circuit and a characteristic analysis is performed. The equivalent circuit allows the analysis to not be bound to the shape of the machine, unlike the FEM, and can simplify the circuit. In addition, it is easy and can derive characteristic results and a reduced analysis time considering the circuit parameters.

In this study, a semi-3D electromagnetic characteristic analysis of a PMSG was performed, considering a bolting and an overhang structure. We used a semi-3D circuit to reduce the initial analysis time. Subsequently, an operating point of the PM obtained from a magnetic equivalent circuit was applied to a semi-3D model for considering the overhang [6,10]. The semi-3D equivalent circuit employed the circuit parameters, which were derived based on the PMSG design specifications. Inductance in the circuit parameters was also considered for accuracy. In addition, the PMSG was divided into regions of the PM with and without the bolting, and a characteristic analysis was conducted by superposition [5]. Therefore, the semi-3D analysis results were compared with the 3D FEM and experimental results.

## 2. Analysis Model

### Analysis Model of PMSG and Design Specification

Figure 1 shows the model shape of the analyzed PMSG in this study. The figure on the left shows the section view of the machine along the axial direction, and the right shows the side view. The latter shows the row of radial PMs that are bolted. In addition, the axial length of the rotor is longer than the length of the stator, as shown in Figure 1, which is the overhang to compensate the leakage flux. Table 1 summarizing the design specification shows that the length is increased by 2 mm due to the overhang. Normal two-dimensional (2D) analysis of the PMSG cannot consider an overhang and bolting because the 2D FEM is based on the axial cross-section. The PMSG should be divided into the overhang and bolting regions to analyze it structurally.
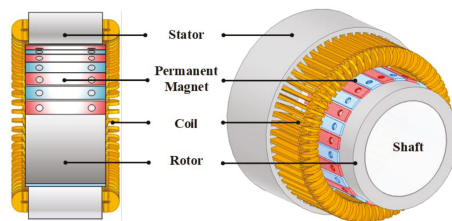


**Figure 1.** Analysis model of PMSG.

**Table 1.** Design Specifications.

| Parameters | Values | Unit |
|---|---|---|
| Stator Outer Radius | 64 | mm |
| Stator Inner Radius | 85 | mm |
| Rotor Outer Radius | 125 | mm |
| Shaft Outer Radius | 87 | mm |
| PM Arc Ratio | 0.85 | - |
| Stator Axial Length | 90 | mm |
| Rotor Axial Length | 92 | mm |
| Rated Speed | 800 | rpm |
| Rated Power | 3 | kW |

## 3. A Semi-3D Technique Method

### 3.1. Magnetic Equivalent Circuit

PM overhang compensates for leakage flux and increases effective air gap flux. The increased air gap flux means a variation in elements through the existing magnetic circuit analysis. The magnetic equivalent circuit is a characteristic analytical method to calculate flux density based on an analogy of the electric circuit. The method can algebraically represent the relationship between the magnetic flux generated by the magnet to the air gap flux. From that, it is possible to define the operating point of PMSG [10,11,16–18].

Figure 2 shows the magnetic equivalent circuit of a surface permanent magnet device. $R_{sy}$ and $R_{ry}$ are the magnetic reluctance of the stator and rotor yoke. $R_{Lmm}$ is the leakage reluctance to express magnetic flux leaking to adjacent poles or other poles. $R_{lmr}$ is the leakage reluctance between the rotor and the magnet. A permanent magnet and airgap consist of a magnetic flux source $\Phi_r$ and a reluctance of $R_{mo}$ and $R_g$ corresponding to the half pole. Figure 2a shows the magnetic equivalent circuit of a surface magnet type permanent magnet device. Figure 2c is the simplified equivalent circuit from (a) to (b) and (b) to (c). $R_{sy}$ and $R_{ry}$ are negligible given the assumption that the magnetic saturation of the stator and rotor cores are neglected [10,11,19–21].

$$P_m = P_{mo} + 2P_{Lmr} + 4P_{Lmm} \tag{1}$$
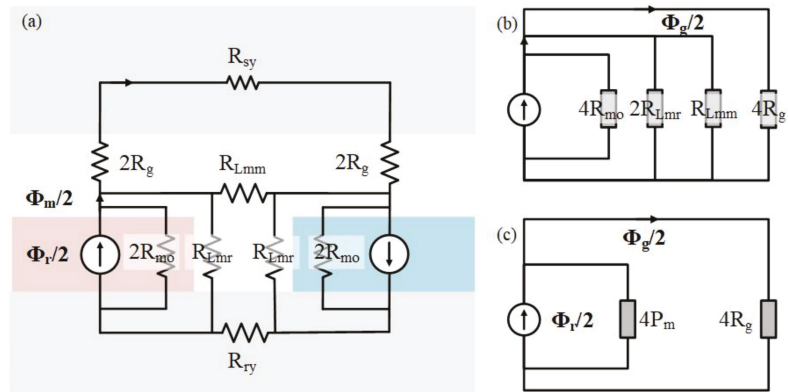


**Figure 2.** Surface-attached permanent magnet device: (**a**) magnetic equivalent circuit, (**b**,**c**) simplifications of the magnetic circuit [10,11].

Equation (1) is the permeance for the magnetic flux source. To express the magnetic flux source and the air gap flux algebraically, first, the reluctance of the magnet was synthesized in parallel. For the convenience of calculating the parallel reluctance, it is expressed as permeance.

$$\Phi_g = \frac{1}{1 + P_m R_g} \Phi_r \tag{2}$$

In Figure 2c, you can see the equivalent circuit composed of permeance and air gap reluctance. As Equation (2), the air gap flux $\Phi_g$ is expressed only as magnetic flux $\Phi_r$ by the equivalent circuit analysis, where $P_L$ is the leakage permeance of the magnet. In addition, the magnetic flux due to the magnet can also be expressed only with the magnetic flux $r$ as follows:

$$\Phi_m = \frac{1 + P_L R_g}{1 + P_m R_g} \Phi_r \tag{3}$$

The magnetic flux $\Phi_m$ was derived from Equation (3) by substituting Equation (2) from the relation between the air gap flux and the magnetic flux source. Therefore, from the derived Equations (2) and (3), the air gap flux along with the leakage factor can be newly

defined [10,11]. The leakage factor is usually defined, in general, as the ratio of airgap flux to magnet flux [8]:

$$f_{LKG} = \frac{\Phi_g}{\Phi_m} < 1 \tag{4}$$

The $\Phi_g$ and $\Phi_m$ from Equation (4) is substituted by Equations (2) and (3) as follows:

$$\Phi_g = \frac{f_{LKG}}{1 + f_{LKG}P_{mo}R_g}\Phi_r \tag{5}$$

Finally, given that $\Phi_g = B_gA_g$ and $\Phi_r = B_rA_m$, Equation (5) gives another convenient formula for $B_g$ [8].

$$B_g = \frac{f_{LKG}}{1 + f_{LKG}P_{mo}R_g} \times \frac{A_m}{A_g}B_r \tag{6}$$

where $B_g$ is the average airgap flux-density across the airgap area $A_g$, and $A_m$ is the magnet pole area, both being circulated for one pole [8].

### 3.2. Operating Point of PMSG Using Magnetic Energy

As the magnetic flux increases using the PM overhang, the overall magnetic energy increases. The magnetic energy equation is as follows:

$$W = \int w_m dv = \int \frac{1}{2} B_m \cdot H_m dv \tag{7}$$

An equation considering the increase in the magnetic energy from Equation (1) can be derived. For the equation, the 3D magnetic energy is calculated the same as in the 2D model [7]. The equation is expressed as follows [19–22]:

$$\frac{1}{2} B_m H_m V = \frac{1}{2} B_m{'} H_m{'} V' \tag{8}$$

The left side of Equation (8) is the magnetic energy of the 3D model, and the right side is the magnetic energy of the semi-3D model. $B_m$ and $H_m$ are the magnetic flux density and the magnetic field at the operating point of the 3D model, respectively. $B_m'$ and $H_m'$ are represented by the operating points of the semi-3D model considering the overhang. $V$ and $V'$ are the volumes of the PM. The volume is calculated using the axial length and the area per pole. Assuming that the thickness values of the PMs of the 3D and semi-3D models are the same, the volume varies depending on the length of the overhang, resulting in a variation in the operating point [15].

Figure 3 shows the demagnetization curve. It can yield the permeance coefficient (PC) as a variation from a to a'. The PC in Equation (9) is defined as the load line slope from being derived in Equation (6). The slope can be expressed algebraically in the Cartesian coordinate system by the magnetic field and magnetic flux density shown in Figure 2. In addition, the PC can be expressed as Equation (9) [8,13,14].

$$PC = \frac{B_m}{\mu_0|H_m|} = \frac{1}{f_{LKG}} \times \frac{L_{PM}}{g} \times \frac{A_g}{A_m} \tag{9}$$

In Equation (9), $f_{LKG}$ is the leakage factor, which typically has a value in the range of 0.85–0.95, with a calculated median value of 0.9, discretionally [8]. $g$ and $L_{PM}$ are the radial width of the air gap and the PM, per pole, respectively. $A_g$ and $A_m$ are areas of the air gap and the axial cross-sectional per pole of the PM, respectively.

From Equations (8) and (9), the semi-3D permanent magnet operating point equation can be derived as follows:

$$B_m{'} = \sqrt{-\mu_0 \times PC \times \frac{V}{V'} \times B_m \times H_m} \tag{10}$$

$$H_m' = -\frac{B_m'}{\mu_0 \times PC} \tag{11}$$

The results of the equation for the operating point are summarized in Table 2. The residual magnetic flux density, $B_r$, obtained from Equations (10) and (11), ranges from 1.1056 [T] to 1.1209 [T]. $B_r$ was applied to the semi-3D model to consider the overhang structure.
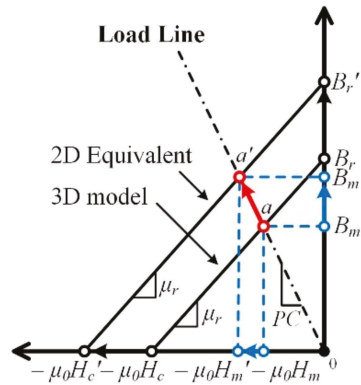


**Figure 3.** Demagnetization curve.

**Table 2.** Equivalent results considering overhang.

| Parameters | Unit | 3D Model | Semi-3D Model |
|---|---|---|---|
| $B_m$ | T | 0.7762 | 0.7869 |
| $H_m$ | A/m | −253,359 | −256,853 |
| $B_r$ | T | 1.1056 | 1.1209 |

*3.3. Analysis Method Considering Bolting and Overhang*

The magnetic energy is used to consider the overhang; however, the method to analyze the bolting is different. The bolting does not need to consider the length of the PM for the overhang. This is because the effect on the increase in the magnetic energy is applied in the overhang region. Instead, it is necessary to understand the bolting structure of the 3D model and change it to a semi-3D model.

The bolting structure has a cylindrical form, as shown in Figure 4a. However, radial cylindrical columns cannot be expressed in the 2D FEM. Therefore, in 2D, the bolting is modeled as a rectangular parallelepiped volume. For simplification, the bolting volumes of the 2D and 3D models are the same in the bolting regions. The equation for calculating the width is expressed as follows:

$$B_{Width} = \frac{V_{Bol}}{D_{Bol} \times M_{Thick}} \tag{12}$$

where $B_{Width}$ is the bolting width obtained from Equation (12) for the semi-3D model. $D_{Bol}$ is the diameter of the 3D bolting. The diameter is used along the axial length of the bolting region. $M_{Thick}$ is the thickness of the PM. Figure 4 shows a part of the analysis model.

Figure 4a–c are the 3D model, bolting region, and overhang region, respectively. The semi-3D model considering a bolting and an overhang can be analyzed by dividing it into corresponding regions, as in the above method. Subsequently, characteristic analyses of the divided regions are performed based on superposition [5]. Table 3 lists the magnetic flux density applied to each region.
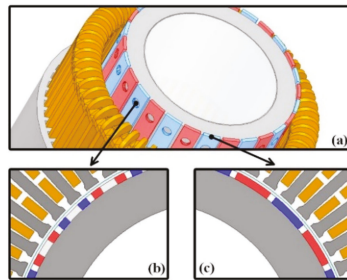
**Figure 4.** Analysis models: (**a**) 3D model, (**b**) PM with bolting, (**c**) PM without bolting.

**Table 3.** Axial length and flux density for analysis model.

| Parameters | Unit | Bolting Model | PM Model |
|---|---|---|---|
| Axial length | mm | 18 | 72 |
| $B_r$ | T | 1.1056 | 1.1208 |

### 3.4. Equivalent Circuit Method

The equivalent circuit method consists of the circuit parameters obtained from the design specifications of a PMSG. It assumes the induced voltage of a generator as a sine wave. Subsequently, the output characteristics are derived using the equivalent resistance, synchronous inductance, and load resistance based on the circuit parameters. Among the circuit parameters, the phase resistance was directly calculated through the equation. The no-load back electromotive force (EMF) and a phase inductance were derived through FEM. The voltage, current, and power calculated using the equivalent circuit vary according to the circuit parameters. Figure 5 presents the equivalent circuit of the PMSG with an AC load.

$$E_{ph} = \pi\sqrt{2}fN_{ph}\phi_f k_\omega, \tag{13}$$

$$R_{ph} = \rho_c \frac{L_c}{A_c} \tag{14}$$

$$L_c = 2L_{stk} + 2r_{coil\_end} \times \pi \tag{15}$$
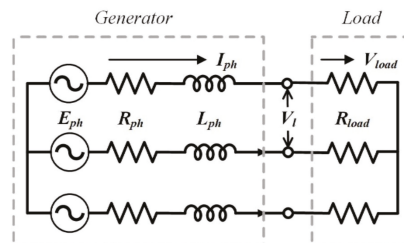


**Figure 5.** Equivalent circuit of PMSG with an AC load.

Equations (13)–(15) yield the circuit parameters. $E_{ph}$ is the no-load EMF of the AC load. $R_{ph}$ is the phase resistance calculated to 1.3 Ω. $L_c$ is the length of winding in a coil. The output characteristics equations are as follows:

$$V_{load} = E_{ph} \sqrt{\frac{R_{load}^2}{\left(R_{ph} + R_{load}\right) + \left(wL_{ph}\right)^2}} \tag{16}$$

$$I_{ph} = \frac{E_{ph}}{\sqrt{\left(R_{ph} + R_{load}\right)^2 + \left(wL_{ph}\right)^2}} \tag{17}$$

$$P_{out} = 3V_{load}I_{ph} \tag{18}$$

$$P_{in} = 3V_{load}I_{ph} + P_{copper} + P_{core} + P_{rotor} + P_{mech} \tag{19}$$

The output voltage can be derived from the no-load back EMF by the voltage divider rule. $V_{load}$ in Equation (16) is derived from $R_{load}$, which is the load resistance [9]. Therefore, the output current is also obtained from Equation (17). The output power, $P_{out}$, is calculated using the output voltage and the current obtained. In addition, among the elements composing the equation, inductance $L_{ph}$ derived through 2D and 3D FEM is the circuit parameter of the equivalent circuit. w is the speed.

Table 4 lists the considered circuit parameters. It also summarizes the output characteristics of PMSG determined from Equations (16)–(18) according to the circuit parameters.

**Table 4.** Circuit parameters.

| Parameter | Unit | Speed [rpm] | $R_{load}$ [Ω] | Value | | |
|---|---|---|---|---|---|---|
| | | | | 2D FEM | 3D FEM | Exp. |
| $E_{ph}$ | $V_{rms}$ | 800 | 40 | 345.9 | 348.9 | 345.8 |
| $L_{ph}$ | $mH$ | | | 10.1 | 12.2 | - |

## 4. Analysis and Experiment Results

### 4.1. Experiment Model

Figure 6a–c show the manufactured model—specifically, the experimental set, stator, and rotor with the PM bolting, respectively. The bolting material is steel, which affects performance. The characteristic analyses of the model have performed the characteristic analysis to AC.



Generator  Speed & Torque Sensor  Servo Motor

(a)

Stator  (b)          Rotor  (c)
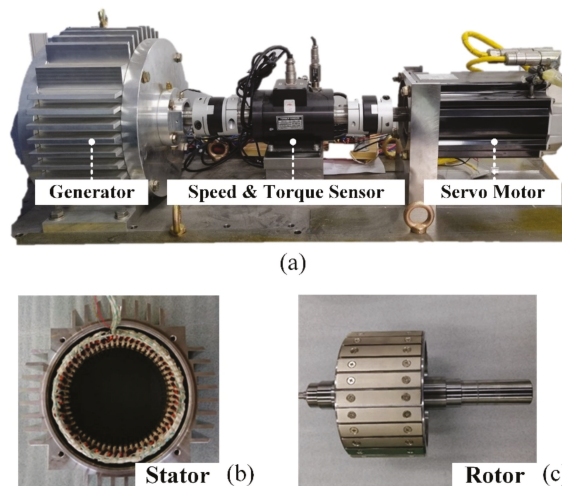
**Figure 6.** Manufactured model: (**a**) experimental set, (**b**) stator, and (**c**) rotor.

### 4.2. No-Load Analysis

Figure 7 shows the phase-to-phase voltage results from the no-load analysis. Figure 7a shows the voltage according to the effect of the overhang and bolting. The overhang

compensated for the leakage flux caused by the end effect and showed a voltage increase rate of about 0.6% compared to that without consideration. Although the bolting of PMs reduces output performance due to the reduction of permanent magnets, the advantages in the manufacturing process are more useful. In addition, it can be seen from the semi-3D analysis that the output is compensated for by the overhang.



(a)

(b)
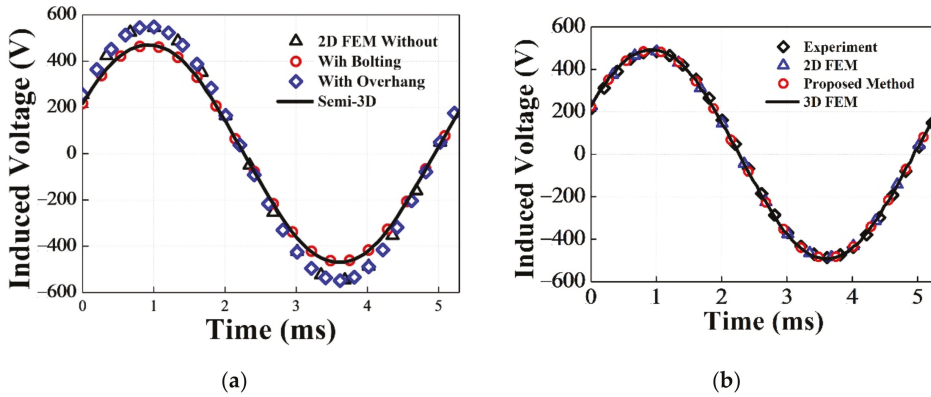
**Figure 7.** No-load characteristic curve: (**a**) effect of the overhang and bolting, (**b**) comparison of the results.

In Figure 7b, The 2D FEM is the characteristic curve that does not consider the operating point of PM. The proposed method considers the overhang and the bolting in the semi-3D model. For verification, the results are compared to the 3D FEM and experimental result. In the analysis specifications, the speed is 800 rpm. Table 4 summarizes the compared results. The error between the semi-3D analysis and the experiment (Exp.) is less than 4%. Although the 3D FEM has a lower error rate than the semi-3D analysis, the results of the latter are similar to the experimental ones.

*4.3. AC Load Analysis*

Figure 8 shows the characteristic curves of the semi-3D model under AC load. Figure 8a,b present the output power–voltage and current–voltage curves, respectively. For the PMSG model analysis, the overhang is considered using the operating point. Subsequently, the circuit parameters are applied to the equivalent circuit with the AC load.



(a)

(b)
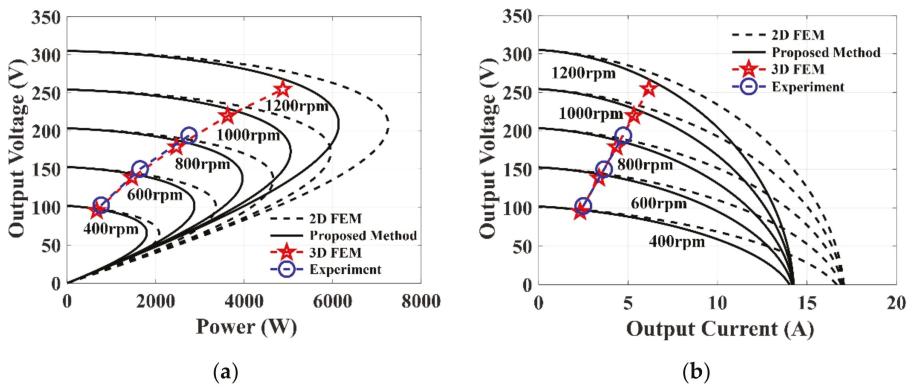
**Figure 8.** Load characteristic curve: (**a**) power–voltage curves, (**b**) current–voltage curves.

For accurate results, inductances derived from 2D and 3D FEMs are used as circuit parameters, as listed in Table 4. The characteristic curve shows that the output has applied inductance, as shown in Figure 8a,b, respectively. The 2D FEM shows the results using the inductance derived from the 2D FEM, and the proposed method presents the results using the inductance derived from the 3D FEM. The result using the inductance derived from 3D FEM matched better with 3D FEM than the result using 2D FEM inductance. Table 5 lists the output power results according to the speed when $R_{load}$ is 40 Ω. From the results, the semi-3D analysis and 3D FEM are compared to the experiment, and the error rate is derived. The error between the semi-3D analysis and Exp. is less than 4% at 600 rpm. Therefore, the semi-3D analysis using the equivalent circuit is similar to the characteristic analysis from Exp.

**Table 5.** AC load analysis results according to speed.

| Speed [rpm] | $R_{load}$ [Ω] | Value [W] | | | | Error [%] | |
|---|---|---|---|---|---|---|---|
| | | 2D FEM | Semi-3D | 3D FEM | Experiment | Semi-3D | 3D FEM |
| 400 | | 720.25 | 717.11 | 699.51 | 766.85 | 6.49 | 8.78 |
| 600 | 40 | 1601.5 | 1586 | 1510.8 | 1646.5 | 3.67 | 8.24 |
| 800 | | 2800.9 | 2754 | 2545.3 | 2753.1 | 0.03 | 7.55 |

## 5. Conclusions

In this study, we performed the characteristic analysis of a PMSG considering an overhang and bolting. First, for considering the overhang structure, the operating point was obtained using the magnetic energy equation. Subsequently, the equivalent circuit of the PMSG considered inductance for the output characteristics analysis. The proposed method uses inductance derived from the 3D FEM. The semi-3D analysis applying two methods derived results based on superposition. The results of the proposed method were compared to 3D FEM and Exp. analysis results. However, the validity of the proposed method was verified by the similarity of these results. Therefore, it is considered that the method using inductance derived from the 3D FEM will be more useful than the previous one using the 2D inductance.

## References

1. Hong, K.P.; Kang, G.H.; Lee, S.K. Design of a 6kW permanent magnet synchronous generator with low speed and high torque for gyro wave power generation. *J. Korean Soc. Mar. Eng.* **2017**, *41*, 878–883.
2. O'Sullivan, D.L.; Lewis, A.W. Generator Selection and Comparative Performance in Offshore Oscillating Water Column Ocean Wave Energy Converters. *IEEE Trans. Energy Convers.* **2011**, *26*, 603–614. [CrossRef]
3. Lee, C.W. Calculation of Self and Mutual Inductances in Multi-Phase Permanent Magnet Synchronous Motor. *J. Korean Magn. Soc.* **2017**, *27*, 9–17. [CrossRef]

4.  Choi, J.Y.; Kang, H.B.; Hong, S.A. Review of Linear Permanent Magnet Generator for Wave Energy Converter according to Magnetic Circuit Construction. *KAOSTS* **2014**, 2397–2402.
5.  Shin, K.H. Characteristic Analysis of Wave Power Generator Considering Bolting to Fix Permanent Magnet Based on Analytical Method. *IEEE Trans. Magn.* **2019**, *55*, 7501805. [CrossRef]
6.  Woo, D.-K.; Lim, D.-K.; Yeo, H.-K.; Ro, J.-S.; Jung, H.-K. A 2-D finite-element analysis for a permanent magnet synchronous motor taking an overhang effect into consideration. *IEEE Trans. Magn.* **2013**, *49*, 4894–4899. [CrossRef]
7.  Lee, T.-Y.; Seo, M.-K.; Kim, Y.-J.; Jung, S.-Y. Motor design and characteristics comparison of outer-rotor-type BLDC motor and BLAC motor based on numerical analysis. *IEEE Trans. Appl. Supercond.* **2016**, *26*, 5205506. [CrossRef]
8.  Hendershot, J.R., Jr.; Miller, T.J.E. *Design of Brushless Permanent-Magnet Motors*; Magna Physics Publishing and Clarendon Press: Oxford, UK, 1994.
9.  Chan, T.F.; Lai, L.L.; Yan, L.-T. Performance of a three-phase AC generator with inset NdFeB permanent-magnet rotor. *IEEE Trans. Energy Convers.* **2004**, *19*, 88–94. [CrossRef]
10. Yeo, H.-K.; Lim, D.-K.; Woo, D.-K.; Ro, J.-S.; Jung, H.-K. Magnetic Equivalent Circuit Model Considering Overhang Structure of a Surface-Mounted Permanent-Magnet Motor. *IEEE Trans. Magn.* **2015**, *51*, 8201004.
11. Qu, R.; Lipo, T.A. Analysis and modeling of air-gap and zigzag leakage fluxes in a surface-mounted permanent-magnet Machine. *IEEE Trans. Ind. Appl.* **2004**, *40*, 121–127. [CrossRef]
12. Delmonte, N.; Barater, D.; Giuliani, F.; Cova, P.; Buticchi, G. Review of Oscillating Water Column Converters. *IEEE Trans. Ind. Appl.* **2016**, *52*, 1698–1710. [CrossRef]
13. Ko, Y.; Song, J.; Seo, M.; Han, W.; Kim, Y.; Jung, S. Analytical Method for Overhang Effect of Surface-Mounted Permanent-Magnet Motor Using Conformal Mapping. *IEEE Trans. Magn.* **2018**, *54*, 8208005. [CrossRef]
14. Koo, M.; Choi, J.; Park, Y.; Jang, S. Influence of Rotor Overhang Variation on Generating Performance of Axial Flux Permanent Magnet Machine Based on 3-D Analytical Method. *IEEE Trans. Magn.* **2014**, *50*, 8205905. [CrossRef]
15. Yeo, H.; Ro, J. Novel Analytical Method for Overhang Effects in Surface-Mounted Permanent-Magnet Machines. *IEEE Access* **2019**, *7*, 148453–148461. [CrossRef]
16. Sheikh-Ghalavand, B.; Vaez-Zadeh, S.; Isfahani, A.H. An Improved Magnetic Equivalent Circuit Model for Iron-Core Linear Permanent-Magnet Synchronous Motors. *IEEE Trans. Magn.* **2010**, *46*, 112–120. [CrossRef]
17. Moallem, M.; Dawson, G.E. An improved magnetic equivalent circuit method for predicting the characteristics of highly saturated electromagnetic devices. *IEEE Trans. Magn.* **1998**, *34*, 3632–3635. [CrossRef]
18. Mi, C.; Filippa, M.; Liu, W.; Ma, R. Analytical method for predicting the air-gap flux of interior-type permanent-magnet machines. *IEEE Trans. Magn.* **2004**, *40*, 50–58. [CrossRef]
19. Tsai, W.-B.; Chang, T.-Y. Analysis of flux leakage in a brushless permanent-magnet motor with embedded magnets. *IEEE Trans. Magn.* **1999**, *35*, 543–547. [CrossRef]
20. Hsieh, M.; Hsu, Y. A Generalized Magnetic Circuit Modeling Approach for Design of Surface Permanent-Magnet Machines. *IEEE Trans. Ind. Electron.* **2012**, *59*, 779–792. [CrossRef]
21. Kano, Y.; Kosaka, T.; Matsui, N. Simple nonlinear magnetic analysis for permanent-magnet motors. *IEEE Trans. Ind. Appl.* **2005**, *41*, 1205–1214. [CrossRef]
22. Song, J.; Lee, J.H.; Kim, Y.; Jung, S. Computational Method of Effective Remanence Flux Density to Consider PM Overhang Effect for Spoke-Type PM Motor With 2-D Analysis Using Magnetic Energy. *IEEE Trans. Magn.* **2016**, *52*, 8200304. [CrossRef]

*Article*

# Prospect of PM Vernier Machine for Wind Power Application [†]

**Pushman Tlali and Rong-Jie Wang \***

Department of Electrical & Electronic Engineering, Stellenbosch University, Stellenbosch 7600, South Africa; pushman.tlali9@gmail.com
\* Correspondence: rwang@sun.ac.za
† This paper is an extended version of our paper published in 2020 International Conference on Electrical Machines, Gothenburg, Sweden, 23–26 August 2020; pp. 2637–2643.

**Abstract:** This paper investigates the prospect of permanent magnet vernier machine (PMVM) technology for wind power applications. Two types of PMVMs are defined based on the winding arrangements and resultant gear ratio ranges. A comprehensive design study of the selected PMVM topologies is conducted at 1 and 3 MW power levels. The optimized candidate designs of the PMVMs are then evaluated and also compared against the equivalent permanent magnet synchronous machine (PMSM) in terms of performance, costs, size and mass. While the existing research publications mainly focused on the PMVM designs of ($G_r = 5$), this study reveals that the pole/slot combinations of PMVMs with ($G_r \leq 5$) are more appealing as there is a good trade-off between a reasonable power factor and high power density in these designs. It shows, in this paper, that the PMVM is a promising alternative to common PMSM technology for utility-scale wind-turbine drive-train applications.

**Keywords:** design optimization; direct-drive generators; finite element analysis; magnetic gearing effect; permanent magnet vernier machines

## 1. Introduction

Wind energy is one of the most important renewable energy sources. The worldwide wind power generation capacity has been growing at a substantial rate over the past decades. Research in wind turbine systems has indicated a crucial need to develop high-performance and cost-effective electrical machine technologies, as they are an integral part of wind turbine power-trains and play a significant role in wind energy conversion. Doubly-fed induction generator (DFIG) with a partial-scale power electronic converter (PEC) and a single or three-stage gearbox has been the most dominant wind turbine power-train technology since the early 2000s. Another common wind turbine power-train technology involves a permanent magnet (PM) synchronous generator with a full-scale PEC and a single or multi-stage gearbox [1,2]. Owing to gearbox issues and related system reliability concerns, there has been a paradigm shift towards the use of direct-drive (DD) generators with full-scale PECs, especially for offshore wind power applications. However, since the direct-drive generators run at a low turbine speed, they are inherently heavier and larger due to high torque handling requirements in wind turbine systems.

In the past decade, there has been much interest in magnetically geared electrical machine technologies [3]. Amongst others, permanent magnet vernier machines (PMVM) received a lot of attention [4–6]. The inherent magnetic gearing effect enables the PMVM to have high torque density, potential for less weight and more compactness than conventional permanent magnet synchronous machines (PMSM), while also keeping the same structural simplicity. Despite these distinct advantages, the PMVMs are notably characterized by poor power factor, which increases the PEC rating requirement. In an attempt to improve the power factor of PMVMs, some researchers proposed more complex machine topologies such as double-stator [7] and double-rotor [8] PMVMs, while others studied special PM arrangements like Halbach [9] or spoke-type [10].

Some early comparison studies between PMVMs and conventional PMSMs can be found in the literature. However, they mainly focused on electric vehicles (EV) and general low-speed industrial drive applications [4,11–13]. A systematic method for designing direct-drive PM vernier wind generators is presented in [14] and validated based on a designed 5 kW prototype [15]. The work reported in [16,17] is probably the first attempt at the design, practical evaluation and comparison of a surface-mounted PMVM with a benchmark conventional PMSM for wind power applications.

More recently, the quantitative analysis of the applicability and potential of PMVM technology for utility-scale wind power applications has been conducted in [18–21]. The general conclusion drawn from these studies is that systems involving PMVM designs are not yet competitive in comparison to those of conventional PMSMs with several-megawatt (MW) power levels. This is because the only benefit that seems to be guaranteed from PMVM is the significant reduction in machine volume, while the advantage of lower active mass is discounted by the fact the total machine mass in direct-drive generator systems is heavily dominated by the structural mass.

Furthermore, other benefits such as higher efficiency and lower cost obtained at the PMVM level seem to be overturned when the whole system is considered, mainly due to the increased power converter costs and losses associated with the PMVM system. Moreover, it was further revealed that when observed from the slot-pitch-ratio (SPR) point of view, the design of PMVM seems to be a trade-off between the improved performance and demagnetization risk [18]. Interestingly, the majority of the available PMVM designs at multi-MW output level are limited to only a pole-ratio ($G_r$) of five (5), including the studies in [18,19]. Hence, this paper will extend the current knowledge gap by further looking into other pole-ratios greater and/or less than five. This will provide a wider picture of what could lead to the optimal design at this power level.

An interesting aspect of the PMVM technology is that a standard PMVM (*with a single-stator and a single-rotor*) has the same mechanical simplicity and gear-less layout as that of a conventional DD-PMSM, which suggests that the PMVM is simply another DD-PMSM. On the other hand, a PMVM usually operates at a slightly higher frequency due to its inherent magnetic gearing features, which are closer to that of the medium-speed (MS) geared PMSMs. A more intuitive view can be gained by putting the PMVM technology alongside current mainstream wind generator technologies, as shown in Figure 1, which clearly shows that the PMVM technology shares some advantages and unique characteristic properties with both the direct-drive (*high torque capability and low maintenance*) and medium-speed (*lower mass*) PMSMs.

This paper is the extended version of [20], which aims at studying the feasibility of implementing the PMVM technology for high-power wind generator systems. To achieve this goal, a detailed design optimization study using the finite element method (FEM) is conducted for a number of selected PMVM topologies/design choices at utility power levels. The realized PMVM designs are then evaluated against a conventional PMSM of corresponding power rating. With the ever-increasing power capacity and size of turbines in the wind energy industry, it becomes more challenging to mount a nacelle on the top of a tower. A lighter and lower-cost wind generator is always preferred in the wind power industry. Thus, the main design objective in this study is to minimize the total mass and cost of active electromagnetic material of a PMVM, while subjecting it to the overall dimensional constraints and design specifications.

In this updated paper, for the sake of completeness, the fundamental working principle of the PMVM is given in Section 2, the basic winding configurations of PMVMs are described in Section 3, and this will be followed by a brief description of the field-circuit model of PMVMs in Section 4 and the explanation of the implemented optimization strategy and specifications in Section 5. Then, the obtained results are presented and discussed in Section 6. In comparison with [20], the validation of the formulated PMVM design optimization approach is also included in Section 7, after which relevant conclusions are drawn in Section 8.
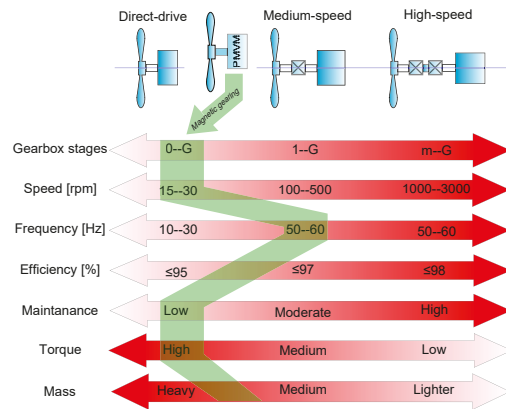
**Figure 1.** PMVM vs. DD-PMSM and MS-PMSM characteristics at utility power levels (© [2020] IEEE. Reprinted, with permission from [20]).

## 2. Fundamental Working Principle

The basic operation of PM Vernier machines relies on the *Magnetic Gearing* principle [22,23]. In this concept, a high-speed low-order space harmonic field is generated by the stator windings, whereas the low-speed high-order space harmonic field originates from the rotor PMs. The two field harmonics are magnetically coupled through modulation by the ferromagnetic pole-pieces (*flux modulator*), which are normally situated in-between their respective exciting components. Flux modulator can be in the form of a separate component or a split stator tooth or even the stator teeth themselves. For the magnetic gearing principle to be effectively realized in PMVMs, the number of winding pole-pairs ($p_s$), rotor pole-pairs ($p_r$) and flux-modulator pole-pieces ($N_s$) is strictly related by [22,24]:

$$N_s = p_r \pm p_s \tag{1}$$

In addition, it has been proven that a pole/slot combination given by $N_s = p_r + p_s$ enables a better performing PMVM design as opposed to the other combination with $N_s = p_r - p_s$ [25]. The number of stator teeth/slots ($Q_s$) can then be separately selected according to the applicable rules to achieve stable field generation with balanced phase flux linkages at the chosen frequency. However, in the case of the PMVM type where the stator teeth also perform the modulation function, it means the stator-slots number is the same as that of the modulating pieces; hence, $N_s$ can be replaced by $Q_s$ in (1).

With regards to the surface-mounted PMVM, a linearized and simplified geometrical structure of which is presented in Figure 2, the modulated air-gap flux density can be approximated as:

$$
\begin{aligned}
B_{PM}(\theta, t) = F_{PM}(\theta, t)\,\Lambda(\theta) &\cong \{F_{PM1}\cos[p_r(\theta - \omega_r t)]\}\,[\Lambda_0 - \Lambda_1 \cos(N_s\theta)] \\
&\cong F_{PM1}\Lambda_0 \cos[p_r(\theta - \omega_r t)] - \frac{F_{PM1}\Lambda_1}{2}\{\cos[(N_s - p_r)\theta - p_r\omega_r t] \\
&\quad + \cos[(N_s + p_r)\theta - p_r\omega_r t]\} \\
&\text{with } F_{PM1} \cong \frac{4}{\pi}\frac{B_r h_m}{\mu_o \mu_r}\sin\left(k_{PM}\frac{\pi}{2}\right) \text{ and } \frac{d}{dt}\theta_r = \omega_r
\end{aligned}
\tag{2}
$$

where $F_{PM}$ is the PMs magneto-motive force (MMF) distribution, the term $\sin(k_{PM}\frac{n\pi}{2})$ reflects the $n$th order PM pitch factor, and $\Lambda$ is the air-gap permeance function, with its average and higher-order harmonic components represented as [22,26]:

$$\Lambda_0 = \frac{\mu_o}{g'}\left(1 - 1.6\beta\frac{\tau_{so}}{\tau_s}\right)$$

$$\Lambda_v = \frac{\mu_o}{vg'}\frac{2\beta}{\pi}\left[\frac{0.78125}{0.78125 - 2\left(\frac{v\tau_{so}}{\tau_s}\right)^2}\right]\sin\left(1.6v\pi\frac{\tau_{so}}{\tau_s}\right) \qquad (3)$$

where $\Lambda_0$ and $\Lambda_v$ are the average and the specific magnitude of the $v$th harmonic permeance coefficients obtained from a conformal mapping method, the parameters, $\tau_s$ and $\tau_{so}$ are respectively the slot pitch and slot opening, as illustrated in Figure 2. Furthermore, the coefficient $\beta$ is determined by the relation [23,26]:

$$\beta = \frac{1}{2} - \frac{1}{2\sqrt{1 + \left(\frac{\tau_{so}}{2g'}\right)^2}} \qquad (4)$$

where $g' = g + \frac{h_m}{\mu_r}$ in Equations (3) and (4) is the equivalent magnetic air-gap length. Both the average ($\Lambda_0$) and $v$th ($\Lambda_v$) harmonic magnitudes depend on the value of $\beta$, which in turn is a function of the slot-opening to air-gap ratio ($\frac{\tau_{so}}{g'}$). That is, Equation (2) shows that in addition to the fundamental field harmonic ($p_r$), the no-load air-gap flux density is composed of the two other harmonic components generated as a result of the modulation effect, namely: $(N_s - p_r)$ and $(N_s + p_r)$. Therefore, when the stator winding pole-pair number is selected as $Q_s - p_r = p_s$, the no-load induced voltage of the machine is:

$$E_{ph_{rms}} \cong \frac{K_{w1}N_{ph}D_g l_{stk}}{\sqrt{2}}\omega_r\left[F_{PM1}\left(\Lambda_0 + \frac{p_r}{p_s}\frac{\Lambda_1}{2} - \frac{p_r}{p_r + Q_s}\frac{\Lambda_1}{2}\right)\right]$$

$$\cong \frac{2\sqrt{2}B_r}{\pi\mu_r}K_{w1}N_{ph}D_g l_{stk}\omega_r\left\{\overbrace{\frac{h_m}{g'}\left[1 - 1.6\beta\frac{\tau_{so}}{\tau_s}\right]}^{K_{conv}}\right.$$

$$\left. + \underbrace{\frac{h_m}{g'}\frac{\beta}{\pi}\left[\frac{0.78125}{0.78125 - 2\left(\frac{\tau_{so}}{\tau_s}\right)^2}\right]\sin\left(1.6\pi\frac{\tau_{so}}{\tau_s}\right)\left[\frac{p_r}{p_s} - \frac{p_r}{p_r + Q_s}\right]}_{K_{add}}\right\} \qquad (5)$$
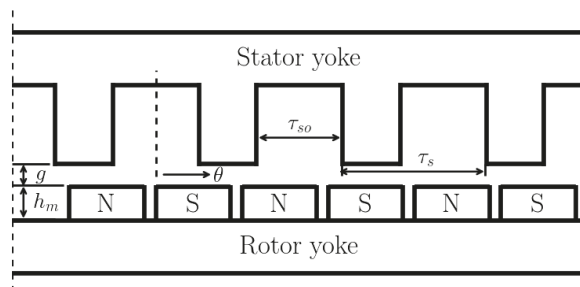


**Figure 2.** Linearized and simplified typical geometry of a PMVM.

Continuing on the similar analogy to that of the back-EMF, and with the assumption that the machine is running at a steady-state speed with pure sinusoidal currents, the air-gap electromagnetic torque for a three-phase PMVM is then formulated as shown below:

$$T_g \cong 3I_{ph}\frac{2\sqrt{2}B_r}{\pi\mu_r}K_{w1}N_{ph}D_g l_{stk}(K_{conv}+K_{add})$$

$$\cong \frac{\sqrt{2}B_r}{\mu_r}K_{w1}K_s D_g^2 l_{stk}(K_{conv}+K_{add}) \qquad \text{with} \quad K_s = \frac{6N_{ph}I_{ph}}{\pi D_g} \tag{6}$$

where $K_s$ is the linear current density in $\left[\frac{\text{kA}}{\text{m}}\right]$.

The presence of three constituent terms is now evident in both the developed open circuit voltage and torque expressions. The first term is equivalent to the component found in classical PMSMs, while the second and the third terms are due to the vernier effect. A further inspection of Equation (5) reveals that $K_{conv}$ and $K_{add}$ are the two terms playing key roles in PMVM's operation, and they can greatly be affected by the variables $D_g$, $l_{stk}$, $h_m$ and the slot opening ratio ($c_o = \frac{\tau_{so}}{\tau_s}$), as also evident from (3) and (4). The characteristics of $K_{conv}$ and $K_{add}$ with various values of PM thickness and slot opening ratio are, respectively, provided in Figure 3 for a small PMV machine with 10 rotor PM pole-pairs and 12 stator slots. In Figure 3a, it can be seen that $K_{conv}$ decreases with an increase in slot opening ratio $c_o$, whereas it increases with PM thickness for each specific $c_o$. As shown in Figure 3b, $K_{add}$ displays a somewhat different tendency, i.e., $K_{add}$ rapidly increases with an increment of PM thickness and reaches its peak point at a specific $h_m$ value, after which it keeps on becoming smaller with larger PM thickness. Moreover, the similar increasing and decreasing tendencies of $K_{add}$ are also observed with respect to increasing the slot opening ratio.
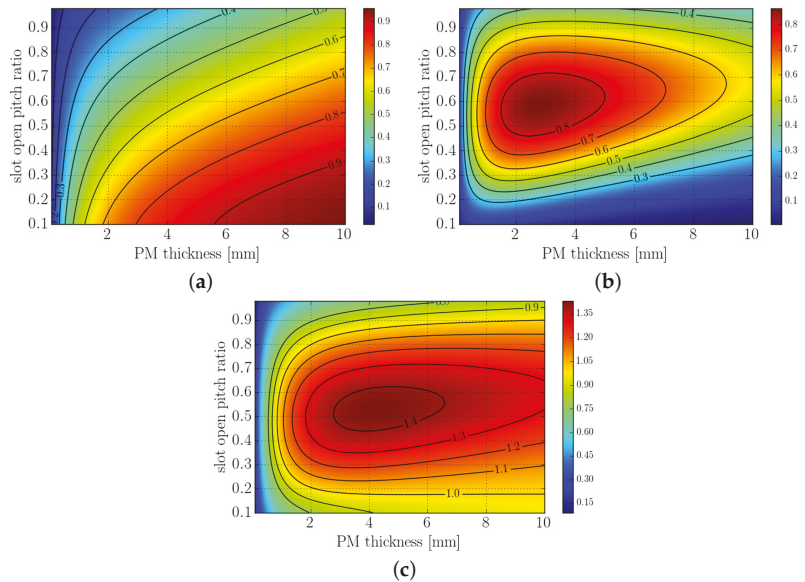


**Figure 3.** Variation of Equation (5) components as a function of PM thickness and slot opening ratio: (**a**) $K_{conv}$, (**b**) $K_{add}$, (**c**) $K_{vern} = K_{conv} + K_{add}$.

Consequently, the sum of $K_{conv}$ and $K_{add}$ gives the $K_{vern}$ term, which reflects the combination characteristics of its constituent terms, as shown in Figure 3c. It can be clearly seen that $K_{vern}$ also reaches its maximum value at a specific $h_m$ but saturates at a slightly lower value with further increasing $h_m$. This can be expected as thicker PMs lead to a

larger effective air-gap rendering a weakened modulation effect of the air-gap flux density. This implies that the optimal PM thickness of PMVMs tends to be smaller than that of conventional PMSMs for the same output performance. Thus, the PMVM has the potential for a comparatively lower PM material usage.

### 3. Basic PMVM Configurations

In single air-gap PMVMs, various PM rotor structures such as surface-mounted, inset, interior and Halbach arrays can all be used. However, judicious selection of slot-pole combinations and winding arrangements can result in different types of PMVM designs. In this paper, the most common types of PMVMs are classified into two major groups based on the winding arrangements and resultant range of gear ratios, namely, Type-A and Type-B PMVMs.

#### 3.1. Type-A PMVMs

These types of machines encompass both the conventional overlap winding PMVMs (OW-PMVM) and the split-tooth concentrated winding PMVMs (Split-tooth PMVM). The common feature between these two machine types is that their ratio of rotor to stator pole-pairs (i.e., $G_r$) has a minimum value of five (5) for the three-phase machines. That is, considering Equation (1):

$$G_r = \frac{p_r}{p_s} = \frac{N_s \mp p_s}{p_s} = \frac{N_s}{p_s} \mp 1 \tag{7}$$

and with $N_s$ equal to $Q_s$ for OW-PMVM and $N_s$ being the number of modulating pieces or *total teeth splits* in the case of Split-tooth PMVMs, $G_r$ can further be expressed in terms of the number of slots/pole/phase ($q$) as:

$$G_r = \frac{N_s}{p_s} \mp 1 = 6q \mp 1 \tag{8}$$

It must be kept in mind that in the case of the Split-tooth PMVMs, $q$ is calculated based on the number of stator tooth-splits (instead of stator teeth) for Equation (8). Hence, the minimum possible $G_r$ in this type of PMVMs is five (5).

The cross-sectional views of some typical PMVM structures in this group are presented in Figure 4. The first structure (Figure 4a) can be seen as a simple derivation from traditional PMSMs through adjustment of their electromagnetic pole/slot combinations to conform with Equation (1). Since there is usually a bigger numerical difference between its stator slots and stator pole-pairs, the distributed overlapping-winding is normally used. In addition, the stator teeth perform both the roles of major flux paths and modulating pieces. Therefore, open stator slots are very common in this configuration as they enhance the flux modulation effect. Relatively longer end-winding length is an obvious drawback for this machine.

On the other hand, the tooth-concentrated, split-tooth PMVM (Figure 4b) directly implements ferromagnetic pieces to modulate fields from either side of the air-gap to realize field coupling. This allows the armature windings to be wound around each of the main stator teeth, giving the possibility of shorter end-winding lengths and fault tolerance capability between the phases. Consequently, this increases the machine's reliability and results in fewer winding losses. Some of the drawbacks of this structure include increased magnetic reluctance due to longer magnetic paths, relatively high torque ripple and significant frequency-dependent losses as a result of the rich harmonic content of the tooth-concentrated winding arrangement.
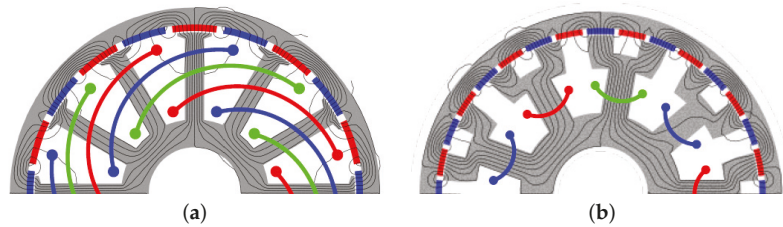
**Figure 4.** Typical structures of Type-A PMVMs with (**a**) conventional overlap-winding, (**b**) tooth concentrated, split tooth (© [2020] IEEE. Reprinted, with permission from [20]).

*3.2. Type-B PMVMs*

A fairly clear approach to calculating the winding factors of the tooth-concentrated fractional slot pitch winding is available from the winding theory. According to Skaar and Nilssen [27], a feasible region of reasonable winding factors exists for $\frac{1}{4} < q < \frac{1}{2}$. Furthermore, the same study showed that all other pole/slot combinations have a balanced air-gap magnetic radial forces except those with $Q_s = 2p_s \pm 1$. To reduce the unbalanced force magnitudes in pole/slot combinations utilizing this winding arrangement, one technique is to double the number of slots while retaining the same number of poles.

Based on this observation, the two-slot pitch windings were developed (Figure 5), and their implementation on PMVMs was demonstrated by several researchers [28]. For the PMVM development, this type of winding is obtained by just doubling the number of slots from the one slot-pitch winding conventional PM machines, including those with balanced magnetic forces. In this case, the purpose of doubling the slot number without changing the original armature poles is to create a bigger numerical difference between them, and this gives more design flexibility which can easily satisfy (1). This then results in a new range of $q$ values with no negative impact on winding factor, i.e., $\left(\frac{1}{2} < q < 1\right)$, and other advantages from their original one slot-pitch are retained. Most of the single slot-pitch combinations give acceptable two-slot pitch windings except those with the basic ratio $\frac{Q_s}{2p_s}=\frac{3}{2}$. Considering all the applicable conditions in developing this type of winding, the corresponding gear ratios of PMVM are defined by (9). It can be clearly seen from Figure 6 that $G_r$ is confined within a range of $(2 < G_r < 5)$, and converges to three (3) as the stator pole-pairs increase.

$$G_r = 3 \pm \frac{2}{p_s} \quad \text{and} \quad G_r = 3 \pm \frac{4}{p_s} \quad \text{with} \quad p_s > 2 \tag{9}$$
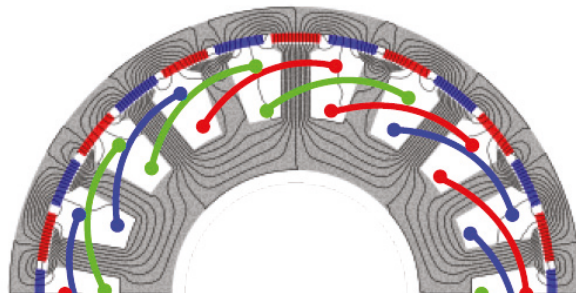


**Figure 5.** A typical structure of Type-B PMVMs (© [2020] IEEE. Reprinted, with permission from [20]).
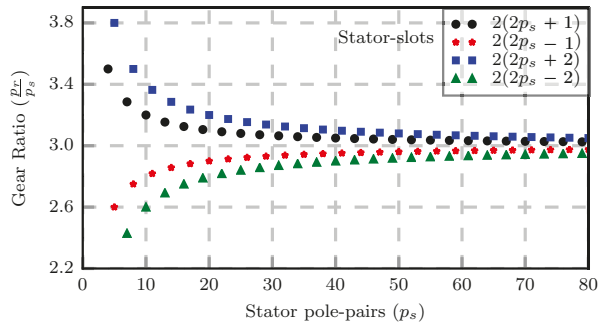
**Figure 6.** Gear ratios of Type-B PMVMs (© [2020] IEEE. Reprinted, with permission from [20]).

## 4. Steady-State Field-Circuit Model of PMVM

The design analysis and performance evaluation of the PMVMs in their steady-state mode of operation is realized by employing a coupled field-circuit model. Thus, the output performance is calculated through the equations derived from the fundamental per-phase equivalent circuit shown in Figure 7. As displayed on this generator mode circuit, $e_m$ is the induced electromotive force (EMF), $R_\phi$, $U_\phi$ and $I_\phi$ are the phase resistance, phase voltage and phase current, respectively. In order to account for the core and magnet eddy-current losses, a shunt resistance $R_{cm}$ is also included. Since the electromagnetic analysis is performed in 2D-FEM, the synchronous inductance is split into $L_m$ and $L_e$, which represents the main and end-winding inductances, respectively. All the equivalent circuit parameters enclosed by the dashed lines in Figure 7 are readily obtained from the 2D FE model. Other remaining parameters are deduced from analytical calculations.
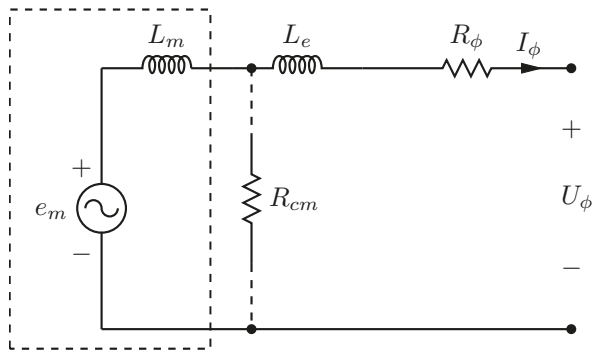


**Figure 7.** Per-phase equivalent circuit of the PMVM.

One of such parameters is the core-loss, which is a function of flux density magnitude, volume of magnetic conducting material within a machine and mainly the rate of change of flux density. In addition, the considered component's material magnetic properties also play a huge role in the resultant core losses. Thus, by using the multi-step static FE analysis, the core losses are approximated by employing the Steinmetz-based Equation (10). Since this model equation uses flux variation and magnitude deduced from several independent static solutions, it gives satisfactory accuracy, albeit much faster compared to transient FEM simulations.

$$P_c = \frac{1}{T} \int_0^T C_{SE} \left| \frac{dB}{dt} \right|^\alpha |\Delta B|^{\beta - \alpha} dt \tag{10}$$

where $T$ is the period, $\Delta B$ is the peak-to-peak flux density, $C_{SE}$, $\alpha$ and $\beta$ are the lamination material loss model coefficients.

In order to simplify the machine performance computations, the instantaneous 3-phase output quantities are projected onto the $dq0$-axis reference frame through the use of the $dq0$ transformation matrix. The $dq$-axis steady-state circuits fixed to the rotor reference frame corresponding to the phase circuit in Figure 7 are provided in Figure 8. From these circuits, the steady-state $dq$-axis voltage equations can be expressed as:

$$V_d = -\lambda_q \omega_r + L_e I_q \omega_r - I_d R_\phi \quad \text{and} \quad V_q = \lambda_d \omega_r - L_e I_d \omega_r - I_q R_\phi \tag{11}$$
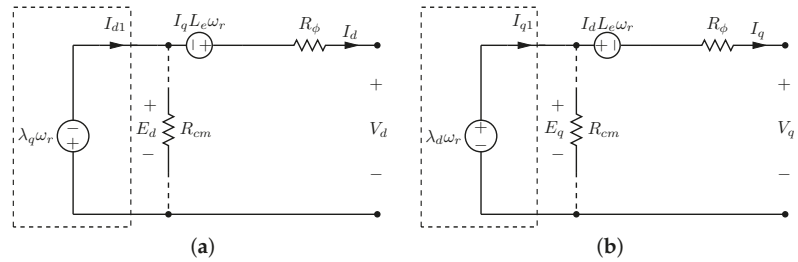


**Figure 8.** Rotor reference frame equivalent circuits: (**a**) $d$-axis and (**b**) $q$-axis.

Furthermore, the $dq$-axis current components are also deduced from the circuits in Figure 8 as follows:

$$I_{d1} = I_d + \frac{E_d}{R_{cm}} \quad \text{and} \quad I_{q1} = I_q + \frac{E_q}{R_{cm}} \tag{12}$$

With the equivalent circuit and other associated parameters known, the air-gap electromagnetic power and developed average electromagnetic torque (for surface-mounted PM rotor) can also be computed from the general equations:

$$\text{T}_{EM} = \frac{3}{2} G_r p_s (\lambda_d I_{q1} - \lambda_q I_{d1}) \quad \text{and} \quad \text{P}_{EM} = \text{T}_{EM} \frac{2\pi}{60} n_s \tag{13}$$

where $n_s$ is the speed in revolutions per minute.

In the generator mode of operation, the difference between the air-gap electromagnetic power and mechanical power at the machine shaft is due to rotational losses and shunt core losses. On the other hand, the air-gap electromagnetic power differs from the output electric power at the machine terminals by the armature copper losses. That is, numerical addition of the developed air-gap power and the sum of rotational and shunt core losses will yield the shaft mechanical input power, while subtraction of armature losses from it gives the generator output power. The output electrical power consists of useful active power and reactive power, both of which can be approximated from the phase circuits in Figure 8:

$$\begin{aligned}
\text{Active Power:} \quad & \text{P}_{out} = \frac{3}{2}(V_d I_d + V_q I_q) \\
\text{Reactive Power:} \quad & \text{Q}_{out} = \frac{3}{2}(V_q I_d - V_d I_q)
\end{aligned} \tag{14}$$

Subsequently, the efficiency and power factor (PF), which is a function of the phase angle difference between the output voltage and current, may also be obtained from the preceding equations. It must be noted that during the early design optimization stage, the windage and frictional losses, which constitute mechanical losses, are ignored in order to simplify the problem.

## 5. Design Optimization Process

For the design and performance evaluation of PMVMs, the corresponding ranges of specifications and parameters of PMSMs, such as input speed, operating frequency, total outer diameter and stack length, etc., are used as a benchmark and reference guide.

Therefore, a highlight of PMSMs' performance and characteristic properties is first given as a preset to the PMVM's specifications. In addition, the design constraints, procedure and strategy are also described in this section. For the wind generator designs, it is desirable to consider a range of operating speeds of a wind turbine by optimizing the generator at several operating points of the wind turbine [29–31]. Given the scope of this work, the design optimization study in this paper is conducted based on the rated operating conditions of a generator.

### 5.1. Specifications

Since the optimization objectives are primarily concerned with the active material weight and volume, a presentation of these characteristic parameters for a PMSM is given in Figure 9 as obtained from the literature. This is performed for 1–5 MW machine output levels to indicate their characteristic relationship against rating up-scaling as well. As these machines were optimized by different researchers based on various specifications, constraints and algorithms, there is a bit of variance in their performance at each rated level. Hence, the ranges in the figure indicate the dispersion of active weight and volume, highlighting the minimum and maximum values as obtained from the relevant literature.

By considering their averages, both the active material weight and volume show a somewhat linear trend against the machine power rating. Furthermore, it appears from Figure 9 that a mass of about 16.5 tons and volume of 20 m³ are deemed reasonable for a 3 MW DD-PMSM generator.
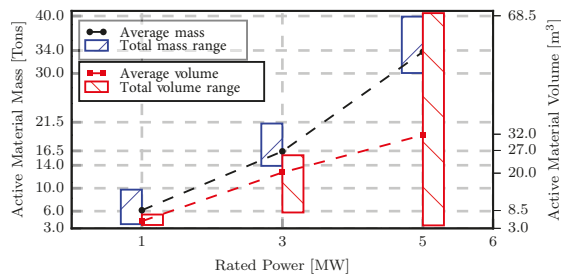


**Figure 9.** Active mass and volume of PMSM as a function of power rating found in the literature (© [2020] IEEE. Reprinted, with permission from [20]).

A breakdown of different material types contributing to the machines' active weights provided in Figure 9 is also shown by Figure 10. As seen in the figure, the lamination mass is always the most dominant since it takes at least 60% of the total mass while the PM material contributes the lowest percentage.

Based on the above information, the main design specifications are summarized in Table 1. A minimum efficiency of 94% is specified for 300 kW machines or less, while 95% is required for 1 MW machines and above. As the output capacity of the machine is increased to the mega-Watt level, the available wind speed distribution, physical generator size and that of turbine blades dictate the rated speed to be decreased accordingly, and the frequency should follow a similar trend to limit the core losses. Theoretically, a larger air-gap radius would also be needed to accommodate a high number of poles and handle large input torque from the blades. However, factors such as available nacelle size, manufacturing and logistic constraints create the upper limits as to how large a machine can be. Therefore, the total outer diameter ($D_{out}$) of active volume is considered in this case to give an approximate size of the machine, and the air-gap radius will be determined by the optimization variables. It is assumed that no special cooling methods will be implemented for the machines; hence, an armature current density of 5 A/mm² is set to be the upper limit for a natural air-cooled machine. Considering the strong magnetic attraction forces and manufacturability of the machine, a reasonable air-gap length corresponding to machine size should be selected, which is taken to be roughly 0.1% of the total diameter in this study.
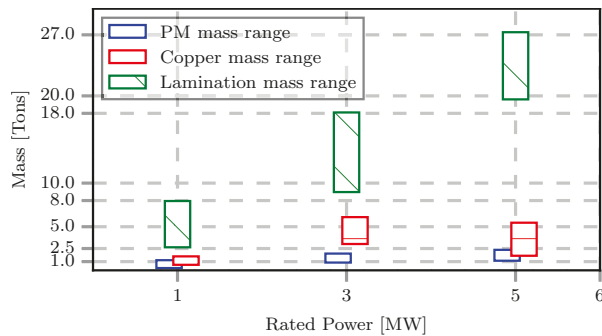
**Figure 10.** Different active material weight distribution vs. power rating of PMSM (© [2020] IEEE. Reprinted, with permission from [20]).

**Table 1.** Main design specifications of machines at different power levels [1,32–37].

| Parameter | 60 kW | 300 kW | 1 MW | 3 MW |
|---|---|---|---|---|
| Maximum outer diameter (m) | 1.2 | 2.5 | 3.5 | 5.0 |
| Air-gap length (mm) | 3.0 | 4.0 | 4.0 | 5.0 |
| Rated speed (rpm) | 80 | 50 | 30 | 15 |
| Efficiency (%) | ≥94 | ≥94 | ≥95 | ≥95 |
| Current density (A/mm$^2$) | ≤5 | ≤5 | ≤5 | ≤5 |

*5.2. Methodology*

Although gradient-based algorithms are time efficient for electrical machine design with many design variables, they are susceptible to becoming trapped into a local optimum and numerical noise [38]. On the other hand, non-gradient-based algorithms are proven to have capabilities of locating the global optimum point, but they are computationally very expensive. In this study, a hybrid optimization approach was implemented in an attempt to leverage their respective advantages, whereby stochastic and a gradient-based algorithms, i.e., *Non-dominated Sorting Genetic Algorithm II* (NSGA-II) and *Method of Modified Feasible Directions* (MMFD), respectively, were used in two sequential steps to obtain one best final solution. The NSGA-II is initially used to determine the search region that contains the global optimum within it. Once in this general vicinity of the global optimum, the MMFD is used with the NSGA-II's results as the starting point to quickly locate the precise optimum point by further zooming into the solution area. In this way, the two algorithms are combined and efficiently employed to find a true optimum point within a very reasonable time. That is because, since the MMFD started from an already improved point, it will quickly converge with fewer evaluation iterations than what would be required if NSGA-II was used alone to find the very best point. Figure 11 illustrates the workflow of this optimization technique.
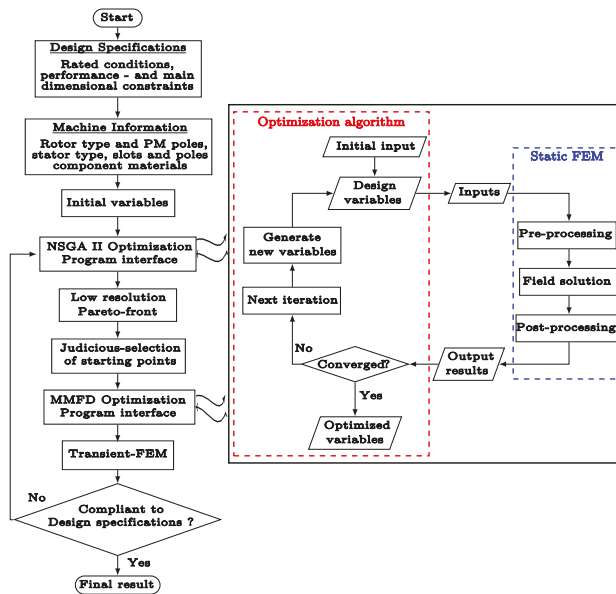
**Figure 11.** Hybrid optimization technique workflow.

In NSGA-II, a number of user-adjustable operators have to be fine-tuned based on the characteristics of the optimization problem in order to enhance the algorithm's efficiency and reliability. The settings of these specific parameters are given in Table 2 for the optimization of all machines (1 and 3 MW).

**Table 2.** NSGA-II user adjustable parameters' set values.

| Parameter | Value |
|---|---|
| Initial population size | 60 |
| Maximum iterations | 600–1200 |
| Probability of mutation | 0.08333 |
| Disindex of mutation | 12 |
| Probability of cross-over | 0.99 |
| Disindex of cross-over | 16 |

A fixed initial population size of 60 was also used for all optimization trials, which is five times the number of optimization variables and deemed reasonable according to the NSGA-II theory as a larger population size would drastically increase the number of solver evaluations and optimization time. The maximum number of generations was set to 600 for 1 MW machines and increased to 1200 for 3 MW machines because the purpose of the NSGA-II in this case was just to identify the zone of the global optimum. The mutation probability was set to 0.0833, which is the reciprocal of the variables number (i.e., 12) as per the relevant theory of NSGA-II as well [39].

The formulated optimization problem has more than one objectives and several design constraints, as follows:

$$
\begin{aligned}
\text{Minimize:} \quad & F(\mathbf{X}) = [\mathbf{Y}] \\
\text{Subject to:} \quad & \mathrm{P}_{out} \geq \mathrm{P}_{rated} \\
& \eta\% \geq \eta_{\min} \\
& J \leq 5\,\mathrm{A/mm^2} \\
& \mathrm{PF} \geq 0.65
\end{aligned}
$$

where $\mathbf{X}$ represents the vector of geometric variables illustrated in Figure 12 with angle ratios defined in (15), including the axial stack length of the machine, and $\mathbf{Y}$ is a set of selected objective functions such as the minimization of mass and cost. The minimum powers and efficiencies are as indicated in Table 1 for each power rating. It should also be noted that the temperature and material characteristics were kept constant throughout the optimization process.

$$
\begin{aligned}
\theta_{pm\_p} &= \frac{\pi}{p_r} \quad ; \quad \theta_{sp} = \frac{2\pi}{Q} \quad ; \quad \theta_{mp} = \frac{2\pi}{N_s} \\
\sigma_{pm} &= \frac{\theta_{pm\_s}}{\theta_{pm\_p}} \quad ; \quad \sigma_s = \frac{\theta_s}{\theta_{sp}} \quad ; \quad \sigma_{so} = \frac{\theta_{so}}{\theta_s}
\end{aligned}
\tag{15}
$$
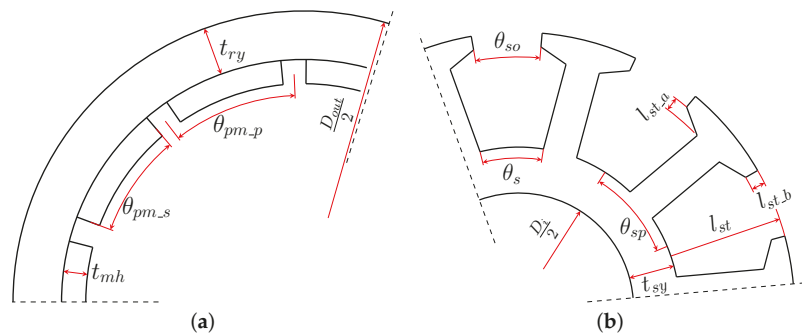


**Figure 12.** Machine geometric optimization variables of (**a**) rotor and (**b**) stator (© [2020] IEEE. Reprinted, with permission from [20]).

## 6. Optimization Results and Discussions

As a preliminary design exercise, the PMVMs are designed and optimized for a rated power of 1 MW. The considered slot/pole combinations of the PMVM are detailed in Table 3. The pole-slots are selected based on the input speed and the expected rated frequency. As indicated in the table, the combinations are further grouped into two frequencies. The lower frequency ($\approx$30 Hz) corresponds to that of a conventional DD-PMSM, while the other one matches that of the medium-speed PMSM with a single-stage gearbox ($\approx$60 Hz). The basic idea behind this is to evaluate the performance of the PMVM when it is operated at the direct-drive and medium-speed PMSM frequency conditions, with similar input speed and gear ratio. This is because a PMVM looks rather similar to a conventional DD-PMSM structurally, but it incorporates a magnetic gearing principle in its operation. This inherent feature makes it look closer to the medium-speed machines from the operational frequency point of view, as illustrated in Figure 1. Thus, it is important to assess the performance characteristics, total active mass, volume and cost of PMVMs for both operating frequencies.

**Table 3.** Investigated slot/pole combinations for 1 MW PMVMs.

| Winding Configuration | Type A | | | | | | Type B | |
|---|---|---|---|---|---|---|---|---|
| Stator slots ($Q_s$) | 72 | 72 | 75 | 135 | 135 | 144 | 84 | 162 |
| Stator pole-pairs ($p_s$) | 12 | 8 | 10 | 18 | 15 | 24 | 20 | 40 |
| Rotor pole-pairs ($p_r$) | 60 | 64 | 65 | 117 | 120 | 120 | 64 | 122 |
| Pole-ratio ($G_r$) | 5.0 | 8.0 | 6.5 | 6.5 | 8.0 | 5.0 | 3.2 | 3.05 |
| Slots/pole/phase ($q$) | 1.0 | 1.5 | 1.25 | 1.25 | 1.5 | 1.0 | 0.7 | 0.68 |
| Rated frequency [Hz] | 30 | 32 | 32.5 | 58.5 | 60 | 60 | 32 | 61 |

To investigate the relations between the gear ratios and the design objectives of large power PMVMs, a comparison is made of the power factor and the active weights at a number of different gear ratios. As shown in Figure 13, in Type-A PMVMs ($G_r \geq 5$), lower gear ratio designs are preferred (for both frequencies) as they tend to have higher power factor and lighter mass. Further, these Pareto fronts clearly reveal the competing relationship between the active mass and power factor in PMVMs. It is also evident that PMVMs operating at higher frequency have less total mass and better power factor.
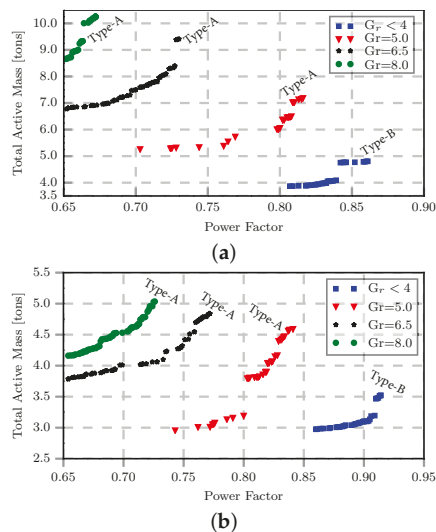


**Figure 13.** A 1 MW PMVM's active mass vs. power factor: (**a**) 30 Hz (**b**) 60 Hz (© [2020] IEEE. Reprinted, with permission from [20]).

Figure 14 shows the optimum designs of PMVMs with both Type-A (*distributed overlapping winding*) and Type-B (*2-slot pitch concentrated winding*) configurations. The graphs illustrate the trend of active mass and power factor as a function of gear ratios at two different frequencies. It can be clearly seen that the mass increases with the gear ratio while the power factor decreases. It should be remembered that the minimum constraint on power factor was set to 0.65 during the optimization, and higher gear ratio designs appear to be testing this threshold, giving an impression that it would likely go lower than that if the constraint was relaxed. It is at this rated power level that the Type-B PMVMs ($G_r \leq 5$) appear to be more attractive in terms of power factor and lighter in weight than the Type-A PMVMs.
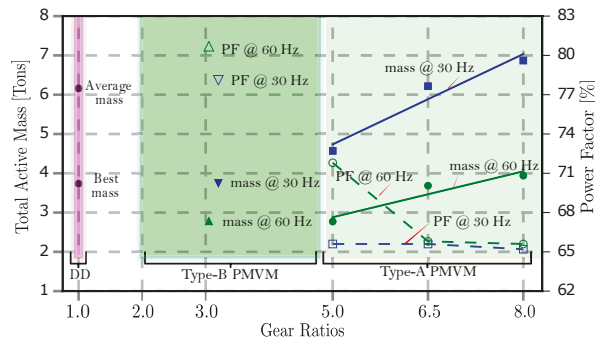
**Figure 14.** Total active mass and power factor vs. gear ratios for 1 MW machines (© [2020] IEEE. Reprinted, with permission from [20]).

As a benchmark, the average DD-PMSM weight is also added in Figure 14 for comparison. Although not shown on the graph, PMSM is known to have a near unity power factor. Thus, all the PMVM designs here have poor power factor compared with the PMSM. However, the Type-A PMVMs with $G_r = 5$ and the Type-B PMVMs are much lighter than the DD-PMSM. There is clearly a trade-off between the light weight and poor power factor in PMVMs.

It can be observed from the results of 1 MW machines that PMVM designs with operating frequency similar to that of their conventional DD-PMSM counterparts offer no benefits. Therefore, for the 3 MW design, the decision was made to go for slot/pole combinations that operate at medium-speed frequency ($\approx$50 Hz) but with equivalent turbine input speed to the DD-PMSM. That is, in addition to the gearing ratio, the generators' rated speed and output frequency were also the main factors considered in the selection of the slot/pole combinations, as presented in Table 4.

**Table 4.** Investigated slot/pole combinations for 3 MW PMVMs.

| Winding Configuration | Type A | | | Type B | |
|---|---|---|---|---|---|
| Stator slots ($Q_s$) | 240 | 240 | 225 | 270 | 276 |
| Stator pole-pairs ($p_s$) | 40 | 32 | 25 | 67 | 68 |
| Rotor pole-pairs ($p_r$) | 200 | 208 | 200 | 203 | 208 |
| Pole-ratio ($G_r$) | 5.0 | 6.5 | 8.0 | 3.03 | 3.06 |
| Slots per pole per phase ($q$) | 1.0 | 1.25 | 1.5 | 0.67 | 0.68 |
| Rated frequency (Hz) | 50 | 52 | 50 | 50.75 | 52 |

For the PMVM, the power factor is one of the performance indexes that always need special attention as it can come out to be detrimental if not properly designed. With that said, Figure 15 shows the Pareto-front between the total active mass and power factor for the five 3 MW PMVM slot/pole combinations with different gear ratios. During the optimizations, the upper limit to the PM material usage was set to be equal to the maximum PM mass requirement of the reference PMSMs indicated in Figure 10, and the minimum efficiency was set to be 95%. Since the PMVMs have similar input speeds to those of the PMSMs, this means a fairly similar ground is created for comparison purposes in these two machine types. From the figure, the higher gear ratios invariably lead to lower power factors and heavier total masses. Furthermore, it is realized that some of the PMVM slot/pole combinations can lead to poor power factors with values less than 0.4. This further asserts the point that at output power capacities larger than 1 MW, it is always better to go for a lower gear ratio in PMVM designs.
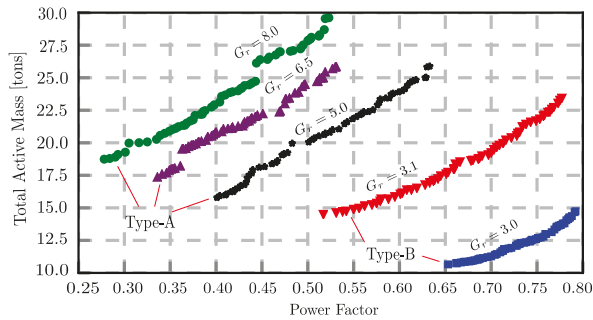
**Figure 15.** Total active mass vs. power factor for 3 MW PMVMs (© [2020] IEEE. Reprinted, with permission from [20]).

In order to estimate the cost of the active materials in a machine, the specific cost of each material has to be known. Table 5 gives the material prices used in this study, which may be slightly different to the market values. Based on the literature [1] and the market trend, 35 *USD*/kVA was assumed to be the cost of the converter. It should be noted that in industry, the actual converter prices usually follow a stepped profile instead of this kind of linearized costing model.

**Table 5.** Approximate costs of different materials for PMSM components [40].

| Material | Cost per Kilogram (USD/kg) |
|---|---|
| Silicon steel (Lamination) | 2.0 |
| Copper (Winding) | 6.67 |
| Neodymium Iron Boron (PM) | 50.0 |

In order to compare the PMVMs with the PMSM, one design point for each slot/pole combination was taken from the Pareto-fronts given in Figure 15 and further optimized. The objective in this case was to have a lighter and low-cost PMVM with the best possible power factor. The results are presented in Figure 16a,b, and in Table 6, with the indicative costs of materials also included.



(**a**)
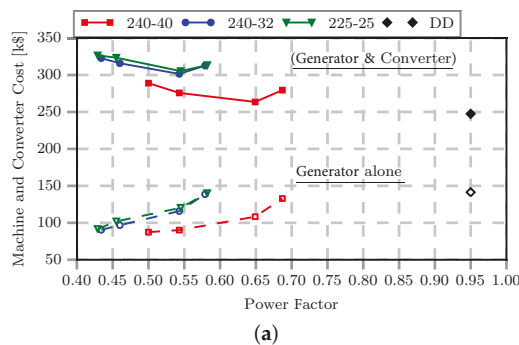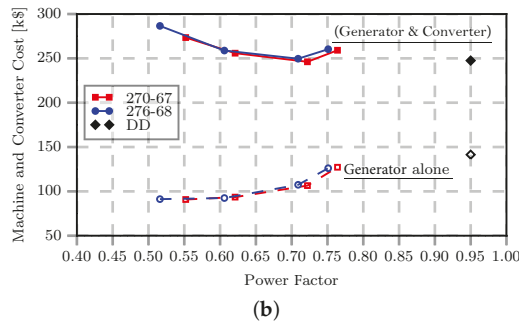
**Figure 16.** *Cont.*

**Figure 16.** Comparison of 3 MW PMVMs and system costs: (**a**) Type-A PMVM (**b**) Type-B PMVM. Note that the solid markers represent the system (generator and converter) costs while the corresponding hollow markers show the generator cost (©[2020] IEEE. Reprinted, with permission from [20]).

**Table 6.** Mass and cost comparisons of different 3 MW PMSM [32,35] and PMVMs.

| Machine Type | DD-PMSM | | PMVM (Type B) | | PMVM (Type A) | | |
|---|---|---|---|---|---|---|---|
| Pole-Ratio | 1.0 | 1.0 | 3.0 | 3.05 | 5.0 | 6.5 | 8.0 |
| **Characteristic Information** | | | | | | | |
| Output power (MW) | 3.0 | 3.0 | 3.04 | 3.06 | 3.0 | 3.04 | 3.04 |
| Efficiency (%) | 95.0 | - | 95.91 | 95.93 | 97.06 | 97.08 | 97.77 |
| Power factor | 0.93 | - | 0.72 | 0.71 | 0.65 | 0.54 | 0.55 |
| Total diameter (m) | 5.0 | 5.0 | 5.0 | 5.0 | 5.0 | 5.0 | 5.0 |
| Stack length (m) | 1.30 | 1.19 | 1.403 | 1.399 | 1.378 | 1.377 | 1.372 |
| **Generator active material mass (tons)** | | | | | | | |
| PM | 1.90 | 1.92 | 1.39 | 1.39 | 1.39 | 1.40 | 1.40 |
| Core iron | 10.30 | 11.70 | 6.87 | 7.08 | 6.98 | 9.71 | 10.36 |
| Winding copper | 3.12 | 3.31 | 3.45 | 3.56 | 3.74 | 3.98 | 4.41 |
| Generator mass | 13.38 | 16.90 | 11.72 | 12.04 | 12.11 | 15.09 | 16.18 |
| **System cost distributions (in USD thousands)** | | | | | | | |
| PM | 95.0 | 96.0 | 69.5 | 69.5 | 69.5 | 70.0 | 70.0 |
| Core iron | 20.6 | 23.4 | 13.74 | 14.16 | 13.96 | 19.42 | 20.72 |
| Winding copper | 20.81 | 22.08 | 23.01 | 23.75 | 24.95 | 26.55 | 29.41 |
| Generator (active) | **136.41** | **141.48** | **106.25** | **107.41** | **108.41** | **115.97** | **120.13** |
| PE converter | 108.39 | 106.11 | 140.0 | 142.0 | 155.1 | 186.7 | 183.3 |
| Total system | 244.8 | 247.59 | 246.25 | 249.41 | 263.51 | 388.9 | 303.43 |

Even though Silicon steel used for machine cores has a slightly lower mass density than winding copper, it has the largest impact on the total active mass because of its larger volume content. The machines' efficiencies are always higher than the minimum constraint of 95 %, even though the operating frequency is relatively high. Increasing the PM mass has relatively little effect on total active mass, but it can significantly increase the cost of the machine and slightly improve the power factor. Figure 16a,b shows that a low-cost generator with low power factor still leads to an expensive system when the power converter costs are included. Thus, to select a good design, a best compromise has to be found between the generator cost and required converter cost.

Figure 17 shows the mass distribution of the chosen designs and compares them to the benchmark PMSM. It can be seen that PMVMs with lower gear ratios have a good advantage in terms of total active weight. It shows that designing for a lighter machine with a reasonable power factor at this power rating favors pole/slot combinations with lower $G_r$. This is a somewhat different trend to the small power PMVMs where the lowest $G_r$ values are not necessarily the best.
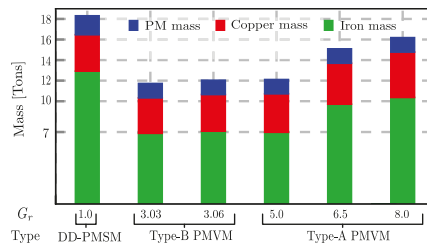
**Figure 17.** Comparison of active material weights of 3 MW PMSM and PMVMs (© [2020] IEEE. Reprinted, with permission from [20]).

The results in Table 6 reveal that the PMVM on its own can be lighter and cheaper than the PMSM. However, when the power converter costs are considered, the overall system costs of PMVMs become similar to those of DD-PMSMs because of their high converter rating requirement. It should be noted that a linear converter costing model was assumed in this study, which may not necessarily reflect the true costs in the industry. In the case that the power converter costs follow a stepped increasing pattern with regard to their MVA rating, the cost of PM vernier generator systems may become more competitive for certain power levels.

The cross-sections of these optimized PMVMs are provided in Figures 18 and 19. It can be observed that these PMVMs have thin teeth, wide and shallow slots, which also explains why they have less active iron content than PMSMs. Furthermore, the slot-pitch to air-gap length ratios from these machines are invariably less than 16 (ranges from 11.5 to 13.8), and this means that they have less risk of irreversible demagnetization [18].
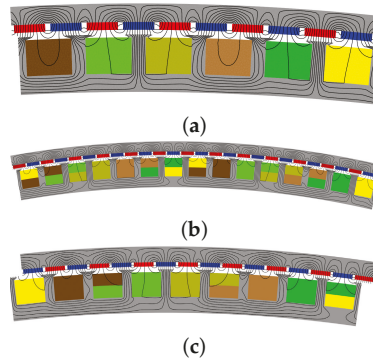


**Figure 18.** Cross sections of optimized 3 MW Type-A PMVMs: (**a**) (1/40th) of Type-A PMVM with Qs/ps/pr = 240/40/200, (**b**) (1/16th) of Type-A PMVM with Qs/ps/pr = 240/32/208, (**c**) (1/25th) of Type-A PMVM with Qs/ps/pr = 225/25/200.
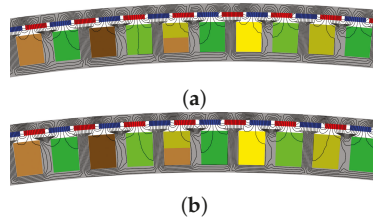


**Figure 19.** Cross sections of optimized 3 MW Type-B PMVMs: (**a**) (1/27th) of Type-B PMVM with Qs/ps/pr = 270/67/203, (**b**) (1/28th) of Type-B PMVM with Qs/ps/pr = 276/68/208.

As illustrated in Figure 20, the color-coded bar charts indicate the normalized mass scales of the investigated designs for different power ratings together with their respective gear ratios. Although the lightest designs are invariably associated with a low gear ratio of 5 for power rating up to 1 MW, the relationship between the mass and gear ratios is not very distinctive. However, at 3 MW output capacity, it becomes clear that the lowest $G_r$ has the lightest mass and the highest $G_r$ has the heaviest mass. This is in stark contrast to smaller output machines (15 kW or less), which seem to be heavier at low gear ratios.
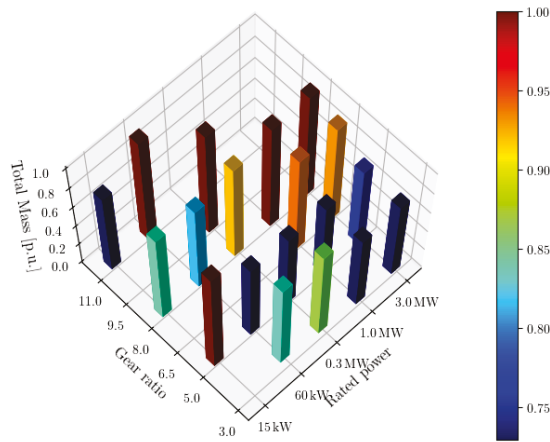


**Figure 20.** Total mass indications as a function of power ratings and gear ratios.

It should be reiterated that the PMVM designs in this work are subject to a minimum power factor constraint, which is a holistic approach for comparing the PMVM power-train with that of conventional DD-PMSM's. From a system cost (*both generator and PE converter*) perspective, judicious selection of gear ratios is very important for effective exploitation of the performance benefits of PMVMs. Based on the study, some specific design guidance of PMVMs for wind power applications can be given for different power levels, as shown in Figure 21. Type-A PMVMs with high gear ratios ($G_r > 5$) are particularly advantageous for small wind power (sub 50-kW) applications, while low gear ratio ($G_r \leq 5$) Type-A and Type-B PMVMs are better suited for medium (sub 1-MW) to high (1–10 MW) power wind applications.



Type-A PMVM
Gear ratio > 5

Type-A PMVM
Gear ratio = 5

Type-B PMVM
Gear ratio < 5

Small wind turbines: sub 50-kW Applications: *Houses, farms or small businesses*

Medium wind turbines: sub 1-MW Applications: *Community, farms or large businesses*

Large wind turbines: 1-10 MW Applications: *Land based or off-shore wind farms*
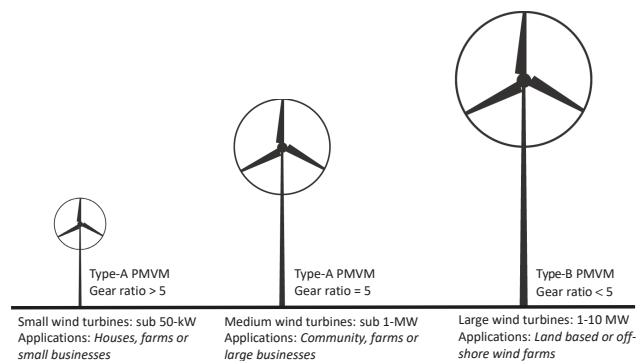
**Figure 21.** Recommended PMVM gear ratios for different wind power applications.

## 7. Prototype Validation

In order to practically verify the theoretical operating principle and validate the formulated FE-based optimal design approach, a 15 kW PMVM prototype was developed. The key dimensions that describe the constructed PMVM are provided in Table 7. Figure 22 shows the machine's no-load flux plot, no-load and full-load flux density distributions. The stator and rotor yokes have maximum flux density magnitudes of approximately 1.5 and 1.7 T, respectively, while the over-saturated regions appear on the edges of the teeth base.

**Table 7.** Prototype machines' dimensional parameters.

| Parameter | Value |
|---|---|
| Outer diameter ($D_{out}$) | 433 mm |
| Stack length ($L_{stk}$) | 151 mm |
| Rotor yoke height ($t_{ry}$) | 13.6 mm |
| Rotor magnet height ($t_{mh}$) | 3.9 mm |
| Magnet pole span ($\sigma_{pm}$) | 0.88 |
| Air-gap length ($g$) | 1.5 mm |
| Stator yoke height ($t_{sy}$) | 13.6 mm |
| Stator slot angle ratio ($\sigma_s$) | 0.74 |
| Slot opening ratio ($\sigma_{so}$) | 0.82 |
| Stator tooth length ($l_{st}$) | 27.96 mm |
| Stator slots ($Q$) | 36 |
| Winding pole-pairs ($p_s$) | 3 |
| Rotor pole-pairs ($p_r$) | 33 |
| Winding type | Overlapping |
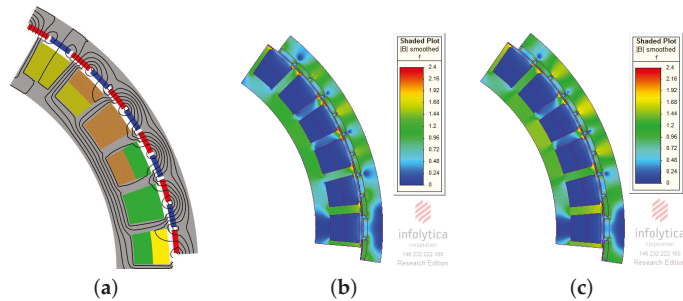


**Figure 22.** Prototype PMVM (1/6th) FEM simulation results: (**a**) no-load flux lines, (**b**) no-load flux density distribution, and (**c**) full-load flux density distribution.

The full machine's structural layout, rotor and stator components are shown in Figures 23 and 24, respectively. Both the stator and rotor are made of M400-50 electrical steel laminations. The grade of NdFeB magnets used is N48H.
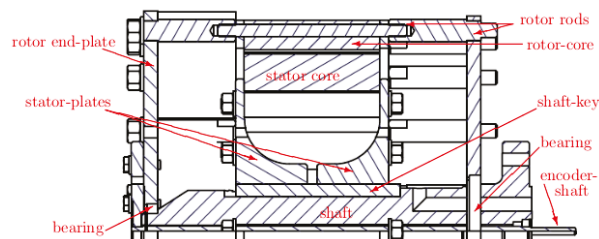


**Figure 23.** Longitudinal cross section of PMVM prototype structure (winding not shown).

**Figure 24.** Machine construction: (**a**) all sets of PMs are mounted onto the rotor core, (**b**) side view of wound stator with distributed overlapping windings, and (**c**) assembling of the PMVM prototype.

A photo of a laboratory test setup is shown in Figure 25. A geared induction motor (prime mover) is used to drive the prototype machine such that its performance is evaluated in the generator mode. A back-to-back converter is implemented for power conditioning and circulation, while the field-oriented technique is used for the machine's torque control.
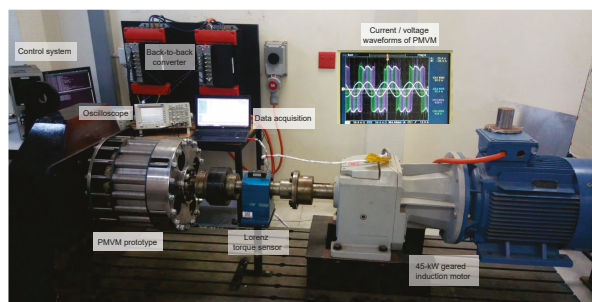


**Figure 25.** The laboratory test setup for the PMVM prototype machine.

Both measured and predicted no-load RMS phase voltages of the PMVM prototype as a function of input rotor speed are depicted in Figure 26, which shows a linear relationship of voltage to rotor speed with a good correlation between the two results. Figure 27 displays the no-load phase back-EMF waveform of the PMVM at a rated speed of 150 rpm. An excellent agreement between the measured and FEM simulated results is evident.
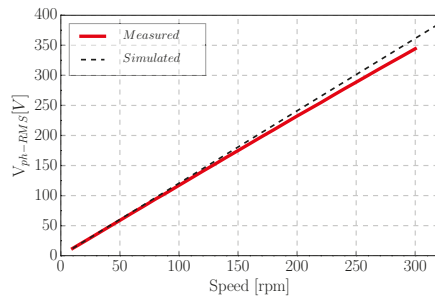
**Figure 26.** Measured and predicted no-load phase voltage versus rotor speed.
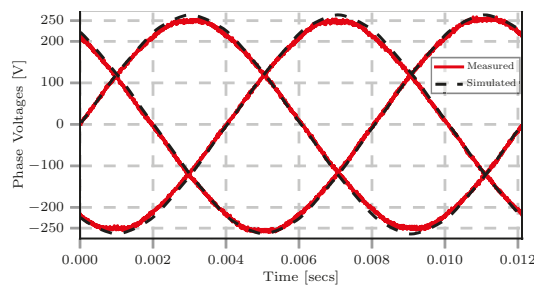


**Figure 27.** Open-circuit phase voltage waveforms at rated speed.

The prototype's no-load power losses, which include the mechanical losses, eddy-current and hysteresis losses in both the electromagnetically active and non-active components at various speeds are provided in Figure 28a. The total loss graph rapidly increases at higher speeds because of the excessive core loss that is frequency-dependent. The measured total losses correlate reasonably well with the sum of the measured bearing loss and simulated frequency-dependent losses up to the rated frequency. However, at higher frequencies, the discrepancy between the measured and predicted total losses becomes more significant.

As shown in Figure 28a, the PM losses and eddy current losses in the stator conductors located in open slots have also been accounted for in the predicted total loss. The remaining discrepancy between the measured and total approximated losses is likely due to (i) the inaccuracy of the implemented core loss model at higher frequency [41,42], (ii) under-estimated mechanical losses, and (iii) the leakage flux-induced losses in the supporting structure since the simulations were only calculated for the active part of the machine.

Figure 28b presents the active output power at various operating speeds, proving that a power of 15 kW is achieved at the rated load current and speed. This result serves as the confirmation that a designed machine is able to practically deliver the expected output power at rated operating conditions, which validates the implemented design optimization approach.

On the one hand, the obtained practical power factor shown in Figure 29a slightly deviates from the FEM predicted result. However, the trend demonstrated by this result also verifies the fact that the PM Vernier machine's power factor varies a lot with its torque loading at the maximum torque angle. Due to the overwhelming practical no-load losses indicated in Figure 28a, the PMVM's efficiency is also reduced from 94% to just above 93%, as shown in Figure 29b. The difference is due to the constructional imperfections and inaccurate approximations of certain parameters during the FE modeling. These include the end-winding leakage inductance, temperature and harmonic effects on the losses.
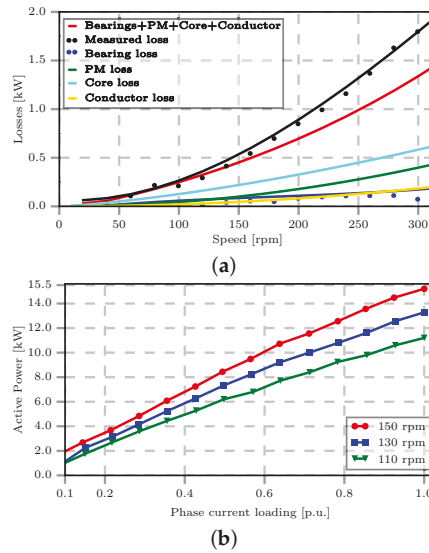
**Figure 28.** Prototype PMVM performance at constant rotational speeds: (**a**) no-load losses as a function of rotor speed, (**b**) active power as a function of phase current.
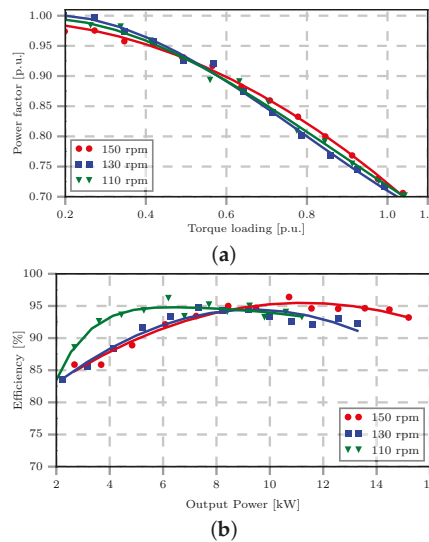


**Figure 29.** Prototype PMVM performance at constant rotational speeds: (**a**) power factor vs. torque loading, (**b**) efficiency at increasing power.

Table 8 presents the machine's steady-state performance comparison between the experimental and FEM-based results. It can be observed that there is a generally good correlation between them. In addition to confirming the PMVM's operational principle, the experimental results presented in Figures 26–29 and Table 8 prove the validity of the implemented design procedure and performance analysis methods. Consequently, it may be inferred that the accuracy of the design and modeling approach for the utility-scale PMVMs is acceptable, and the deduced predictions from FEM will be in reasonable agreement with actual manufactured high-power PMVMs.

**Table 8.** FEA results comparison with the measurements.

| Parameter | Predicted | Measured | Unit |
| --- | --- | --- | --- |
| Average torque | 1042 | 1038.23 | Nm |
| Torque ripple | 1.25 | 3.45 | % |
| Cogging torque | 1.66 | 1.8 | % |
| Winding losses | 480.4 | 570.2 | W |
| No-load losses | 476.4 | 506 | W |
| Output power | 15.4 | 15.2 | kW |
| Power factor | 0.78 | 0.71 | p.u. |
| Efficiency | 94.2 | 93.2 | % |

## 8. Conclusions

This paper presents an investigation study on the design and potential implementation of PMVM for large power wind generator applications. Although high gear ratios are usually preferred for small power PMVMs to realize dense torque designs, it is found that lower gear ratios are more attractive to achieve optimum machine designs with reasonable total mass and power factor for utility-scale PMVMs. This is partly attributed to larger equivalent air-gaps and increased leakage flux experienced by large-sized PMVMs.

The study shows that optimum PMVM designs at utility-scale usually push for the lowest gear ratio of five in Type-A machines. This tendency unveiled the competency of Type-B machines with a gear ratio of around three.

The lower PM material usage in a PMVM is advantageous as this translates to a low-cost design (about 20% cheaper than an equivalent PMSM at 3 MW level), but this advantage is offset by the cost of bigger converter capacity needed for a PMVM, which at the end causes the total cost of the two systems to level up. Although this study was based on a relatively conservative PM price, the conclusions drawn here are still legitimate even with higher PM prices (e.g., 60–70% increase in PM prices).

Even though the PMVM is designed to operate at a direct-drive generator input speeds, its operating frequency may need to be in the same range as that of medium-speed generators in order to enhance its best potential. This implies that its inherent soft gearing effects make it an intermediate alternative between the direct-drive and medium-speed concepts. The study predicts that it is feasible and economically viable to develop high-power PM vernier generators for the wind power applications.

**Author Contributions:** Conceptualization, P.T. and R.-J.W.; methodology, P.T. and R.-J.W.; software, P.T.; formal analysis, P.T.; investigation, P.T.; data curation, P.T.; writing—original draft preparation, P.T.; writing—review and editing, P.T. and R.-J.W.; supervision, R.-J.W. All authors have read and agreed to the published version of the manuscript.

**Institutional Review Board Statement:** Not applicable.

**Informed Consent Statement:** Not applicable.

**Data Availability Statement:** Not applicable.

**Conflicts of Interest:** The authors declare no conflict of interest.

## References

1. Polinder, H.; Van der Pijl, F.F.; De Vilder, G.J.; Tavner, P.J. Comparison of direct-drive and geared generator concepts for wind turbines. *IEEE Trans. Energy Convers.* **2006**, *21*, 725–733. [CrossRef]
2. Wang, R.-J.; Gerber, S. Magnetically geared wind generator technologies: Opportunities and challenges. *Appl. Energy* **2014**, *136*, 817–826. [CrossRef]
3. Tlali, P.M.; Wang, R.-J.; Gerber, S. Magnetic gear technologies: A review. In Proceedings of the 2014 International Conference on Electrical Machines (ICEM), Berlin, Germany, 2–5 September 2014; pp. 544–550.
4. Gerber, S.; Wang, R.-J. Design and evaluation of a PM vernier machine. In Proceedings of the 2015 IEEE Energy Conversion Congress and Exposition (ECCE), Montreal, QC, Canada, 20–24 September 2015; pp. 5188–5194.

5.  Li, J.; Chau, K.T.; Jiang, J.Z.; Liu, C.; Li, W. A new efficient permanent-magnet vernier machine for wind power generation. *IEEE Trans. Magn.* **2010**, *46*, 1475–1478. [CrossRef]
6.  Liu, G.; Jiang, S.; Zhao, W.; Chen, Q. A new modeling approach for permanent magnet vernier machine with modulation effect consideration. *IEEE Trans. Magn.* **2017**, *53*, 1–12. [CrossRef]
7.  Liu, C.; Chau, K.T.; Zhang, Z. Novel design of double-stator single-rotor magnetic-geared machines. *IEEE Trans. Magn.* **2012**, *48*, 4180–4183. [CrossRef]
8.  Niu, S.; Ho, S.L.; Fu, W.N.; Wang, L.L. Quantitative comparison of novel vernier permanent magnet machines. *IEEE Trans. Magn.* **2010**, *46*, 2032–2035. [CrossRef]
9.  Li, D.; Qu, R.; Zhu, Z. Comparison of halbach and dual-side vernier permanent magnet machines. *IEEE Trans. Magn.* **2014**, *50*, 801–804. [CrossRef]
10. Liu, W.; Lipo, T.A. Analysis of consequent pole spoke type vernier permanent magnet machine with alternating flux barrier design. *IEEE Trans. Ind. Appl.* **2018**, *54*, 5918–5929. [CrossRef]
11. Fu, W.; Ho, S. A quantitative comparative analysis of a novel flux-modulated permanent-magnet motor for low-speed drive. *IEEE Trans. Magn.* **2010**, *46*, 127–134. [CrossRef]
12. Liu, C.; Lee, C.H.; Chen, M. Comparison of outer-rotor permanent magnet machines for in-wheel drives. In Proceedings of the 2013 IEEE International Symposium on Industrial Electronics, Taipei, Taiwan, 28–31 May 2013; pp. 1–6.
13. Du, Z.S.; Lipo, T.A. Torque performance comparison between a ferrite magnet vernier motor and an industrial interior permanent magnet machine. *IEEE Trans. Ind. Appl.* **2017**, *53*, 2088–2097. [CrossRef]
14. Kim, B. Design of a direct drive permanent magnet vernier generator for a wind turbine system. In Proceedings of the 2018 IEEE Energy Conversion Congress and Exposition (ECCE), Portland, OR, USA, 23–27 September 2018; pp. 4275–4282.
15. Kim, B. Design method of a direct-drive permanent magnet vernier generator for a wind turbine system. *IEEE Trans. Ind. Appl.* **2019**, *55*, 4665–4675. [CrossRef]
16. Tlali, P.M.; Wang, R.-J.; Gerber, S. Comparison of PM vernier and conventional synchronous 15 kW wind generators. In Proceedings of the 2018 XIII International Conference on Electrical Machines, Alexandroupoli, Greece, 3–6 September 2018; pp. 2065–2071.
17. Tlali, P.M.; Wang, R.-J.; Gerber, S.; Botha, C.D.; Kamper, M.J. Design and performance comparison of vernier and conventional PM synchronous wind generators. *IEEE Trans. Ind. Appl.* **2020**, *56*, 2570–2579. [CrossRef]
18. Kumar, D.K.P.; Li, G.J.; Zhu, Z.Q.; Foster, M.P.; Stone, D.A.; Griffo, A.; Odavic, M.; Clark, L.; Thomas, A. Influence of demagnetization on selecting the optimum slot/pole number combination for 3MW surface mounted permanent magnet vernier machine. In Proceedings of the 22nd International Conference on Electrical Machines and Systems (ICEMS), Harbin, China, 11–14 August 2019; pp. 1–6.
19. Padinharu, D.K.K.; Li, G.J.; Zhu, Z.Q.; Clark, R.; Thomas, A.S.; Azar, Z. System-level investigation of multi-MW direct-drive wind power PM vernier generators. *IEEE Access* **2020**, *8*, 191433–191446. [CrossRef]
20. Tlali, P.M.; Wang, R.-J. PM Vernier machine for utility scale wind generator applications: Design and evaluation. In Proceedings of 2020 International Conference on Electrical Machines (ICEM), Gothenburg, Sweden, 23–26 August 2020; pp. 2637–2643.
21. Padinharu, D.K.K.; Li, G.J.; Zhu, Z.Q.; Clark, R.; Thomas, A.; Azar, Z.; Duke, A. Permanent magnet vernier machines for direct-drive offshore wind power: Benefits and challenges. *IEEE Access* **2022**, *10*, 20652–20668. [CrossRef]
22. Kim, B.; Lipo, T.A. Operation and design principles of a PM vernier motor. *IEEE Trans. Ind. Appl.* **2014**, *50*, 3656–3663. [CrossRef]
23. Li, D.; Qu, R.; Li, J.; Xiao, L.; Wu, L.; Xu, W. Analysis of torque capability and quality in vernier permanent-magnet machines. *IEEE Trans. Ind. Appl.* **2016**, *52*, 125–135. [CrossRef]
24. Kim, B.; Lipo, T.A. Design of a surface PM vernier motor for a practical variable speed application. In Proceedings of the 2015 IEEE Energy Conversion Congress and Exposition (ECCE), Montreal, Canada, 20–24 September 2015; pp. 776–783.
25. Toba, A.; Lipo, T.A. Generic torque-maximizing design methodology of surface permanent-magnet vernier machine. *IEEE Trans. Ind. Appl.* **2000**, *36*, 1539–1546.
26. Heller, B.; Hamata, V. *Harmonic Field Effects in Induction Machines*; Elsevier Scientific Pub. Co.: Amsterdam, The Netherlands; New York, NY, USA, 1977; 330p.
27. Skaar, S.E.; Krøvel, O.; Nilssen, R. Distribution, coil-span and winding factors for PM machines with concentrated windings. In Proceedings of the ICEM 2006, Crete Island, Greece, 2–5 September 2006.
28. Wang, K.; Zhu, Z.Q.; Ombach, G. Synthesis of high performance fractional-slot permanent-magnet machines with coil-pitch of two slot-pitches. *IEEE Trans. Energy Convers.* **2014**, *29*, 758–770. [CrossRef]
29. Jung, S.-Y.; Jung, H.; Hahn, S.-C.; Jung, H.-K.; Lee, C.-G. Optimal design of direct-driven PM wind generator for maximum annual energy production. *IEEE Trans. Magn.* **2008**, *44*, 1062–1065. [CrossRef]
30. Isfahani, A.H.; Boroujerdi, A.H.S.; Hasanzadeh, S. Multi-objective design optimization of a large-scale direct-drive permanent magnet generator for wind energy conversion systems. *Front. Energy* **2014**, *8*, 182–191. [CrossRef]
31. Dmitrievskii, V.; Prakht, V.; Kazakbaev, V. Design optimization of a permanent-magnet flux-switching generator for direct-drive wind turbines. *Energies* **2019**, *12*, 3636. [CrossRef]
32. Potgieter, J.H.J.; Kamper, M.J. Double PM-rotor, toothed, toroidal-winding wind generator: A comparison with conventional winding direct-drive PM wind generators over a wide power range. *IEEE Trans. Ind. Appl.* **2016**, *52*, 2881–2891. [CrossRef]

33. Grauers, A. Design of Direct Driven Permanent Magnet Generators for Wind Turbines. Ph.D. Thesis, School of Electrical and Computer Engineering, Chalmers University of Technology, Göteborg, Sweden, 1996.
34. Strous, T.D.; Shipurkar, U.; Polinder, H.; Ferreira, J. Comparing the brushless DFIM to other generator systems for wind turbine drive-trains. *J. Phys. Conf. Ser.* **2019**, *753*, 112014. [CrossRef]
35. Li, H.; Chen, Z.; Polinder, H. Optimization of multibrid permanent-magnet wind generator systems. *IEEE Trans. Energy Convers.* **2009**, *24*, 82–92. [CrossRef]
36. Yang, X.; Patterson, D.; Hudgins, J. Permanent magnet generator design and control for large wind turbines. In Proceedings of the 2012 IEEE Power Electronics and Machines in Wind Applications, Denver, CO, USA, 16–18 July 2012; pp. 1–5.
37. Tsai, W.-C. Robust design of a 5 MW permanent magnet synchronous generator using Taguchi method. In Proceedings of the 2012 7th International Conference on Computing and Convergence Technology, Seoul, Korea, 3–5 December 2012; pp. 1328–1334.
38. Pastellides, S.G.; Gerber, S.; Wang, R.-J.; Kamper, M.J. Evaluation of drive cycle-based traction motor design strategies using gradient optimisation. *Energies* **2022**, *15*, 1095. [CrossRef]
39. Deb, K.; Pratap, A.; Agarwal, S.; Meyarivan, T. A fast and elitist multiobjective genetic algorithm: NSGA-II. *IEEE Trans. Evol. Comput.* **2002**, *6*, 182–197. [CrossRef]
40. Johnson, M.; Gardner, M.C.; Toliyat, H.A.; Englebretson, S.; Ouyang, W.; Tschida, C. Design, construction, and analysis of a large-scale inner stator radial flux magnetically geared generator for wave energy conversion. *IEEE Trans. Ind. Appl.* **2018**, *54*, 3305–3314. [CrossRef]
41. Mthombeni, T.L.; Pillay, P. Physical Basis for the variation of lamination core loss coefficients as a function of frequency and flux density. In Proceedings of the 32nd Annual Conference on IEEE Industrial Electronics (IECON), Paris, France, 6–11 November 2006; pp. 1381–1387.
42. Ionel, D.M.; Popescu, M.; Dellinger, S.J.; Miller, T.J.E.; Heideman, R.J.; McGilp, M.I. On the variation with flux and frequency of the core loss coefficients in electrical machines. *IEEE Trans. Ind. Appl.* **2006**, *42*, 658–667. [CrossRef]

**MDPI**

*Article*

# Investigation of a Novel Consequent-Pole Flux-Intensifying Memory Machine

**Rui Tu [1], Hui Yang [1,*], Heyun Lin [1], Hanlin Zhan [2], Di Wu [3], Minghu Yu [3], Liang Chen [4] and Wenjie Chen [4]**

[1] School of Electrical Engineering, Southeast University, Nanjing 210096, China; ruitu_seu@163.com (R.T.); hyling@seu.edu.cn (H.L.)

[2] School of Mechanical Engineering and Automation, Harbin Institute of Technology (Shenzhen), Shenzhen 518055, China; zhanhanlin@hit.edu.cn

[3] Guangdong Welling Motor Manufacturing Co., Ltd., Foshan 528311, China; wudi9@welling.com.cn (D.W.); yumh1@chinagmcc.com (M.Y.)

[4] Midea Group Corporate Research Center, Foshan 528311, China; chenliang30@midea.com (L.C.); chenwj42@midea.com (W.C.)

*  Correspondence: huiyang@seu.edu.cn

**Abstract:** This paper mainly focuses on the investigation and analysis of a novel consequent-pole flux-intensifying memory machine (CP-FIMM). The proposed CP-FIMM exhibits the advantages of a satisfactory flux-regulation range, reduction of the required magnetizing current magnitude, as well as similar torque with much less PM utilization compared to its conventional counterpart. By designing the *q*-axis flux barriers, the flux-intensifying structure can be realized to enhance the demagnetization withstand capability of the CP-FIMM. The machine topology and operating principle are described. Moreover, the equivalent magnetic circuit model is developed to highlight the performance improvement of the proposed CP-FIMM. Finally, the electromagnetic performance of the proposed CP-FIMM is compared with that of a benchmark conventional FIMM by 2-D and 3-D finite element analysis.

**Keywords:** consequent-pole; flux-intensifying; memory machine; variable flux

## 1. Introduction

Permanent magnet synchronous machines (PMSMs) have been extensively applied and industrialized in the fields of vehicle traction, home appliances, and industrial manufacture owing to their merits of high efficiency and high reliability [1–6]. However, conventional PMSMs are usually confronted with unchangeable air-gap flux density, which causes limitations in their speed range and further brings some restrictions on the high-speed application. In order to broaden the speed range, flux weakening *d*-axis currents are conventionally applied to reduce the magnetic field of PMSM at high speed, which unintentionally brings additional copper loss and reduces overall efficiency.

In order to address the problem of unchangeable air-gap flux density, a variable flux memory machine (VFMM) [6–14] was proposed and has become a hot research focus. Memory machines utilize low coercive force (LCF) magnets such as AlNiCo, and the magnetization state (MS) can be flexibly adjusted with different transient current pulses with negligible loss. Therefore, VFMM can achieve high efficiency over a wide speed range. The existing VFMMs are divided into DC- [6–8] and AC- [9–14] magnetized types according to the winding category to provide current pulses. The DC-magnetized VFMMs [6–8] usually have LCF magnets on the stator side, and the additional magnetization coils can provide MS manipulation currents conveniently. However, DC-magnetized VFMMs generally suffer from a complicated structure. On the other hand, AC-excited VFMMs [9–16] utilize *d*-axis current pulses generated by the armature windings to manipulate the MS of LCF magnets, which feature a simple configuration with magnets on the rotor side.

For AC-magnetized VFMMs with a single LCF magnet, flux barriers are often set on the *q*-axis to realize reverse saliency ($L_d > L_q$), i.e., a flux-intensifying (FI) property, which can ensure that the maximum torque per ampere (MTPA) operation of the machine happens under the $i_d > 0$ situation, and thus can effectively decrease the risk of on-load demagnetization. The first AC-magnetized VFMM is proposed in [11], in which the rotor is characterized by a sandwich structure, including AlNiCo PM, iron core, and non-magnetic material. In [9], a radially magnetized FI VFMM with flux leakage paths is designed and analyzed. The designed machine shows benefits in improving efficiency and extending the range of the torque-speed map. In [13–15], spoke-type flux-intensifying VFMMs are proposed. The AlNiCo PMs are tangentially magnetized, which increases the air-gap flux density when fully magnetized, and brings the torque density of the VFMM to a comparable level to a conventional PMSM.

Nevertheless, AC-magnetized VFMMs generally require large amplitudes of magnetizing currents due to the high thickness of LCF magnets, which inevitably leads to an increased requirement for inverter capacity. Consequent-pole (CP) rotor design is a favorable way to reduce magnet usage and magnetization current, as well as maintain torque output at the same time [17–19]. Thus, this paper proposes a novel consequent-pole flux-intensifying memory machine (CP-FIMM) to address the above-mentioned problems for AC-magnetized VFMMs. The combination of FI variable-flux characteristics [20–22] and a consequent-pole [17–19] structure can reduce the amount of AlNiCo magnet, and meanwhile increase the *d*-axis inductance. Thus, the proposed CP design is advantageous for the reduction of the required magnetizing current magnitude, improvement of magnetic stability and PM utilization simultaneously.

This paper is organized as follows. First, in Section 2, the machine topology and operating principle including the flux regulation principle and magnetic circuit analysis are introduced. In Section 3, the electromagnetic performance of the CP-FIMM and FIMM is investigated and compared based on finite element analysis (FEA) with respect to the open-circuit and on-load performances, as well as magnetization characteristics and efficiency. In Section 4, a 3-D FE analysis is conducted to confirm the validity of the 2-D analysis. Section 5 is devoted to a comprehensive conclusion.

## 2. Machine Topology and Operating Principle

### 2.1. Machine Topology

Figure 1 shows the machine topologies of conventional FIMM [9] and the proposed CP-FIMM, respectively. Both machines have two layers of *q*-axis flux barriers in order to reduce *q*-axis inductance and create the reverse saliency ratio, which is beneficial for the unintentional demagnetization withstand ability. For CP-FIMM, nearly half of the magnet poles are replaced by iron cores, forming a CP structure, which can reduce the usage of AlNiCo PM by approximately 40%. It should be noted that the optimal pole-arc coefficient of the CP-FIMM is slightly larger than 1 in order to achieve higher torque. Table 1 illustrates the key design parameters of the CP-FIMM and FIMM. For a fair comparison, the major design parameters of the two topologies are kept the same except for different PM volumes.

### 2.2. Flux Regulation Principle

Figure 2 reveals the simplified hysteresis model of the AlNiCo PM. By applying certain transient *d*-axis current pulses to generate demagnetizing or remagnetizing MMF, the working point of AlNiCo PM will move along the recoil lines and finally stabilizes at the load line. Consequently, the MS of AlNiCo PM can be flexibly changed and maintained according to different operation requirements.
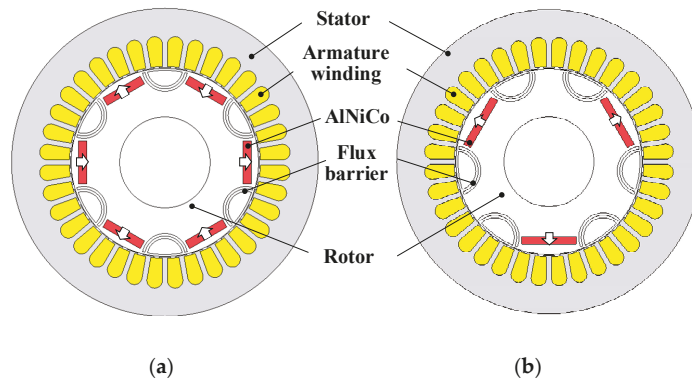
**Figure 1.** Machine topology. (**a**) FIMM, (**b**) CP-FIMM.

**Table 1.** Key design parameters of FIMM and CP-FIMM.

| Items | FIMM | CP-FIMM |
|---|---|---|
| Rated power (W) | 600 | |
| Rated speed (rpm) | 1000 | |
| Outer diameter of stator (mm) | 122 | |
| Inner diameter of stator (mm) | 75 | |
| Air-gap length (mm) | 0.5 | |
| Outer diameter of rotor (mm) | 74.5 | |
| Inner diameter of rotor (mm) | 36.5 | |
| Active stack length (mm) | 55 | |
| Steel grade | 50JN1000 | |
| AlNiCo PM grade | AlNiCo9 | |
| AlNiCo volume (cm$^3$) | 66.0 | 39.6 |
| Armature winding turns per phase | 360 | |
| Rated current (Arms) | 7.5 | |
| DC-link voltage (V) | 120 | |
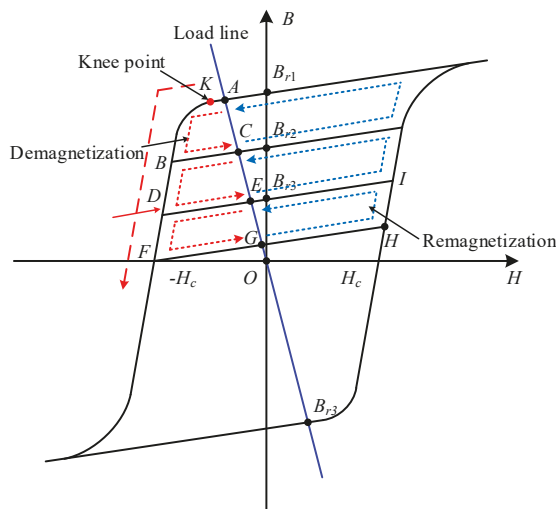


**Figure 2.** The simplified hysteresis model of the AlNiCo PM.

In order to characterize the magnetization state (MS) of the memory machine, the magnetization ratio $k_{mr}$ is defined as

$$k_{mr} = \frac{B_{rk}}{B_r} \times 100\% \tag{1}$$

where $B_r$ is the remanence of the major hysteresis loop, $B_{rk}$ is the specific remanence corresponding to the specific PM working point on the $k$th recoil line. The above percentage $k_{mr}$ is then adopted to characterize the magnetization level of the FIMM and CP-FIMM.

### 2.3. Magnetic Circuit Analysis

Figure 3a shows the magnetic circuit paths of the FIMM and CP-FIMM, respectively. For the two machines, since double-layer flux barriers are placed on the $q$-axis, $L_q$ is significantly decreased. Moreover, because the AlNiCo PM usage of CP-FIMM on the $d$-axis is reduced, the $L_d$ is increased. By realizing the relationship of $L_d > L_q$, "$i_d > 0$" control is adopted for rated MTPA operation to fully utilize the magnet torque and reluctance torque, which can meanwhile reduce the risk of on-load demagnetization.
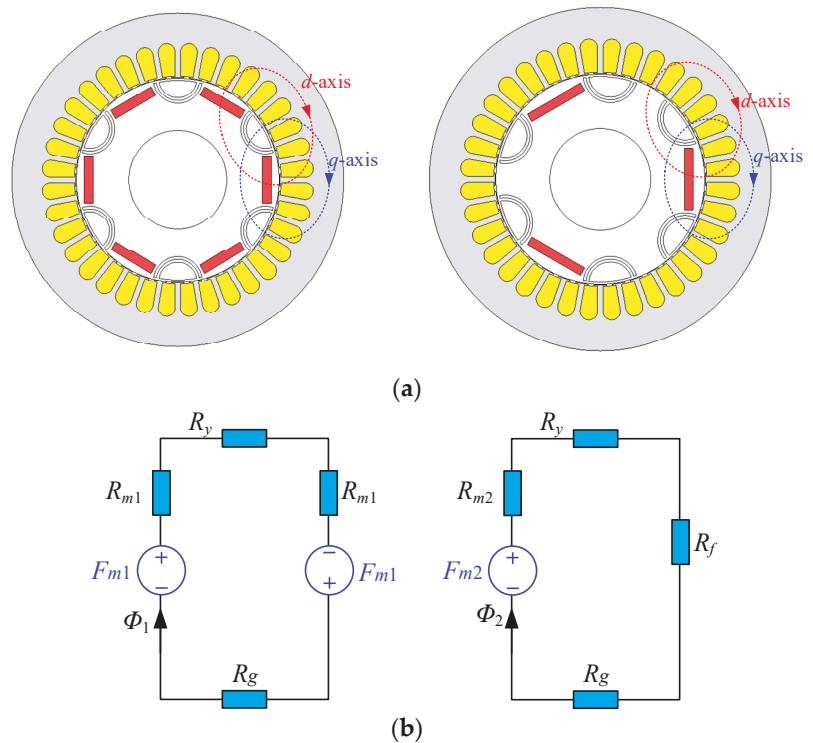


**Figure 3.** Magnetic circuits of FIMM and CP-FIMM, (**a**) $d$- and $q$-axis; (**b**) equivalent magnetic circuit of $d$-axis.

Figure 3b shows the equivalent $d$- and $q$-axis magnetic circuits of the FIMM and CP-FIMM, respectively. The corresponding parameters are listed in Table 2.

**Table 2.** Parameters in equivalent magnetic circuits.

| Symbols | Parameters |
|---------|------------|
| $R_y$ | magnetic reluctance of stator yoke |
| $R_g$ | magnetic reluctance of air-gap |
| $R_f$ | magnetic reluctance of iron pole |
| $R_{m1}$ | magnetic reluctance of AlNiCo in the FIMM |
| $R_{m2}$ | magnetic reluctance of AlNiCo in the CP-FIMM |
| $F_{m1}$ | magnetomotive force MMF of AlNiCo in the FIMM |
| $F_{m2}$ | magnetomotive force MMF of AlNiCo in the CP-FIMM |

The corresponding air-gap flux $\Phi_1$ and $\Phi_2$ can be illustrated as (2) and (3). Since the volume of a single AlNiCo PM of the CP-FIMM is larger than that of the FIMM, $F_{m2}$ is larger than $F_{m1}$. Additionally, $R_f$ is smaller than $R_{m2}$. Consequently, $\Phi_2$ is close to $\Phi_1$, which indicates that the electromagnetic performance of the CP-FIMM is close to that of the conventional FIMM.

$$\Phi_1 = \frac{2F_{m1}}{R_y + 2R_{m1} + R_g} \tag{2}$$

$$\Phi_2 = \frac{F_{m2}}{R_y + R_{m2} + R_g + R_f} \tag{3}$$

In addition, the relationship in the flux regulation process can be shown as

$$\Psi_{df} = L_d i_{dm} \tag{4}$$

where $\Psi_{df}$ is the required flux linkage to realize MS manipulation, and $i_{dm}$ refers to the required MS manipulation current amplitude. It can be deduced that with a smaller amount of AlNiCo PM, the CP-FIMM has a relatively smaller *d*-axis reluctance as well as a larger $L_d$. Therefore, lower *d*-axis magnetomotive force (MMF) is needed for the flux regulation process for CP-FIMM, i.e., lower magnetization currents are required, which can help reduce the capacity of the inverter.

*2.4. Control Scheme*

Figure 4 shows the control scheme of the proposed CP-FIMM. The MTPA control method for which $i_d > 0$ is adopted for its rated operation. Based on the machine operation properties, different MSs are flexibly adjusted by the command of the magnetization state controller. When the speed exceeds the base speed, the negative $i_d$ flux-weakening method is conducted to offset the PM flux-linkage in order to widen the speed range.
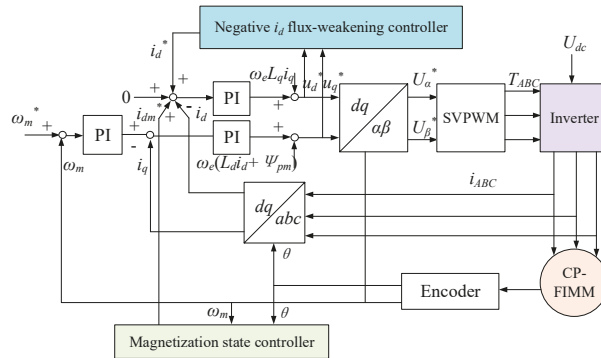


**Figure 4.** Control scheme of the CP-FIMM.

## 3. Electromagnetic Performance Investigation of the Proposed CP-FIMM

### 3.1. Open-Circuit Performance

The foregoing CP-FIMM and FIMM machine topologies are designed, and finite element analysis and comparison are conducted based on the JMAG 20.0 package.

Figure 5 shows the flux line distributions of the two machines under different MSs. It can be observed that although a smaller volume of the magnet is utilized in CP-FIMM, similar flux distribution patterns can be found in the two machines. It can also be seen that both topologies can realize variable MSs effectively. Figure 6 shows the flux distributions of FIMM and CP-FIMM under different MSs, respectively. It can be observed that both topologies exhibit excellent flux regulation capability. More severe magnetic saturation can be found around the flux barriers of CP-FIMM due to larger pole-end flux leakage of the AlNiCo PM, which accounts for a smaller air-gap flux density of the CP-FIMM. Moreover, the stator flux density of the CP-FIMM is larger, especially under low MSs, which accounts for more iron loss.
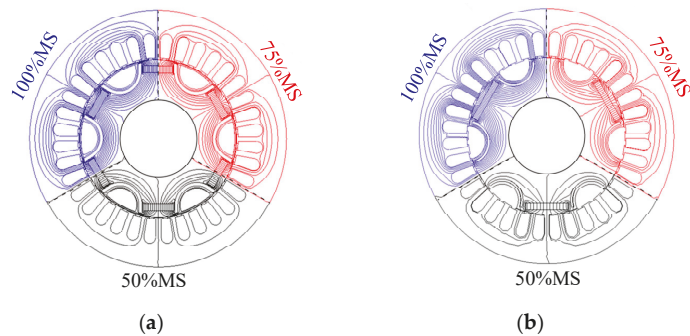


**Figure 5.** Flux line distributions under different MSs. (**a**) FIMM; (**b**) CP-FIMM.
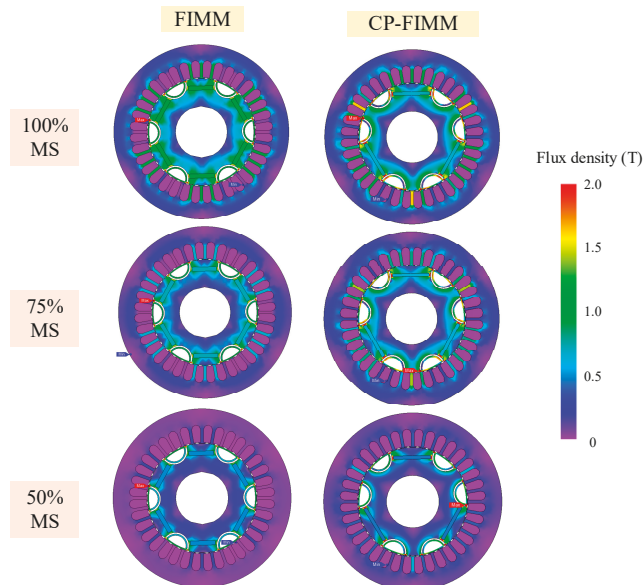


**Figure 6.** Flux density distributions of the two machines under different MSs.

Figure 7 illustrates the flux linkage waveforms and harmonic analysis of FIMM and CP-FIMM under different MSs, respectively. It can be seen that both topologies have excellent MS manipulation capabilities. Besides, the fundamental flux linkage amplitudes of CP-FIMM are slightly lower than those of the conventional FIMM due to its relatively smaller PM usage. The high-order harmonics are zoomed in and shown in Figure 5b. It can be observed that the two machines share similar distribution patterns of harmonics, while the proposed CP-FIMM has a relatively smaller level of harmonics, which is beneficial for the sinusoidal back-EMF waveform and reduction of torque ripple.
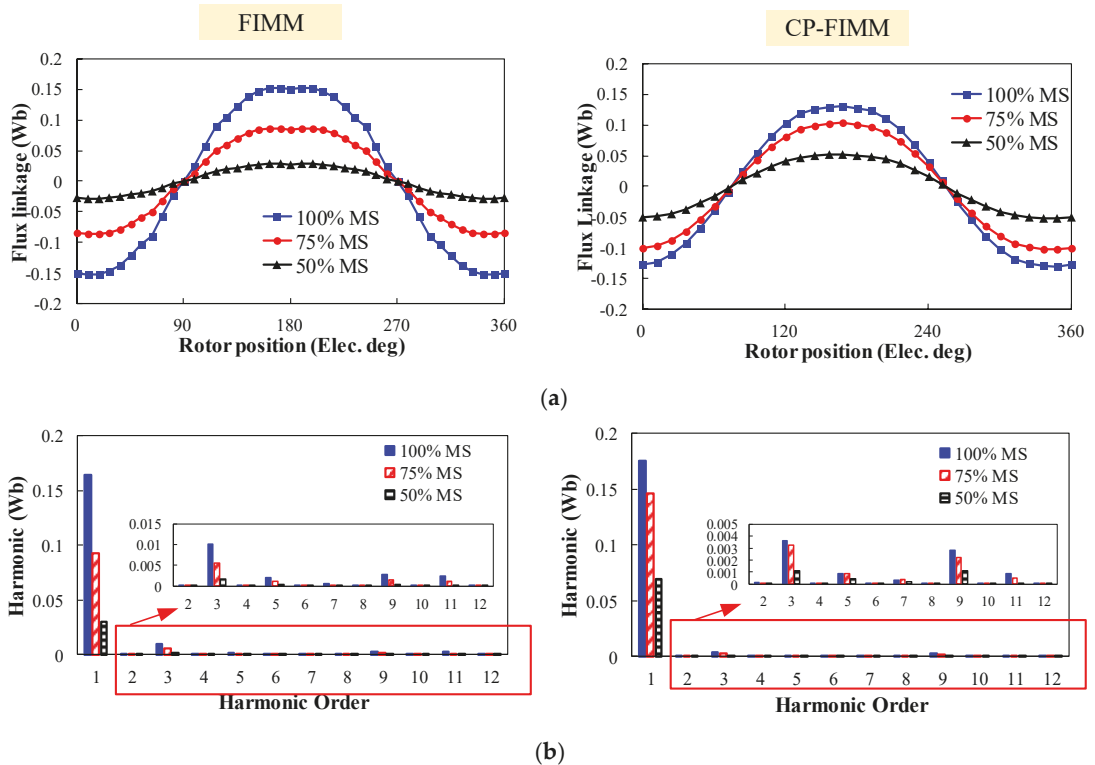


**Figure 7.** Flux linkage of the two machines. (**a**) Waveforms; (**b**) harmonic spectra.

Figure 8 shows the air-gap flux density waveforms of the FIMM and CP-FIMM. Due to the existence of iron poles, the air-gap flux density of CP-FIMM shows an asymmetry and has more even-order harmonics. In addition, the fundamental amplitude of air-gap flux density of CP-FIMM is slightly lower than FIMM since 40% of AlNiCo PM is replaced by iron poles. Since more AlNiCo PMs are involved in MS manipulation in the FIMM, the flux densities under 75% and 50% MSs of FIMM are lower than the CP-FIMM, respectively.

The open-circuit back-EMFs as well as harmonic analysis of the CP-FIMM and FIMM under different MSs are shown in Figure 9. It can be observed that the even-order harmonics in air-gap flux are canceled, and the back-EMF of CP-FIMM has a lower fundamental component and a lower total harmonic distortion (THD) with eliminated high-order harmonics.
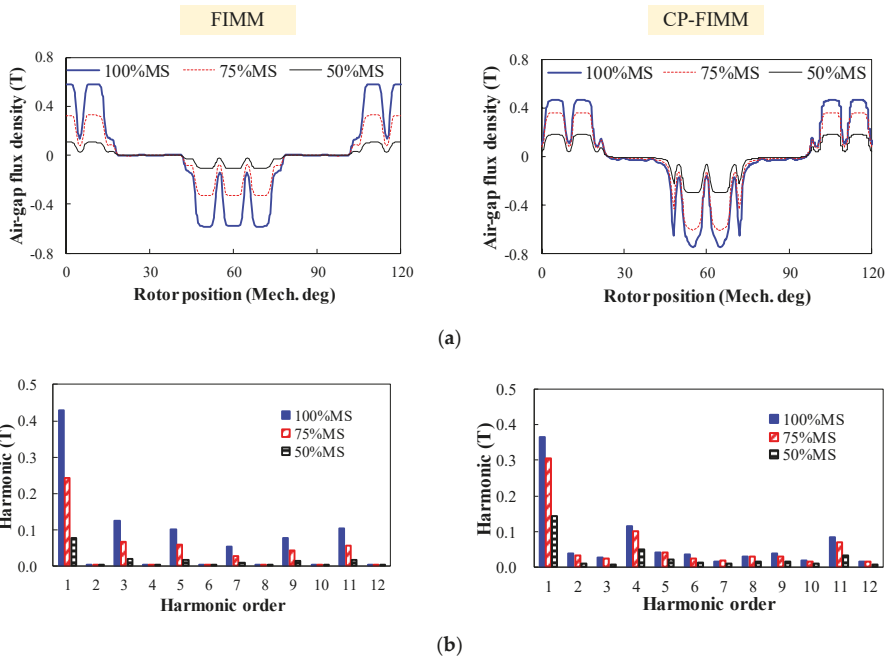
**Figure 8.** Air-gap flux density of the two machines under different MSs. (**a**) Waveforms, (**b**) spectra.
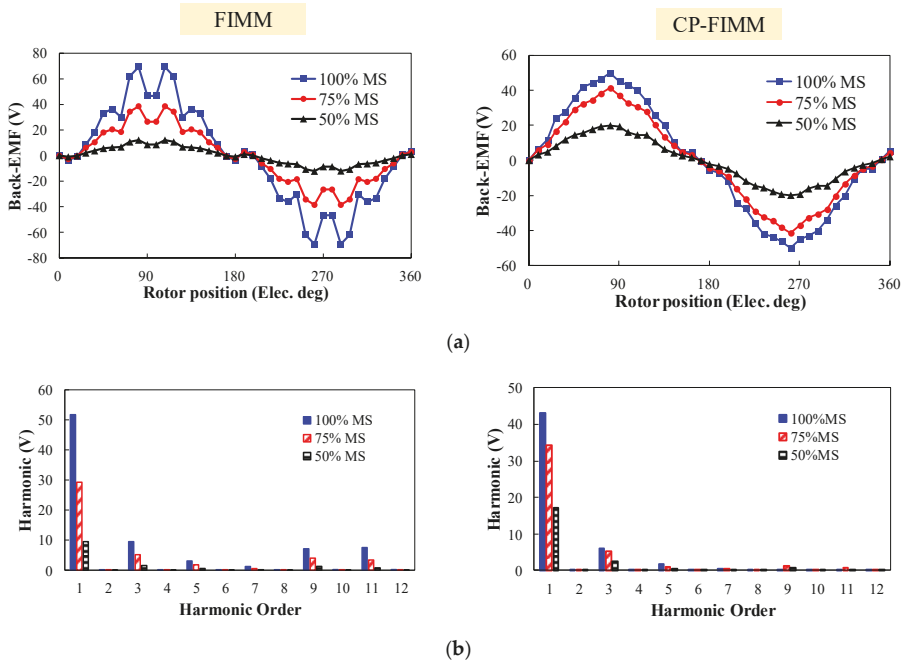


**Figure 9.** Back-EMF waveforms and harmonic analysis CP-FIMM and FIMM under different MSs. (**a**) Waveforms; (**b**) spectra.

### 3.2. Torque Performance

Figure 10 shows the average torque of CP-FIMM and FIMM subject to different current angles. It can be seen that the maximum torque of CP-FIMM is acquired with a positive $i_d$, which confirms that the FI property, i.e., $L_d > L_q$, can be well obtained with the design of the CP structure. On the other hand, due to a similar magnetic reluctance of the $d$- and $q$-axis, the values of $L_d$ and $L_q$ of FIMM are close to each other, and the FIMM shows negligible saliency.
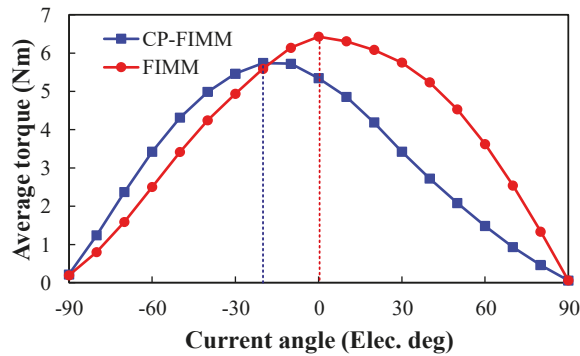


**Figure 10.** Average torque versus current angle plots of the CP-FIMM and FIMM.

Figure 11 shows the cogging torque waveforms of the CF-FIMM and FIMM. Since the rotor iron poles serve as half of the magnetic poles, CP-FIMM shares identical cogging torque period with the FIMM. In addition, the two machines have comparable cogging torque amplitude.
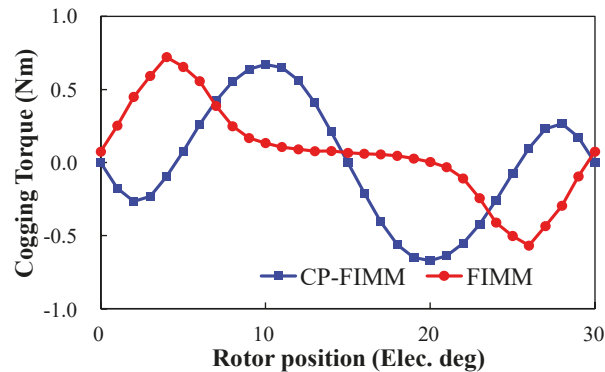


**Figure 11.** Cogging torque waveforms.

The torque characteristics of the two machines are compared in Table 3. It can be observed that the proposed CP-FIMM can achieve 93.49% of the average torque by reducing 40% of AlNiCo PM volume, and has a larger PM utilization rate. Due to the limitation of cost and restriction on PM volume, the torque of CP-FIMM is slightly lower. However, it should be noted that with a slightly larger PM volume, the CP-FIMM is able to achieve the same torque compared with the FIMM. Moreover, the CP-FIMM has a smaller torque ripple than the FIMM owing to a more sinusoidal back-EMF.

**Table 3.** Torque characteristics of the analyzed machines.

| Items | FIMM | CP-FIMM |
|---|---|---|
| Average torque (Nm) | 6.54 | 5.74 |
| Torque ripple (%) | 50.18 | 23.98 |
| Cogging torque (Nm) | 1.29 | 1.34 |
| Average torque/PM volume (Nm/cm$^3$) | 0.099 | 0.145 |

*3.3. Flux Regulation Performance*

The flux regulation characteristics of the CP-FIMM and FIMM are analyzed based on the required transient current amplitude to change the fundamental open-circuit back-EMF. Figures 12 and 13 show the waveforms of fundamental back-EMF versus different flux regulation current amplitude of the two machines. It can be seen that compared with the conventional FIMM, it is significantly easier to magnetize or demagnetize the CP-FIMM, which is consistent with the foregoing analyses. Consequently, with a smaller demagnetizing current amplitude, the required inverter capacity can be reduced.
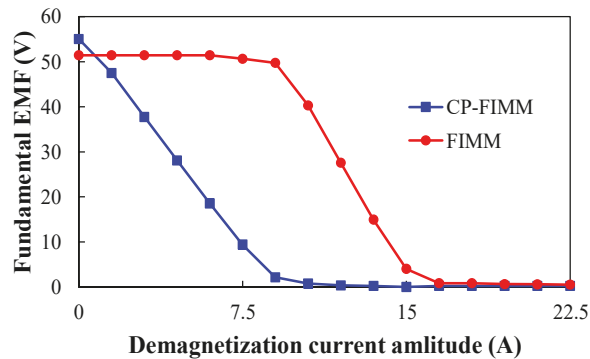


**Figure 12.** Fundamental back-EMF versus demagnetization current.
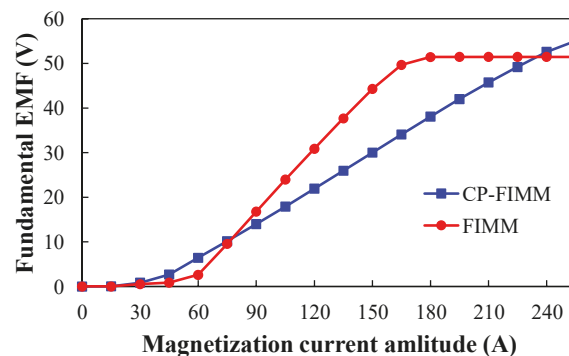


**Figure 13.** Fundamental back-EMF versus magnetization current.

*3.4. External Characteristics*

The external characteristics of the two machines are acquired based on the control method in Figure 4, and the corresponding waveforms are shown in Figures 14 and 15, respectively. It can be seen that the CP-FIMM has a relatively smaller torque and electromagnetic power under a flux-enhanced state, which is mainly due to the smaller usage of

the magnet. On the other hand, the CP-FIMM has a larger output power and torque under the flux-weakened state, which is compromised with a lower maximum speed.
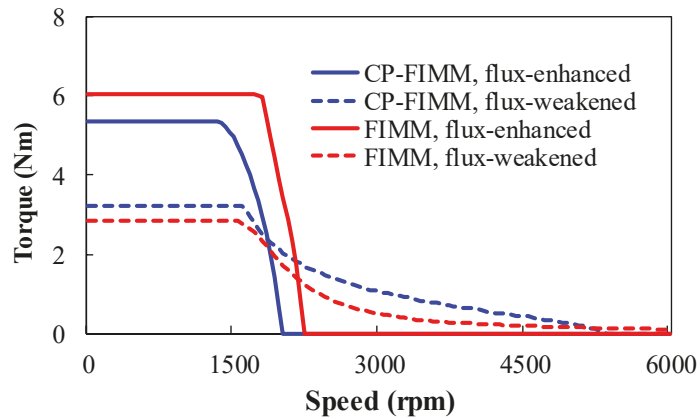


**Figure 14.** Torque-speed waveforms of the CP-FIMM and FIMM under different MSs.
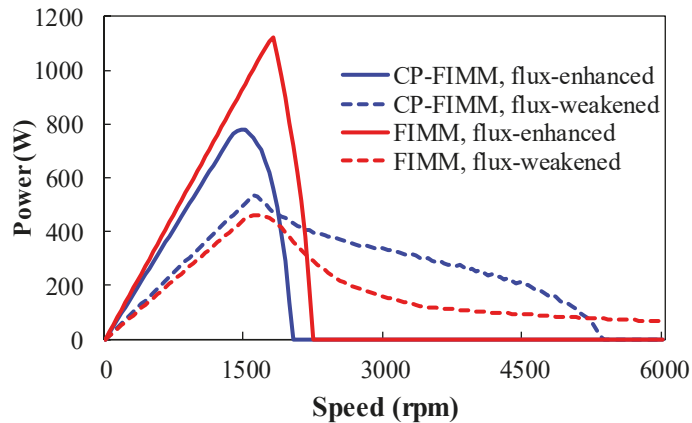


**Figure 15.** Power-speed waveforms of the CP-FIMM and FIMM under different MSs.

*3.5. Efficiency*

Figure 16 shows the efficiency maps of the proposed CP-FIMM and FIMM under different MSs, respectively. It can be found that the CP-FIMM can realize a wide speed range with high overall efficiency. Additionally, the CP-FIMM shows a relatively smaller overall efficiency than the conventional counterpart.

Figures 17 and 18 show the copper and iron loss maps of the two machines under different MSs, respectively. It can be seen that the two machines share similar copper loss patterns and the CP-FIMM has a lower copper loss under high-speed operation region due to better flux-weakening performance. On the other hand, the CP-FIMM has a larger iron loss under high-speed operation, which is due to the larger flux density distribution in the stator, which can be found in Figure 6. As a result, the efficiency of CP-FIMM is slightly lower than the FIMM, especially under the flux-weakened state.
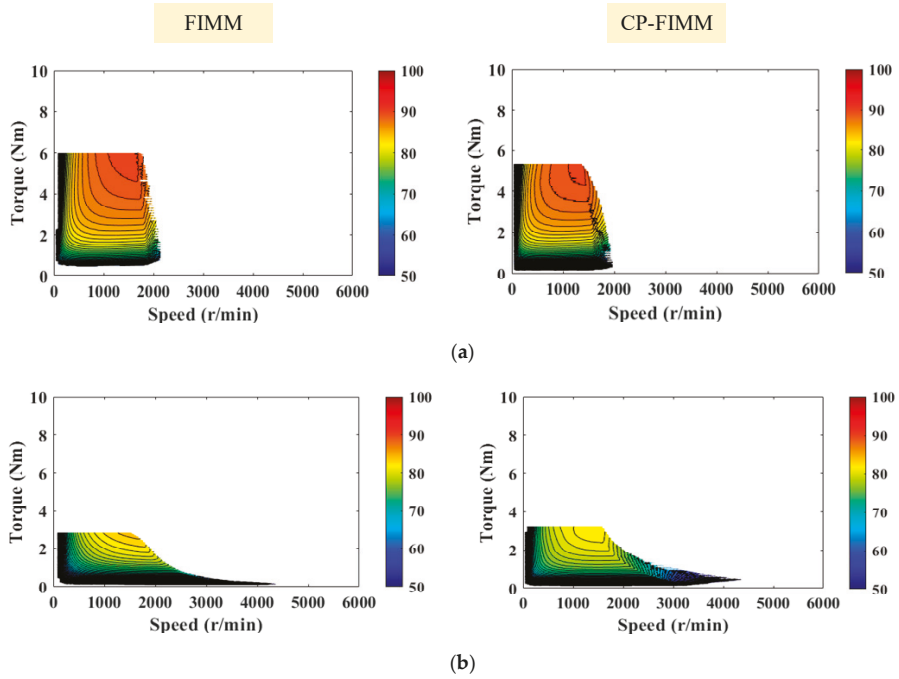
**Figure 16.** Efficiency maps of FIMM and CP-FIMM. (**a**) Flux-enhanced; (**b**) flux-weakened.
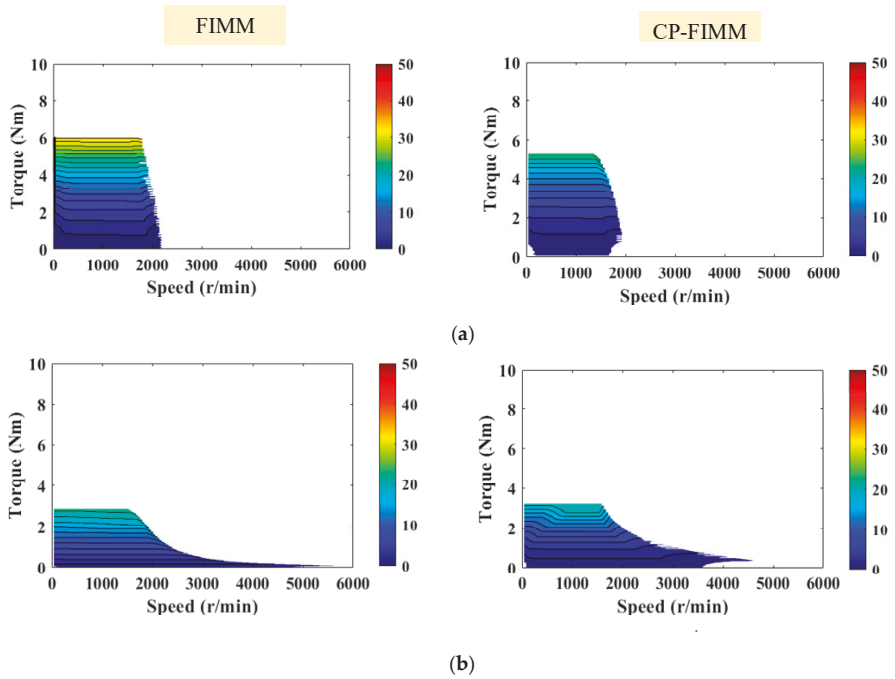


**Figure 17.** Copper loss maps of FIMM and CP-FIMM. (**a**) Flux-enhanced; (**b**) flux-weakened.
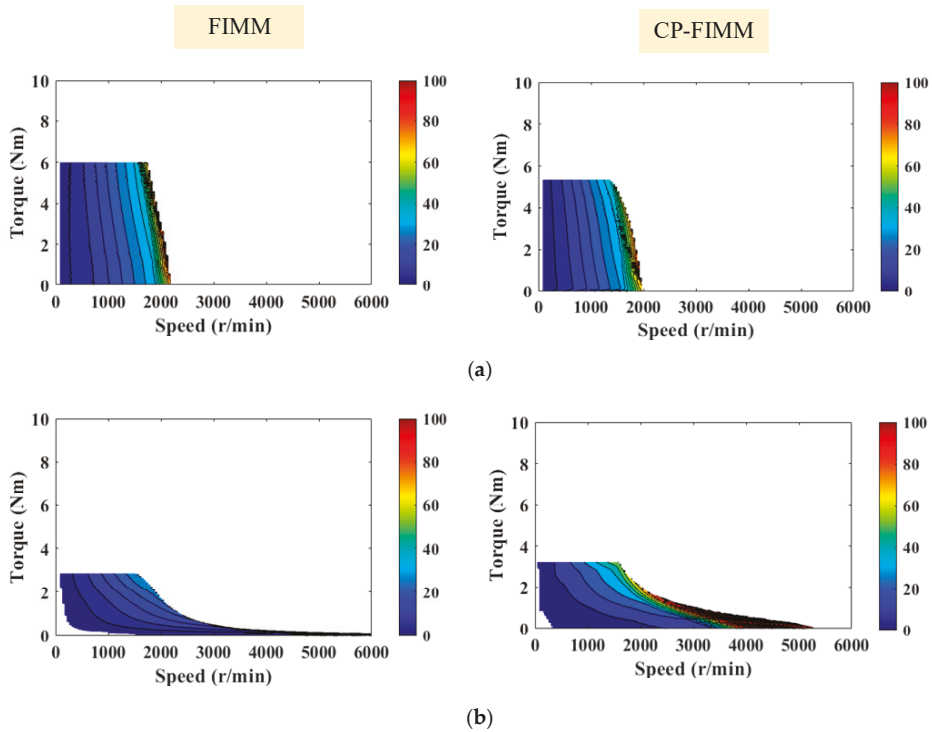
**Figure 18.** Iron loss maps of FIMM and CP-FIMM. (**a**) Flux-enhanced; (**b**) flux-weakened.

## 4. Three-Dimensional FE analysis

In order to further validate the above 2-D FE analysis, 3-D models are built in Figure 19 according to the stack lengths and the torque performance of the two machines are analyzed. The corresponding results are shown in Figure 20 and Table 4. It can be seen that the average torque and torque ripple results are close between the 2-D and 3-D FE analyses, which confirms the validity of the foregoing analysis.
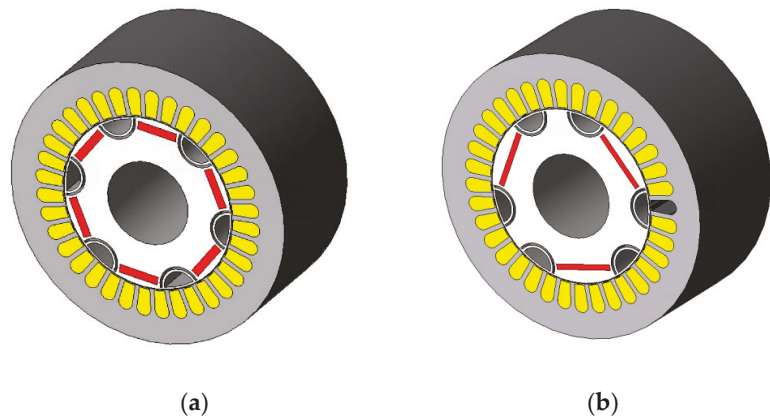


**Figure 19.** Three-dimensional models of the two machines. (**a**) FIMM. (**b**) CP-FIMM.
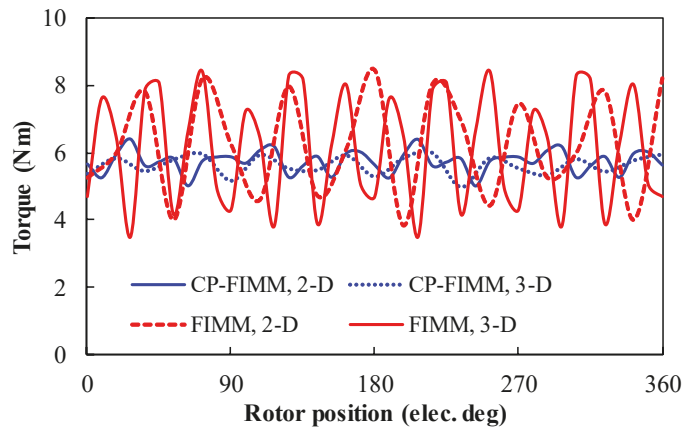
**Figure 20.** Torque waveforms of 2-D and 3-D FE analysis.

**Table 4.** Torque comparison between 2-D and 3-D analysis.

| Items | FIMM | | CP-FIMM | |
|---|---|---|---|---|
| | **2-D** | **3-D** | **2-D** | **3-D** |
| Average torque (Nm) | 6.54 | 6.25 | 5.74 | 5.98 |
| Torque ripple (%) | 50.18 | 63.50 | 23.98 | 17.65 |

## 5. Conclusions

In this paper, a novel CP-FIMM is developed and analyzed. The flux regulation and operating principle of the CP-FIMM are firstly described based on the simplified hysteresis model and equivalent magnetic circuit. It is deduced that the torque capability of CP-FIMM is close to that of the conventional FIMM, and requires a lower level of magnetization currents due to a larger *d*-axis inductance. Then, the electromagnetic performance of CP-FIMM and a benchmark conventional FIMM are investigated and compared based on the FE method. It is found that the CP-FIMM can realize similar torque output to the conventional FIMM with an approximate 60% reduction in PM volume. Additionally, the required magnetizing current of CP-FIMM can be significantly reduced due to a larger *d*-axis inductance. The efficiency distribution patterns of the two machines are similar, with a slightly lower efficiency of CP-FIMM. Finally, a 3-D FE analysis is carried out to confirm the validity of the 2-D analysis.

## References

1. Wu, L.; Tian, Z. Analysis of a Triple-Stator Axial-Flux Spoke-Type Permanent Magnet Vernier Machine. *IEEE Trans. Ind. Appl.* **2022**. [CrossRef]
2. Liu, C.; Xu, Y.; Zou, J.; Yu, G.; Zhuo, L. Permanent Magnet Shape Optimization Method for PMSM Air Gap Flux Density Harmonics Reduction. *CES Trans. Electr. Mach. Syst.* **2021**, *5*, 284–290. [CrossRef]
3. Zhao, W.; Yang, Z.; Liu, Y.; Wang, X. Analysis of a Novel Surface-Mounted Permanent Magnet Motor with Hybrid Magnets for Low Cost and Low Torque Pulsation. *IEEE Trans. Magn.* **2021**, *57*, 8104804. [CrossRef]
4. Paul, S.; Chang, J. Fast Model-Based Design of High Performance Permanent Magnet Machine for Next Generation Electric Propulsion for Urban Aerial Vehicle Application. *CES Trans. Electr. Mach. Syst.* **2021**, *5*, 143–151. [CrossRef]
5. Oka, T.; Hasebe, S.; Ogawa, J.; Fukui, S.; Nakano, T.; Yokoyama, K.; Miryala, M.; Sakai, N.; Murakami, M. Magnetizing Technique for Permanent Magnets in IPM Motor Rotors Using HTS Bulk Magnet. *IEEE Trans. Appl. Supercond.* **2020**, *30*, 5206304. [CrossRef]
6. Cheng, M.; Sun, L.; Buja, G.; Song, L. Advanced Electrical Machines and Machine-Based Systems for Electric and Hybrid Vehicles. *Energies* **2015**, *8*, 9541–9564. [CrossRef]
7. Yang, H.; Lin, H.; Zhu, Z.Q.; Lyu, S.; Liu, Y. Design and Analysis of Novel Asymmetric-Stator-Pole Flux Reversal PM Machine. *IEEE Trans. Ind. Electron.* **2020**, *67*, 101–114. [CrossRef]
8. Zhu, X.; Xiang, Z.; Quan, L.; Wu, W.; Du, Y. Multimode Optimization Design Methodology for a Flux-Controllable Stator Permanent Magnet Memory Motor Considering Driving Cycles. *IEEE Trans. Ind. Electron.* **2018**, *65*, 5353–5366. [CrossRef]
9. Limsuwan, N.; Kato, T.; Akatsu, K.; Lorenz, R.D. Design and Evaluation of a Variable-Flux Flux-Intensifying Interior Permanent-Magnet Machine. *IEEE Trans. Ind. Appl.* **2014**, *50*, 1015–1024. [CrossRef]
10. Xu, H.; Li, J.; Chen, J.; Lu, Y.; Ge, M. Analysis of a Hybrid Permanent Magnet Variable-Flux Machine for Electric Vehicle Tractions Considering Magnetizing and Demagnetizing Current. *IEEE Trans. Ind. Appl.* **2021**, *57*, 5983–5992. [CrossRef]
11. Ostovic, V. Memory Motors-a New Class of Controllable Flux PM Machines for a True Wide Speed Operation. In Proceedings of the Industry Applications Conference, 36th IAS Annual Meeting, Chicago, IL, USA, 30 September 2001–4 October 2001; pp. 2577–2584.
12. Xie, Y.; Ning, Z.; Ma, Z.; Cai, W.; Wei, J. Design and Research of Novel Variable Flux Memory Motor with Series Hybrid Magnets. In Proceedings of the 2020 23rd International Conference on Electrical Machines and Systems (ICEMS), Hamamatsu, Japan, 24–27 November 2020; pp. 2142–2147.
13. Sun, A.; Li, J.; Qu, R.; Chen, J.; Lu, H. Rotor Design Considerations for a Variable-Flux Flux-Intensifying Interior Permanent Magnet Machine with Improved Torque Quality and Reduced Magnetization Current. In Proceedings of the 2015 IEEE Energy Conversion Congress and Exposition (ECCE), Montreal, QC, Canada, 20–24 September 2005; pp. 784–790.
14. Lu, Y.; Li, J.; Qu, R.; Sun, A.; Fang, H. A Method to Improve Torque Density and Reduce Magnetization Current in a Variable-Flux Flux-Intensifying Interior Permanent Magnet Machine. In Proceedings of the 2016 IEEE Vehicle Power and Propulsion Conference (VPPC), Hangzhou, China, 17–20 October 2016.
15. Ibrahim, M.; Masisi, L.; Pillay, P. Design of Variable-Flux Permanent-Magnet Machines Using Alnico Magnets. *IEEE Trans. Ind. Appl.* **2015**, *51*, 4482–4491. [CrossRef]
16. Qiao, G.; Liu, Y.; Zheng, P.; Chen, J.; Zhang, S.; Wang, M. Analysis of Magnetic Properties of AlNiCo and Methods of Mitigating Dynamic Voltage Limits in the Combined-Magnetic-Pole Memory Motor. In Proceedings of the 21st International Conference on Electrical Machines and Systems (ICEMS), Jeju, Korea, 7–10 October 2018; pp. 1175–1180.
17. Wei, F.; Zhu, Z.Q.; Sun, X.; Yan, L.; Qi, J. Investigation of Asymmetric Consequent-Pole Hybrid Excited Flux Reversal Machines. *IEEE Trans. Ind. Appl.* **2022**, *58*, 3434–3446. [CrossRef]
18. Yang, H.; Lin, H.; Li, H.; Lyu, S. Analysis of Consequent-Pole Flux Reversal Permanent Magnet Machine with Biased Flux Modulation Theory. *IEEE Trans. Ind. Electron.* **2020**, *67*, 2107–2121. [CrossRef]
19. Qi, J.; Zhu, Z.Q.; Li, Y.; Jewell, G.W.; Hilton, C. Effect of Pole Shaping on Torque Characteristics of Consequent Pole PM Machines. In Proceedings of the IEEE International Electric Machines & Drives Conference (IEMDC), Hartford, CT, USA, 17–20 May 2021.
20. Zhu, X.; Yang, S.; Du, Y.; Xiang, Z.; Xu, L. Electromagnetic Performance Analysis and Verification of a New Flux-Intensifying Permanent Magnet Brushless Motor with Two-Layer Segmented Permanent Magnets. *IEEE Trans. Magn.* **2016**, *52*, 8204004. [CrossRef]
21. Ngo, D.; Hsieh, M.; Huynh, T.A. Torque Enhancement for a Novel Flux Intensifying PMa-SynRM Using Surface-Inset Permanent Magnet. *IEEE Trans. Magn.* **2019**, *55*, 8106108. [CrossRef]
22. Liu, F.; Quan, L.; Zhu, X.; Xiang, Z.; Wu, W. Investigation of Reverse Saliency Characteristic in Flux-Intensifying Hybrid Permanent Magnet Motor Considering Various Operation Conditions. In Proceedings of the 2018 IEEE International Conference on Applied Superconductivity and Electromagnetic Devices (ASEMD), Tianjin, China, 15–18 April 2018; pp. 1–2.

# Development of a Transient Synchronization Analysis Tool for Line-Start PM Motors

**Phillip Schommarz and Rong-Jie Wang ***

Department of Electrical & Electronic Engineering, Stellenbosch University, Stellenbosch 7600, South Africa
* Correspondence: rwang@sun.ac.za

**Abstract:** With more stringent IEC energy efficiency standards, electrical machine industry increasingly focuses on new motor technologies. Amongst others, the line-start permanent magnet synchronous machine (LSPMSM) is considered as an attractive alternative to induction machine, especially for low power and fixed-speed applications. However, the design of LSPMSMs is rather complex as both steady-state and transient synchronization performances need to be considered. The synchronization capability determination of a LSPMSM design usually relies on time-consuming transient finite-element simulations, which is impractical for use in an iterative design optimization process. This paper compares and evaluates various existing analytical synchronization analysis methods in an attempt to identify most suitable equations and methods for fast synchronization analysis. Using the selected methods, a software tool is developed that can seamlessly work with ANSYS Electronics Desktop to perform rapid transient synchronization analysis. Given its ability to quickly determine the critical inertia factor of a LSPMSM design, the software tool is further adapted for use in a highly iterative, multi-objective design optimization procedure. It shows that the developed software tool can be successfully used in the design of LSPMSMs.

**Keywords:** analytical modeling; finite element method; line-start motor; permanent magnet machine; software development; synchronization; transient performance

## 1. Introduction

Industrial application of electrical motors consumes between 30% and 40% of generated electrical energy worldwide [1]. With the advent of the new industrial revolution brought forth by the development of e-mobility and renewable energy systems, the use of electrical motors will continue to grow at a fast pace. However, hand-in-hand with this growing demand for electrical motors comes the demand for improvement in their energy efficiency. With more stringent IEC efficiency standards, electrical motor manufacturers increasingly focus on new motor technologies as induction motors (IMs) are approaching their efficiency limits. This is especially true for low power general purpose IMs that drive fixed-speed loads such as fans, pumps and conveyors.

The line-start permanent magnet synchronous motor (LSPMSM) is an attractive alternative as it promises both higher efficiency and power factor than an IM [2]. While the efficiency of super-premium (IE4) 2.2 kW IMs has been observed to lie between 86 and 89% [3], LSPMSMs of the same power rating carry the potential to breach the 90% efficiency barrier. However, the design of LSPMSMs is rather complicated as its rotor structure contains both permanent magnets and cage windings, both of which can be configured in numerous ways. Furthermore, LSPMSMs have two distinct regions of operation, namely asynchronous operation during start-up, and synchronous operation during steady-state. The trade-off between starting/synchronization capability and higher efficiency and power factor is a key challenge for LSPMSMs [4].

Determining whether a LSPMSM candidate design synchronizes usually requires transient finite-element (FE) analysis, which is computationally expensive and not suited

for use in any iterative design optimization procedure [5–7]. As an alternative, various fast analytical approaches for the synchronization analysis of LSPMSMs have been proposed such as energy methods [8,9], time-domain method [9], semi-numerical method [10], multi-damping-circuit model [11], reluctance network model [12], and sizing equation based mathematical model [13], which promise to provide at least a good estimate of a design's synchronization capability. The work reported in [14] was probably the first attempt of incorporating both analytical steady-state and synchronization analysis into the multi-objective design optimization process of LSPMSMs. However, the optimization was conducted using the Taguchi method. Apart from that, these analytical approaches are only captured in literature with hardly any practical implementation in LSPMSM designs. Since both transient and steady-state operations need to be considered in the design of LSPMSMs, there is clearly a need to develop a transient synchronization analysis tool that can be integrated into mainstream electromagnetic simulation software.

This paper presents the development of a time-efficient transient synchronization analysis tool for use with ANSYS Electronics Desktop software environment, which determines the critical inertia factor ($x_{cr}$), a figure of merit for the synchronization capability for a LSPMSM design. The remainder of the paper is organized as follows: In Section 2, the electromagnetic torque characteristics of the LSPMSM during transient synchronization process is first described, followed by the a discussion of recent development of analytical synchronization determination methods. In Section 3, different variants of synchronization torque equations and analytical synchronization methods are compared and evaluated in order to identify most suitable equations and methods for the software tool development. The detailed steps of software design and implementation is given in Section 4. The application example of the developed software tool is demonstrated in Section 5. Relevant conclusions are drawn in Section 6.

## 2. Synchronization Analysis of LSPMSMs

With both magnets and cage winding in the rotor of a LSPMSM, there is an inherent competition of space between them. This requires judicious arrangement of the cage winding and PM array within a rotor in order to realize a good design. As a result, a variety of rotor topologies have been created. Some common rotor designs can be observed in Figure 1. In comparison with IMs, the manufacturing of LSPMSMs are more costly, particularly for more complex topologies such as the V-type and W-type designs (Figure 1b,c). These additional costs arise from both the expensive PM materials and the added mechanical complexity of the interior ducts for hosting the PMs. However, a more prevalent problem across all rotor topologies is the synchronization capability—and related critical inertia—of a candidate design [15].
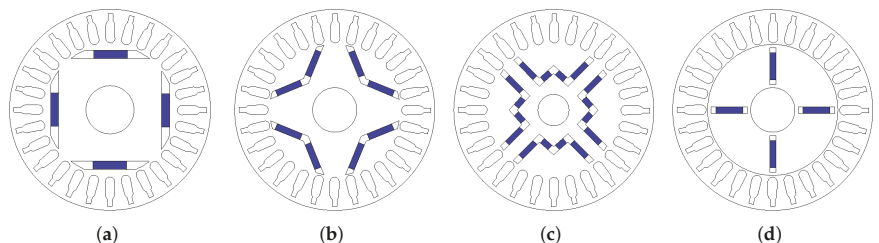


**Figure 1.** Various LSPMSM rotor layouts: (**a**) radial-type; (**b**) V-type; (**c**) W-type; (**d**) spoke-type.

### 2.1. Electromagnetic Torque Characteristics

To better understand the synchronization capabilities of a LSPMSM design, the electromagnetic torque components present at all stages of the synchronization process and their interactions need to be understood. A visual representation of these torque components during the asynchronous operation can be seen in Figure 2.
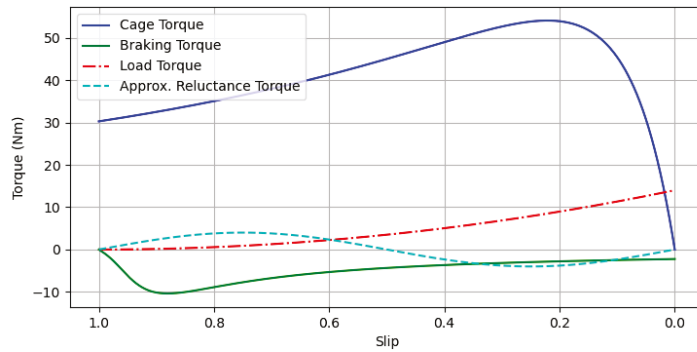
**Figure 2.** Various torque components during the asynchronous operation of a LSPMSM.

### 2.1.1. Braking Torque

The braking torque, sometimes also called the magnet torque, is the torque component contributed during start-up by the PMs. The magnets induce current in the stator at a frequency of $(1-s)f$, which negatively affect synchronization capabilities [16,17]. The analytical braking torque equation is given by (1).

$$T_b = -\frac{mpE_0^2 R_1}{2\pi f} \cdot \frac{[R_1^2 + (1-s)^2 X_q^2](1-s)}{[R_1^2 + (1-s)^2 X_q X_d]^2} \tag{1}$$

where $E_0$ is the induced back-EMF, $R_1$ is the stator resistance, and $X_d$ and $X_q$ are the direct and quadrature axis synchronous reactances, respectively. While the volume of magnets impacts braking torque greatly (as shown in Figure 3), it also plays an important role to the power factor of a LSPMSM at steady-state.
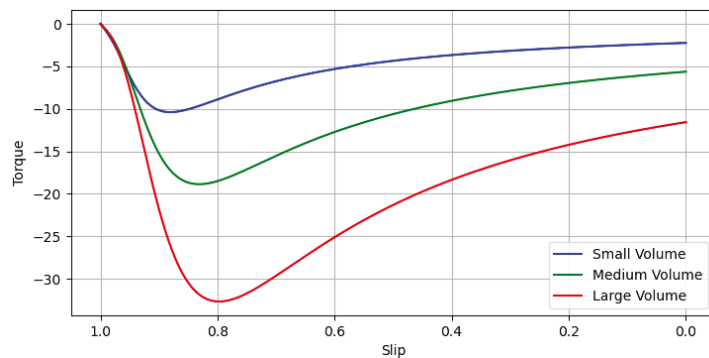


**Figure 3.** Braking torque for various magnet volumes.

### 2.1.2. Cage and Reluctance Torque

In literature the cage torque of a LSPMSM is often treated the same as that of standard squirrel-cage IMs [8]. However, as explained in [17], owing to the non-symmetric magnetic circuit in a LSPMSM rotor, the rotating magnetic field created by rotor current may be decomposed into two counter-rotating fields. The positive sequence rotating field of the rotor winding results in an asynchronous torque while the negative sequence rotating field leads to a reluctance torque component, which hinders the synchronization process for $s < 0.5$ and aids it for $s > 0.5$ [17].

To avoid unnecessary complexity, the reluctance torque is sometimes lumped in together with the cage torque to form a combined equation [9]. Since different approaches

are used in literature to represent cage torque of LSPMSMs, it is necessary to compare and evaluate them.

### 2.1.3. Pulsating Torque

Apart from the cage torque and braking torque, which are essentially average torque components, there are other pulsating torque components that are resulted from the interaction of rotor and stator rotating fields of different speed and the slotting effects. These pulsating torque components are functions of load angle $\delta$ and often included in the synchronization analysis [18,19]. However, there are also published work that neglects the pulsating component entirely [20]. As the oscillations contributed by the pulsating torques are known to impact synchronization capabilities [14], it seems unwise to neglect the effect of these torque components.

### 2.2. Analytical Synchronization Methods

The dynamic performance of LSPMSM is mainly concerned with the starting process of the machine. Owing to the existence of PMs in the rotor, the starting of the LSPMSM is more complicated than that of the IM. Furthermore, during the starting process the $d$- and $q$-axis armature reaction reactance vary with time due to the influence of magnetic saturation. Some researchers use a combination of analytical representation and finite element modelling for the synchronization analysis [10,21], which, while yielding more accurate solutions, is time consuming and not suitable for design optimization purposes.

Recently, there are some new developments of the analytical synchronization analysis methods, which are based on the classical approaches by Miller and Honsinger [18,22]. Amongst others, the energy-based analytical approaches by Rabbi et al. [8] and Chama et al. [9], and the time-domain method by Chama et al. [9] are the most representative. To facilitate further discussion in the paper, these methods are referred hereinafter as Energy method (Rabbi et al.), Energy method (Chama et al.), and Time-domain method (Chama et al.), respectively.

For all the three methods, the analytical representation of the instantaneous torque $T_i$ is established from a design's parameters, which is a combination of the torque components described in Section 2.1 and represented by (2).

$$T_i(s, \delta) = T_p(\delta) + T_c(s) + T_b(s) - T_l(s) \tag{2}$$

where $T_p$ refers to pulsating torque. Subsequently, the instantaneous torque $T_i$ follows the equation of motion in the slip-load angle plane, captured in (3).

$$-\frac{J\omega_s^2}{p} \cdot s\frac{ds}{d\delta} = T_i(s, \delta) \tag{3}$$

Further treatment of (3) is where analytical approaches differ.

### 2.2.1. Energy Method (Rabbi et al.)

The treatment of (3) by Rabbi et al. [8] is focused around approximating the last pole slip of the instantaneous torque. Initially, slip is set to 0, with the aim of solving the equation $T_i(0, \delta) = 0$. For a majority of cases, this results in two solutions as shown in Figure 4, namely the load angle $\delta_s'$ that is the load angle for which the motor reaches synchronous speed for the first time, and $\delta_s$ that binds the domain in which the critical slip $s_{cr}$ will be found. The critical slip is the local maximum situated between $\delta_s'$ and $\delta_s$.

Then, using the value found for $\delta_s'$, the last pole slip is approximated as $s = s_{cr} \sin\frac{1}{2}(\delta_s' - \delta)$ in order to find $s_{cr}$. Mathemtically, this is conducted by solving $T_i(s, \delta_s' - \pi) = 0$ as shown in Figure 5. With $\delta_s'$ and $s_{cr}$ acquired, the required kinetic energy $E_{scr}$ to pull the motor into synchronization is calculated using (4).

$$E_{scr} = \int_{s_{cr}}^{0} -\frac{1}{p}J\omega_s^2 s \, ds = \frac{1}{2p}J\omega_s^2 s_{cr}^2 \tag{4}$$
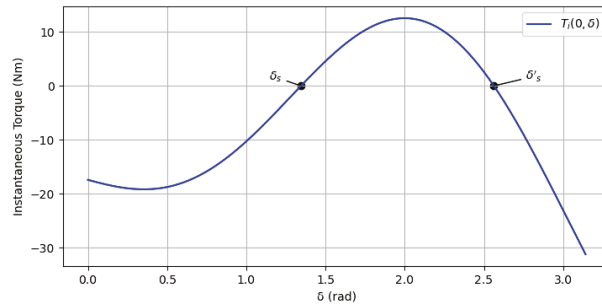
**Figure 4.** Finding $\delta'_s$.
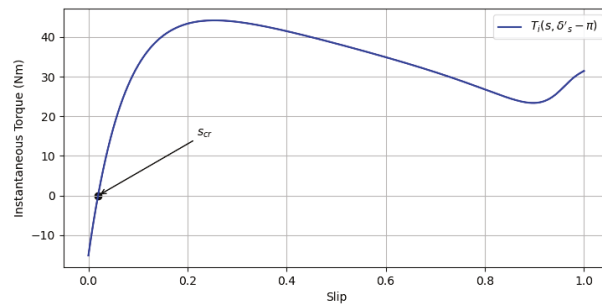


**Figure 5.** Finding the critical slip.

The approximated synchronization energy $E_{syn}$, or the energy actually provided by the instantaneous torque, is calculated using (5).

$$E_{syn} = \int_{\delta'_s - \pi}^{\delta'_s} T_i\left(s_{cr}\sin\frac{1}{2}(\delta'_s - \delta), \delta\right) d\delta \tag{5}$$

When the apparent rotor kinetic energy $E_{syn}$ matches the required pull-in energy $E_{scr}$, the critical inertia $J_{cr}$ is reached, which is the largest system inertia a motor design can successfully synchronize. Using (4) and (5), $J_{cr}$ can be formulated as (6). Furthermore, by normalizing the critical inertia to the rotor inertia, the critical inertia factor $x_{cr}$ can be defined, which can be very useful to quantify the synchronization capability in the design process.

$$J_{cr} = \frac{2pE_{syn}}{s_{cr}^2\omega_s^2} \tag{6}$$

2.2.2. Energy Method (Chama et al.)

The energy-based method by Chama et al. [9] once again starts off by forming the equation of motion (3) from the instantaneous torque. Instead of relying on any approximations, the equation of motion is rewritten into the form seen in (7); an implicit, nonlinear ordinary differential equation (ODE).

$$\frac{ds}{d\delta} = -\frac{p}{J\omega_s^2 s}T_i(s, \delta) = f(s, \delta) \tag{7}$$

Instead of approximating the last pole slip, as proposed by Rabbi et al. [8], the energy-based method proceeds to solve the ODE using the implicit Runge–Kutta–Fehlberg method. The advantages of this ODE solver is its high order of convergence. However, the ODE can be solved by other numerical methods for ODEs as well, such as the backward differentiation formula (BDF) or the Gauss–Radau method. The choice for ODE method to be

used depends on the stiffness of the problem at hand, and thus further comparison will be performed in Section 4.2.2.

The ODE, when solved, establishes the slip as a function of load angle, an example of which can be seen in Figure 6. From this direct resolution of the ODE, $\delta'_s$ and $s_{cr}$ can be obtained.
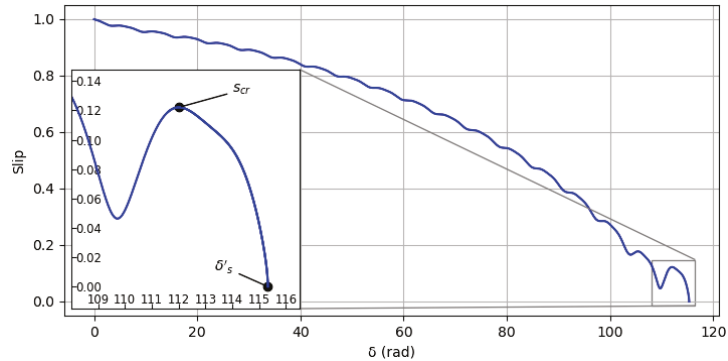


**Figure 6.** Slip as a function of $\delta$.

With these values readily available, $E_{scr}$ and $E_{syn}$ can be calculated and compared again. In the case of $E_{scr}$, the method used by Chama et al. is essentially the same as that of Rabbi et al., i.e., (4). Given the fact that the slip has been established as a function of load angle, the approximation present in (5) is not necessary anymore. Instead, (8) can be used to compute $E_{syn}$, where $s_{cr} = s(\delta_{scr})$.

$$E_{syn} = \int_{\delta_{scr}}^{\delta'_s} T_i(s(\delta), \delta)\, d\delta \tag{8}$$

Once again, when $E_{syn} \geq E_{scr}$, the candidate design synchronizes.

### 2.2.3. Time-Domain Method (Chama et al.)

The time domain model presented by Chama et al. [9] takes a slightly different approach. The equation of motion (3) is formulated into a transient variation taking the form of (9) and (10), where $\omega_{rm}$ represents the motor speed in rad/s and $\theta$ represents the rotor angle in radians.

$$J\frac{\partial \omega_{rm}}{\partial t} = T_i(s, \theta) \tag{9}$$

$$-\frac{1}{p}J\omega_s^2 s\frac{\partial s}{\partial \theta} = T_i(s, \theta) \tag{10}$$

Given the relationship between motor speed and slip $\omega_{rm} = \frac{\omega_s(1-s)}{p}$, and expressing $\frac{\partial s}{\partial \theta}$ as $\frac{\partial s}{\partial t}\frac{\partial t}{\partial \theta}$, (9) and (10) can be algebraically transformed into the initial value problem seen below. This system of equations can also be solved using any implicit ODE method over any desired period of time.

$$\frac{\partial s}{\partial t} = -\frac{p}{J\omega_s}T_i(s, \theta)$$

$$\frac{\partial \theta}{\partial t} = s\omega_s$$

Once the solution to the ODE has been computed, the motor's speed versus time graph can be extracted. Two cases can arise: The first case being when synchronization

occurs, resulting in the motor's speed settling around its rated speed $n_{rated}$. The second case arising when the motor fails to synchronize; the speed oscillating below rated speed. Both cases are visualized in Figure 7.
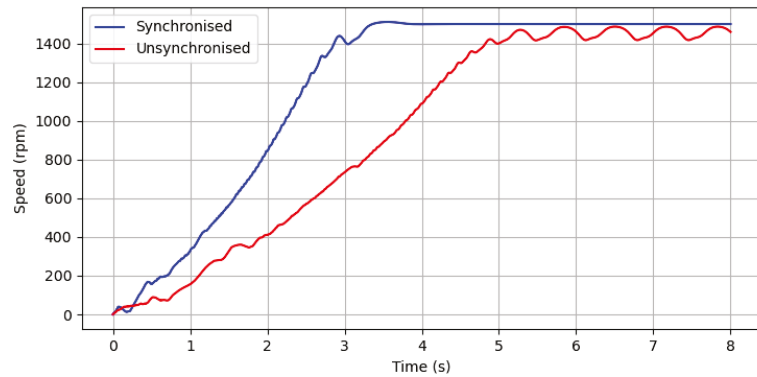


**Figure 7.** Speed vs. time graphs for a synchronized and un-synchronized motor.

To mathematically determine whether this synchronization process has occurred, the average speed $\overline{n_{rm}}$ and gradient of the average speed $\overline{n'_{rm}}$ of the tail end of the generated graphs can be calculated. If the following conditions hold, then synchronization occurs.

$$|\overline{n_{rm}} - n_{rated}| \leq 10^{-2}$$
$$\overline{n'_{rm}} \leq 10^{-2}$$

### 3. Appraisal of Analytical Synchronization Equations and Methods

In order to identify most suitable analytical synchronization equations and methods to be implemented in the software tool, the analytical methods described in Section 2.2 are compared and evaluated in this section. To facilitate the subsequent comparison, the set of torque components will be standardized and individually examined. A number of LSPMSM candidate designs with different rotor topologies (radial, V-type, W-type and spoke-type) are created in ANSYS Electronics Desktop for test and verification purposes. The details of these designs can be found in Figure A1.

*3.1. Cage Torque Equations*

To determine the most appropriate cage torque equation for a general use case, ANSYS Electronics Desktop was used to generate the cage torque curves of the aforementioned LSPMSM designs. This provides the benchmark cage torque characteristics that various analytical formulae strive to replicate.

Three different equations selected for comparison are from Soulard et al. [19], Rabbi et al. [8], and Chama et al. [9]. The required machine parameters for the analytical cage torque curve are extracted from the ANSYS RMxprt and summarized in Table A1.

Figure 8 shows a cage torque comparison for a radial-type rotor design. To compare these cage torque curves more generally, each analytical cage torque curve was then subtracted from the ANSYS-generated benchmark cage torque curve, and the average of their discrepancy was calculated. This was conducted for each candidate machine design in the aforementioned test set. The average torque difference for the 12 test machines can be seen in Figure 9. A condensed box plot data of Figure 9 is shown in Figure 10, summarizing the medium, minimum, maximum, and interquartile range for each analytical cage torque equation.
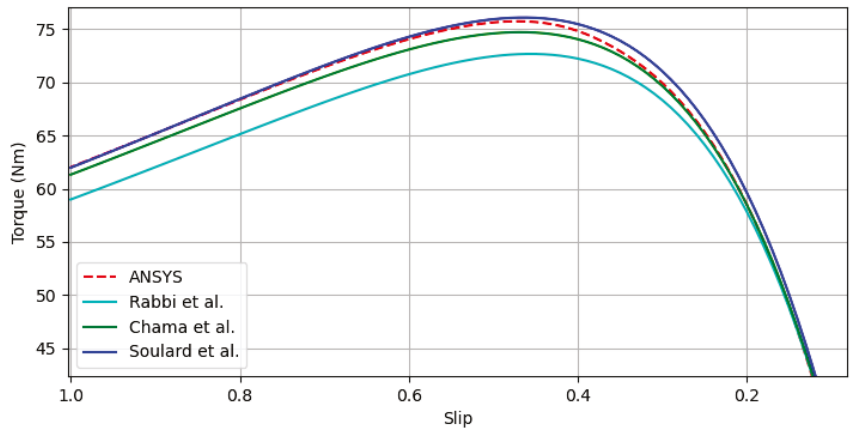
**Figure 8.** Various (Rabbi et al. [8], Chama et al. [9], Soulard et al. [19]) analytical cage torque curves for the Radial 1 design.
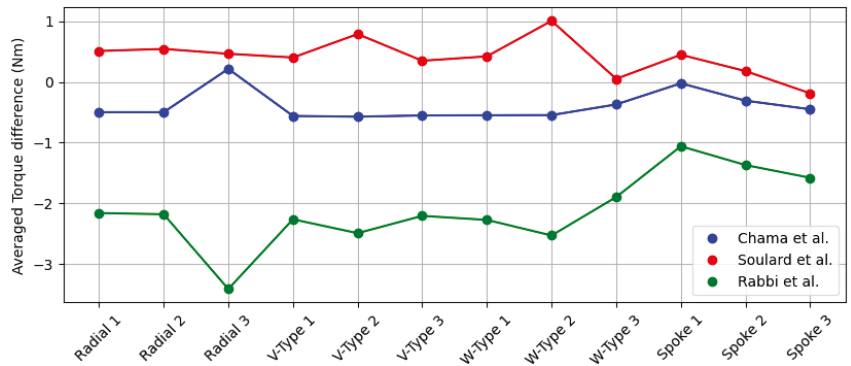


**Figure 9.** Average torque difference of various (Rabbi et al. [8], Chama et al. [9], Soulard et al. [19]) analytical $T_c$s from target $T_c$ for each motor design.

It is evident that the cage torque equations presented by Chama et al. [9] and Soulard et al. [19] compare favorably with that of Rabbi et al.'s [8]. When comparing the equations by Chama et al. and Soulard et al., Figure 10 highlights that Chama et al.'s cage torque equation is much more consistent over a variety of designs, with only one outlier in the form of the Radial 3 design.

Furthermore, closer inspection of Figure 8 reveals that Chama et al.'s [9] analytical cage torque equation tends to approximate the target cage torque curve better in the region nearing $s = 0$; closer to synchronization. This is confirmed by the box plot in Figure 11, which only takes the latter half of synchronization into account. Soulard et al.'s [19] equation approximates better near the region $s = 1$; the start of the synchronization process.

For determining synchronization capabilities of LSPMSM designs, the region between asynchronous and synchronous operation is of utmost importance. Therefore, the analytical cage torque Equation (11) used by Chama et al. [9] appears to be a good option.
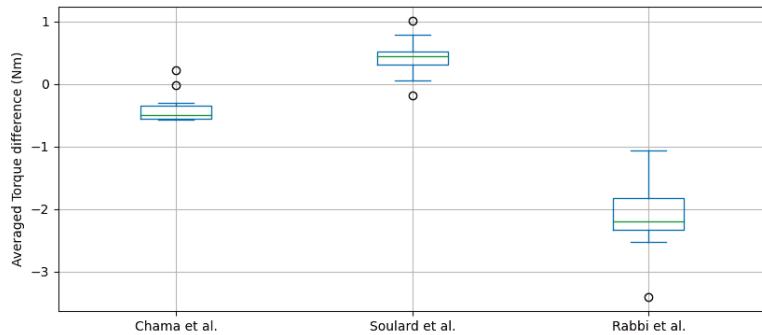
**Figure 10.** Box plot of average torque difference of various (Rabbi et al. [8], Chama et al. [9], Soulard et al. [19]) analytical $T_c$ equations from target $T_c$ for the design set.
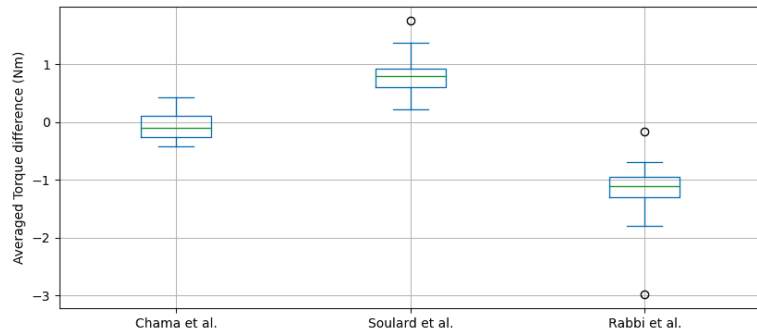


**Figure 11.** Box plot of average torque difference of various (Rabbi et al. [8], Chama et al. [9], Soulard et al. [19]) analytical $T_c$ equations from target $T_c$ for the region $0.5 > s \geq 0$ for the design set.

$$T_c = \frac{mp}{2\pi f} \cdot \frac{sR_2'V_{ph}^2}{(sR_1 + c_1R_2')^2 + s^2(X_1 + c_1X_2')^2} \tag{11}$$

where the factor $c_1$ is given by $c_1 = 1 + \frac{X_1}{X_m}$.

### 3.2. Pulsating Torque

The direct comparison of various pulsating torque equations found across literature to a benchmark pulsating torque curve generated by a FE program such as ANSYS Electronics Desktop is unfortunately impossible, seeing as isolating this component is not feasible.

However, an alternative approach can be taken. Firstly, the instantaneous torque is created from the selected best suited equations, i.e., (1) for $T_b$, (11) for $T_c$, and (12) for $T_l$ will be used to populated (13).

Since LSPMSMs are often used for constant speed operation such as in pumps, compressors, and fans [23], for the sake of simplicity, a general fan load torque curve will be used in this study, which takes the form seen in (12).

$$T_l = T_{rated}(1 - s)^2 \tag{12}$$

This leaves only $T_p$ to be varied, where analytical pulsating torque equations from Soulard et al. [19], Rabbi et al. [8], and Tang [17] can be inserted for comparison.

$$T_i(s, \delta) = T_p(\delta) + T_c(s) + T_b(s) - T_l(s) \tag{13}$$

To form a basis for comparison, a transient FE synchronization simulation is first conducted using ANSYS Maxwell for a LSPMSM design. Then the following steps are performed:

- extract time-varied slip $s(t)$ and rotor angle $\theta(t)$ curves from ANSYS Maxwell;
- approximate load angle $\delta(t)$ from rotor angle $\theta(t)$;
- select $T_p$ equation for comparison and create $T_i(s(t), \delta(t))$ by inserting extracted $s(t)$ and $\delta(t)$;
- compare analytical $T_i$ curve to actual ANSYS Maxwell $T_i$ curve.

Following these steps, Figure 12 was created for the pulsating analytical equations mentioned above.

Unlike Soulard et al. [19], Tang [17] and Rabbi et al.'s [8] analytical formulae correctly meet the target curve once synchronisation has occurred and can be argued for. Tang's [17] $T_p$ seems to result in a curve more accurately representing the magnitude of the initial instantaneous torque, while Rabbi et al.'s [8] $T_p$ seems to be a better fit nearing the region of synchronization.

For this reason, both $T_p$ equations will be carried forward into the analytical methods comparison in Section 3.3. To simplify notation, Tang's [17] $T_p$ will be hence referred to as $T_{pa}$ and Rabbi et al.'s [8] will be referred to as $T_{pb}$. The equations for $T_{pa}$ and $T_{pb}$ are given in (14) and (15), with the individual components listed in Appendix B.1.

$$T_{pa} = T_{pa1} \sin \delta + T_{pa2} \cos \delta + T_{pa3} \sin 2\delta + T_{pa4} \cos 2\delta \tag{14}$$

$$T_{pb} = T_{pb0} + T_{pb1} \sin \delta + T_{pb2} \sin 2\delta + T_{pb3} \cos \delta + T_{pb4} \cos 2\delta \tag{15}$$
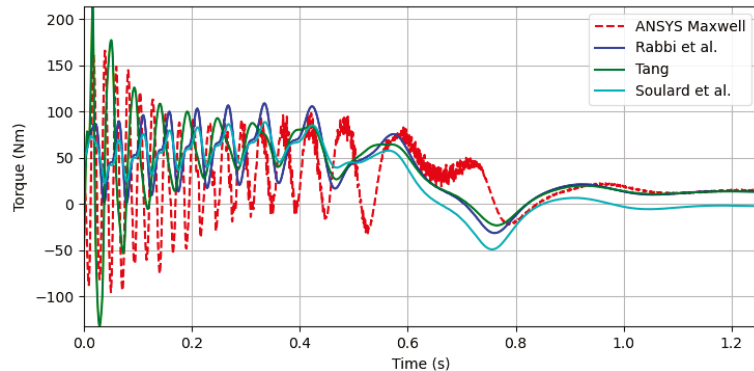


**Figure 12.** $T_i$ for various (Rabbi et al. [8], Tang [17], Soulard et al. [19]) $T_p$ cases.

*3.3. Analytical Methods*

When comparing different analytical synchronization methods mentioned in Section 2.2, two factors will be considered. Firstly, the consistency/accuracy of the method in determining the critical inertia factor, and secondly, any additional resulting outcomes which might prove meritorious to a designer.

3.3.1. Critical Inertia Factor

In order to compare the critical inertia factors produced by each method, the actual critical inertia factors of the test machines need to be determined. This was conducted through a binary search approach using transient FE analysis. The values determined by this process can be seen in the column labelled "FEM" in Table 1 and represent the target which the analytical methods aim to meet. For the three different analytical methods, each method follows a somewhat different approach for the critical inertia factor ($x_{cr}$) determination. Rabbi et al.'s method, mentioned in Section 2.2.1, determined $x_{cr}$ using (6), while both Chama et al. methods used a linear search approach. The linear search approach

was implemented by simply increasing the load inertia by a factor, until this factor fails synchronization; the factor before that is $x_{cr}$.

The results of this comparison can be seen in Table 1. While accuracy is of some importance, a consistent trend in increase/decrease of $x_{cr}$ seen across a cluster of machines is much more so. This is due to the fact, that when a designer makes a design change, the critical factor should accurately reflect the resulting impact on $x_{cr}$ as well. Additionally, if the trend is not obeyed, $x_{cr}$ would be of little use in the cost function of an iterative design optimization procedure. In Table 1, a cluster of green represents where a trend was correctly followed, while a cluster of pink represents where it was not.

**Table 1.** $x_{cr}$ determined by various analytical methods for the machine set.

| | | Chama et al. (Time) | | Chama et al. (Energy) | | Rabbi et al. | |
|---|---|---|---|---|---|---|---|
| **Design** | **FEM** | $T_{pa}$ | $T_{pb}$ | $T_{pa}$ | $T_{pb}$ | $T_{pa}$ | $T_{pb}$ |
| Radial 1 | 44 | 110 | 52 | 111 | 52 | 213 | 69 |
| Radial 2 | 40 | 112 | 49 | 113 | 50 | 225 | 67 |
| Radial 3 | 93 | 0 | 66 | 0 | 66 | 556 | 44 |
| V-Type 1 | 55 | 114 | 57 | 114 | 58 | 193 | 72 |
| V-Type 2 | 39 | 120 | 40 | 121 | 40 | 306 | 58 |
| V-Type 3 | 58 | 110 | 60 | 111 | 60 | 175 | 72 |
| W-Type 1 | 65 | 121 | 60 | 122 | 60 | 218 | 77 |
| W-Type 2 | 48 | 122 | 31 | 124 | 31 | 386 | 47 |
| W-Type 3 | 164 | 200 | 158 | 201 | 158 | 174 | 120 |
| Spoke 1 | 48 | 59 | 42 | 59 | 42 | 67 | 42 |
| Spoke 2 | 45 | 42 | 34 | 43 | 34 | 38 | 28 |
| Spoke 3 | 152 | 199 | 154 | 200 | 154 | 131 | 72 |

From Table 1 it is clear, that for use across a variety of different rotor topologies, both of Chama et al.'s methods with $T_{pb}$ (Equation (15)) are the most fitting to accurately determine the trend of $x_{cr}$. While $T_{pa}$ demonstrates the correct trend for some rotor design and method combinations, the predicted critical inertia values are much less comparable than when $T_{pb}$ is used.

### 3.3.2. Influence of an ANSYS Electronics Bug to $X_{cr}$ Determination

While Table 1 demonstrates Chama et al.'s analytical methods correctly following the $x_{cr}$ trend for the V-Types, W-Types, and Radial Types, there are cases (e.g., Radial 3) which show a large difference between the FEM and analytically predicted $x_{cr}$ values. It was later found that a certain geometry conversion bug in ANSYS Electronics Desktop is largely responsible for this discrepancy.

One of such cases is demonstrated in Figure 13, where Figure 13a,c display two RMxprt LSPMSM designs with the only difference of 0.01 mm in PM thickness. While the RMxprt model layouts look identical, the respective Maxwell-2D FEM models seen in Figure 13b,d distinctly vary, as the red circles highlight. Clearly, for the 4.58 mm case, the cage slot was accidentally shifted by 1-slot pitch.

The time-domain method (Chama et al.) predicts a critical inertia factor of 60 for both designs from their RMxprt models. However, because of the unexpected slot shifting, the actual critical inertia factors, as determined through FE analysis in ANSYS Maxwell, differ greatly. The actual $x_{cr}$ for the 4.59 mm case is 58, very close to the analytically predicted $x_{cr}$. For the 4.58 mm case on the other hand, where the alignment was shifted, the actual $x_{cr}$ is 32, far from what was predicted for it by the analytical model and thus disturbing the trend.
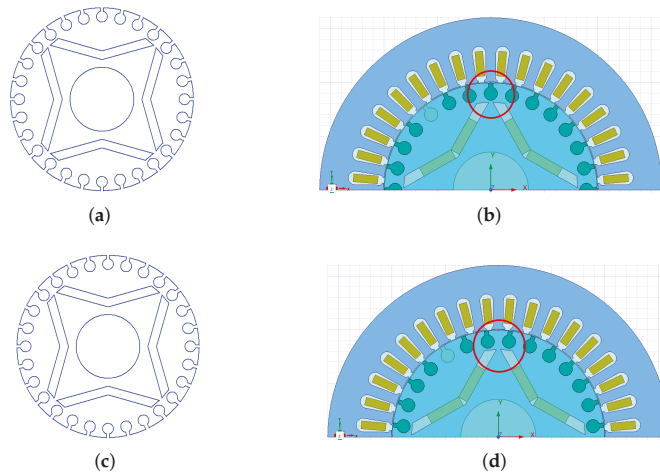
**Figure 13.** Geometry conversion bug found in ANSYS Electronics Desktop. (**a**) ANSYS RMxprt geometry (PM thickness 4.58 mm); (**b**) generated ANSYS Maxwell model for (**a**); (**c**) ANSYS RMxprt geometry (PM thickness 4.59 mm); (**d**) generated ANSYS Maxwell model for (**c**).

### 3.3.3. Computational Aspects

During the creation of Table 1, the computational time to calculate the critical factors of all machines was noted, and can be seen in Table 2. The energy approach by Chama et al. is most time consuming among the three methods. The computational time of a specific method may not be a major concern for a single-run critical inertia factor analysis. However, it is critically important when the analysis is used in a multi-objective, highly iterative optimization procedure.

**Table 2.** Computational time to determine test machine's $x_{cr}$ per method.

| Type of Method | Time (s) |
| --- | --- |
| Time-Domain Method (Chama et al.) | 33.667 |
| Energy Method (Chama et al.) | 450.852 |
| Energy Method (Rabbi et al.) | 0.500 |

Computationally, Rabbi et al.'s energy method outperforms both Chama et al.'s methods greatly. This is because Rabbi et al.'s method only focuses on the last pole slip and uses a sinusoidal approximation to estimate $x_{cr}$ with (6). Chama et al.'s methods on the other hand take the entire asynchronous region into account and rely on linearly increasing the multiplier factor to determine $x_{cr}$, which is a far more computationally intensive approach. However, the energy method by Rabbi et al. fails to consistently predict the critical inertia factor trend (see Table 1). The time-domain method (Chama et al.) appears to be the best option, given the fact that it correctly predicts the critical inertia factor trend while at the same time not being too time demanding. Thus, it will be implemented in the multi-objective optimization procedure in Section 5. Note that all the computer simulations in this paper were conducted on a PC with Intel Core i7-3700 CPU 3.4 GHz, 16 GB RAM running 64-bit Windows 10.

## 4. Software Design

*Python* was selected as the programming language for this development. Given its maturity and prevalence for scientific use, a variety of libraries to perform such tasks exist, the most notable being *SciPy*. In addition, a variety of graphical user interfacing (GUI) libraries exist as well, such as *Tkinter* and *PyQt*. The language also allows for compilation into executable files, thus meeting all necessary criteria for the development.

### 4.1. Overall Layout

Although the time-domain method (Chama et al.) has been identified as the most appropriate method to be implemented by the program, it would be beneficial to also include the energy-based methods in the implementation. This can be useful when a designer wants additional confirmation for a factor or graph produced by the time-based method. To accommodate these multiple methods, a facade structural pattern approach—as described in [24]—will be used. This facade will control a single "solver" class which, in turn, will interface with the various methods.

The solver class controls which methods are used, which $x_{cr}$ approach is taken, and which parameters are passed between GUI and synchronization method. A list of all input and output parameters the solver class controls can be seen in Figure 14.
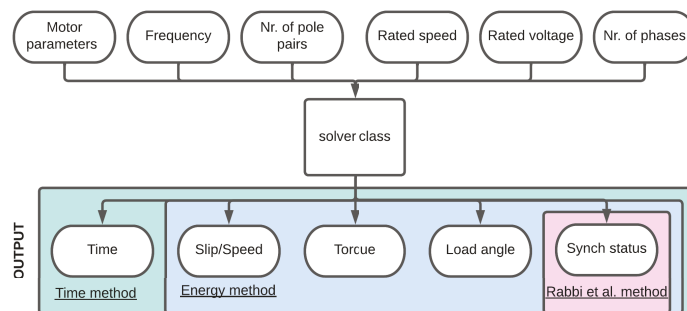


**Figure 14.** Input and output parameters managed by solver class.

### 4.2. Implementation of Methods

The methods as a whole are implemented as functions, with the required machine values being passed as arguments. Seeing as all methods require for the creation of $T_i$, as outlined in Section 2.2, the instantaneous torque equation is captured in a nested function, with parameters $s$ and $\delta$. Implementing the instantaneous torque as a function will allow for a variety of different actions to be performed on it.

#### 4.2.1. Energy Method (Rabbi et al.)

The steps needed for the energy method (Rabbi et al.) are summarized in the flowchart below (Figure 15), where steps 1 and 2, as highlighted in yellow, require root finding algorithms. For this purpose, SciPy's *root* function is used, with the $T_i$ function as implemented in Section 4.2 passed as argument. Step 3's $E_{syn}$ requires functional integration, which is performed using SciPy's *quad* function. $E_{scr}$ is simply computed, and the final return value of the process is the Boolean value defined by $E_{syn} \geq E_{scr}$. This value is passed to the "solver" class, with the facade updating accordingly.
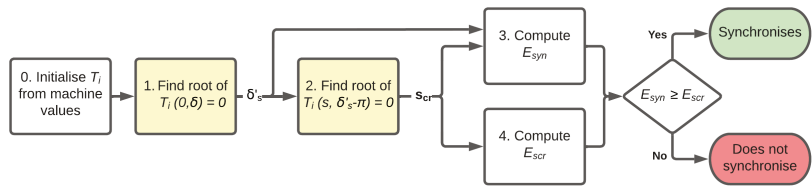
**Figure 15.** Flowchart implementing the energy method (Rabbi et al.).

4.2.2. Energy Method (Chama et al.)

The steps needed for the energy method (Chama et al.) can be seen in Figure 16. Step 1 requires solving the ODE seen in (7). While Chama et al. recommend solving this with the Runge–Kutta–Fehlberg method (RK45), by choosing to use SciPy's *solve_ivp* function, other approaches can be considered as well.

Table 3 compares the critical inertia factors $x_{cr}$ found by using FEM and different ODE solver methods such as the recommended RK45, Radau IIA, backward differentiation formula (BDF), and combined Adams and BDF method (LSODA). All of these are methods specifically aimed at numerically integrating implicit ODE equations.

From the table, the proposed RK45 method seems to deviate from the target $x_{cr}$ values the most, especially for the V-Type 3 and W-Type 3 designs. While the other methods fall relatively close in terms of $x_{cr}$ predicted, when it comes to computational time taken greater variation can be observed across the various methods. Table 4 summarizes the run-times for the different ODE methods, with the adaptive LSODA method executing noticeably faster than its peers.
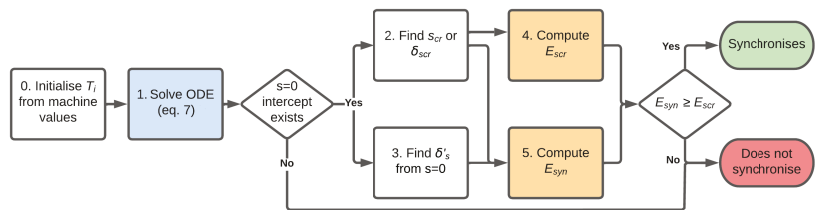


**Figure 16.** Flowchart implementing the energy method (Chama et al.).

Since the ODE solver returns the slip versus load angle curve as a numerical array, steps 4 and 5—highlighted in orange in Figure 16—cannot be performed in the same manner as steps 3 and 4 were for the energy method (Rabbi et al.) in Figure 15. Thus for this numerical integration step, SciPy's *Simpson* method is used.

However, while the energy comparison step $E_{syn} \geq E_{scr}$ is mentioned in Chama et al.'s method, the paper also mentions that one advantage of the direct resolution of the ODE is that it allows for "easily recognizing the synchronization capability of the machine" [9] as well. This happens when the slip never reaches zero, and thus Figure 16 can be reduced to the flowchart seen in Figure 17.

This has no impact on the $x_{cr}$ determination, but in combination with a binary search approach, reduces the computational time of the LSODA ODE solver to 161.292 s.

**Table 3.** $x_{cr}$ determined by the energy method (Chama et al.) with various ODE solvers compared to target $x_{cr}$ determined through FEM.

| Type of LSPMSM | FEM | RK45 | Radau | BDF | LSODA |
|---|---|---|---|---|---|
| Radial 1 | **44** | 55 | 51 | 52 | 52 |
| Radial 2 | **40** | 53 | 49 | 50 | 49 |
| Radial 3 | **93** | 72 | 66 | 66 | 66 |
| V-Type 1 | **55** | 61 | 57 | 58 | 58 |
| V-Type 2 | **39** | 43 | 39 | 40 | 40 |
| V-Type 3 | **58** | 81 | 59 | 59 | 60 |
| W-Type 1 | **65** | 65 | 60 | 60 | 60 |
| W-Type 2 | **48** | 34 | 31 | 31 | 31 |
| W-Type 3 | **164** | 0 | 157 | 158 | 109 |
| Spoke 1 | **48** | 60 | 42 | 42 | 42 |
| Spoke 2 | **45** | 50 | 34 | 34 | 34 |
| Spoke 3 | **152** | 175 | 154 | 154 | 154 |

**Table 4.** Computational time to determine $x_{cr}$ using the energy method (Chama et al.) with different ODE solvers.

| ODE Method | Time (s) |
|---|---|
| RK45 | 402.086 |
| Radau | 550.320 |
| BDF | 450.852 |
| LSODA | 276.545 |
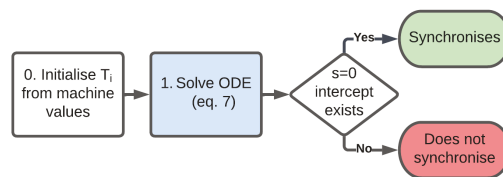


**Figure 17.** Adapted flowchart implementing the eneryg method (Chama et al.).

### 4.2.3. Time-Domain Method (Chama et al.)

The steps needed for the time-domain method (Chama et al.) are illustrated in Figure 18. Step 1, solving the ODE problem, is performed using the LSODA method, which was identified as the fastest ODE solver in Section 4.2.2. For fast computation of the averages $\overline{n_{rm}}$ and $\overline{n'_{rm}}$ (steps 3 and 4 in purple), the last section of the generated curve and its derivative are accumulated using the built-in Python function *sum* and then divided using the function *len*. The aforesaid derivative is calculated using SciPy's *splev* function.
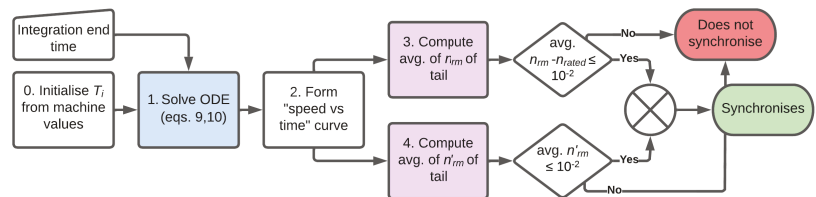


**Figure 18.** Flowchartimplementing the time-domain method (Chama et al.).

To determine the critical inertia factor, a binary search approach is taken, following the logic seen in Figure 19. The minimum factor is initialized as 0, and the maximum factor as 500. This maximum value was chosen, seeing as it provides enough headroom above the commonly observed $x_{cr}$ values, but not too far above to slow the search process down substantially. While the linear search approach used earlier in Section 3.3.3 took 33.667 s, determination of the same 12 $x_{cr}$ values was reduced to 18.822 s with the binary search method.
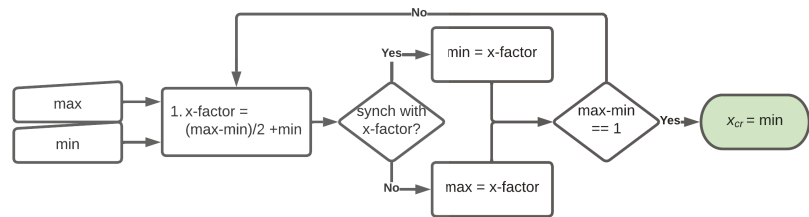


**Figure 19.** Flowchart implementing binary search approach to determine $x_{cr}$.

*4.3. Graphical User Interface*

To implement the graphical user interface for the program, the PyQt library was used. This library was chosen, seeing as it allows for a drag-and-drop design process using the *Qt Designer* software tool. *Qt Designer* then produces a *.ui file, which can be easily loaded with a specific PyQt function. This approach allows for independent changing of user interface elements, without needing to change the code behind them.

The interface is divided into 4 areas. The first area is used for inputting the machine's parameters needed to perform the analytical synchronization process. While these fields will be automatically filled by the script mentioned in Section 4.4, allowing the user access to these fields makes the program free-standing from ANSYS Electronics. The fields available in this area are for machine parameters $E_0$, $X_d$, $X_q$, $R_1$, $X_1$, $R_2$, $X_{2d}$, $X_{2q}$, and $J_{rot}$. Additionally, the area adjusts dynamically to support a slider and button used for loading specific machine parameters after the additional features mentioned in Section 4.3.1 are used.

The second area contains the selection of the synchronization method to be used, along with any additional input fields. These input fields are for testing synchronization with a specific rotor inertia multiplier, testing for synchronization with specific additional load inertia, and for selecting whether the critical inertia factor should be determined. Additionally, the solver area adjusts to incorporate supplementary input fields dependent on solver type. An example of this can be seen in Figure 20.

The third area is used for displaying the various graphs generated by the methods. The selection for available graphs also adjusts according to the synchronization method selected earlier. The graphing area is implemented by using an embedded *Matplotlib* area. A "Clear Graphs" button is implemented as well, allowing for comparison of curves for different input values. The legend is auto-generated depending on whether a constant inertia value or a rotor inertia multiplier is added.

The last area is an output logging area, showing the critical inertia factor (if the option is selected) and whether synchronization has occurred. Any additional information is also displayed here.

All areas combine into the final layout seen in Figure 21. The width of the machine parameter and solver areas is fixed, while the shared space between console and graph area can be adjusted in order to meet the user's needs.
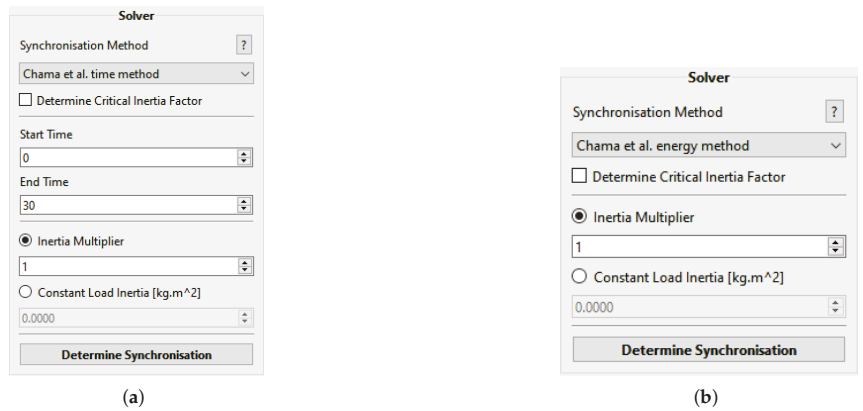
**Figure 20.** Solver UI area adjusting by solver method: (**a**) solver area for the time-domain method (Chama et al.), (**b**) solver area for the energy method (Chama et al.).
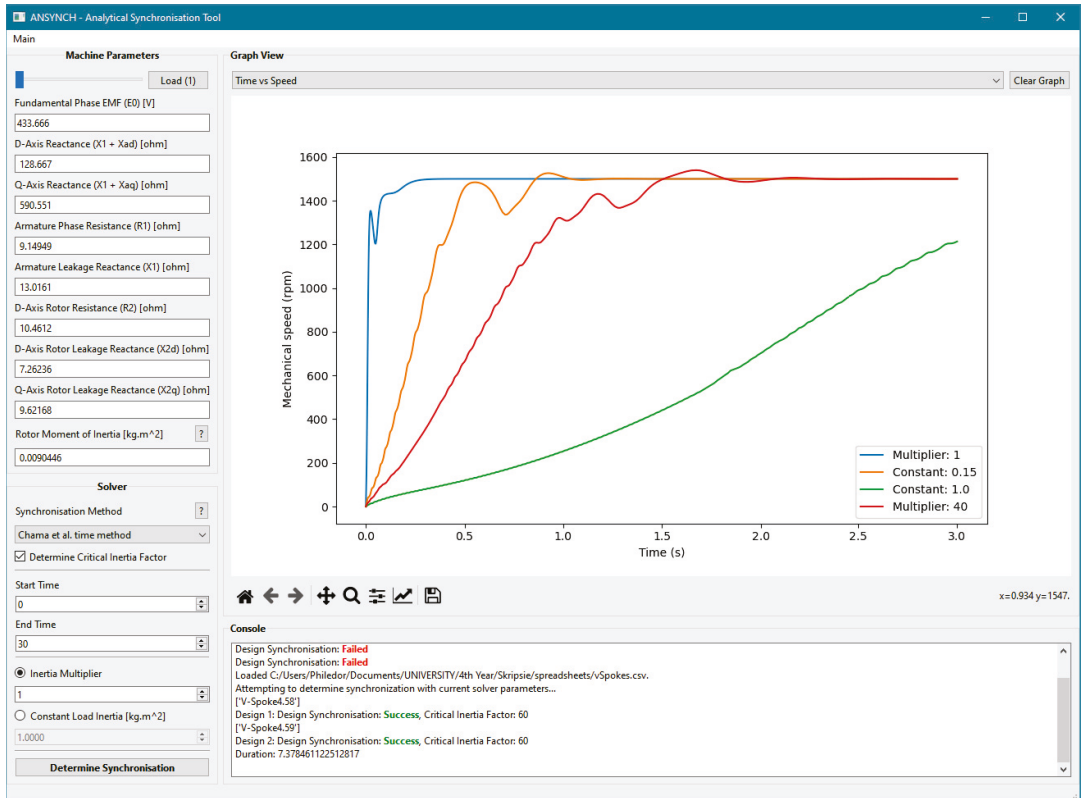


**Figure 21.** Final GUI layout of analytical synchronization program.

4.3.1. Additional Features

Three additional features (namely, *Loading, saving, and batch testing*) are added for convenience sake, accessible through the top left menu button as can be seen in Figure 22a. All three features use comma-separated values (CSV) files.

The "Load Parameters" feature loads a number of machines' parameters from a CSV file into the program. Using the slider in the top right as seen in Figure 21, these various parameters can then be loaded into their respective fields for testing.

The "Save Parameters" feature appends the machine parameters currently present in the program to a CSV file of choice. If no file exists, a new one can be created.

The "Batch Test Parameters" feature uses the current solver settings to test the synchronization and—if selected—critical inertia factor of machine parameters contained within a CSV file. These machine parameters are also loaded into the program, similar to the load feature, and the output of the tests is shown in the console.

To remove clutter from the program, some of the input settings listed in Figure 14 have been extracted to an "Additional Settings" dialog. The dialog is accessible through the menu, as can be seen in Figure 22a, and opens the window seen in Figure 22b. Common machine settings occupy these fields by default.
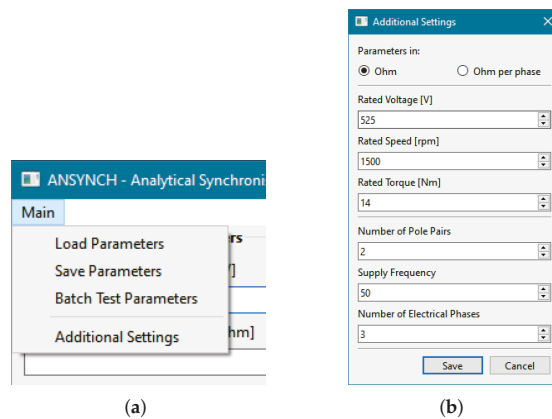


**Figure 22.** Additional program features: (**a**) menu connecting to additional features and settings, (**b**) additional settings window.

*4.4. Integration with ANSYS Electronics Desktop*

ANSYS Electronics Desktop offers programming capabilities through their scripting environment [25]. Further, ANSYS specific libraries are also accessible. The scripting environment implements IronPython 2.7, which implements Python 2.7 and NET framework 4.0. Thus, scripts can be coded in either Python or VBScript. Considering Python's additional flexibility, all scripts were written in Python. These scripts can also be added to ANSYS Electronics Desktop as "Tools", allowing them to be run from the "Tools" tab by the press of a button.

To integrate the program flawlessly into ANSYS Electronics Desktop, a script was written which:

- Extracts available machine parameters from an RMxprt design.
- Approximates inaccessible machine parameters.
- Launches and automatically populates the analytical synchronization program with the required values.

4.4.1. Extraction of Available Parameters

The scripting library's functionality is limited, seeing as it is mainly used to change ANSYS specific features. As a result, no direct function is present in the scripting environment for accessing the solution data of an RMxprt design.

In order to overcome this problem, the "output variable" commands of the scripting environment are exploited. The script contains the names of the desired machine parameters, as listed in ANSYS. Then, for each parameter, the following steps are taken:

- create temporary output variable using *CreateOutputVariable*;
- obtain output variable value using *GetOutputVariable*;
- delete temporary output variable using *DeleteOutputVariable*.

Using this approach, eight of nine parameters needed for analytical synchronization determination can be extracted from an RMxprt design. These parameters are $E_0$, $X_d$, $X_q$, $R_1$, $X_1$, $R_2$, $X_{2d}$, and $X_{2q}$.

4.4.2. Approximation of Inaccessible Parameters

The machine parameter that cannot be extracted from RMxprt is the rotor inertia $J_{rot}$, which is only available after a Maxwell design was created from the RMxprt design. To make the analytical synchronization program standalone, an approximation of the combined rotor inertia is computed and then passed to the program. This approximated inertia value can still be changed by the user in the program.

The rotor's inertia can be modeled as three separate inertia values. Firstly, the rotor body inertia, which contains the cage windings, magnets, and the steel rotor core. Secondly, the end rings' combined inertia which are located at the ends of the rotor. Lastly, the shaft inertia internal to the rotor.

Using the scripting function *GetPropertyValue* allows for retrieval of the rotor inner radius $r_i$ and rotor outer radius $r_o$. Using the approach mentioned in Section 4.4.1, the total cage bar mass, total magnet mass, and rotor steel mass can be extracted as well. The rotor body is then approximated as a hollow cylinder, with the cage bar mass being approximated at the edge of the rotor radius. The end rings are also approximated as two hollow cylinders. The shaft is assumed to be roughly 1.75 times longer than the rotor body length, which can be extracted from RMxprt.

The final rotor inertia approximation is then computed using (16).

$$J_{rot} = J_{body} + J_{rings} + J_{shaft} \tag{16}$$

The approximate rotor inertias are compared to the rotor inertias generated by ANSYS Maxwell in Table 5, which shows that the approximated rotor inertias are reasonably close to the ones generated by Maxwell.

**Table 5.** Approximate and Maxwell rotor inertias.

| Machine | Maxwell $J_{rot}$ (kgm$^2$) | Approximated $J_{rot}$ (kgm$^2$) | % Difference |
|---|---|---|---|
| Radial 1 | 0.0090446 | 0.0081215 | 10.21 |
| Radial 2 | 0.0090446 | 0.0081178 | 10.25 |
| Radial 3 | 0.0090446 | 0.007938 | 12.23 |
| V-Type 1 | 0.0090446 | 0.0081899 | 9.45 |
| V-Type 2 | 0.0090446 | 0.0082991 | 8.24 |
| V-Type 3 | 0.0090446 | 0.0081992 | 9.35 |
| W-Type 1 | 0.0090446 | 0.0080894 | 10.56 |
| W-Type 2 | 0.0090446 | 0.0082279 | 9.03 |
| W-Type 3 | 0.0090446 | 0.0077131 | 14.72 |
| Spoke 1 | 0.0090446 | 0.0083418 | 7.77 |
| Spoke 2 | 0.0090446 | 0.0083635 | 7.53 |
| Spoke 3 | 0.0090446 | 0.0077431 | 14.39 |

*4.5. Software Design Summary*

The program described in this section is bundled into an executable using the *pyinstaller* library, after which the path to the executable is linked into the ANSYS script. The script gathers all retrievable parameters as shown in Section 4.4.1, and approximates all inaccessible parameters as described in Section 4.4.2.

The analytical synchronization program is then automatically launched with all parameters passed as system arguments. These arguments are then parsed into the program's machine parameter fields. The aforementioned script can be linked to the 'Tool' bar in ANSYS Electronics Desktop allowing for retrieval, approximation, launching, and parsing to happen with the click of one button.

## 5. Application of the Developed Software Tool

The analytical program developed in Section 4 has the ability to predict the critical inertia factor $x_{cr}$ of a LSPMSM motor design. Using the critical inertia factor as a design objective in a multi-objective design procedure is of interest, but has so far only been achieved through use of the Taguchi method, a low-iteration multi-objective design strategy [14].

Given the developed program's integration with ANSYS Electronics Desktop, this section aims to evaluate the effectiveness of the developed program in a highly iterative, multi-objective optimization procedure using more conventional iterative strategies.

### 5.1. Software Adaptation

In order to be used for this iterative procedure, the developed software tool needs to be adapted for the task at hand: it needs to be as fast as possible. A light-weight version was thus developed, which does not feature the GUI, forces use of the time-domain method (Chama et al.), and returns the critical inertia factor upon completion. Given the simplification present here, it would have been ideal to perform this calculation in the ANSYS scripting environment for even faster speeds. However, due to the scripting environment's restricted nature, no additional libraries can be installed into it, preventing the use of *SciPy* functions.

Initially, the light-weight program was compiled in *Python* directly from its larger counterpart, and then converted into an executable file using the *pyinstaller* library. However, early testing of the program in the iterative process showed that it was still far too slow to be used for a highly iterative procedure. In an attempt to correct this, the light-weight program was rewritten into the *Go* programming language. *Go* was chosen due to the fact that it is designed around speed, easily and cleanly compiles into light-weight executables, and has a growing supplementation of user created libraries. To replace the role *SciPy's* ODE solver played, the *Godesim* library was used. *Godesim* only employs the Runge–Kutta–Fehlberg method at the moment, but as Table 6 demonstrates, this does not cause it to differ too much from it's Python counterpart, and the correct $x_{cr}$ trend is obeyed, making it suitable for the task at hand.

The Go program's execution time proves to be far superior compared to its Python counterpart. Initialization scores and five iterations of the procedure described in Section 5.2 took the Python version 35 min and 17 s, while the Go version only needed 8 min and 26 s.

**Table 6.** Comparing Go and Python ODE solvers for predicting $x_{cr}$.

| Machine | Python LSODA $x_{cr}$ | Go RK45 $x_{cr}$ |
|---|---|---|
| Radial 1 | 52 | 51 |
| Radial 2 | 49 | 49 |
| Radial 3 | 66 | 61 |
| V-Type 1 | 57 | 57 |
| V-Type 2 | 40 | 39 |
| V-Type 3 | 60 | 59 |

**Table 6.** *Cont.*

| Machine | Python LSODA $x_{cr}$ | Go RK45 $x_{cr}$ |
|---|---|---|
| W-Type 1 | 60 | 60 |
| W-Type 2 | 31 | 31 |
| W-Type 3 | 158 | 108 |
| Spoke 1 | 42 | 42 |
| Spoke 2 | 34 | 34 |
| Spoke 3 | 154 | 120 |

*5.2. Differential Evolution Implementation*

Differential evolution (DE) was chosen as the multi-objective optimization procedure to be implemented. DE begins by initializing a starting population with a set number of members. Each member $x$ has a number of features $y$. Then, three members of the population are chosen at random and each of their features are mutated following (17) to produce a mutated member.

$$y_{mutation} = y_{x1} + (y_{x2} - y_{x3}) \qquad (17)$$

Crossover is then performed between the mutated member and a chosen member of the population. This involves, for each feature, generating a random value between 0 and 1 and comparing it to the crossover rate, which was set at 0.5. If the value is greater than the crossover rate, the mutated feature replaces the chosen member's feature. After crossover is completed, the new member's score is generated according to the overall evaluation criterion (OEC), and if it is greater than the chosen member's score, the chosen member is replaced. Each iteration of DE performs mutation, crossover, and comparison for each member of the population.

Ideally, DE would have been performed in ANSYS Electronics Desktop using ANSYS Optimetrics; however, interfacing with Optimetrics for each iteration of the optimization process is not possible. Instead, DE was coded in the scripting environment in Python. Figure 23 demonstrates how these various environments are iteratively used and interact.
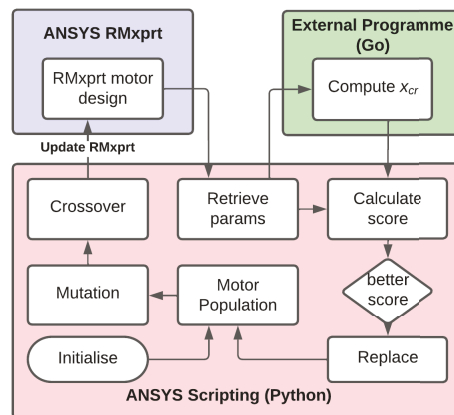


**Figure 23.** The differential evolution process.

Optimization Problem

It is known that there is a competing relationship between the critical inertia factor ($x_{cr}$) and the power factor (*PF*) for the design of a LSPMSM [14], which means finding a design that maximizes both factors is unfeasible. Instead, a trade-off between the two factors can

be found. Thus, the optimization problem has multiple objectives and constraints, which is formulated as follows:

$$\text{Maximize}: \ F(\mathbf{X}) = \sum_{m=1}^{3} \omega_m f_m \tag{18}$$

where **X** represents the vector of geometric variables illustrated in Figure 24, and $f_m$ is populated by the objective functions seen below, which can be weighted differently through $\omega_m$.

$$f_1 = \frac{x_{cr}}{x_{cr\,max}}; \qquad f_2 = \frac{PF}{PF_{max}}; \qquad f_3 = \frac{1}{1 + (P_{out} - P_{rated})^2}$$

The output power $P_{out}$ is included in the optimization problem to ensure a working design. Essentially, $P_{out}$ is a constraint and not in contest with the other objectives. Its weighting is kept as 0.5 in this optimization study.
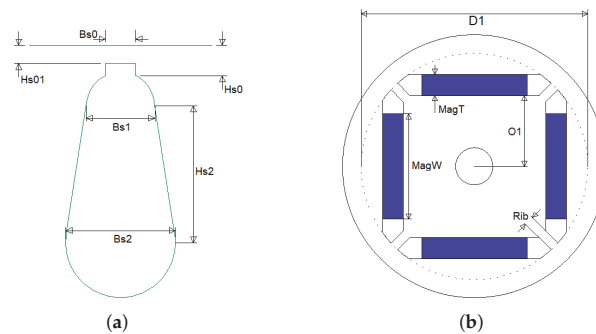


**Figure 24.** Parameters to be varied during optimization: (**a**) available slot parameters, (**b**) available magnet parameters.

*5.3. Parameter Restrictions*

Given the extreme variety of possible rotor layouts, invalid designs are more than likely to be created during crossover and random initialization. While the DE method will simply replace these designs in the next iteration, some software restrictions are implemented as well to limit the occurrence of this happening.

For the DE procedure, the radial rotor topology seen in Figure 1a was chosen, and thus the successive restrictions implemented are specifically for this type. The stator design remains constant, leaving only the slot design and rotor dimensions to be varied. Figure 24a shows the slot parameters which can be varied, while Figure 24b shows the magnet dimensions which can be varied.

Initialization begins by pre-defining a minimum and maximum value for all parameters. These initial minima and maxima are only used during the initialization process, and are then replaced per DE iteration.

Magnet Restrictions

While the slot parameters exhibit no complicated relationships, the magnet parameters do, and thus the order in which magnet parameters are changed matters greatly. The order is determined such that the subsequent parameter restrictions are only dependent on the ones before it. Table 7 summarizes these relationships.

**Table 7.** Restrictions for magnet dimensional parameters.

| Parameters | Minimum | Maximum |
|---|---|---|
| 1. D1 | $2\,r_i$ | $2(r_o - \text{slot depth} - \text{CDG})$ |
| 2. O1 | $r_i$ | D1/2 |
| 3. MagT | $> 0$ | D1/2 − O1 |
| 4. Rib | $\sqrt{2}\left(\text{O1} - \sqrt{\frac{D1}{2}^2 - \text{O1}^2}\right)$ | $\sqrt{2}\text{O1} - 1$ |
| 5. MagW | $> 0$ | Equation (22) |

D1's maximum restriction is defined by the outer rotor radius, slot depth, and cage duct gap (CDG), which was set as 0.1 mm. The CDG ensures that there is at least some gap between D1 and the created slots. The slot depth is calculated using (19).

$$\text{slot depth} = \text{Hs0} + \text{Hs2} + \frac{\text{Bs1}}{2} + \frac{\text{Bs2}}{2} \tag{19}$$

The minimum rib restriction makes sure that the slot in which the magnet sits does not protrude D1. The maximum rib restriction ensures that MagW is not forced to be 0.

The maximum magnet width is restricted by two cases which can arise. The inner case is demonstrated in Figure 25a and thus is restricted by (20). The outer case is demonstrated in Figure 25b and as a result, restricted by (21).



**(a)**      **(b)**
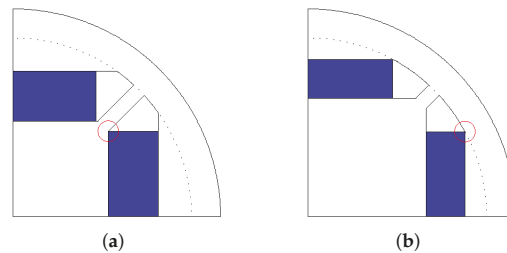
**Figure 25.** Possible magnet width restrictions: (**a**) inner magnet width restriction, (**b**) outer magnet width restriction.

$$\text{innermax} = 2\left(\text{O1} - \sqrt{2}\frac{\text{Rib}}{2}\right) \tag{20}$$

$$\text{outermax} = 2\left(\sqrt{\left(\frac{D1}{2}\right)^2 - (\text{O1} + \text{MagT})^2}\right) \tag{21}$$

$$\text{MagW}_{max} = \min(\text{outermax}, \text{innermax}) \tag{22}$$

These restrictions were coded in the scripting environment. Mutation ignores the maximum and minimum values and simply creates the mutated parameters. Then, crossover is performed first for all slot properties, followed by crossover for the magnet properties in the order seen in Table 7. The minimum and maximum values for each parameter are first calculated from the preceding parameters, after which the mutated value is—if necessary—clamped into its respective range.

*5.4. Optimization Procedure Results*

5.4.1. Initial DE Procedure

The DE procedure described in Section 5.2 was run for 100 iterations, with the OEC set as seen in (18). Given the importance of reaching the desired output power, $\omega_3$ was set as 0.5. For initial demonstration purposes, $\omega_1$ and $\omega_2$ were set as 0.25 each, thus directing the DE process to find a 50/50 balance between the critical inertia factor and the power factor.

$PF_{max}$ is always 1 and from experience $x_{cr\,max}$ was set as 100. The average population score per iteration can be seen in Figure 26, with a clear increase in average score being observable.
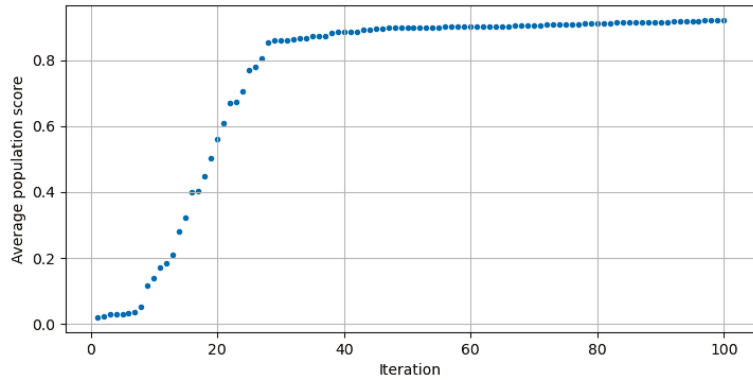


**Figure 26.** Average population score per iteration.

Evolution of both the power factor and critical inertia factor can be observed in Figure 27. Note that the colour map represents when last a machine design was present in an iteration's population. From Figure 27 it is clear that early iterations of the procedure produced designs which predicted a zero critical inertia factor. However, at around iteration 20, designs were created which predicted a low $x_{cr}$. One machine can also be seen with a full zero score during initialization due to an invalid rotor layout. Without the restrictions placed in Section 5.3, a high number of invalid initial designs could occur.
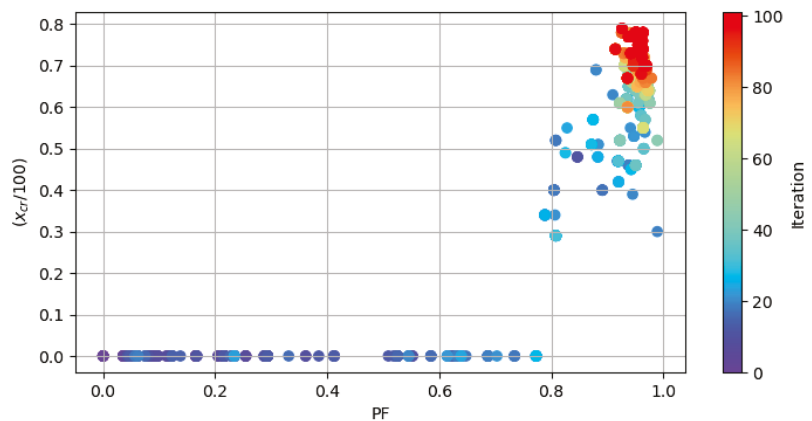


**Figure 27.** Evolution of the power factor and critical inertia factor per iteration.

5.4.2. Varying Weightings

To further test the applicability of the analytical critical inertia factor program for multi-objective optimization, the weightings $\omega_1$ and $\omega_2$ were adjusted to various distributions in order to shift priority between the critical inertia factor and the power factor. $\omega_3$ was kept constant at 0.5.

Figure 28 summarizes later members of the DE populations with these varied weightings. A clear competing relationship between the critical inertia factor and the power factor can be observed. By varying these weightings, designs can be created which prioritize either the critical inertia factor or the power factor. This establishes what is known as a Pareto front, a set of non-dominated solutions a designer can choose from [14]. While some outliers exist, a general trend between critical inertia factor and power factor is observable.
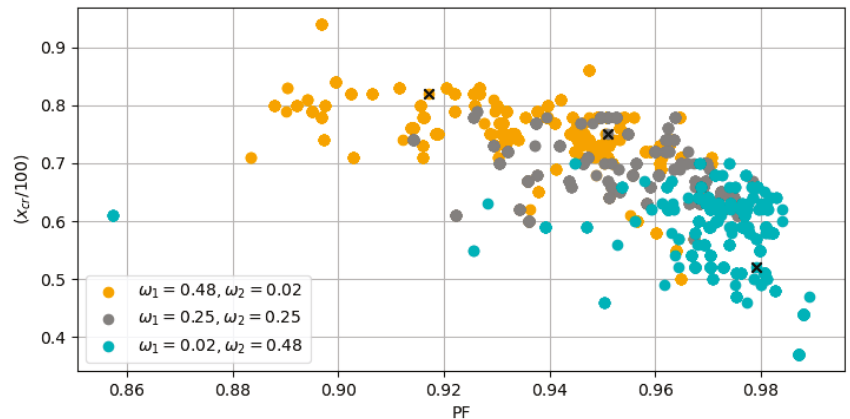


**Figure 28.** Late DE iterations with varied weightings.

5.4.3. Confirmation of Optimized Critical Inertia Factors

To check the validity of the optimization procedure, three different LSPMSM designs (marked by crosses in Figure 28) from differently weighted populations were chosen for comparison, and their actual critical inertia factors were determined by FE analysis. The rotor layouts of the three LSPMSM designs can be seen in Figure 29.
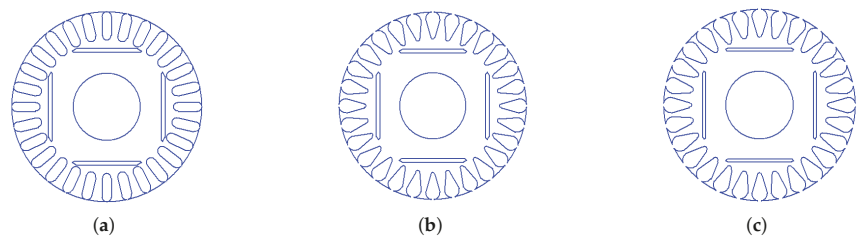


**Figure 29.** Three designs chosen from the DE optimization results for comparison: (**a**) design 1, (**b**) design 2, (**c**) design 3.

The analytically predicted and actual critical inertia factors, as well as power factors, output power, and weightings which produced the designs, are given in Table 8. As can be seen from the table, the predicted $x_{cr}$ values fall short of the actual ones. The bug mentioned in Section 3.3.2 was present in all three designs when their Maxwell 2D models were created. While this distortion of $x_{cr}$ values due to the geometry conversion bug is undesirable, Table 8 demonstrates that the trend set by the analytical program is still maintained, proving the validity of use for the analytical program in the procedure. It may be inferred that a better correlation between the $x_{cr}$ values by analytical method and FE analysis can be expected without the influence of the identified ANSYS bug.

**Table 8.** Critical inertia factors, lifetimes, and scores of DE designs.

|  | Analytical $x_{cr}$ | FEM $x_{cr}$ | $\omega_1$ | $\omega_2$ | *PF* | $P_{out}$ (kW) |
|---|---|---|---|---|---|---|
| Design 1 | 63 | **43** | 0.02 | 0.48 | 0.979 | 2.2 |
| Desing 2 | 75 | **55** | 0.25 | 0.25 | 0.951 | 2.2 |
| Design 3 | 82 | **57** | 0.48 | 0.02 | 0.917 | 2.2 |

5.4.4. Computational Time

While some improvements in computational time were achieved in Section 5.1, performing the process in the ANSYS scripting environment adds to the computational cost greatly. For each machine design tested, the ANSYS model needs to be set and analyzed by ANSYS before the required parameters can be retrieved and the critical inertia factor calculated. On average, one iteration of the DE process took approximately 1.5 min or 6 s per design. Better computational time could be achieved if the program were to be merged with ANSYS Optimetrics, a task currently impossible.

**6. Conclusions**

The work in this paper began by gathering and comparing various methods and equations for determining the synchronization status of LSPMSMS. For synchronization torque equations, (1), (11), and (15) were identified as the most fitting equations. The time-domain method (Chama et al.) was determined to be the best method in terms of computational time and the ability of predicting the critical inertia factor trend.

Using the selected methods, a software tool was created which captured their individual advantages in terms of speed and visual aid. Some useful features were added to broaden the tool's use. Utilizing ANSYS scripting, the software tool was then integrated with ANSYS Electronics Desktop. The script was developed to automatically extract available parameters and to approximate inaccessible ones, providing a seamless interface between ANSYS Electronics Desktop and the analytical synchronization tool.

Given the software tool's ability to quickly determine the critical inertia factor, it was subsequently adjusted to be used in a highly iterative optimization procedure. This involved re-coding it into a programming language more suited for this recursive operation. Next, the optimization method 'differential evolution' was programmed in the ANSYS scripting environment, where the analytical tool and ANSYS RMxprt were employed recursively to successfully perform multi-objective highly iterative optimization for LSPMSMs. The results highlighted the usefulness of the tool's ability to quickly determine a machine's critical inertia factor and how it can be used in conjunction with ANSYS Electronic Desktop software suite to form a multi-objective design optimization procedure for LSPMSMs.

Although the critical inertia factors predicted by both the FEM and the analytical software tool show the same trend and consistency, there are often discrepancies between their values. It was found that a geometry conversion bug of ANSYS Electronics Desktop is most likely the cause. Better correlation between these $x_{cr}$ values may be expected without the influence of this ANSYS bug.

**Author Contributions:** Conceptualization, P.S. and R.-J.W.; methodology, P.S. and R.-J.W.; software, P.S.; validation, P.S. and R.-J.W.; formal analysis, P.S.; investigation, P.S.; resources, P.S. and R.-J.W.; data curation, P.S.; writing—original draft preparation, P.S.; writing—review and editing, P.S. and R.-J.W.; visualization, P.S.; supervision, R.-J.W. All authors have read and agreed to the published version of the manuscript.

**Institutional Review Board Statement:** Not applicable.

**Informed Consent Statement:** Not applicable.

**Conflicts of Interest:** The authors declare no conflict of interest.

## List of Symbols

| Symbols | Definition |
|---|---|
| $s$ | Slip |
| $s_{cr}$ | Critical slip |
| $\delta$ | Load angle (rad) |
| $\theta$ | Rotor angle (rad) |
| $f$ | Frequency (Hz) |
| $\omega_s$ | Electrical synchronous speed (rad/s) |
| $\omega_{rm}$ | Motor rotational speed (rad/s) |
| $\overline{n_{rm}}$ | Average motor rotational speed (rpm) |
| $n_{rated}$ | Motor rated speed (rpm) |
| $x_{cr}$ | Critical inertia factor |
| $J_{cr}$ | Critical inertia |
| $T_b$ | Braking torque (Nm) |
| $T_c$ | Cage torque (Nm) |
| $T_p$ | Pulsating torque (Nm) |
| $T_l$ | Load torque (Nm) |
| $T_{rated}$ | Rated torque (Nm) |
| $T_i$ | Instantaneous torque (Nm) |
| $E_0$ | RMS induced back-EMF (V) |
| $R_1$ | Stator resistance ($\Omega$) |
| $X_1$ | Stator reactance ($\Omega$) |
| $X_d$ | Direct axis synchronous reactance ($\Omega$) |
| $X_q$ | Quadrature axis synchronous reactance ($\Omega$) |
| $R_{2d}$ | Direct axis rotor resistance ($\Omega$) |
| $R_{2q}$ | Quadrature axis rotor resistance ($\Omega$) |
| $R_2'$ | Referred rotor resistance ($\Omega$) |
| $X_{ad}$ | Direct axis reaction reactance ($\Omega$) |
| $X_{aq}$ | Quadrature axis reaction reactance ($\Omega$) |
| $E_{scr}$ | Critical synchronisation energy (J) |
| $E_{syn}$ | Synchronisation energy (J) |
| $PF$ | Power factor |
| $P_{out}$ | Output power (W) |
| $P_{rated}$ | Rated power (W) |

## Appendix A. Test Machine Set

**Table A1.** Test machine parameters.

|  | $E_0$ | $X_d$ | $X_q$ | $R_1$ | $X_1$ | $R_2'$ | $X_2$ |
|---|---|---|---|---|---|---|---|
| Radial 1 | 433.666 | 128.667 | 590.551 | 9.14949 | 13.0161 | 10.4612 | 8.44202 |
| Radial 2 | 449.729 | 125.196 | 590.551 | 9.14949 | 13.0161 | 10.4612 | 8.43316 |
| Radial 3 | 301.781 | 122.485 | 526.218 | 19.542 | 11.4 | 5.46636 | 5.78165 |
| V-Type 1 | 458.604 | 141.214 | 590.551 | 9.14949 | 13.0161 | 10.1826 | 7.56974 |
| V-Type 2 | 479.15 | 106.323 | 590.551 | 9.14949 | 13.0161 | 10.1826 | 7.48063 |
| V-Type 3 | 453.474 | 149.655 | 590.551 | 9.14949 | 13.0161 | 10.1826 | 7.5913 |
| W-Type 1 | 445.096 | 136.028 | 590.551 | 9.14949 | 13.0161 | 9.85417 | 7.83725 |
| W-Type 2 | 497.386 | 93.797 | 590.551 | 9.14949 | 13.0161 | 9.85417 | 7.72939 |
| W-Type 3 | 335.239 | 216.471 | 527.534 | 9.14949 | 12.716 | 5.46636 | 7.6169 |
| Spoke 1 | 436.092 | 206.069 | 590.551 | 9.14949 | 13.0161 | 12.2775 | 7.719285 |
| Spoke 2 | 403.516 | 252.735 | 590.551 | 9.14949 | 13.0161 | 12.2775 | 7.83847 |
| Spoke 3 | 270.129 | 187.855 | 527.534 | 9.14949 | 12.716 | 5.46636 | 7.543815 |
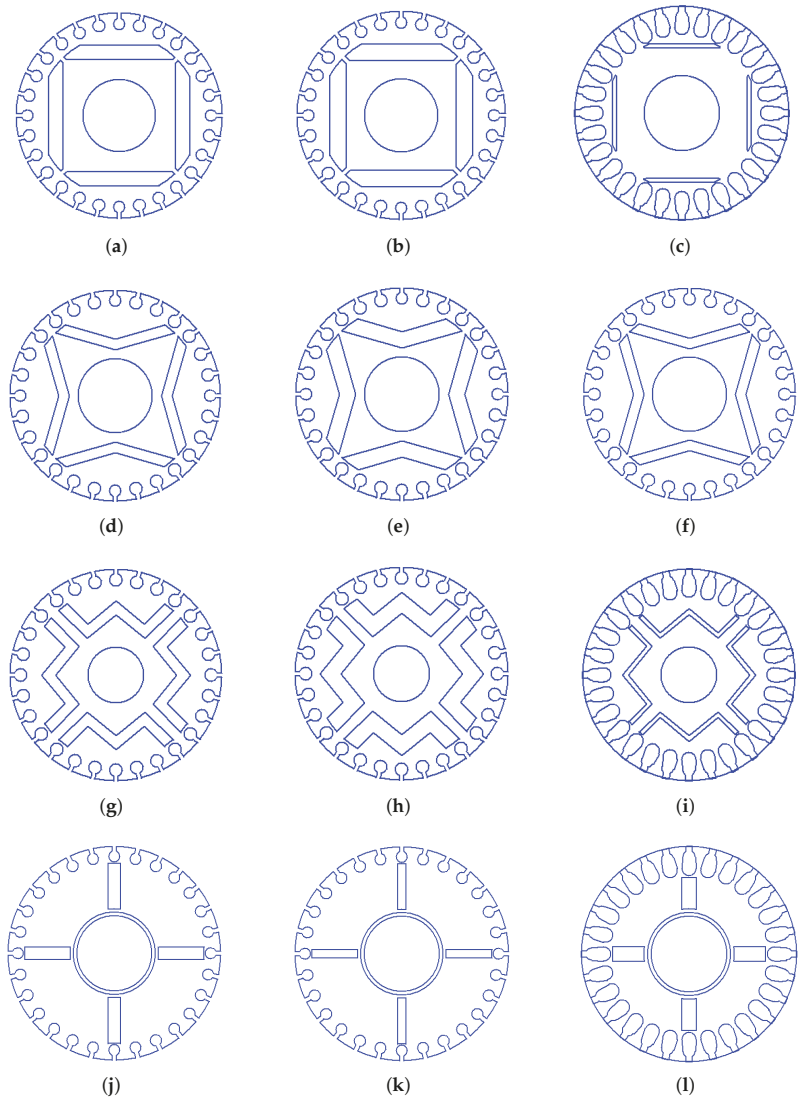
**Figure A1.** Test machine set rotor layouts: (**a**) Radial 1, (**b**) Radial 2, (**c**) Radial 3, (**d**) V-type 1, (**e**) V-type 2, (**f**) V-type 3, (**g**) W-type 1, (**h**) W-type 2, (**i**) W-type 3, (**j**) Spoke-type 1, (**k**) Spoke-type 2, (**l**) Spoke-type 3.

## Appendix B. Detailed Equations

*Appendix B.1. Pulsating Torque Equation Components*

Appendix B.1.1. Tang

$$T_{pa1} = mp(bg' + ha' - de' - f_1c') \tag{A1a}$$

$$T_{pa2} = mp(ce' + ec' - ag' - ga') \tag{A1b}$$

$$T_{pa3} = \frac{mp}{2}(ah + bg - cf_1 - de) \tag{A1c}$$

$$T_{pa4} = \frac{mp}{2}(ce + bh - df_1 - ag) \tag{A1d}$$

$$a = K_{d1}V_{ph}$$

$$b = K_{d2}V_{ph}$$

$$c = K_{q1}V_{ph}$$

$$d = K_{q2}V_{ph}$$

$$e = \frac{V_{ph}}{2\pi f}(a_2K_{d1} + b_2K_{d2})$$

$$f_1 = \frac{V_{ph}}{2\pi f}(a_2K_{d1} - b_2K_{d2})$$

$$g = \frac{V_{ph}}{2\pi f}(c_2K_{q1} + d_2K_{q2})$$

$$h = \frac{V_{ph}}{2\pi f}(c_2K_{q1} - d_2K_{q2})$$

$$a' = -(1-s)^2X_q\frac{E_0}{D_m}$$

$$c' = -(1-s)R_1\frac{E_0}{D_m}$$

$$e' = \frac{X_da' + E_0}{2\pi f}$$

$$g' = \frac{X_qc'}{2\pi f}$$

$$D_m = R_1^2 + X_dX_q(1-s)^2$$

$$K_{d1} = \frac{[R_1 - (1-2s)d_2]f_2 + (1-2s)c_2e_2}{e_2^2 + f_2^2}$$

$$K_{d2} = \frac{[R_1 - (1-2s)d_2]e_2 - (1-2s)c_2f_2}{e_2^2 + f_2^2}$$

$$K_{q1} = \frac{[R_1 - (1-2s)b_2]e_2 - (1-2s)a_2f_2}{e_2^2 + f_2^2}$$

$$K_{q2} = -\frac{[R_1 - (1-2s)b_2]f_2 + (1-2s)a_2e_2}{e_2^2 + f_2^2}$$

$$a_2 = X_d - \frac{s^2X_{ad}^2X_{2d}}{R_{2d}^2 + (sX_{2d})^2}$$

$$b_2 = \frac{sX_{ad}^2R_{2d}}{R_{2d}^2 + (sX_{2d})^2}$$

$$c_2 = X_q - \frac{s^2X_{aq}^2X_{2q}}{R_{2q}^2 + (sX_{2q})^2}$$

$$d_2 = \frac{s X_{aq}^2 R_{2q}}{R_{2q}^2 + (s X_{2q})^2}$$

$$e_2 = R_1^2 + s R_1 (b_2 + d_2) + (1 - 2s)(a_2 c_2 - b_2 d_2)$$

$$f_2 = s R_1 (a_2 + c_2) - (1 - 2s)(a_2 d_2 + b_2 c_2)$$

Appendix B.1.2. Rabbi et al.

$$T_{pb0} = \frac{m p R_1 X_q}{\pi f (R_1^2 + X_d X_q)^2} \left[ (X_d - X_q) \left( \frac{V_{ph}^2}{2} - 1 + E_0^2 \right) - E_0^2 \left( \frac{R_1^2}{X_q} + X_d \right) \right] \tag{A2a}$$

$$T_{pb1} = \frac{m p E_0 V_{ph}}{2\pi f (R_1^2 + X_d X_q)^2} [(X_d - X_q)(R_1^2 - X_d X_q) + (R_1^2 + X_d X_q) X_d] \tag{A2b}$$

$$T_{pb2} = \frac{m p V_{ph}^2}{4\pi f (R_1^2 + X_d X_q)^2} [(X_d - X_q)(X_d X_q - R_1^2)] \tag{A2c}$$

$$T_{pb3} = \frac{m p E_0 V_{ph} R_1}{2\pi f (R_1^2 + X_d X_q)^2} [(R_1^2 + X_d X_q) - 2 X_q (X_d - X_q)] \tag{A2d}$$

$$T_{pb4} = \frac{m p V_{ph}^2 R_1}{4\pi f (R_1^2 + X_d X_q)^2} [(X_d - X_q)(X_d + X_q)] \tag{A2e}$$

## References

1. De Almeida, A.T.; Ferreira, F.J.T.E.; Fong, J.A. Standards for Efficiency of Electric Motors. *IEEE Ind. Appl. Mag.* **2011**, *17*, 12–19. [CrossRef]
2. Stoia, D.; Cernat, M.; Jimoh, A.G.; Nicolae, D. Analytical design and analysis of Line-Start Permanent Magnet Synchronous Motors. In Proceedings of the IEEE AFRICON Conference, Nairobi, Kenya, 23–25 September 2009; pp. 1–7. [CrossRef]
3. Oshurbekov, S.; Kazakbaev, V.; Prakht, V.; Dmitrievskii, V.; Goman, V.V. Energy Efficiency Analysis of Fixed-Speed Pump Drives with Various Types of Motors. *Appl. Sci.* **2019**, *9*, 5295. [CrossRef]
4. Palangar, M.F.; Soong, W.L.; Bianchi, N.; Wang, R.J. Design and Optimization Techniques in Performance Improvement of Line-Start Permanent Magnet Synchronous Motors: A Review. *IEEE Trans. Magn.* **2021**, *57*, 1–14. [CrossRef]
5. Niaz Azari, M.; Mirsalim, M. Performance Analysis of a Line-start Permanent Magnet Motor with Slots on Solid Rotor Using Finite-element Method. *Electr. Power Compon. Syst.* **2013**, *41*, 1159–1172. [CrossRef]
6. Mingardi, D.; Bianchi, N. FE-aided analytical method to predict the capabilities of line-start synchronous motors. In Proceedings of the 2014 IEEE Energy Conversion Congress and Exposition (ECCE), Pittsburgh, PA, USA, 14–18 September 2014; pp. 5123–5130. [CrossRef]
7. Vannini, A.; Simonelli, C.; Marfoli, A.; Papini, L.; Bolognesi, P.; Gerada, C. Modelling, Analysis, and Design of a Line-Start Permanent Magnet Synchronous Motor. In Proceedings of the 2022 International Conference on Electrical Machines (ICEM), Valencia, Spain, 5–8 September 2022; pp. 834–840. [CrossRef]
8. Rabbi, S.F.; Rahman, M.A. Critical Criteria for Successful Synchronization of Line-Start IPM Motors. *IEEE J. Emerg. Sel. Top. Power Electron.* **2014**, *2*, 348–358. [CrossRef]
9. Chama, A.; Sorgdrager, A.; Wang, R.J. Analytical synchronization analysis of line-start permanent magnet synchronous motors. *Prog. Electromagn. Res.* **2016**, *48*, 183–193. [CrossRef]
10. Yan, B.; Yang, Y.; Wang, X. A semi-numerical method to assess start and synchronization performance of a line-start permanent magnet synchronous motor equipped with hybrid rotor. *IET Electr. Power Appl.* **2021**, *15*, 487–500. [CrossRef]
11. Zhou, Y.; Huang, K.; Sun, P.; Dong, R. Analytical Calculation of Performance of Line-Start Permanent-Magnet Synchronous Motors Based on Multidamping-Circuit Model. *IEEE Trans. Power Electron.* **2021**, *36*, 4410–4419. [CrossRef]
12. Farooq, H.; Bracikowski, N.; La Delfa, P.; Hecquet, M. Modelling of Starting and Steady-State performance of Line Start Permanent Magnet Synchronous Motor using Reluctance Network. In Proceedings of the 2022 International Conference on Electrical Machines (ICEM), Valencia, Spain, 5–8 September 2022; pp. 226–231. [CrossRef]
13. Palangar, M.F.; Mahmoudi, A.; Kahourzade, S.; Soong, W.L. Optimum Design of Line-Start Permanent-Magnet Synchronous Motor Using Mathematical Method. In Proceedings of the 2020 IEEE Energy Conversion Congress and Exposition (ECCE), Detroit, MI, USA, 11–15 October 2020; pp. 2064–2071. [CrossRef]
14. Sorgdrager, A.J.; Wang, R.J.; Grobler, A.J. Multiobjective Design of a Line-Start PM Motor Using the Taguchi Method. *IEEE Trans. Ind. Appl.* **2018**, *54*, 4167–4176. [CrossRef]
15. Hassanpour Isfahani, A.; Vaez-Zadeh, S. Line start permanent magnet synchronous motors: Challenges and opportunities. *Energy* **2009**, *34*, 1755–1763. [CrossRef]

16. Sorgdrager, A. Development of Line-Start Permanent Magnet Synchronous Machines Using the Taguchi Method. Ph.D. Thesis, Stellenbosch University, Stellenbosch, South Africa, 2017.
17. Tang, R.Y. *Modern Permanent Magnet Machines: Theory and Design*; China Machine Press: Beijing, China, 1997.
18. Miller, T.J.E. Synchronization of Line-Start Permanent-Magnet AC Motors. *IEEE Power Eng. Rev.* **1984**, *PER-4*, 57–58. [CrossRef]
19. Soulard, J.; Nee, H.P. Study of the synchronization of line-start permanent magnet synchronous motors. In Proceedings of the Conference Record of the 2000 IEEE Industry Applications Conference, Thirty-Fifth IAS Annual Meeting and World Conference on Industrial Applications of Electrical Energy (Cat. No. 00CH37129), Rome, Italy, 8–12 October 2000; Volume 1, pp. 424–431. [CrossRef]
20. Elistratova, V.; Hecquet, M.; Brochet, P.; Vizireanu, D.; Dessoude, M. Analytical approach for optimal design of a line-start internal permanent magnet synchronous motor. In Proceedings of the 2013 15th European Conference on Power Electronics and Applications (EPE), Lille, France, 2–6 September 2013; pp. 1–7. [CrossRef]
21. Jędryczka, C.; Knypiński, U.; Demenko, A.; Sykulski, J.K. Methodology for Cage Shape Optimization of a Permanent Magnet Synchronous Motor Under Line Start Conditions. *IEEE Trans. Magn.* **2018**, *54*, 1–4. [CrossRef]
22. Honsinger, V.B. Permanent Magnet Machines: Asynchronous Operation. *IEEE Trans. Power Appar. Syst.* **1980**, *PAS-99*, 1503–1509. [CrossRef]
23. Behbahanifard, H.; Sadoughi, A. Line Start Permanent Magnet Synchronous Motor Performance and Design: A Review. *J. World's Electr. Eng. Technol.* **2015**, *4*, 58–66.
24. Gamma, E.; Helm, R.; Johnson, R.; Vlissides, J. *Design Patterns: Elements of Reusable Object-Oriented Software*; Addison-Wesley Professional Computing Series; Pearson Education: London, UK, 1994.
25. ANSYS, Inc. *ANSYS Electronics Desktop: Maxwell Scripting Guide*; ANSYS, Inc.: Canonsburg, PA, USA, 2021.

# Sensorless Control of Dual Three-Phase Permanent Magnet Synchronous Machines—A Review

**Vahid Teymoori [1], Maarten Kamper [1], Rong-Jie Wang [1,\*] and Ralph Kennel [2]**

1   Department of Electrical and Electronic Engineering, Stellenbosch University, Stellenbosch 7600, South Africa
2   Department of Electrical and Computer Engineering, Technical University of Munich,
    80333 Munich, Germany
\*   Correspondence: rwang@sun.ac.za

**Abstract:** This paper presents an overview of various sensorless control methods, with a focus on dual three-phase permanent magnet synchronous machines (DTP-PMSM). Owing to the important role that DTP-PMSMs play in motion-control applications in industry, most academic researchers and industry activists seek to reduce costs and size while increasing the capability and efficiency of motion applications. This has led to an increase in the number of publications about multiphase machines in recent years. The purpose of this article is to review the most important sensorless control techniques, which are divided into two main categories, namely saliency-based control method for low-speed range and model-based control method for high-speed range. Both methods are subdivided into other categories, with a focus on DTP-PMSMs. The methods are compared with each other for the purpose of selecting the most suitable control technique for implementation in applications such as ship propulsion, wind turbines, and aerospace.

**Keywords:** dual three-phase (DTP); model-based techniques; permanent magnet synchronous machine; saliency-based techniques; sensorless control

## 1. Introduction

In recent years, multiphase motor drives have attracted much attention in both academic institutions and industry due to their numerous advantages over typical three-phase drives, such as reduced torque ripple, lower stator current per phase, and enhanced reliability. As a result of these advantages, multiphase drives are especially suitable for high power density and safety-critical applications such as electric cars, electric aircrafts, and ship propulsion.

Different forms of multiphase PMSM drives, such as five-phase, six-phase, and nine-phase, have been addressed in the literature [1–8]. Owing to the absence of the sixth-order pulsating torque, the six-phase system, also known as dual three-phase (DTP), is widely adopted. However, DTP-PMSMs are also known for high current harmonics due to the voltage harmonics caused by inverter nonlinearity and back-EMF harmonics from non-sinusoidal permanent magnet (PM) flux-coupling [9].

DTP-PMSM drives are categorised as symmetrical and asymmetrical based on their winding configuration [10], where asymmetrical six-phase windings are DTP-PMSM drives with two sets of windings that are spatially displaced by 30 degrees electrically, as shown in Figure 1a, while the symmetrical counterpart is displaced by 60 degrees electrically, as shown in Figure 1b. Furthermore, the winding of DTP-PMSMs can be configured with a single neutral or two isolated neutrals, as shown in Figure 2.
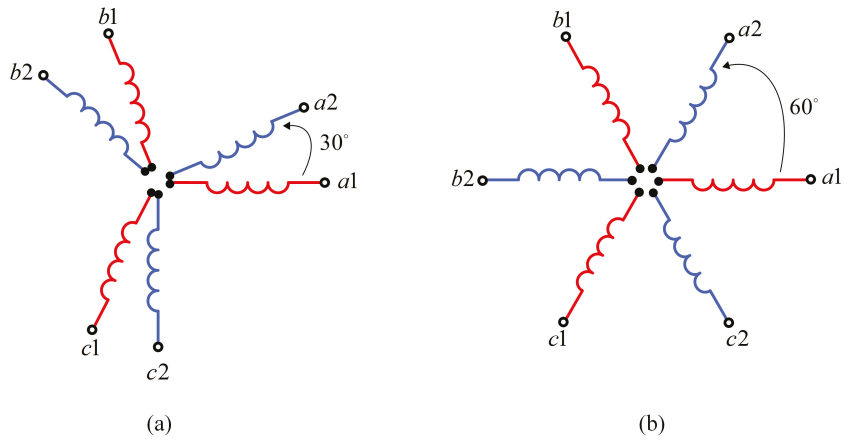
**Figure 1.** Arrangement of winding in DTP-Machine: (**a**) asymmetrical; (**b**) symmetrical.
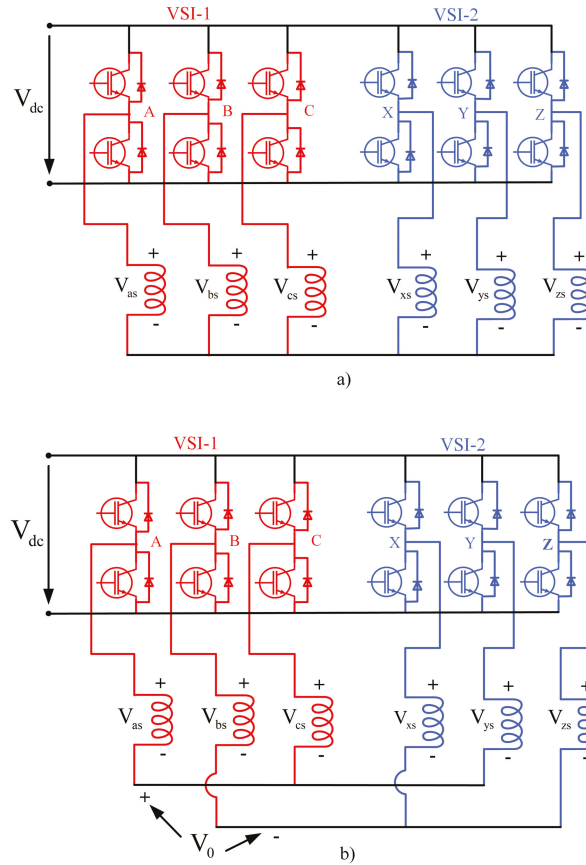


**Figure 2.** Voltage source inverter-fed DTP-PMSM drive with stator winding connection. (**a**) single neutral topology; (**b**) two isolated neutrals topology [11].

Both direct torque control (DTC) and vector control are commonly implemented for permanent magnet motors [11–13]. In direct torque control, the goal is the precise control of the torque, while speed control and transient state control require less consideration. In the vector control strategy, the responses of the steady state and the transient state are controlled primarily.

In Figure 3a, the historical development of sensorless control for PMSMs is illustrated and in Figure 3b the classification of the methods that are used for DTP-PMSMs is described, which is also discussed in Sections 3 and 4. Designing and implementing these control methods require accurate mathematical modelling of the systems, which is usually challenging.
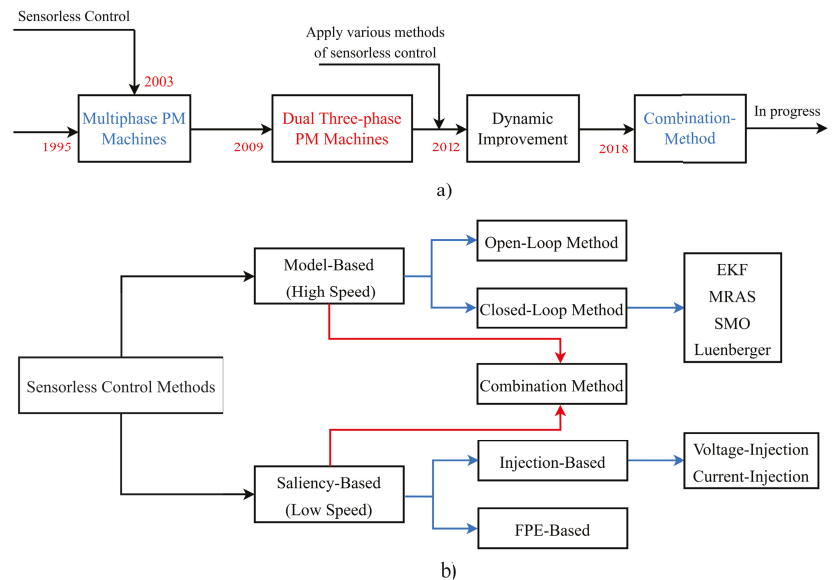


**Figure 3.** (**a**) Historical development of sensorless control for multiphase and DTP-PMSM drives; (**b**) classification of sensorless control.

The absence of mechanical sensors from PMSM control increases the overall system reliability, while decreasing system cost. This makes sensorless control preferable to sensor-based control. In recent years, the development of a wide range of sensorless control systems has gained momentum, the most common of which are model-based approaches and saliency tracking. Based on back-EMF or excitation flux, model-based approaches may be classified into open- and closed-loop techniques. In the open-loop case, the back-EMF of the machine is integrated without any correction term, whereas in the closed-loop case, the difference in estimated and measured quantities is taken into account. The latter approach was initially suggested and implemented in [14]. However, it suffers from a low signal-to-noise ratio due to modelling error, inverter non-linearity, etc. The open-loop approach also often gives poor position estimates at frequencies of less than 1 Hz.

Two methods are used to determine a machine's rotor position via saliency tracking. The first is called *signal injection-based sensorless control*, which uses a continuous high-frequency signal, while the second method is based on fundamental PWM excitation (also known as *FPE-based*), and uses the transient effect of phase currents that are built into the basic PWM cycles. A popular FPE method is called the "INFORM method" [15].

Multiphase electrical machines have been around since the late 1960s as an expansion of variable-speed AC drives [16]. Owing to the increased number of phases in DTP-PMSMs, similar control techniques for three-phase PMSMs are not applicable [14,17,18].

However, given the extra degrees of freedom in DTP-PMSMs, several unique methods for rotor position estimation have been developed, showing some distinct advantages of DTP-PMSMs in the sensorless control domain [19]. Although there are a few recent review studies on the sensorless control of PMSMs, they either focus exclusively on three-phase PMSMs [14,17] or only briefly discuss the sensorless control of DTP-PMSMs [18]. A comprehensive review of the sensorless control of DTP-PMSMs is clearly needed.

This paper aims to provide a comprehensive review of past and current research on the sensorless control of DTP-PMSMs. The remainder of the paper is organised as follows: in Section 2, the mathematical models of DTP-PMSM are provided. The evolution of model-based sensorless control in DTP-PMSM is presented in Section 3, while the work on saliency-based sensorless control techniques for DTP-PMSM is discussed in Section 4. The combination of different sensorless control methods for the entire range of speeds for the operation of DTP-PMSMs is described in Section 5. Controlling fault-tolerant DTP-PMSMs is explained in Section 6, followed in Section 7 by a survey of typical power levels and application areas of DTP-PMSMs using sensorless control techniques. Relevant conclusions and recommendations for future research are given in Section 8.

## 2. Multiple Three-Phase Machine Modelling Methods

It is possible to represent DTP-PMSMs using two methods, viz., vector space decomposition (VSD) and multiple individual three-phase models (MITP). The latter is based on the three-phase machines' synchronous $dq$-axis model, which uses multiple three-phase sub-machines as its basis. In the VSD model, variables of various orders are separated into numerous orthogonal subspaces using a mathematical transformation. Most papers on DTP-PMSM simulation employ separate subspaces due to their advantages, such as relative simplicity in modelling, controller design, and harmonics control. However, as summarised in Table 1, both VSD and MITP models have their share of merits and demerits [20,21].

### 2.1. Vsd Model

The vector space decomposition technique in the modelling of multiphase machines makes it simpler to establish independent current regulation in decoupled subspaces. This is because the complicated high-order electromagnetic system can be clearly reduced to two-order subsystems in numerous decomposed subspaces. The DTP machine's VSD transformation is as follows [22,23]:

$$
\begin{bmatrix} F_\alpha \\ F_\beta \\ F_{z1} \\ F_{z2} \end{bmatrix} = \frac{1}{3} \begin{bmatrix} 1 & -\frac{1}{2} & -\frac{1}{2} & \frac{\sqrt{3}}{2} & -\frac{\sqrt{3}}{2} & 0 \\ 0 & -\frac{\sqrt{3}}{2} & \frac{\sqrt{3}}{2} & \frac{1}{2} & \frac{1}{2} & -1 \\ 1 & -\frac{1}{2} & -\frac{1}{2} & -1 & \frac{1}{2} & \frac{1}{2} \\ 0 & -\frac{\sqrt{3}}{2} & \frac{\sqrt{3}}{2} & 0 & \frac{\sqrt{3}}{2} & -\frac{\sqrt{3}}{2} \end{bmatrix} \begin{bmatrix} F_{A1} \\ F_{B1} \\ F_{C1} \\ F_{A2} \\ F_{B2} \\ F_{C2} \end{bmatrix}
\tag{1}
$$

where $F$ is either the current, flux linkagem or the voltage. Using (1), the current and voltage can be decomposed into $\alpha\beta$ and $z_1z_2$ components. The fundamental component and the harmonics of order $m = 12n \pm 1$ ($n = 1, 2, 3, \ldots$), i.e., $m = 11, 13, 23, 25$, etc., are mapped in the $\alpha\beta$ subspace, while the harmonics of order $m = 6n \pm 1 (n = 1, 3, 5, \ldots)$, i.e., $m = 5, 7, 17, 19$, etc. are mapped in the $z_1z_2$ subspace.

The DTP-PMSM may be defined by the following models after the VSD conversion:

$$
\mathbf{u}_{\alpha\beta} = \mathbf{R}_s \mathbf{i}_{\alpha\beta} + s\boldsymbol{\psi}_{\alpha\beta}
\tag{2}
$$

$$
\boldsymbol{\psi}_{\alpha\beta} = \mathbf{L}_{s\alpha\beta} \mathbf{i}_{\alpha\beta} + \boldsymbol{\psi}_f \mathbf{e}^{j\theta_e}
\tag{3}
$$

$$
\mathbf{u}_{z1z2} = \mathbf{R}_s \mathbf{i}_{z1z2} + s\boldsymbol{\psi}_{z1z2}
\tag{4}
$$

$$
\boldsymbol{\psi}_{z1z2} = \mathbf{L}_\sigma \mathbf{i}_{z1z2}
\tag{5}
$$

$$\mathbf{T}_e = 3\mathbf{P}(\boldsymbol{\psi}_\alpha \mathbf{i}_\beta - \boldsymbol{\psi}_\beta \mathbf{i}_\alpha) \tag{6}$$

**Table 1.** Advantages and disadvantages of VSD and MITP models.

| Method | Advantages | Disadvantages |
|---|---|---|
| **VSD** | - Separated and simpler models in several subspaces.<br>- Improved simplicity in the controller design.<br>- A simpler approach for controlling harmonics. | - Less equipped to cope with imbalance due to the asymmetry of the sets.<br>- Requires more effort to establish active power and torque sharing. |
| **MITP** | - Forthright.<br>- Three-phase set design as well as control modularisation. | - Increased interconnectivity between sets.<br>- As the number of sets rises, so does the level of model and control sophistication. |

*2.2. Multiple Individual Three-Phase PMSM Model*

The models of multiphase PMSMs (MP-PMSM) may be considered as the sum of individual three-phase machine sets with additional coupling voltage terms between them. For each three-phase set, the machine model is executed in a synchronous *dq* frame [20]. For a DTP-PMSM, the voltage equations of the two *dq* sets are given by

$$\begin{bmatrix} u_{d_1} \\ u_{q_1} \end{bmatrix} = \begin{bmatrix} R_s + L_d s & -\omega_e L_q \\ \omega_e L_d & R_s + L_q s \end{bmatrix} \begin{bmatrix} i_{d_1} \\ i_{q_1} \end{bmatrix} + \begin{bmatrix} M_d s & -\omega_e M_q \\ \omega_e M_d & M_q s \end{bmatrix} \begin{bmatrix} i_{d_2} \\ i_{q_2} \end{bmatrix} + \begin{bmatrix} 0 \\ \omega_e \psi_{f_d} \end{bmatrix} \tag{7}$$

$$\begin{bmatrix} u_{d_2} \\ u_{q_2} \end{bmatrix} = \begin{bmatrix} R_s + L_d s & -\omega_e L_q \\ \omega_e L_d & R_s + L_q s \end{bmatrix} \begin{bmatrix} i_{d_2} \\ i_{q_2} \end{bmatrix} + \begin{bmatrix} M_d s & -\omega_e M_q \\ \omega_e M_d & M_q s \end{bmatrix} \begin{bmatrix} i_{d_1} \\ i_{q_1} \end{bmatrix} + \begin{bmatrix} 0 \\ \omega_e \psi_{f_d} \end{bmatrix} \tag{8}$$

The electromagnetic torque can be stated as

$$T_e = \frac{1}{3} P[\psi_{f_d}(i_{q_1} + i_{q_2}) + (L_d - L_q)(i_{d_1} i_{q_1} + i_{d_2} i_{q_2}) + (M_d - M_q)(i_{d_1} i_{q_2} + i_{d_2} i_{q_2})] \tag{9}$$

where the inductances are given by

$$\begin{aligned} L_d &= M_d + L_\sigma \\ L_q &= M_q + L_\sigma \end{aligned} \tag{10}$$

In (10), $L_\sigma$ represents leakage inductance. As DTP-PMSM has only two three-phase sets, the sophistication of the level of control is not high.

**3. Model-Based Sensorless Control Methods**

In low- to zero-speed range, sensorless control based on saliency is shown to be effective. However, a number of undesired effects, such as increased noise, torque ripple, and losses, may be caused by the injected signal. Furthermore, the required additional voltage signal injected could be limited by the maximum output voltage of the inverter when it is working in a higher speed range. Thus, in sensorless control, saliency-based approaches with signal injection should be used exclusively for low- to zero-speed ranges, while alternative methods such as model-based methods should be used once the speed surpasses a certain threshold.

Industrial applications often employ model-based methodologies. It is possible to get better results in medium- and high-speed fields by using various techniques, such as different kinds of observers, to estimate the EMF or flux linkage of the PMSM, as shown in Figure 4. Model-based sensorless control could be used in either the stationary $\alpha\beta$ frame or the synchronous *dq* frame. The information for this form of control is obtained from measured voltages and current signals, after which it estimates EMF or flux and position/speed. Notably, the misaligned or estimated *dq* frame needs to be set up, and the EMF, or flux, can be estimated by making the difference between the actual and estimated

*dq* frames equal to zero for the implementation in the *dq* frame. There will always be a position-estimate error due to parameter fluctuations, independent of the observer format and application reference frames. Researchers are still working to find a solution to the problem of parameter variation, which has a large effect on the accuracy of position estimates. Both online and offline methods can be used for parameter identifications, after which the position error can be corrected.
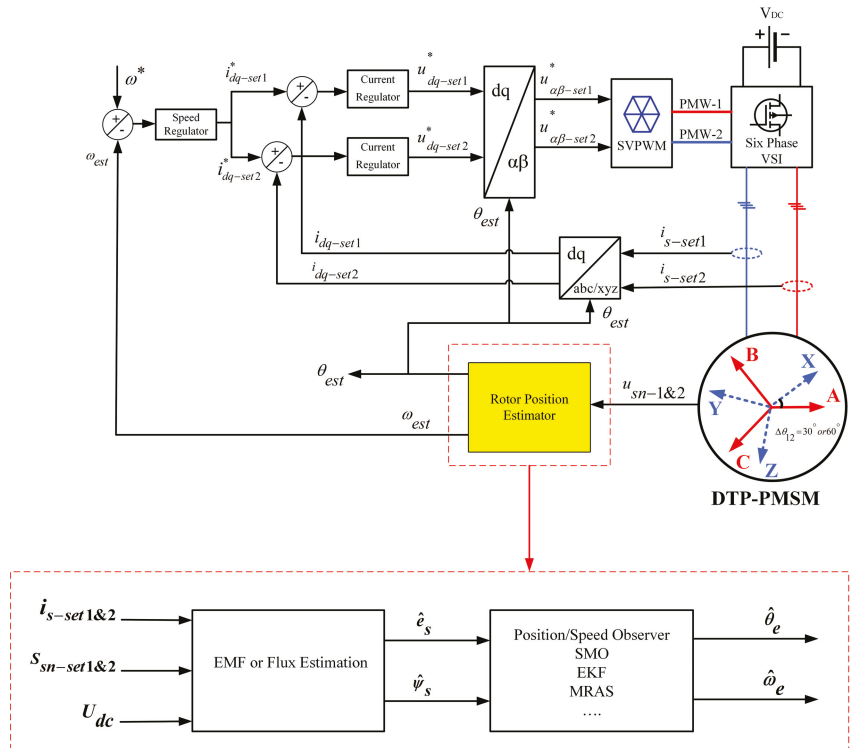


**Figure 4.** Block diagram of all methods for the control and estimation of position and speed.

### 3.1. Flux or EMF Estimation

The closed-loop and open-loop approaches may both be used to directly compute flux or EMF information in the model-based sensorless control. For reasons of robustness and precision, closed-loop estimation is better. To precisely estimate position and speed, the EMF or flux estimation has a substantial impact on the reference frame, mathematical model, and error convergence technique [14].

While this method has frequently been used for conventional (three-phase) machines, the first application of the method in DTP electrical machines was only reported in 2018 [24], where a new position sensorless approach based on extended EMF was applied to a DTP wound-field synchronous motor. Closed-loop estimating approaches often need a mathematical formula to ensure that the estimated measured output error is zero. Various methods may be used for this purpose. To aid in the estimating process, linear state and sliding mode observers may be utilised, among others. The estimate of EMF or flux is rather mature, which has a lot to do with how well you handle flux spatial harmonics and the inverter non-linearities. EMF and flux measurements also face key hurdles in terms of stability and reproducibility at low frequencies. Estimated flux may be determined by integrating the flux model as a function of stator current and voltage to give the estimated rotor position [25]. In [26], an online compensation strategy for errors in relation to rotor

position estimation has been proposed for model-based sensorless control methods. This strategy conducts direct back-EMF measurement on one set of temporarily isolated three-phase winding while generating rated motor torque using the other set of winding for a short duration of time.

### 3.2. Position/Speed Observer

To determine position and speed, the EMF or flux must be determined and the observer error must be zero. In order to compute the rotor position, the Arctan function may be utilised directly. Traditionally, the position/speed observer has been favoured to increase estimate accuracy. The observer's input is the position error signal, which may be derived by vector cross-product or other straightforward mathematics approaches. It is therefore possible to employ a Luenberger observer of the PI or PID type to force the position error signal to zero and retrieve the position/speed information. The PID-type Luenberger observer, although requiring a moment of inertia, has higher dynamic performance than the phase-locked loop (PLL)-type estimators. Estimated position and speed are often computed using a time-derivative approximation, such as a first-order Euler approximate, in the above-mentioned scenarios. This results in a sequential estimator. Using this approach, noise is amplified in the high-frequency range. A different solution is conceivable, since it is possible to estimate both speed and position simultaneously. The identity observer is a popular estimator for this purpose. The information that is offered by EMFs in $\alpha\beta$-axes is utilised by these estimators. The majority of them include a high-gain observer structure in their designs. Given that the system is assumed to be

$$px = f(x) + g(x)u; y = h(x), \tag{11}$$

then the following is a form of the equation that describes the dynamics of high-gain observers:

$$p\hat{x} = \underbrace{f(\hat{x}) + g(\hat{x})u}_{1} + \underbrace{G(\hat{x})(y - h(\hat{x}))}_{2} \tag{12}$$

where term 1 in (12) is the prediction that duplicates the dynamics of the variables to be estimated, while term 2 is the correction that is multiplied by a high-gain observer. A variety of high-gain observers are discussed in [17]. To achieve accurate estimations, a structure is required to ensure that the estimation error is zero. It is important to note the nonlinearity of the dynamics of EMFs that relate EMFs to rotor position and speed.

### 3.2.1. Extended Kalman Filter (EKF)

The Kalman Filter and its nonlinear variant, the EKF, may both be called high-gain observers. Many researchers obtain an approximate speed estimate using a rough approximation of the position-time derivative, as the time-derivative operator is not causal. The class of high-gain observers includes estimators of this kind. In this case, the prediction term is set to zero. Flux linkages generated from the observed triple harmonic back-EMF are orthogonal to each other and constant in amplitude due to a phase shift of $\pi/6$ between the two sets of winding in some DTP-PMSMs. It is also possible to directly use the triple harmonic EMF for determination of the rotor position using an estimator with speed-variable parameters without any filtering. The rotor position can be determined based on triple harmonic back-EMFs or flux linkages using an EKF-based rotor position estimator, even in the presence of many high-order harmonic components [27]. Figure 5 depicts a simple EKF for DTP machines, showing the closed-loop transfer function that can be stated as a relationship between the estimated and real rotor locations. A simple formula can be used to determine the high-resolution estimated rotor position, $\theta_r^e$

$$\theta_r^e = \theta_0 + \int_0^t \omega_r \, dt \; = \theta_0 + \int_0^t \frac{\pi}{3t_d} \, dt \tag{13}$$

$$\frac{\theta_r^e}{\theta_r} = \frac{3\psi_3 k_d.s^2 + 3\psi_3 k_p.s + 3\psi_3 k_i}{s^3 + 3\psi_3 k_d.s^2 + 3\psi_3 k_p.s + 3\psi_3 k_i} \tag{14}$$

It was possible to show that since $\psi_3$ is constant, the $k_p$, $k_i$, and $k_d$ values of the PID controller used in the rotor position estimator could likewise be constant in order to keep the bandwidth constant.

As discussed in [28], the inherent harmonic currents in traditional switching table-based DTC (ST-DTC) for DTP-PMSM may negatively affect the performance of sensorless control, but this effect may be mitigated by using a modified switching-table method. The effect of non-sinusoidal stator currents on the accuracy of position and speed estimates has been investigated for both the standard flux-linkage observer (FO) and the simplified EKF [28]. In [29], a novel approach to estimating the rotor position based on the third harmonic back-EMF for conventional and DTP-PMSMs is proposed to cope with unbalanced situations. It shows that the enhanced technique to estimate rotor position may considerably compensate for unbalanced parameters. As a result, increased resilience allows for significant improvements in the steady-state and dynamic performance of single and DTP-PMSMs. In [30], the impact of back-EMF and current harmonics on the performance of sensorless control for single and dual three-phase PMSMs is discussed. Extensive experimental findings indicate that, in comparison to FO, the simplified EKF model has a larger capacity for noise rejection, which contributes to the model's superior performance in terms of rotor position and accuracy of speed estimation.
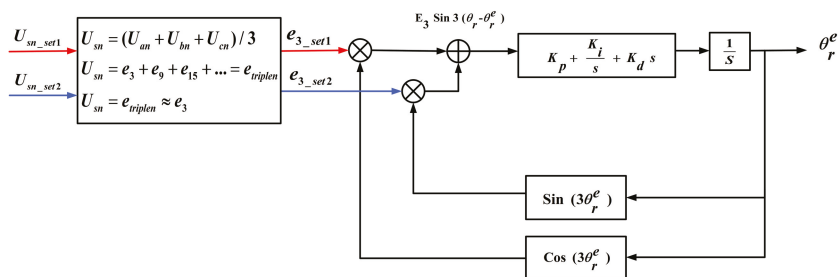


**Figure 5.** EKF-based rotor position estimator for DTP Machines [27].

### 3.2.2. Model Reference Adaptive System (MRAS)

MRAS typically picks the equation with no parameters as the reference model and the one with parameters as the adjustable equation. Adjustable parameters are estimated by comparing two models' outputs in an adaptation process. Because of this, the control object's real output reflects that of the reference model. Great progress is achieved in applying MRAS to the servo motion system using a variety of methods. Effective and physically clear, the MRAS algorithm has been used extensively for sensorless control of an induction motor. Two models are required by the MRAS method: a reference model and an adaptive model. The motor itself may serve as both an adaptive model and a reference model in the mathematical model of the DTP-PMSM. Rotor speed is used as a corrective factor in the adaption process in order to determine the present inaccuracies between two models. This approach can be used by the MRAS control method of three-phase PMSM to control a DTP-PMSM, since it is identical in $(d, q)$ subspace to three-phase PMSM [27].

It is critical to accurately determine the rotor position in sensorless control of DTP-PMSMs. In the literature, different starting processes may be categorised into three categories: a predefined rotor position established by correct feeding; open-loop startup; and a specialised algorithm for determining the rotor position at standstill. Because the stator current can be regulated precisely, this approach has the potential to provide the highest level of rotor positioning precision, while also requiring the least amount of additional complexity in the system. This method's dependability is affected by the existence of the load torque, whose magnitude might induce a shift between the imposed alignment posi-

tion and the real one [31,32], as seen in Figure 6. When calculating the stator current of the machine, the MRAS estimator in this scenario utilises two different models. The first model is known as a reference model, whereas the second model is known as an adaptive model. The difference in outputs between these two models is employed to drive an appropriate adaptation mechanism, which in turn yields an estimated rotor speed. A comprehensive MRAS sensorless control system design technique in discrete-time domain for high-speed drives is proposed and discussed in [33,34].
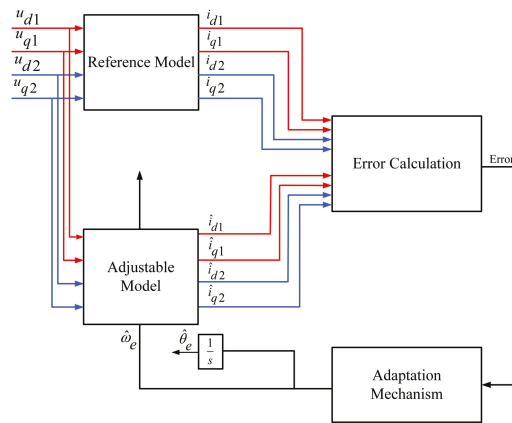


**Figure 6.** Block diagram of MRAS [31].

### 3.2.3. Sliding-Mode Observer

For practical rotor speed/position estimates, the sliding-mode control (SMO) approach is commonly utilised due to its simple methodology and reliability. Although sensorless control of multiphase machines is not a new issue and has been researched for decades, some researchers have attempted to fill in the study gaps for DTP-PMSM. A sign function is often employed to adjust for discontinuous gains. The estimation error reaches a specified surface and then glides along this surface, eventually reaching zero. Chattering is an undesired side effect of discontinuous functions like the sign function. As a result, modifications to reduce the chattering effect have been suggested. A sigmoid function, as shown in Figure 7, for example, may alter the sign function. In some situations, a low-pass filter (LPF) can be used to get rid of the signal's high frequencies. The LC filter, on the other hand, will introduce a new kind of resonance issue [35].
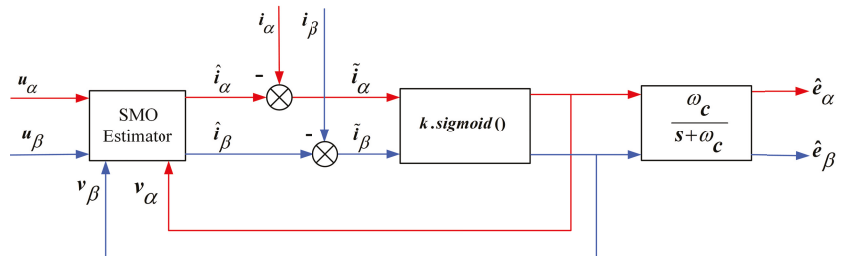


**Figure 7.** Block diagram of conventional SMO method [36].

As a result of using an LC filter, the resonance in the capacitor circuit must be suppressed using an extra resistor. Since the motor resistance is relatively high, adding resistance will cause insignificant losses. It is necessary to incorporate an extra current feedback loop in order to effectively suppress the resonance without causing more damage.

Hence, the LPF is removed and replaced with two synchronous frequency-tracking filters (SFTFs), which can extract the fundamental wave component from the back-EMF. This enhances conventional sensorless control.

It is possible to use SMO in order to estimate the rotor position and speed of the DTP-PMSM. Rotor position information can be found in the extended EMF. To obtain the estimated rotor position, the extended EMF must be estimated first. The DTP-PMSM is subjected to a variety of SMO techniques, such as the conventional SMO method and the adoptive SMO method, which are shown in Figures 7 and 8, respectively. The Arctan function and PLL-based estimators are used to estimate the rotor's speed and position after obtaining an estimated extended EMF [36,37].
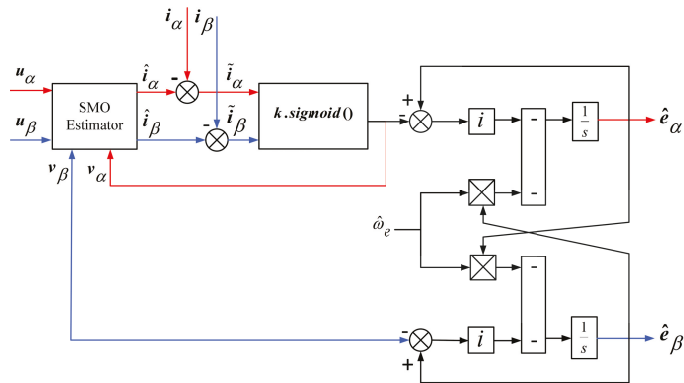


**Figure 8.** Block diagram of adaptive SMO method [36].

A model predictive torque control system is described in [35], and it is constructed using the mathematical model of DTP-PMSM with vector space decoupling (VSD). For the purpose of obtaining the speed, a model predictive torque control approach has been suggested, as shown in Figure 9. In order to reduce the design cost and enhance the anti-interference ability of the system, an SMO strategy is suggested in [35] to estimate the motor speed. This method would include extended rotor resistance compensation, which would increase the system's resilience. The findings of the simulation indicate that the suggested control system has a rapid dynamic reaction and a high degree of resilience.
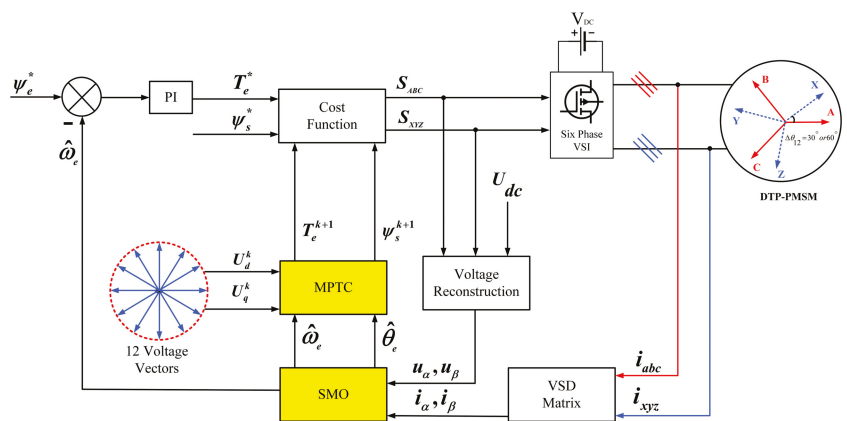


**Figure 9.** Model predictive torque control system [35].

### 3.2.4. Luenberger Observer

A nonlinear gain-correction term is included in this kind of observer, which uses the prediction term to copy the EMF's dynamic equations. The estimated error converges to zero when the nonlinear observer gain is constructed as recommended in those works, assuming an accurate model, i.e., the parameters in the prediction terms match the parameters in the motor and there is no uncertainty in the measured variable. The key benefit is that convergence is ensured across a large area of state space. Furthermore, the rate of convergence can also be adjusted.

In [38], there is a comparison between two back-EMF based sensorless control techniques, one of them using a phase-locked loop (PLL) speed and rotor position estimator, and the other a Luenberger observer estimator. In the mentioned article, improved dynamic performance is provided by a Luenberger-type estimator. It is stated that the predicted speed error suffers from high-frequency noise and the usage of machine characteristics is required. The PLL-type estimators, on the other hand, have a lower but still adequate level of performance. Low-pass filtering eliminates high-frequency interference. In addition, the PLL type does not involve the usage of any kind of mechanical data.

As a result of the PLL's simple construction and mechanical independence, it is favoured for future investigation and prospective applications. The rotor speed and position can alternatively be estimated using a Luenberger observer-type speed and position estimator, as illustrated in Figure 10. An observer-type position estimator's transfer function can then be described in this way, as by [38]:

$$\frac{\hat{\theta}_e}{\theta_e} = \frac{JK_a s^2 + (BK_a + K_b)s + K_c}{Js^3 + (JK_a + B)s^2 + (BK_a + K_b)s + K_c} \tag{15}$$

where $J$ is rotational inertia and $B$ is viscous friction.

By adjusting the gains of the estimator shown in Figure 10, roots of the characteristic equation in (15) can be forced to coincide with those in the following expressions [38]:

$$K_a = -\alpha, K_b = j\alpha^2, K_c = -J\alpha^3 \tag{16}$$

where $\alpha$ is the root of the characteristic equation.

Table 2 provides an explanation of the benefits and drawbacks of the observers that are used in DTP-PMSM.
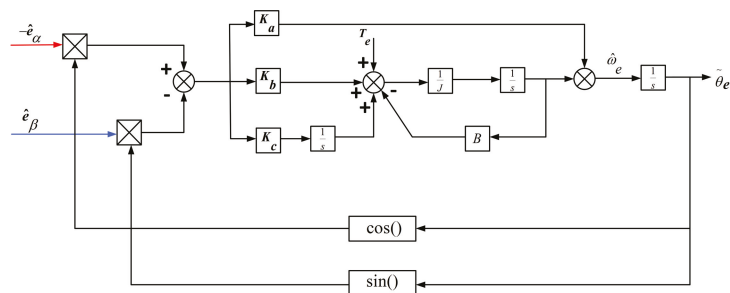


**Figure 10.** Block diagram of Luenberger observer-based speed and position estimator [38].

**Table 2.** Comparison of position observers.

| Types | EKF | MRAS | SMO | Luenberger |
|---|---|---|---|---|
| Advantages | Less influence of noise; low computational time | A fail-safe machine model; high-velocity adaptation | Guaranteeing no mistakes; very reliable; independent of motor parameters | Convergence is certain all across a large chunk of the possible states; convergence times are completely arbitrary |
| Disadvantages | Weak low-speed performance | Struggle with a wide range of motor characteristics | Ineffective at rest and at slow speeds | Can make the sensor noise issue much worse |

**4. Saliency-Based Sensorless Control Methods**

For zero- and low-speed operating condition, model-based techniques cannot be employed due to the lack of back-EMF. In contrast, saliency-based techniques are able to overcome this limitation and can accurately estimate the rotor position in the zero- and low-speed operating range. These strategies are used as a result of either geometric rotor saliency or magnetic saturation. Saliency-based approaches include PWM signal injection (SI), transient voltage vector injection, and other techniques. Rotating–pulsating sinusoidal SI in the estimated reference frame, and sinusoidal SI in a stationary reference frame are the most common ways of persistent carrier SI.

*4.1. SI-Based Systems*

Carrier SI-based sensorless control systems typically inject either high-frequency current or voltage signals into the basic excitation windings of the machine. Then the rotor position information is extracted from the position-dependent carrier signal, viz., carrier current or zero-sequence voltage. For the rotating carrier signal-injection method, it has been proven that both negative-sequence carrier current signal and zero-sequence carrier voltage signal can be used to estimate the rotor position. For DTP-PMSM drives, SI-based sensorless control is the most common method used to obtain the position by monitoring the saliency in the low-speed area. The voltage drop on the stator resistance can be omitted, as can the terms associated with $\omega_e$, since the injection frequency is much greater than the operating speed [39,40]. Figure 11 presents a sensorless control scheme with high-frequency (HF) SI. The zero-sequence carrier voltage exhibits low total harmonic distortion and shows less sensitivity to the distortion of the injected carrier signal compared to the carrier's current response. Furthermore, it has been found that the estimation accuracy of the the system bandwidth and rotor position can be enhanced significantly when utilising a zero-sequence carrier voltage.
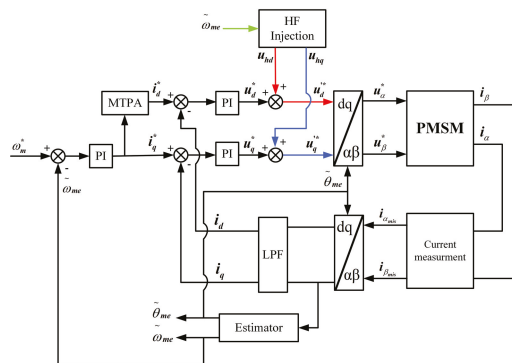


**Figure 11.** Sensorless control scheme with HF signal injection [39].

### 4.1.1. Voltage Injection

Voltage injection combines the large bandwidth of the zero-sequence voltage method with the high precision of the pulsating injection strategy for estimating position, as shown in Figures 12 and 13. Due to undesired harmonic components in the zero-sequence carrier voltage, the position-estimation error of a single three-phase PMSM is considerable, and the current compensating solutions often require complicated designs or extensive offline measurements. With two separate high-frequency injections into each stator winding set, DTP-PMSM with separated neutral points offers more degrees of freedom. It is possible to alter the phase angle between the two injected high-frequency signals, allowing for the resolution of this problem. When the pulsating carrier signal is injected into the estimated $dq$ synchronous reference frame as two superimposed rotating carrier voltages with opposing directions, the injected voltages for the three phases are as follows:

$$
\begin{aligned}
v_a &= V_c cos(\omega_c t)cos(\hat{\theta}_e) \\
v_b &= V_c cos(\omega_c t)cos(\hat{\theta}_e - 2\pi/3) \\
v_c &= V_c cos(\omega_c t)cos(\hat{\theta}_e + 2\pi/3)
\end{aligned}
\tag{17}
$$

$\hat{\theta}_e$ = estimated rotor position
$V_c$ = carrier voltage
$\omega_c$ = carrier frequency

Figure 12 illustrates the pulsating injection that may be seen in the estimated reference frame.
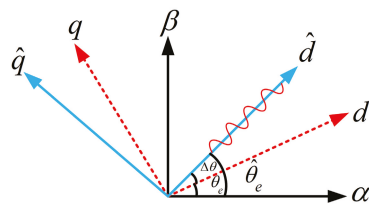


**Figure 12.** HF d-axis pulsating voltage for the signal injection [41].
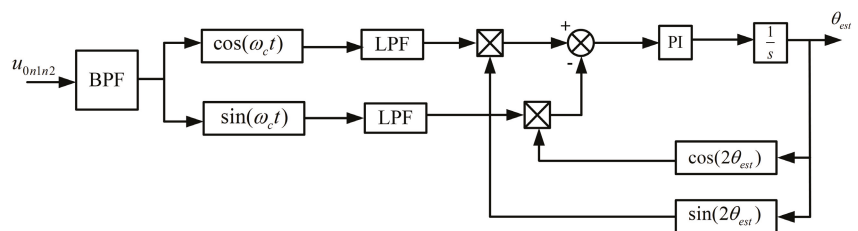


**Figure 13.** Block diagram of zero-sequence carrier signal process with rotating injection [42].

In DTP-PMSM drives, the harmonic components may be reduced by using a modified pulsating injection approach with zero-sequence voltage, which applies an optimal phase shift between the two injected HF carrier signals. According to [41–43], these strategies work well for DTP-PMSM. It has also been stated that a novel technique of measuring zero-sequence voltage utilising just one voltage sensor has been developed. Injecting HF voltage into dual three-phase may be accomplished in other ways as well. For instance, HF voltages with the same amplitude and frequency are injected into both three-phase sets in the same spatial direction (parallel injection method), or HF voltages with the same amplitude and frequency are injected into both three-phase sets in opposing directions (opposing injection method).

An HF voltage injection method for determining position is described in [44]. One of the known disadvantages of high-frequency voltage injection is the acoustic noise that is generated. However, the acoustic noise can be minimised by utilising this injection technique only at specific frequencies. The resultant zero-sequence carrier voltage is typically measured by utilising one of the two most used measurement methods, namely (1) measurement utilising phase-to-neutral-voltages, as shown in Figure 14a, or (2) measurement utilising the auxiliary resistor network, as shown in Figure 14b.
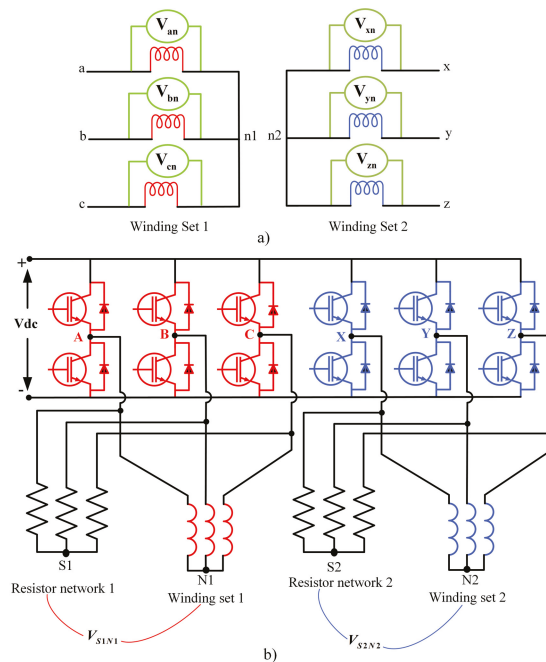


**Figure 14.** (**a**) Measurement of zero-sequence voltage using phase-to-neutral voltages. (**b**) Measurement of zero-sequence voltage using auxiliary resistor network [41].

### 4.1.2. Current Injection

It is possible to obtain information about the position and degree of saliency of a salient machine by injecting a carrier signal current into the machine and then measuring the resulting voltages. A comparison for the use of voltage and current injection techniques for the estimation of flux angle or rotor position are included in [45]. In [45], two problems of carrier signal current injection are offered to a basis for fair comparison: the first is the extraction of the spatial information contained in the induced voltages, and the second is the regulation of high-frequency currents with current regulators of limited bandwidth. Based on this comparison, choosing which method to use depends on the application, the desired performance, and the bandwidth of fundamental current regulator. Predominantly, higher performance (higher bandwidth) is possible with carrier signal voltage injection, since the current regulator does not directly limit its bandwidth.

As a parameter identification and position sensorless control approach for motor drives, VSI nonlinearity compensation is critical. For DTP-PMSM drives, an online estimate and compensation approach for VSI nonlinearity has been suggested in [46]. To determine the magnitude of error voltages due to VSI nonlinearity, this approach utilizes voltage differences with $z_1z_2$-axis current injection as its input. An improved recursive least-square (RLS) algorithm and a current injection-based parameter estimation method for DTP-PMSM, considering inverter nonlinearity and magnetic saturation, are proposed in [47].

### 4.2. Pulsating Signal Injection

Using pulsating signal injection as a sensorless control method is another viable option. In order for pulsating signal injection to work, the rotor reference frame must be known from the beginning. Pulsating signal injection can be split into two groups, based on the types of signals that are injected: pulsating square-wave injection and pulsating sinusoidal injection [48].

Square-Wave Sensorless Injection

Half-switching frequency signal-injection sensorless control (SISC) and switching-frequency SISC are the two types of SISCs with fast dynamic characteristics. Ideally, their dynamic properties should resemble one another. If the frequency of the injected voltage signal would increase to pulse-width modulation (PWM) switching frequency and if the switching frequency is near or above an audible range, the dynamics of the sensorless control can be improved, and the acoustic noise can be remarkably reduced or totally eliminated [49]. Switching-frequency SISC, on the other hand, is more susceptible to inverter nonlinearity effects than half-switching-frequency SISC. Switching-frequency injection adds first- and third-order harmonic distortion to position estimation [50]. When it comes to SISC, this means that the greatest possible frequency is half the switching frequency. The block diagram of the conventional SISC is represented in Figure 15. For DTP-PMSM, SISC could be applied in the two three-phase windings individually [51].
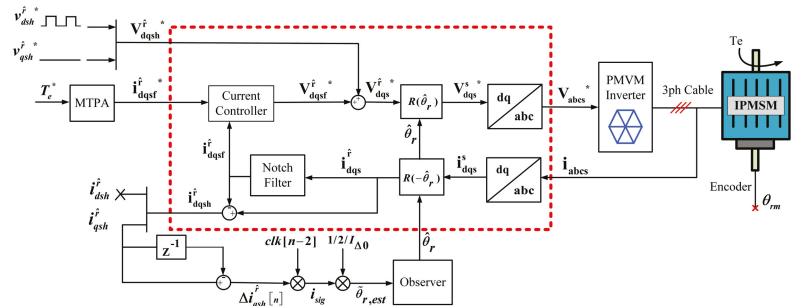


**Figure 15.** Block diagram of conventional square-wave injection sensorless drive system [51].

### 4.3. Fundamental PWM Excitation

The fundamental PWM excitation technique has been refined by various researchers in order to make it easier to analyse the results. For instance, using the transient response of the line current to basic PWM vectors, a sensorless algorithm is created in a two-dimensional orthogonal frame, as shown as Figure 16. For multiphase machines, this strategy is ideal [19,52]. Table 3 provides an explanation of the benefits and drawbacks of the saliency-based methods that are used in DTP-PMSM.
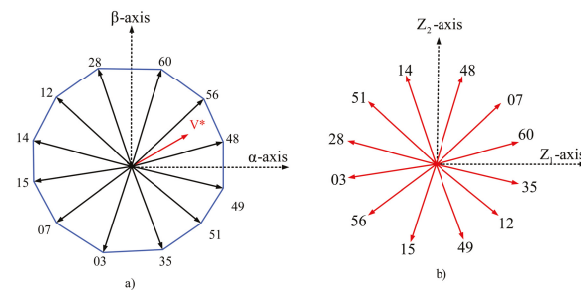


**Figure 16.** Voltage vector map in stationary frame. (**a**) Projection of voltages on $\alpha\beta$ plane. (**b**) Projection of voltages on $z_1 z_2$ plane [19].

**Table 3.** Comparison of saliency-based methods.

| Types | Voltage Injection | Current Injection | Pulsating Signal Injection | Fumdamental PWM Excitiation |
|---|---|---|---|---|
| **Advantages** | No acoustic noise; independent of motor parameter | High performance; independent of motor parameter | Small effect on inverter nonlinierities; magnetude modulated | Insensetive to parameter variation |
| **Disadvatage** | Do not support high speed operation | High computational requirement, which needs powerful hardware devices | Requiring initial position information | High current ripple; flux distortion causes estimation error |

## 5. Combination of Low-Speed and High-Speed Methods

As mentioned previously, an EMF-based observer operates well at medium and high speeds, but a saliency-based observer excels only at low speeds. Therefore, it would appear logical to combine the two approaches in order to obtain an estimator that performs well over the whole speed range. As a result of this, several researchers have developed observers that combine two distinct methods from those described in the previous paragraphs, namely model-based and saliency-based. For instance, for DTP-PMSM, the integration of high-frequency SI and extended EMF-based techniques for sensorless control, or injecting current signal and an EMF estimator, have been proposed [25,53,54]. In Figure 17, an overall block diagram of the DTP-PMSMs control system with a combination of methods is illustrated. Very few studies have been conducted in this area for DTP-PMSM drives, which might be a promising area for future study.
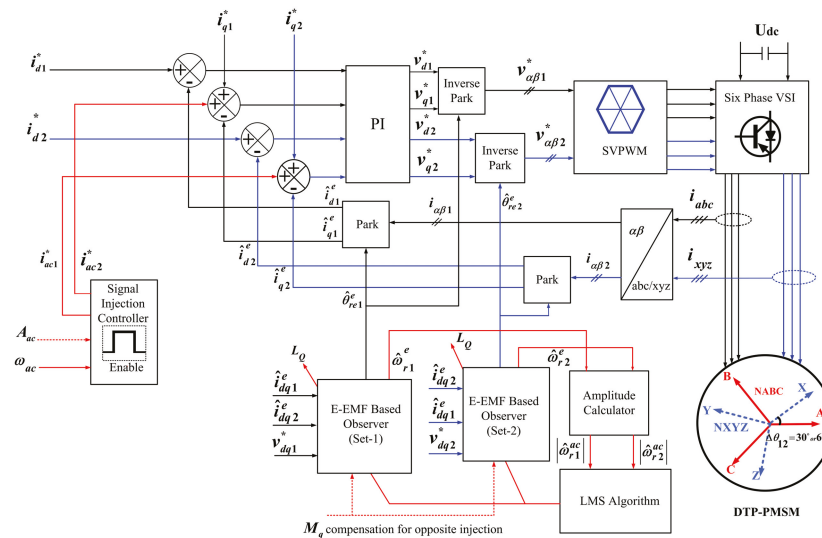


**Figure 17.** Overall block diagram of DTP-PMSMs control system with combination methods [54].

## 6. Fault-Tolerant Sensorless Control for DTP-PMSMs

DTP-PMSMs have intrinsic fault-tolerant capability due to the physical separation between the phase windings. In this regard, controlling a fault-tolerant DTP-PMSM system without sensors at high and low speeds has been the subject of recent studies [39]. In [55], a fault-tolerant sensorless speed control strategy is discussed for the case of an open-phase fault. The speed control strategy of [55] is realised through a redundant extended back-EMF observer structure for an asymmetrical DTP-PMSM. In [56,57], a new sensorless control

is proposed without requiring coordinate transformation by injecting the HF signal into two non-fault phase windings for a six-phase fault-tolerant PMSM. This control method can guarantee the low-speed sensorless control performance under both fault-free and fault-tolerant operation conditions.

## 7. Applications and Applied Sensorless Control Techniques of DTP-PMSMs

In Table 4, the details of the applications, power levels, and applied sensorless control techniques of DTP-PMSMs from the literature are listed. The table shows that DTP-PMSMs with sensorless control have many industrial applications. Although some of the research focuses on high-power applications, the experimental implementation and evaluation have been limited to low-power levels. Additionally, some researchers are attempting to employ combination methods.

**Table 4.** Application and power levels of sensorless control of DTP-PMSM.

| Power level | Techniques | Application | Reference |
|---|---|---|---|
| 50 W | Saliency-based (Signal Injection) | Aerospaces | [57] |
| 170 W | Model-based (EKF) | High power and high current | [28] |
| 170 W | Model-based (EKF) | Industrial applications | [28] |
| 170 W | Saliency-based (Signal Injection) | High power and high current | [41] |
| 170 W | Saliency-based (Voltage injection) | High power and high current | [42] |
| 230 W | Model-based (EKF) | Power applications, high speed | [27,29] |
| 230 W | Saliency-based (Signal Injection) | Power applications | [45] |
| 500 W | Saliency-based (Signal Injection) | Low speed applications | [48] |
| 1 kW | Model-based (Luenberger) | Electric vehicles | [55] |
| 2.3 kW | Back EMF | Industrial applications | [9] |
| 3 kW | Model-based (MRAS) | Industrial applications | [32] |
| 3.7 kW | Combination method | Power applications | [25] |
| 4.2 kW | Model-based (Luenberger) | Small and medium machines | [26] |
| 4.5 kW | Saliency-based (Current Injection) | Special applications in aircraft drives, Automotive tractions, and electric ship propulsions | [47] |
| 5 kW | Saliency-based (FPE) | Low- and zero-speeds applications | [19] |
| 5.5 kW | Model-based (SMO) | Military applications | [35] |
| 6.7 kW | Model-based (Back EMF) | High-speed applications | [58] |
| 20 kW | Model-based (MRAS) | Aircraft and high-speed applications | [33] |
| 240 W | Current control | High-power industrial applications | [23] |
| 200 W | Model-based | Electric vehicles | [24] |
| Undefined | Signal injection | Industrial applications | [39] |
| Undefined | Saliency-based (FPE) | Low speed applications | [52] |
| Undefined | Combination method | High-power applications | [53,54] |

## 8. Conclusions

This paper has conducted a review of sensorless control of dual three-phase PMSMs (DTP-PMSMs). Sensor-free control is a major area of interest in DTP-PMSM. Sensorless control is superior to sensor-based control when it comes to overall system reliability and cost. Multiphase drives have also attracted the interest of academics and industry over the last three decades. A variety of rotor-position and speed-estimate algorithms have been discussed in the literature, with the aim of determining the most appropriate control

approach for use in applications such as ship propulsion, wind turbines, and aerospace, to mention just a few. Based on the research reviewed in this article, there are areas for potential research and development:

1. Some applications, such as aircraft, need an ultra-fast, sensorless DTP-PMSM drive; however, researchers are now faced with the difficulty of figuring out how to acquire the position information under low carrier ratios.

2. Improving the dynamic performance of position sensorless drives for DTP-PMSM is difficult in comparison to motor drives that include a position sensor. It is envisaged that there will be a greater focus on optimising dynamic sensorless performance for use in high-performance applications in the future.

3. PMSM characteristics are known to fluctuate significantly with load changes. It therefore is necessary to improve the robustness of the sensorless PMSM drives to machine parameter fluctuation in order to acquire the rotor position accurately across a broad range of loads.

4. For preferable performance, a combination of two or more techniques is beneficial for estimating the rotor position. Very few studies have been conducted on this for DTP-PMSMs, which might be a promising area for future study.

5. In order to further strengthen the power density and the reliability of the electric actuating system, a sensorless control strategy for fault-tolerant operation (e.g., losing one set of three-phase windings) of DTP-PMSM is important. From the literature reviewed in this article, there are few publications that explain how to control the fault-tolerant operation of DTP-PMSM without sensors at both high and low speeds, which could be an interesting topic for research in the future.

### List of Symbols

| Symbols | Description | Symbols | Description |
|---|---|---|---|
| $R_s$ | stator resistance | $s$ | derivative |
| $\omega_e$ | electrical angular speed | $\omega_c$ | carrier frequency |
| $\psi_f$, $\psi_{fd}$ | permanent magnet flux linkage | $\psi$ | flux linkage |
| $u_{d_1}$, $u_{q_1}$ | voltages of the first winding set | $u$, $i$ | voltage, current |
| $i_{d_1}$, $i_{q_1}$ | currents of the first winding set | $\theta_e$ | electrical rotor position in radians |
| $u_{d_2}$, $u_{q_2}$ | voltages of the second winding set | $V_c$ | carrier voltage |
| $i_{d_2}$, $i_{q_2}$ | currents of the second winding set | $T_e$ | electromagnetic torque |
| $L_d$, $L_q$ | $dq$-axis inductances | $k_p$, $k_i$, $k_d$ | values of the PID controller |
| $M_d$, $M_q$ | mutual inductances | $\theta_r^e$, $\hat{\theta}_e$ | estimated rotor position |

## References

1. Alves de Souza, S.; Issamu Suemitsu, W. Five-Phase Permanent-Magnet Synchronous Motor. *IEEE Lat. Am. Trans.* **2017**, *15*, 639–645. [CrossRef]
2. Jung, E.; Yoo, H.; Sul, S.K.; Choi, H.S.; Choi, Y.Y. A Nine-Phase Permanent-Magnet Motor Drive System for an Ultrahigh-Speed Elevator. *IEEE Trans. Ind. Appl.* **2012**, *48*, 987–995. [CrossRef]

3. Eldeeb, H.M.; Abdel-Khalik, A.S.; Hackl, C.M. Dynamic Modeling of Dual Three-Phase IPMSM Drives With Different Neutral Configurations. *IEEE Trans. Ind. Electron.* **2019**, *66*, 141–151. [CrossRef]

4. Teymoori, V.; Eskandaria, N.; Arish, N.; Khalili, A. Design of permanent magnetic motor speed controller drive with power supply inverter based on a new switching method. In Proceedings of the 2019 International Power System Conference (PSC), Tehran, Iran, 9–11 December 2019; pp. 453–458. [CrossRef]

5. Parsa, L.; Toliyat, H. Multi-phase permanent magnet motor drives. In Proceedings of the 38th IAS Annual Meeting on Conference Record of the Industry Applications Conference, Salt Lake City, UT, USA, 12–16 October 2003; Volume 1, pp. 401–408. [CrossRef]

6. Parsa, L.; Toliyat, H.A. Sensorless Direct Torque Control of Five-Phase Interior Permanent-Magnet Motor Drives. *IEEE Trans. Ind. Appl.* **2007**, *43*, 952–959. [CrossRef]

7. Pulvirenti, M.; Da Rù, D.; Bianchi, N.; Scarcella, G.; Scelba, G. Secondary saliencies decoupling technique for self-sensing integrated multi-drives. In Proceedings of the 2016 IEEE Symposium on Sensorless Control for Electrical Drives (SLED), Nadi, Fiji , 5–6 June 2016; pp. 1–6. [CrossRef]

8. Arish, N.; Ardestani, M.; Teymoori, V. Comparison of Dual Stator Consequent-pole Linear Permanent Magnet Vernier Machine with Toroidal and Concentrated Winding. In Proceedings of the 2020 11th Power Electronics, Drive Systems, and Technologies Conference (PEDSTC), Tehran, Iran, 4–6 February 2020; pp. 1–5. [CrossRef]

9. Yan, L.; Zhu, Z.Q.; Qi, J.; Ren, Y.; Gan, C.; Brockway, S.; Hilton, C. Suppression of Major Current Harmonics for Dual Three-Phase PMSMs by Virtual Multi Three-Phase Systems. *IEEE Trans. Ind. Electron.* **2022**, *69*, 5478–5490. [CrossRef]

10. Slunjski, M.; Dordevic, O.; Jones, M.; Levi, E. Symmetrical/Asymmetrical Winding Reconfiguration in Multiphase Machines. *IEEE Access* **2020**, *8*, 12835–12844. [CrossRef]

11. Zhao, Y.; Lipo, T. Space vector PWM control of dual three-phase induction machine using vector space decomposition. *IEEE Trans. Ind. Appl.* **1995**, *31*, 1100–1109. [CrossRef]

12. Shao, B.; Zhu, Z.Q.; Feng, J.H.; Guo, S.Y.; Li, Y.F.; Feng, L.; Shuang, B. Improved Direct Torque Control Method for Dual-Three-Phase Permanent-Magnet Synchronous Machines With Back EMF Harmonics. *IEEE Trans. Ind. Electron.* **2021**, *68*, 9319–9333. [CrossRef]

13. Zhang, P.; Zhang, W.; Shen, X. Comparative study of Field-Oriented Control in different coordinate systems for DTP-PMSM. In Proceedings of the 2013 International Conference on Electrical Machines and Systems (ICEMS), Busan, Korea, 26–29 October 2013; pp. 1015–1019. [CrossRef]

14. Singh, S.; Tiwari, A.N. Various techniques of sensorless speed control of PMSM: A review. In Proceedings of the 2017 Second International Conference on Electrical, Computer and Communication Technologies (ICECCT), Coimbatore, India, 22–24 February 2017; pp. 1–6. [CrossRef]

15. Robeischl, E.; Schroedl, M. Optimized INFORM measurement sequence for sensorless PM synchronous motor drives with respect to minimum current distortion. *IEEE Trans. Ind. Appl.* **2004**, *40*, 591–598. [CrossRef]

16. Wang, S.; Imai, K.; Doki, S. Analysis of an Application of the Extended Electromotive Force Model Based Position Sensorless Control on the Wound-Field Synchronous Motor with Dual-Three Phases in Standstill/Low Speed Region. In Proceedings of the IECON 2018—44th Annual Conference of the IEEE Industrial Electronics Society, Washington, DC, USA, 21–23 October 2018; pp. 5789–5794. [CrossRef]

17. Wang, G.; Valla, M.; Solsona, J. Position Sensorless Permanent Magnet Synchronous Machine Drives—A Review. *IEEE Trans. Ind. Electron.* **2020**, *67*, 5830–5842. [CrossRef]

18. Zhu, Z.; Wang, S.; Shao, B.; Yan, L.; Xu, P.; Ren, Y. Advances in Dual-Three-Phase Permanent Magnet Synchronous Machines and Control Techniques. *Energies* **2021**, *14*. [CrossRef]

19. Ahmad, M.; Zhang, W.; Gao, Q. Low and zero speed position estimation of dual three-phase PMSMs based on the excitation of PWM waveforms. In Proceedings of the 2017 IEEE 3rd International Future Energy Electronics Conference and ECCE Asia (IFEEC 2017—ECCE Asia), Kaohsiung, Taiwan, 3–7 June 2017; pp. 1652–1658. [CrossRef]

20. Hu, Y.; Zhu, Z.Q.; Odavic, M. Comparison of Two-Individual Current Control and Vector Space Decomposition Control for Dual Three-Phase PMSM. *IEEE Trans. Ind. Appl.* **2017**, *53*, 4483–4492. [CrossRef]

21. Wang, B.; Wei, G.; Chu, J.; Yi, G. A novel modeling for a dual three-phase permanent magnet synchronous machine. In Proceedings of the 2008 10th International Conference on Control, Automation, Robotics and Vision, Hanoi, Vietnam, 17–20 December 2008; pp. 1630–1634. [CrossRef]

22. Wang, Z.; Chen, J.; Cheng, M.; Ren, N. Vector space decomposition based control of neutral-point-clamping (NPC) three-level inverters fed dual three-phase PMSM drives. In Proceedings of the IECON 2016—42nd Annual Conference of the IEEE Industrial Electronics Society, Florence, Italy, 23–26 October 2016; pp. 2988–2993. [CrossRef]

23. Hu, Y.; Zhu, Z.Q.; Liu, K. Current Control for Dual Three-Phase Permanent Magnet Synchronous Motors Accounting for Current Unbalance and Harmonics. *IEEE J. Emerg. Sel. Top. Power Electron.* **2014**, *2*, 272–284. [CrossRef]

24. Imai, K.; Doki, S.; Fujii, K.; Jung, S. Position sensorless control for wound-field synchronous motor with double three-phase wound stator using extended electromotive force model. In Proceedings of the 2018 IEEE International Conference on Industrial Technology (ICIT), Lyon, France, 20–22 February 2018; pp. 492–497. [CrossRef]

25. Liu, T.; Zhu, Z.Q.; Wu, Z.Y.; Stone, D.; Foster, M. A Simple Sensorless Position Error Correction Method for Dual Three-Phase Permanent Magnet Synchronous Machines. *IEEE Trans. Energy Convers.* **2021**, *36*, 895–906. [CrossRef]

26. Scelba, G.; Scarcella, G.; Cacciato, M.; Pulvirenti, M.; Testa, A. Compensation of rotor positon estimation errors in sensorless dual-three phase PMSM drives through back-EMF sensing. In Proceedings of the 2017 IEEE International Symposium on Sensorless Control for Electrical Drives (SLED), Catania, Italy, 18–19 September 2017; pp. 199–206. [CrossRef]
27. Liu, J.; Zhu, Z. Rotor position estimation for dual-three-phase permanent magnet synchronous machine based on third harmonic back-EMF. In Proceedings of the 2015 IEEE Symposium on Sensorless Control for Electrical Drives (SLED), Sydney, Australia, 7–8 June 2015; pp. 1–8. [CrossRef]
28. Almarhoon, A.H.; Ren, Y.; Zhu, Z.Q. Sensorless switching-table-based direct torque control for dual three-phase PMSM drives. In Proceedings of the 2014 17th International Conference on Electrical Machines and Systems (ICEMS), Hangzhou, China, 22–25 October 2014; pp. 1616–1621. [CrossRef]
29. Liu, J.; Zhu, Z.Q. Rotor position estimation for single- and dual-three-phase permanent magnet synchronous machines based on third harmonic back-EMF under imbalanced situation. *Chin. J. Electr. Eng.* **2017**, *3*, 63–72. [CrossRef]
30. Almarhoon, A.H.; Ren, Y.; Zhu, Z.Q. Influence of back-EMF and current harmonics on sensorless control performance of single and dual three-phase permanent magnet synchronous machines. *Compel- Int. J. Comput. Math. Electr. Electron. Eng.* **2016**, *35*, 744–763. [CrossRef]
31. Fan, L.; Yang, T.; Rashed, M.; Bozhko, S. Sensorless control of dual-three phase PMSM based aircraft electric starter/generator system using model reference adaptive system method. In Proceedings of the CSAA/IET International Conference on Aircraft Utility Systems (AUS 2018), Guiyang, China, 19–22 June 2018; pp. 787–794. [CrossRef]
32. He, Y.; Hu, W.; Wang, Y.; Wu, J.; Wang, Z. Speed and Position Sensorless Control for Dual-Three-Phase PMSM Drives. In Proceedings of the 2009 Twenty-Fourth Annual IEEE Applied Power Electronics Conference and Exposition, Washington, DC, USA, 15–19 February 2009; pp. 945–950. [CrossRef]
33. Chen, Y.; Yang, T.; Khowja, M.; La Rocca, A.; Nasir, U.; Chowdhury, S.; Evans, D.; Kember, D.; Klonowski, T.; Arnaud, Y.; et al. Mild hybridisation of turboprop engine with high-power-density integrated electric drives. *IEEE Trans. Transp. Electrif.* **2022**, *8*, 4148–4162. [CrossRef]
34. Chen, Y.; Yang, T.; Fan, L.; Bozhko, S. Sensorless Control Design of High-Speed Electric Drives in Discrete Time Domain for Mild-Hybrid Turboprop Aircraft Applications. *IEEE Trans. Transp. Electrif.* **2022**, 1. [CrossRef]
35. Yang, Y.; Song, W.; Ren, H. Encoderless Model Predictive Torque Control of DTP-PMSM with Sliding Mode Speed Observer. In Proceedings of the 2021 IEEE International Conference on Predictive Control of Electrical Drives and Power Electronics (PRECEDE), Jinan, China, 20–22 November 2021; pp. 202–206. [CrossRef]
36. Fan, L.; Yang, T.; Chen, Y.; Bozhko, S. Comparative Study of Sensorless Methods Based on Sliding Mode Observer for Dual Three-Phase Permanent Magnet Synchronous Machine. In Proceedings of the 10th International Conference on Power Electronics, Machines and Drives (PEMD 2020), Online Conference, 15–17 December 2020; pp. 850-854.
37. Yu, H.; Gan, C.; Wang, H.; Chen, Y.; Ni, K.; Qu, R. Speed Adaptive Sensorless Control Method of a High-speed Dual Three-phase Permanent Magnet Synchronous Motor. In Proceedings of the 2020 23rd International Conference on Electrical Machines and Systems (ICEMS), Hamamatsu, Japan, 24–27 November 2020; pp. 155–160. [CrossRef]
38. Fan, L.; Yang, T.; Rashed, M.; Bozhko, S. Comparative Study Of Back EMF Based Sensorless Control Methods For Dual Three-Phase PMSM. In Proceedings of the 2018 IEEE International Conference on Electrical Systems for Aircraft, Railway, Ship Propulsion and Road Vehicles and International Transportation Electrification Conference (ESARS-ITEC), Nottingham, UK, 7–9 November 2018; pp. 1–6. [CrossRef]
39. Barcaro, M.; Faggion, A.; Bianchi, N.; Bolognani, S. Sensorless Rotor Position Detection Capability of a Dual Three-Phase Fractional-Slot IPM Machine. *IEEE Trans. Ind. Appl.* **2012**, *48*, 2068–2078. [CrossRef]
40. Barcaro, M.; Faggion, A.; Bianchi, N.; Bolognani, S. Predicted and experimental anisotropy of a dual three-phase interior permanent magnet motor for sensorless rotor position control. In Proceedings of the 6th IET International Conference on Power Electronics, Machines and Drives (PEMD 2012), Bristol, UK, 27–29 March 2012; pp. 1–6. [CrossRef]
41. Almarhoon, A.H.; Zhu, Z.Q.; Xu, P.L. Improved Pulsating Signal Injection Using Zero-Sequence Carrier Voltage for Sensorless Control of Dual Three-Phase PMSM. *IEEE Trans. Energy Convers.* **2017**, *32*, 436–446. [CrossRef]
42. Almarhoon, A.H.; Zhu, Z.Q.; Xu, P. Improved Rotor Position Estimation Accuracy by Rotating Carrier Signal Injection Utilizing Zero-Sequence Carrier Voltage for Dual Three-Phase PMSM. *IEEE Trans. Ind. Electron.* **2017**, *64*, 4454–4462. [CrossRef]
43. Wang, K.; Zhang, J.Y.; Gu, Z.Y.; Sun, H.Y.; Zhu, Z.Q. Torque Improvement of Dual Three-Phase Permanent Magnet Machine Using Zero Sequence Components. *IEEE Trans. Magn.* **2017**, *53*, 1–4. [CrossRef]
44. Roetzer, M.; Vollmer, U.; Chen, L.; Kennel, R. Anisotropy-based position estimation approach for symmetrical dual three-phase permanent magnet synchronous machines. In Proceedings of the 2017 IEEE International Symposium on Sensorless Control for Electrical Drives (SLED), Catania, Italy, 18–19 September 2017; pp. 157–164. [CrossRef]
45. Ribeiro, L.; Degner, M.; Briz, F.; Lorenz, R. Comparison of carrier signal voltage and current injection for the estimation of flux angle or rotor position. In Proceedings of the Conference Record of 1998 IEEE Industry Applications Conference. Thirty-Third IAS Annual Meeting (Cat. No.98CH36242), St. Louis, MO, USA, 12–15 October 1998; Volume 1, pp. 452–459. [CrossRef]
46. Yu, K.; Wang, Z. An Online Compensation Method of VSI Nonlinearity for Dual Three-Phase PMSM Drives Using Current Injection. *IEEE Trans. Power Electron.* **2022**, *37*, 3769–3774. [CrossRef]
47. Li, Z.; Feng, G.; Lai, C.; Banerjee, D.; Li, W.; Kar, N.C. Current Injection-Based Multi-parameter Estimation for Dual Three-Phase IPMSM Considering VSI Nonlinearity. *IEEE Trans. Transp. Electrif.* **2019**, *5*, 405–415. [CrossRef]

48. Bin, X.; Luo, X.; Zhu, L.; Zhao, J. Sensorless Control of Dual Three-Phase PMSM with High Frequency Voltage Signal Injection. In Proceedings of the 2019 22nd International Conference on Electrical Machines and Systems (ICEMS), Harbin, China, 11–14 August 2019; pp. 1–4. [CrossRef]
49. Kim, S.; Ha, J.I.; Sul, S.K. PWM Switching Frequency Signal Injection Sensorless Method in IPMSM. *IEEE Trans. Ind. Appl.* **2012**, *48*, 1576–1587. [CrossRef]
50. Hwang, C.E.; Lee, Y.; Sul, S.K. Analysis on Position Estimation Error in Position-Sensorless Operation of IPMSM Using Pulsating Square Wave Signal Injection. *IEEE Trans. Ind. Appl.* **2019**, *55*, 458–470. [CrossRef]
51. Lee, Y.R.; Yoo, J.; Sul, S.K. Switching Frequency Signal-Injection Sensorless Control Robust to Non-Ideal Characteristics of Inverter System for Dual Three-Phase PMSM. In Proceedings of the 2021 IEEE Energy Conversion Congress and Exposition (ECCE), Vancouver, Canada, 10–14 October 2021; pp. 4761–4768. [CrossRef]
52. Chen, H.; Gao, Q.; Zhu, H. Low and zero speed sensorless control of dual three-phase permanent magnet synchronous machines using the fundamental PWM excitation. In Proceedings of the 10th International Conference on Power Electronics, Machines and Drives (PEMD 2020), Online, 15–17 December 2020; Volume 2020, pp. 152–157. [CrossRef]
53. Liu, T.; Zhu, Z.Q.; Wu, X.; Wu, Z.; Stone, D.A.; Foster, M.P. A Position Error Correction Method for Sensorless Control of Dual Three-Phase Permanent Magnet Synchronous Machines. *IEEE Trans. Ind. Appl.* **2022**, *58*, 3589–3601. [CrossRef]
54. Liu, T.; Zhu, Z.; Wu, X.; Wu, Z.; Stone, D.; Foster, M. A Position Error Correction Method for Sensorless Control of Dual Three-Phase Permanent Magnet Synchronous Machines. In Proceedings of the 2021 IEEE International Electric Machines and Drives Conference (IEMDC), Hartford, CT, USA, 17–20 May 2021; pp. 1–7. [CrossRef]
55. Furmanik, M.; Scelba, G.; Rafajdus, P. Fault-Tolerant Sensorless Control for Six-Phase PMSM with Dual Back-EMF Observer. In Proceedings of the 2022 International Symposium on Power Electronics, Electrical Drives, Automation and Motion (SPEEDAM), Sorrento, Italy, 22–24 June 2022; pp. 305–311. [CrossRef]
56. Fang, H.; Xu, J.; Du, Y. A Novel High Frequency Signal Injection Based Sensorless Control Method for Six-Phase FTPMSM System. In Proceedings of the 2019 22nd International Conference on Electrical Machines and Systems (ICEMS), Harbin, China, 11–14 August 2019; pp. 1–6. [CrossRef]
57. Xu, J.; Fang, H.; Liang, Z.; Zhang, B.; Guo, H. Sensorless Fault-Tolerant Control via High-Frequency Signal Injection for Aerospace FTPMSM Drives With Phase Open- and Short-Circuit Faults. *IEEE Trans. Transp. Electrif.* **2022**, *8*, 3401–3410. [CrossRef]
58. Qiu, X.; Ji, J.; Zhou, D.; Zhao, W.; Chen, Y.; Huang, L. A Modified Flux Observer for Sensorless Direct Torque Control of Dual Three-Phase PMSM Considering Open-Circuit Fault. *IEEE Trans. Power Electron.* **2022**, *37*, 15356–15369. [CrossRef]

MDPI